

**TRANSFER TRAJECTORY DESIGN STRATEGIES
INFORMED BY QUASI-PERIODIC ORBITS**

by

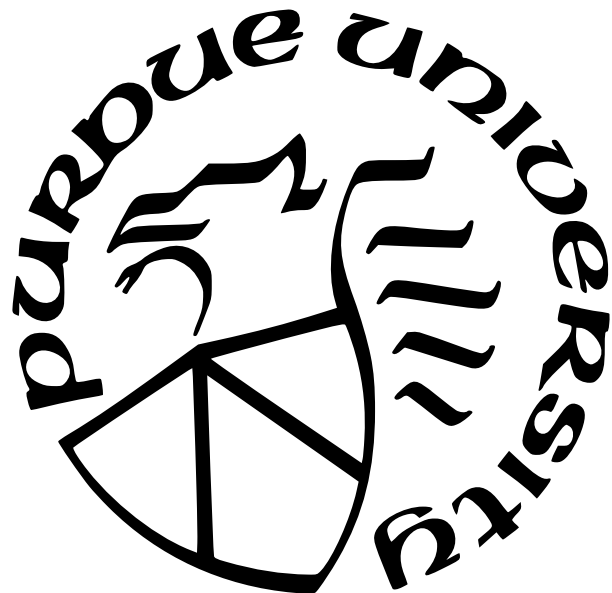
Dhruv Jain

A Thesis

Submitted to the Faculty of Purdue University

In Partial Fulfillment of the Requirements for the degree of

Master of Science in Aeronautics and Astronautics



School of Aeronautics and Astronautics

West Lafayette, Indiana

December 2023

**THE PURDUE UNIVERSITY GRADUATE SCHOOL
STATEMENT OF COMMITTEE APPROVAL**

Dr. Kathleen C. Howell, Chair

School of Aeronautics and Astronautics

Dr. Carolin Frueh

School of Aeronautics and Astronautics

Dr. Kenshiro Oguri

School of Aeronautics and Astronautics

Approved by:

Dr. Gregory A. Blaisdell

To my parents, Vardhman and Ruchi, and my brother Aryan

ACKNOWLEDGMENTS

I am extremely fortunate for the unparalleled love and unwavering support of my parents Vardhman and Ruchi, and my brother Aryan. Mom and Dad, your guidance has instilled in me the values of perseverance, curiosity, and staying centered, along with the importance of focusing on the positives in challenging situations. I am deeply appreciative of all the sacrifices you have made and the leap of faith you took in supporting my pursuit of my passion. Aryan, it is heartening to see you also experiencing the wonders of Purdue University, and I cannot wait to see the exciting journey that lies ahead of you. I am equally grateful to my grandparents and extended family for their role in shaping the person I am today.

I extend my heartfelt gratitude to my advisor, Prof. Kathleen Howell. I vividly remember a keynote speech of yours that I attended during my first semester at Purdue, and it profoundly influenced the trajectory of my life. Learning about astrodynamics under your guidance has been a dream come true. Your work ethic and passion for research and teaching are truly inspiring. I am equally thankful to my committee members, Prof. Carolin Frueh and Prof. Kenshiro Oguri, for their invaluable feedback on my thesis and their mentorship.

I am thankful for the remarkable individuals who have been part of my research group, past and present. Brian, Kenza, Vivek, David, Nick, Collin, Cody, Noah, JP, Liam, Dale, Rohith, Maaninee, Josiah, Ricardo, Nadia, Sam, Jonathon, Alex, Stephen, RJ, Drew, Beom, Colton, Mitch, and Antony, your insights and support have been instrumental in my academic and personal growth. A special thanks to Brian for patiently guiding me when I started learning about the world of QPOs. To my friends, Vidhush, Winston, Pranshul, Jie, Saw and Shreyas, your unwavering encouragement and support mean the world to me.

I would like to express my gratitude to the Engineering Undergraduate Research Office, Minority Engineering Program, Elmore Family School of Electrical and Computer Engineering, and the Honors Engineering Program for providing me with professional development opportunities and financial support during my MSAAE journey.

TABLE OF CONTENTS

LIST OF TABLES	7
LIST OF FIGURES	9
ABSTRACT	15
1 INTRODUCTION	16
1.1 Problem Statement	16
1.2 Previous Contributions	18
1.2.1 Transfer Design Strategies	18
1.2.2 Construction of Quasi-Periodic Orbits and their Use in Transfer Design	19
1.3 Document Overview	20
2 DYNAMICAL MODEL	23
2.1 Circular Restricted Three-Body Problem	24
2.2 Equations of Motion	25
2.3 Equilibrium Solutions	31
2.4 Integral of Motion and Zero Velocity Surfaces	32
2.5 First-Order Linear Variational Equations of Motion	36
3 NUMERICAL METHODS	44
3.1 State Transition Matrix	44
3.2 Differential Correction	46
3.2.1 Single Shooting	49
3.2.2 Multiple Shooting	50
3.3 Numerical Continuation	54
3.3.1 Natural Parameter Continuation	54
3.3.2 Pseudo-Arclength Continuation	55
4 PERIODIC ORBITS	59
4.1 Targeting: Symmetry, Periodicity, and Phase Constraint	59
4.2 Monodromy Matrix and Stability	63
4.3 Hyperbolic Invariant Manifolds	66
4.3.1 Effect of Varying Step-off Distance	68
5 QUASI-PERIODIC ORBITS	71
5.1 Characterization of Quasi-Periodic Behavior	71
5.2 Construction of <i>2-dimensional</i> Quasi-Periodic Tori	76
5.3 Biparametric Families of <i>2-dimensional</i> Quasi-Periodic Tori and Phase Constraints	83
5.3.1 Multiple Shooting for the Construction of Quasi-Periodic Tori	89
5.4 Stability and Hyperbolic Manifolds	97
6 END-TO-END TRANSFER DESIGN FRAMEWORK	102
6.1 Departure and Arrival Periodic Orbits	102
6.2 Intermediate Dynamical Structures	104

6.3	Inbound Segment to the Arrival Orbit	107
6.3.1	Initial Guess Generation	108
6.3.2	Differential Correction	112
6.4	Outbound Segment from the Departure Orbit	122
6.5	Interior-type Transfers	127
6.5.1	Intermediate Periodic Orbits	127
6.5.2	Intermediate Quasi-Periodic Orbits	133
6.5.3	Optimized Transfers	138
6.6	Exterior-type Transfers	140
7	CONCLUDING REMARKS	149
7.1	Recommendations for Future Work	150
A	PLOTS OF PERIODIC ORBITS AND THEIR STABILITY INDICES	152
B	INITIAL CONDITIONS FOR QPT	155
	REFERENCES	157

LIST OF TABLES

2.1	Lagrange points of Earth-Moon and Mars-Phobos system in [nd] units	33
5.1	Characteristic constraints and their partial derivatives	84
6.1	Initial conditions, period, JC value and stability indices of an L_2 9:2 southern NRHO and a DRO.	104
6.2	Initial conditions, period, JC value, and stability indices of the selected intermediate periodic orbits.	105
6.3	Maneuver costs and times of flight of the three transfer options, depicted in Figure 6.15, constructed with an L_2 vertical orbit as the intermediate orbit.	116
6.4	Maneuver costs and times of flight of the two transfer options, depicted in Figure 6.18, constructed with an L_2 vertical orbit as the intermediate orbit.	124
6.5	Maneuver costs and times of flight of the outbound transfer options, depicted in Figure 6.22(a), constructed with an L_2 southern halo orbit as the intermediate orbit.	129
6.6	Maneuver costs and times of flight of the inbound transfer options, depicted in Figure 6.22(b), constructed with an L_2 southern halo orbit as the intermediate orbit.	129
6.7	Maneuver costs and times of flight of the outbound transfer options, depicted in Figure 6.23(a), constructed with an L_2 P2HO ₁ orbit as the intermediate orbit. .	130
6.8	Maneuver costs and times of flight of the inbound transfer options, depicted in Figure 6.23(b), constructed with an L_2 P2HO ₁ orbit as the intermediate orbit. .	130
6.9	Maneuver costs and times of flight of the outbound transfer options, depicted in Figure 6.24(a), constructed with an L_2 P2HO ₂ orbit as the intermediate orbit. .	131
6.10	Maneuver costs and times of flight of the inbound transfer options, depicted in Figure 6.24(b), constructed with an L_2 P2HO ₂ orbit as the intermediate orbit. .	131
6.11	Maneuver costs and times of flight of the two transfer options, depicted in Figure 6.33, constructed with a planar 3:4 RPO as the intermediate orbit.	141
6.12	Maneuver costs and times of flight of the two transfer options, depicted in Figure 6.34, constructed with a DPO as the intermediate orbit.	141
B.1	Initial conditions for an invariant curve on the L_2 quasi-halo ($T^0 = 6.56235$ days, $\rho^0 = 0.80705$ rad, $JC_{\text{avg}} = 3.04606$) in the Earth-Moon system ($\mu = 0.0121506$, $l^* = 384400$ km), depicted in Figure 5.5(c). The torus is obtained through continuation along the constant mapping time family originating from the center subspace associated with an L_2 halo orbit ($JC = 3.04649$, $\mathbb{P} = 6.56235$ days). It is suggested to retarget the torus with $N=45$ initial states of the Fourier series described by the following 25 states.	155

LIST OF FIGURES

2.1	CR3BP inertial and rotational frames	26
2.2	CR3BP important quantities in the rotational frames.	28
2.3	Location of the Lagrange points in the R frame	33
2.4	ZVC and ZVS for $JC = 3.20 > JC_{L_1}$ in the Earth-Moon system.	35
2.5	ZVC and ZVS for $JC_{L_{4,5}} > JC = 3.01 > JC_{L_3}$ in the Earth-Moon system.	35
2.6	In-plane(blue) and out-of-plane(yellow) linear periodic orbits about the L_2 point in the Earth-Moon System.	42
2.7	Linear quasi-periodic orbit around the L_2 point in the Earth-Moon system.	43
3.1	Single shooting method problem setup	49
3.2	Multiple shooting method problem setup	51
3.3	Multiple shooting method problem setup with n nodes	52
3.4	Multiple shooting method intermediate correction step	54
3.5	PALC predicted step schematic. Adapated from Keller [49].	58
4.1	The L_1 Lyapunov orbit family members in the Earth-Moon system and stability index, where crimson: family members with atleast one non-trivial 2 -dimensional center subspace	64
4.2	The northern L_1 halo orbit family members in the Earth-Moon system and stability index, where crimson: family members with atleast one non-trivial 2 -dimensional center subspace	65
4.3	The L_1 vertical orbit family members in the Earth-Moon system and stability index, where crimson: family members with atleast one non-trivial 2 -dimensional center subspace	65
4.4	The stable and unstable global manifolds corresponding to an L_1 Lyapunov orbit	68
4.5	The stable and unstable global manifolds associated with an L_1 halo orbit	69
4.6	Effect of varying step-off distance to approximate unstable manifold arcs associated with nearby fixed points on a periodic orbit	70
5.1	L_1 halo orbit in the Earth-Moon system, $JC = 3.10$ and its apoapse state.	73
5.2	Stroboscopic map about the apoapse state of an L_1 halo orbit in the Earth-Moon system, $JC = 3.10$	74
5.3	Phase states on a QPO defined by θ_{T^0} and θ_{ρ^0} angles.	75

5.4	Schematic of a <i>2-dimensional</i> solution surface representing the biparametric family of QPOs.	85
5.5	A constant mapping time family with $T^0=6.56235$ days originating from an L_2 southern halo orbit ($JC=3.04649$, $T^0=6.56235$ days) in the Earth-Moon system. Three QPT, as identified in the JC_{avg} vs ρ^0 plot, are visualized in the configuration space.	90
5.6	A constant frequency ratio family with $\rho^0=0.08385$ rad emanating from an L_1 Lyapunov orbit ($JC=3.17745$, $T^0=11.86024$ days) in the Earth-Moon system. Three QPT, as identified in the T^0 vs JC_{avg} plot, are shown in the configuration space.	91
5.7	A constant energy family with $JC_{\text{avg}}=1.97268$ originating from an L_4 axial orbit ($JC=1.97268$, $T^0=27.33317$ days) in the Earth-Moon system. Three QPT, as identified in the T^0 vs ρ^0 plot, are depicted in the configuration space.	92
5.8	Multiple shooting schematic for construction of QPT.	93
5.9	The spectrum of eigenvalues of \mathbf{DG}_{qpo} of the QPO depicted in Figure 5.6(c).	98
5.10	Approximation of positive-half global unstable manifold associated with an L_2 quasi-vertical orbit ($JC_{\text{avg}} = 3.04647$, $T^0 = 16.82590$ days) in the Earth-Moon system. The global unstable manifold trajectories(black) associated with $N = 55$ states, for $\nabla = 50$ km, emanating from an invariant curve(purple) are depicted in the plots. Additionally, the surface of manifold states(red) generated at 19.95786 days, 23.0283 days, and 30.39736 days along the manifold are visualized in Figures 5.10(a), 5.10(b) and 5.10(d), respectively. The evolution of manifold states corresponding to three invariant curves(purple, orange, navy) at 0 days and 23.0283 days along the manifold are depicted in Figure 5.10(c).	101
6.1	Interior-type end-to-end transfer schematic.	103
6.2	Exterior-type end-to-end transfer schematic.	103
6.3	An L_2 9:2 NRHO (orange) and a DRO (yellow).	104
6.4	An L_2 vertical (green), L_2 southern halo (orange), L_2 southern P2HO ₁ (crimson), L_2 southern P2HO ₂ (navy) at the same JC value as an L_2 9:2 NRHO.	106
6.5	A planar 3:4 RPO (green) and a DPO (navy) at the same JC value as an L_2 9:2 NRHO	106
6.6	A constant energy family of L_2 quasi-vertical orbits with $JC = 3.04649$. Plot of the evolution of ρ^0 and T^0 values of the QPOs along the family and a member (green) with $\rho^0 = 0.42259$ rad, as well as the underlying periodic orbit (yellow).	107
6.7	A constant energy family of L_2 quasi-P2HO ₂ orbits with $JC = 3.04649$. Plot of the evolution of ρ^0 and T^0 values of the QPOs along the family and a member (green) with $\rho^0 = 1.59184$ rad, as well as the underlying periodic orbit (yellow).	107

6.8	Continuous representation of the DRO of interest is generated through two cubic spline interpolation functions with x position as the independent variable.	109
6.9	Unstable manifold states (black) and manifold arcs (red) associated with an L_2 vertical orbit (green) that cross near a DRO (orange).	110
6.10	Unstable manifold states (black) associated with an L_2 quasi-vertical orbit ($\rho^0 = 0.42259$ rad) that cross near a DRO (orange).	110
6.11	Position and velocity discontinuities between the unstable manifold states associated with an L_2 quasi-vertical orbit ($\rho^0 = 0.42259$ rad) and the corresponding nearest arrival orbit states.	112
6.12	Position and velocity discontinuities between the manifold states corresponding with an L_2 quasi-vertical orbit ($\rho^0 = 0.51490$ rad) and the corresponding nearest arrival orbit states.	113
6.13	Position and velocity discontinuities between the manifold states corresponding with an L_2 quasi-vertical orbit ($\rho^0 = 0.60913$ rad) and the corresponding nearest arrival orbit states.	113
6.14	Position and velocity discontinuities between the manifold states corresponding with an L_2 quasi-vertical orbit ($\rho^0 = 0.64859$ rad) and the corresponding nearest arrival orbit states.	114
6.15	Three converged inbound segments (red) to the DRO (orange) informed by the initial guess generated through an L_2 vertical orbit (green). The transfer arcs require a single impulsive maneuver (black) to overcome the velocity discontinuity with the arrival orbit. The maneuver costs and flight times are tabulated in Table 6.3.	117
6.16	Differential corrected inbound segments to the arrival orbit constructed through the initial guess obtained in Figure 6.11. The solutions in the local basins 1' and 2' are mirror configurations of the options in local basins 1 and 2 about the $\hat{x} - \hat{y}$ plane.	122
6.17	Transfer geometries corresponding to the local basin 1' and 2 as highlighted in Figure 6.16. The local solutions generated with an L_2 quasi-vertical orbit (green) as the intermediate orbit require a single maneuver (pink) to overcome the velocity discontinuity with the arrival orbit state (orange). The time of flight of the transfer arcs plotted above ranges from 26.8 to 28.1 days.	123
6.18	Two converged outbound segments (blue) from an NRHO (orange) informed by the initial guess generated through an L_2 vertical orbit (green). The transfer arcs require a single impulsive maneuver (black) to overcome the velocity discontinuity with the departure orbit. The maneuver costs and flight times are tabulated in Table 6.4.	124

6.19 Position and velocity discontinuities between the stable manifold states associated with an L_2 quasi-vertical orbit ($\rho^0 = 0.42259$ rad) and the corresponding nearest departure orbit states.	125
6.20 Differential corrected inbound segments to the arrival orbit constructed through the initial guess obtained in Figure 6.19 with an L_2 quasi-vertical orbit as the intermediate orbit	125
6.21 Transfer geometries corresponding to the local basin 1, 2, 3, and 4 as highlighted in Figure 6.20. The local solutions generated with an L_2 quasi-vertical orbit (green) as the intermediate orbit require a single maneuver (pink) to overcome the velocity discontinuity with the departure orbit state (orange).	126
6.22 Five converged outbound segments (blue) from an L_2 NRHO (orange) and four inbound segments (red) to a DRO (orange) informed by the initial guess generated through an L_2 southern halo orbit (green). The transfer arcs require a single impulsive maneuver (black) to overcome the velocity discontinuity with the departure/arrival orbit. The departure and arrival maneuver costs and flight times are tabulated in Table 6.5 and Table 6.6, respectively.	129
6.23 Two converged outbound segments (red, blue) from an L_2 NRHO and an inbound segment to a DRO (orange) informed by the initial guess generated through an L_2 P2HO ₁ orbit (green). The transfer arcs require a single impulsive maneuver (black) to overcome the velocity discontinuity with the departure/arrival orbit. The departure and arrival maneuver costs and flight times are tabulated in Table 6.7 and Table 6.8, respectively.	130
6.24 Two converged outbound segments (blue) from an L_2 NRHO (orange) and two inbound segments (red) to the DRO (orange) informed by the initial guess generated through an L_2 P2HO ₂ orbit (green). The transfer arcs require a single impulsive maneuver (black) to overcome the velocity discontinuity with the departure/arrival orbit. The departure and arrival maneuver costs and flight times are tabulated in Table 6.9 and Table 6.10, respectively.	131
6.25 Interior-type end-to-end transfers informed by intermediate periodic orbits. The blue, green and red colored portions of the full-state continuous trajectory are post differential correction remanants of the initial guess of the three segments.	132
6.26 Angular variable representation of stable and unstable manifold step-off locations corresponding to families of differentially corrected outbound and inbound segments constructed through an L_2 quasi-vertical orbits. A candidate $\bar{x}_{\text{int,} \text{arr}}$ state is identified that lies 1 revolution of the intermediate QPO downstream from a $\bar{x}_{\text{int,} \text{dep}}$ state.	134
6.27 Interior-type end-to-end transfer informed by an L_2 quasi-vertical orbit. The blue, green, and red colored portions of the full-state continuous trajectory are post differential correction remanants of the initial guess of the three segments, $\Delta V_{\text{tot}} = \Delta V_{\text{dep}} + \Delta V_{\text{arr}} = 153.213 + 292.010 = 445.223$ m/s, TOF = 69.938 days	135

6.28 Angular variable representation of stable and unstable manifold step-off locations corresponding to families of differentially corrected outbound and inbound segments constructed through an L_2 quasi-P2HO ₂ orbits. A candidate $\bar{x}_{\text{int,arr}}$ state is identified that lies in the immediate upstream of a $\bar{x}_{\text{int,dep}}$ state.	136
6.29 Plot of an outbound and inbound segment corresponding to the selected $\bar{x}_{\text{int,dep}}$ and $\bar{x}_{\text{int,dep}}$ states in Figure 6.28.	137
6.30 Interior-type end-to-end transfer informed by an L_2 quasi-P2HO ₂ orbit. The blue and red colored portions of the full-state continuous trajectory are post differential correction remanants of the initial guess of the two segments, $\Delta V_{\text{tot}} = \Delta V_{\text{dep}} + \Delta V_{\text{arr}} = 7.815 + 473.403 = 481.217$ m/s, TOF = 73.944 days.	137
6.31 Interior-type end-to-end locally mass-optimal transfer initialized by a feasible solution, Figure 6.25(d), that is characterized by an L_2 P2HO ₂ orbit. The blue, green and red colored portions of the full-state continuous trajectory are post-optimization remanants of the three colored arcs along the initial guess, $\Delta V_{\text{tot}} = \Delta V_{\text{dep}} + \Delta V_{\text{arr}} = 232.164 + 231.569 = 463.733$ m/s, TOF = 45.314 days.	139
6.32 Interior-type end-to-end locally mass-optimal transfer initialized by a feasible solution, Figure 6.27, that is characterized by an L_2 quasi-vertical orbit. The blue, green and red colored portions of the full-state continuous trajectory are post-optimization remanants of the three colored arcs along the initial guess, $\Delta V_{\text{tot}} = \Delta V_{\text{dep}} + \Delta V_{\text{arr}} = 220.288 + 141.960 = 362.245$ m/s, TOF = 82.448 days.	139
6.33 Two converged inbound segments (red) to the DRO (orange) informed by the initial guess generated through a planar 3:4 RPO (green). The transfer arcs require a single impulsive maneuver (black) to overcome the velocity discontinuity with the arrival orbit. The maneuver costs and flight times are tabulated in Table 6.11.	141
6.34 Two converged inbound segments (red) to the DRO (orange) informed by the initial guess generated through a DPO (green). The transfer arcs require a single impulsive maneuver (black) to overcome the velocity discontinuity with the arrival orbit. The maneuver costs and flight times are tabulated in Table 6.12.	142
6.35 Unstable manifolds (red) associated with an L_2 vertical orbit (green) propagated till the first crossing of a Poincaré map at y=0 on the far-side of the Earth.	143
6.36 Exterior-type end-to-end differentially corrected and optimized transfers informed by an L_2 vertical orbit and a 3:4 RPO. The outbound segment from an NRHO to the far-side of the Earth (blue) requires a maneuver to overcome the velocity discontinuity with the inbound segment from the far-side of the Earth to a DRO (red).	145

6.37 Exterior-type end-to-end differentially corrected and optimized transfers informed by an L_2 quasi-vertical orbit and a 3:4 RPO. The outbound segment from an NRHO to the far-side of the Earth (blue) requires a maneuver to overcome the velocity discontinuity with the inbound segment from the far-side of the Earth to a DRO (red).	146
6.38 Exterior-type end-to-end differentially corrected and optimized transfers informed by an L_2 P2HO ₂ orbit and a DPO. The outbound segment from an NRHO to the far-side of the Earth (blue) requires a maneuver to overcome the velocity discontinuity with the inbound segment from the far-side of the Earth to a DRO (red).	147
6.39 Exterior-type end-to-end differentially corrected and optimized transfers informed by an L_2 quasi-P2HO ₂ orbit and a DPO. The outbound segment from an NRHO to the far-side of the Earth (blue) requires a maneuver to overcome the velocity discontinuity with the inbound segment from the far-side of the Earth to a DRO (red).	148
A.1 The L_2 Lyapunov orbit family members in the Earth-Moon system and stability index, where crimson: family members with atleast one non-trivial <i>2-dimensional</i> center subspace	152
A.2 The southern L_2 halo orbit family members in the Earth-Moon system and stability index, where crimson: family members with atleast one non-trivial <i>2-dimensional</i> center subspace	152
A.3 The L_2 vertical orbit family members in the Earth-Moon system and stability index, where crimson: family members with atleast one non-trivial <i>2-dimensional</i> center subspace	153
A.4 The northern L_4 axial orbit family members in the Earth-Moon system and stability index, where crimson: family members with atleast one non-trivial <i>2-dimensional</i> center subspace	153
A.5 The Moon-centered distant prograde orbit family members in the Earth-Moon system and stability index, where crimson: family members with atleast one non-trivial <i>2-dimensional</i> center subspace	154

ABSTRACT

In the pursuit of establishing a sustainable space economy within the cislunar region, it is vital to formulate transfer design strategies that uncover economically viable highways between different regions of the space domain. The inherent complexity of spacecraft dynamics in the cislunar space poses challenges in determining feasible transfer options. However, the motion characterized by known dynamical structures modeled through the circular restricted three-body problem (CR3BP) aids in the identification of pathways with reasonable maneuver costs and flight times. A framework is proposed that incorporates a quasi-periodic orbit (QPOs) as an option to design transfer scenarios. This investigation focuses on the construction of transfers between periodic orbits. The framework is exemplified by the construction of pathways between an L_2 9:2 synodic resonant Near-Rectilinear Halo Orbit (NRHO) and a planar Moon-centered Distant Retrograde Orbit (DRO). The innate difference in the geometries of the departure and arrival orbits of the sample case, along with the lack of natural flows towards and away from them, imply that links between these orbits may necessitate costly maneuvers. A strategy is formulated that leverages the stable and unstable manifolds associated with intermediate periodic orbits and quasi-periodic orbits to construct end-to-end trajectories. As part of this strategy, a systematic methodology is outlined to streamline the determination of transfer options provided by the *5-dimensional* manifolds associated with a QPO family. This approach reveals multiple local basins of solutions, both interior and exterior-types, characterized by selected intermediate orbits. The construction of transfers informed by the manifolds associated with QPOs is more intricate than those based on periodic orbits. However, QPO-derived solutions allow for the recognition of alternative local basins of solutions and often offer more cost-effective transfer options when compared to trajectories designed using periodic orbits that underlie the QPOs.

1. INTRODUCTION

The recent surge in interest surrounding cislunar space exploration, surveillance, and the establishment of sustainable infrastructure has attracted significant attention in both private and public sectors. Notably, numerous private companies and government organizations have allocated substantial resources to lunar exploration efforts, as exemplified by missions such as Luna-25, Chandrayaan-3, Chang-5, Hakutro-R, and IM-1 [1]–[5]. Additionally, NASA is leading the Artemis program to establish a sustainable human presence on and around the Moon through the planned Gateway space station and Human Landing System [6], [7]. Concurrently, China plans to deploy a manned research station on a lunar pole along with the necessary infrastructure by 2035 [8]. The expected proliferation of multi-billion dollar assets in cislunar regime has spurred heightened surveillance efforts and the development of essential technologies by defense agencies. The U.S. Air Force Research Laboratory is poised to launch the Oracle spacecraft by 2026, specifically designed to showcase technologies sought after by the U.S. Space Force and the Department of Defense for identifying and tracking objects within cislunar space [9]. Moreover, the first National Cislunar Science and Technology Strategy of the U.S. government underscores the perceived significance of cislunar space and the anticipated uptick in activities in the region by the government [10]. For the upcoming endeavors in cislunar space to be sustainable, it is imperative to identify viable pathways that enable efficient travel between different regions of this space domain, all while adhering to practical fuel constraints, reasonable flight durations, and operational feasibility.

1.1 Problem Statement

The design of low-cost transfer highways is challenging due to the chaotic dynamics of a spacecraft in the cislunar space. A specific problem of constructing pathways in the cislunar space is the transfer design between periodic orbits. The solutions of this general scenario can be fuel-expensive to traverse through due to the possible inherent difference in the geometry of the departure and arrival orbits. An additional challenge is posed if the departure and arrival periodic orbits do not possess natural flows away and towards the orbits, respectively. A sample case of such a problem is the design of transfer options between an L_2 9:2 NRHO in

the Earth-Moon system and a planar Moon-centered DRO. These two orbits are of particular interest as NASA plans to leverage an L_2 9:2 NRHO to host the Gateway [6]. Additionally, planar DROs are advantageous in positioning a spacecraft to remain in the vicinity of the Moon as exemplified by the Artemis 1 mission that leveraged a DRO to test the Orion vehicle’s capabilities in the proximity of the Moon [11]. The motion of a spacecraft in the cis-lunar space is fundamentally governed by the gravity of the Earth and the Moon. Consequently, to reduce the complexity of modeling the trajectories in the cis-lunar space the CR3BP model is employed, instead of an ephemeris model. Furthermore, the CR3BP model allows for the application of dynamical systems theory to identify dynamical structures, i.e. periodic and quasi-periodic orbits, as well as their associated stable and unstable invariant manifolds. These structures assist in characterizing the phase space of the system and inform the design of transfer trajectories.

A methodology is presented that leverages a quasi-periodic orbit as an option for design of transfer scenarios. The objectives of this investigation are to:

- Construct families of *2-dimensional* quasi-periodic orbits and their associated stable and unstable invariant manifolds.
- Define a framework that leverages intermediate dynamical structures to uncover transfer highways.
- Assess the local solution basins for interior-type and exterior-type transfer geometries.

Quasi-periodic orbits characterize a greater hypervolume of phase space than periodic orbits due to their higher dimensionality. Thus, QPOs assist in identifying solutions that are commonly not captured by periodic orbits. However, it is more complicated to incorporate the manifolds associated with QPOs in the design process compared to periodic orbits. The methodology defined in this investigation demonstrates a systematic approach to leverage stable and unstable manifolds associated with periodic orbits and constant energy families of *2-dimensional* quasi-periodic orbits for preliminary end-to-end transfer design. Consequently, the strategy extends the known local solution basins of the sample case.

1.2 Previous Contributions

The trajectory design problem in multi-body regimes commonly relies on user-supplied initial guess and numerical methods to refine the guess. The initial guess formulation is complicated due to the chaotic dynamics of a spacecraft in multi-body systems. A spectrum of strategies have been formulated by several researchers to construct feasible transfer pathways. The spectrum of techniques, on one end, exploits the known dynamical structures and on the other end relies on extensive grid search. In general, the techniques that rely on known dynamical structures offer low-cost families of solutions but require the identification of desirable structures. Conversely, grid search-dependent methods potentially assist in locating a point mass or time-optimal solution. However, it is commonly challenging to modify the point solution to meet additional desirable constraints. The previous works across the spectrum of techniques that influence the formulation of the proposed end-to-end transfer design strategies are discussed below. Additionally, the contributions of many authors are listed that assist in the construction of quasi-periodic orbits and their associated stable and unstable invariant manifolds, as well as their use in transfer trajectory design.

1.2.1 Transfer Design Strategies

For the problem scenario, Zimovan-Spreen et al. exploit known periodic orbits and their associated manifolds to facilitate the transfer trajectory design process to uncover interior-type and exterior-type transfers [12]. Pritchett et al. and Prado et al. leverage periodic orbit chaining techniques to construct feasible interior-type transfers [13], [14]. Muralidharan and Howell employ stretching directions corresponding to the departure and arrival orbits to constrain the computation of interior and exterior-type class of solutions [15]. Vutukuri utilizes resonant periodic orbits and tangential maneuvers for recognition of exterior-type transfers [16]. Das formulates a framework to identify "Accessible Regions" through machine learning techniques to inform exterior-type transfer design process [17]. McCarty et al. use monotonic basin hopping to locate a feasible exterior transfer [18]. Lantoine considers a patched model approach that incorporates the solar perturbation, a DPO family, and a grid search to produce exterior-type transfer geometries [19]. The alternative methodologies

assist in the identification of various pathways to initialize the design process, and no single framework captures all the solutions.

1.2.2 Construction of Quasi-Periodic Orbits and their Use in Transfer Design

The construction of *2-dimensional* Quasi-Periodic Orbits for mission design has been investigated by numerous researchers since the 1970s. Farquhar and Kamel, as well as Richardson and Cary, presented analytical approximation of QPOs near collinear Lagrange points using the Lindstedt-Poincaré method and method of dual time scales, respectively [20], [21]. While these analytical methods provide insights into local dynamics, their accuracy is confined to regions near the Lagrange points and for short flight times. Howell and Pernicka built on the previously developed analytical methods to devise a numerical scheme for the determination of continuous quasi-periodic trajectories [22]. The numerical framework enables the computation of multiple revolutions on a quasi-periodic torus and extends to QPOs that are further away from the Lagrange point. But it does not capture the flow along an entire invariant torus and is not intuitive for the computation of the biparametric family of QPOs. In the 1990s, Gómez et al., as well as Jorba and Masdemont introduced semi-analytical procedures for constructing QPOs [23], [24]. Gómez and Mondelo further extended these methods into a purely numerical technique, enabling the computation of QPT across a wider region of interest [25]. Olikara and Scheers modified Gómez's and Mondelo's numerical scheme and termed it the GMOS algorithm [26]. The GMOS algorithm is more intuitive and model-agnostic compared to its predecessor. The algorithm has gained widespread acceptance as a reliable choice for the construction of QPOs as evidenced by the work of McCarthy [27], Romero [28], Damennick et al. [29], Bonasera [30], and others. The popularity of the algorithm is in part due to the computational efficiency and accuracy advantages over a few other numerical techniques, as outlined in the study carried out by Baresi et al.[31]. However, it is worth noting that other algorithms also exist, as demonstrated by Haro et al. [32] and Kumar et al. [33]. The aforementioned authors even describe techniques to approximate the stable/unstable manifolds associated with a QPO to allow for their use in transfer design.

In some scenarios, it is advantageous to incorporate quasi-periodic orbits to construct transfers. Gómez et al., Calleja et al., Dammenick et al. and McCarthy et al. employ the manifolds associated with QPOs to construct heteroclinic connections between QPOs, as well as QPOs and periodic orbits [29], [34]–[36]. Restrepo et al. leverage the manifolds associated with a Lissajous orbit to design Europa lander trajectories [37]. Folta et al. utilizes the stable/unstable manifolds corresponding to Lissajous orbits to design the ARTEMIS mission trajectory [38]. McCarthy incorporates QPOs to design transfers between periodic orbits and their corresponding manifolds to construct ballistic lunar transfers [27]. This investigation extends the methodologies formulated by previous authors to define a framework that leverages the stable/unstable manifolds associated with a QPO as an option to design end-to-end transfer trajectories.

1.3 Document Overview

The main objective of this research effort is to define a transfer design framework that incorporates a quasi-periodic orbit as an option. The theory and numerical tools to accomplish the same are presented in this document and organized as follows:

- **Chapter 2:** In this chapter, the dynamical model employed in this investigation is described. It includes the assumptions made to the \mathfrak{N} -body problem to devise the CR3BP model, as well as the derivation of non-dimensionalized equations of motion of the model in a rotating frame. Additionally, the computation of the five equilibrium points of the model and an integral of motion are presented. The concept of zero-velocity surfaces is also introduced. The first-order variational equations of motion about the Lagrange points are derived and leveraged to identify linear periodic and quasi-periodic orbits around the collinear Lagrange points.
- **Chapter 3:** Due to the absence of a useful analytical solution for the CR3BP model, numerical methods are utilized to design trajectories with desirable characteristics. The concept of the state transition matrix is described. The idea of single shooting and multiple shooting methods are elucidated with an example. Additionally, numer-

ical continuation schemes, specifically natural parameter continuation and pseudo-arc length continuation, are discussed for the construction of families of solutions.

- **Chapter 4:** Differential corrections schemes to construct periodic orbits by leveraging the symmetry properties of the model and their periodicity are described. Additionally, their stability properties are identified through the construction of a monodromy matrix. A metric termed the stability index is leveraged to capture the Lyapunov stability properties and presented for a number of periodic orbit families in the Earth-Moon system. A technique to approximate the stable and unstable manifolds associated with a periodic orbit is also presented.
- **Chapter 5:** The behavior of the flow along a quasi-periodic orbit is detailed and exploited for the construction of QPOs. The GMOS algorithm is described for the computation of QPOs. The construction of the biparametric families of QPOs is decomposed into the computation of three uniparametric families: constant mapping time, constant frequency ratio, and constant energy family. A set of initial conditions for the construction of QPOs is also included. Additionally, a multiple shooting scheme for the construction of the three families is detailed. Thereafter, the Lyapunov stability property of QPOs is assessed via a monodromy-like matrix and a technique to estimate the corresponding stable/unstable manifolds is presented.
- **Chapter 6:** This chapter details the proposed strategies that leverage the stable and unstable manifolds associated with periodic and quasi-periodic orbits to design transfers between an L_2 NRHO and a DRO. The properties of the selected departure and arrival orbits, as well as intermediate orbits, are specified. Two classes of transfers are constructed: interior-type and exterior-type. The design of the two transfer types is decomposed into multiple segments. The initial guess-generation strategy for each segment, along with the differential correction schemes to refine the guess are elucidated. A visualization technique is presented that aids in the comparison of solutions offered by different QPOs along the constant energy family and the design of bridging arcs along a QPO. The resultant end-to-end geometries are visualized and the associ-

ated maneuver costs and flight times are tabulated. Lastly, a constraint optimization scheme is leveraged to uncover locally mass-optimal solutions.

- **Chapter 7:** A summary of the results obtained from the proposed framework is presented, along with concluding remarks and recommendations for future work.

2. DYNAMICAL MODEL

The dynamics of a spacecraft are modeled by constructing a mathematical framework that incorporates the various forces acting on it. Ultimately, an exhaustive list of forces influences the dynamics of a spacecraft, including gravitational forces, electromagnetic forces, aerodynamic forces, relativistic forces, solar radiation pressure, and others. This investigation is focused on the preliminary design of motion in a multi-body regime, dynamical structures as well as transfer trajectories in the neighborhood of a planet-moon system. Thus, it is reasonable to accommodate only the gravitational effects of the nearby celestial bodies in the mathematical framework.

The \mathfrak{N} -body problem is employed to mathematically describe the dynamics of a centrobaric spacecraft under the gravitational influence of $\mathfrak{N}-1$ centrobaric bodies in a closed system. But the model is challenging for application even in preliminary design and dynamical analysis. The model is realized by the application of the second law of motion, from Sir Isaac Newton as presented in the *Principia* [39]. It is mathematically expressed as,

$$m_i \bar{R}_i'' + \tilde{G} \sum_{\substack{j=1 \\ j \neq i}}^{\mathfrak{N}} \frac{m_i m_j}{R_{ji}^2} \hat{R}_{ji} = m_i \bar{R}_i'' + \tilde{G} \sum_{\substack{j=1 \\ j \neq i}}^{\mathfrak{N}} \frac{m_i m_j}{R_{ji}^3} \bar{R}_{ji} = 0 \quad (2.1)$$

$$\bar{R}_{ji} = \bar{R}_j - \bar{R}_i \quad (2.2)$$

where, m_j is the mass of the j^{th} centrobaric body, \bar{R}_j is the position vector of the j^{th} body with respect to an inertial observer in an inertial frame, \tilde{G} is the universal gravitational constant ($\approx 6.674 \times 10^{-11} \text{ m}^3 \text{kg}^{-1} \text{s}^{-2}$), and \bar{R}_i'' is the second time derivative of the position vector of the i^{th} body from the origin and the time is in seconds. In this investigation, the time derivative of a parameter with respect to the dimensional time, t , is represented using the prime notation as in the case for \bar{R}_i'' . The equation of motion, Equation (2.1), requires $6\mathfrak{N}$ integrals of motion to be analytically solvable, or $6\mathfrak{N}$ initial states of the \mathfrak{N} bodies to be numerically simulated. There are only 10 known integrals of motion that are derived through translational symmetry (6 integrals), rotational symmetry (3 integrals), and conservation of energy (1 integral) as detailed by Meyer et al.[40]. Even for the simplest case, i.e., a model

with $\mathfrak{N}=2$ there exists no closed-form analytical solution as it is defined by 12 first-order equations of motion, requiring more than the 10 known integrals of motion. In addition, it is challenging to identify the initial states of the \mathfrak{N} bodies as the lack of an analytical solution precludes any knowledge of the innate flows, and it is infeasible to obtain initial conditions that would lead to the desired behaviors by relying on trial-and-error. Due to the stated challenges, the use of the model for the purpose of preliminary design is not appropriate but the model is essential for the validation of designs formulated in lower-fidelity models.

A lower-fidelity model is straightforwardly derived from the \mathfrak{N} -body problem by assuming that the effects of only a handful of the celestial bodies are incorporated to determine the fundamental motion of a spacecraft possibly with some other simplifying assumptions. The assumptions reduce the complexity of the problem but even the general two-body model ($\mathfrak{N}=2$) does not have a closed-form analytical solution. However, the two-body problem is commonly formulated as a relative two-body problem to produce a closed-form analytical solution. The relative two-body problem is an effective model to realize the dynamics of a spacecraft if only one other body dominates the fundamental behavior of the spacecraft but often more than one celestial body significantly influences the dynamics. It may be necessary to consider the influence of at least two dominating celestial bodies to capture the foundational geometries of a spacecraft that would exist when it is transitioned to the \mathfrak{N} -body problem. However, it is challenging to analyze the motion of a spacecraft in a general three-body system due to the lack of an analytical solution. Nonetheless, certain assumptions ease the analysis of the behavior of a spacecraft under the significant influence of two celestial bodies.

2.1 Circular Restricted Three-Body Problem

Circular Restricted Three-Body Problem (CR3BP) is a useful model to understand the motion of a spacecraft in a three-body system. The three centrobaric bodies are referenced as P_1 , P_2 , P_3 with mass m_1 , m_2 , m_3 , respectively, where $m_1 \geq m_2 > m_3$. The model is deduced by adding three assumptions beyond those in the general three-body problem, i.e., the $\mathfrak{N}=3$ case of the \mathfrak{N} -body problem. The assumptions are as follows:

1. The mass of P_3 is negligible compared to P_1 and P_2 ($m_1, m_2 \gg m_3$). It is a reasonable assumption for a spacecraft in a planet-moon or star-planet system.
2. The infinitesimal mass body, P_3 , does not influence the motion of P_1 and P_2 . Thus, the motion of the P_1 and P_2 is modeled as the relative two-body problem. Hence, P_1 and P_2 lie in the same plane.
3. In the relative two-body problem, the only closed-form motion is an ellipse. The P_1 and P_2 (primary bodies) are assumed to move in a particular type of ellipse, i.e., in a circular orbit relative to their barycenter (B) and each other. Hence, the mean motion (\underline{N}) of the primary system is *constant*, and the equations of motion are time-invariant in a rotating reference frame.

Note that P_3 potentially moves in any spatial dimension. The model is a Hamiltonian system and chaotic in nature as elucidated by Szebehely [41]. The simplifying assumptions allow for the application of dynamical systems theory that assists in the analysis and characterization of global dynamics.

2.2 Equations of Motion

The CR3BP equations of motions are formulated in a rotational frame (R) rather than an inertial frame (I) as a R frame offers some advantages. The two reference frames are defined as:

- Inertial frame (I), $\hat{X} - \hat{Y} - \hat{Z}$: dextral orthogonal triad, centered at $P_1 - P_2$ barycenter (B), $\hat{X} - \hat{Y}$ plane spans the $P_1 - P_2$ orbital plane and \hat{Z} is parallel to the $P_1 - P_2$ angular momentum vector.
- Rotating frame (R), $\hat{x} - \hat{y} - \hat{z}$: dextral orthogonal triad, centered at B , \hat{x} is parallel to $B - P_2$ vector and \hat{z} is parallel to the $P_1 - P_2$ angular momentum vector.

The R frame moves with the line joining the primaries about the $P_1 - P_2$ angular momentum vector with an angle θ with respect to the I frame. As the mean motion of the primaries is constant, the first-time derivative of θ , θ' , is also constant. The relationship between the

two frames and the position vector of P_3 with respect to the barycenter, \bar{R}_3 , is illustrated by Figure 2.1.

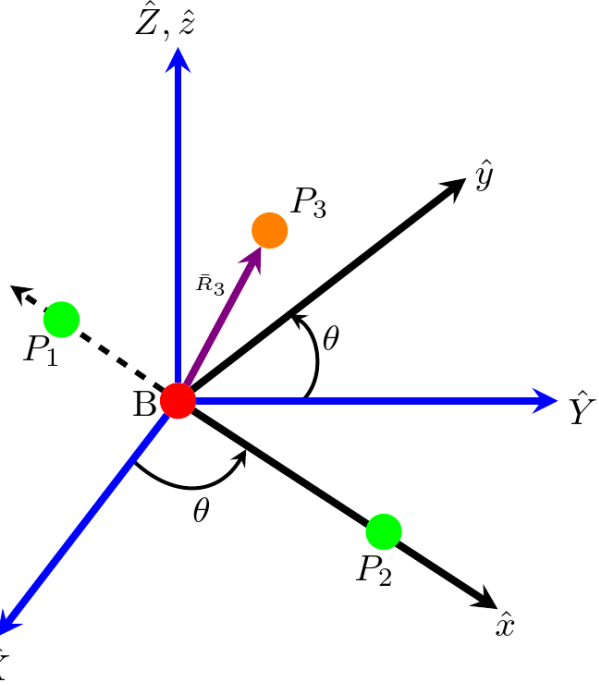


Figure 2.1. CR3BP inertial and rotational frames

The equations of motion of a spacecraft (P_3) in CR3BP as viewed in the R frame are derived through a two-step process. Initially, the equations are devised in the I frame by leveraging the assumptions of the framework on the general three-body problem. Subsequently, the basic kinematic equation is employed for frame change from an observer in the I frame to the R frame. The equations of motion for the general three-body problem in the I frame are represented as a simplified form of Equation (2.1), expressed as,

$${}^I\ddot{\bar{R}}_3'' = -\tilde{G}\frac{m_1}{R_{13}^3}\bar{R}_{13} - \tilde{G}\frac{m_2}{R_{23}^3}\bar{R}_{23} \quad (2.3)$$

The equations as formulated in the R frame ascertains an integral of motion as well as a set of equilibrium solutions of the system. In addition, the equations are autonomous as a consequence of the choice of the R frame and due to the assumption that the primaries are in circular orbits. To reformulate the Equation (2.3), consider the left side of the equation and

let \bar{R}_3 be arbitrarily represented in terms of rotational coordinates as $X_r\hat{x} + Y_r\hat{y} + Z_r\hat{z}$. Due to the circular assumption of the model, the angular velocity of the R frame with respect to the I frame is constant and represented as ${}^I\bar{\omega}^R = \underbrace{N}_{\hat{z}}\hat{z} = \theta'\hat{z}$. The kinematic expansion for velocity and acceleration of P_3 in terms of the rotating frame is thus written as,

$${}^I R'_3 = \frac{{}^R dR_3}{dt} + {}^I \bar{\omega}^R \times R_3 = (X'_r - \theta' Y_r)\hat{x} + (Y'_r + \theta' X_r)\hat{y} + Z'_r\hat{z} \quad (2.4)$$

$${}^I R''_3 = \frac{{}^R d^2 R_3}{dt^2} + {}^I \bar{\omega}^R \times \frac{{}^R dR_3}{dt} = (X''_r - 2\theta' Y'_r - \theta'^2 X_r)\hat{x} + (Y''_r + 2\theta' X''_r - \theta'^2 Y_r)\hat{y} + Z''_r\hat{z} \quad (2.5)$$

The position vectors of P_3 relative to the primaries are defined in terms of the \bar{R}_3 and the position of the primaries. The position vector of P_1 and P_2 as expressed in the R frame are $-D_1\hat{x}$ and $D_2\hat{x}$, respectively, and are illustrated in Figure 2.2. Thus, \bar{R}_{13} and \bar{R}_{23} are represented as,

$$\bar{R}_{13} = (X_r + D_1)\hat{x} + Y_r\hat{y} + Z_r\hat{z} \quad (2.6)$$

$$\bar{R}_{23} = (X_r - D_2)\hat{x} + Y_r\hat{y} + Z_r\hat{z} \quad (2.7)$$

By substituting Equations (2.5) to (2.7) to Equation (2.3), and rearranging the terms, the scalar differential equations in the R frame are expressed as,

$$\hat{x} : X''_r - 2\theta' Y'_r - \theta'^2 X_r = -\tilde{G} \frac{m_1}{R_{13}^3} (X_r + D_1) - \tilde{G} \frac{m_2}{R_{23}^3} (X_r - D_2) \quad (2.8)$$

$$\hat{y} : Y''_r + 2\theta' X'_r - \theta'^2 Y_r = -\tilde{G} \frac{m_1}{R_{13}^3} Y_r - \tilde{G} \frac{m_2}{R_{23}^3} Y_r \quad (2.9)$$

$$\hat{z} : Z''_r = -\tilde{G} \frac{m_1}{R_{13}^3} Z_r - \tilde{G} \frac{m_2}{R_{23}^3} Z_r \quad (2.10)$$

where

$$R_{13} = [(X_r + D_1)^2 + Y_r^2 + Z_r^2]^{1/2} \quad (2.11)$$

$$R_{23} = [(X_r - D_2)^2 + Y_r^2 + Z_r^2]^{1/2} \quad (2.12)$$

It is apparent from the above formulation that the equations of motion admit two singularities located at the two primaries. Thus, caution is necessary when simulating the motion close to the primaries but these singularities are removed by regularization as detailed by Szebehely [41] and Howell [42].

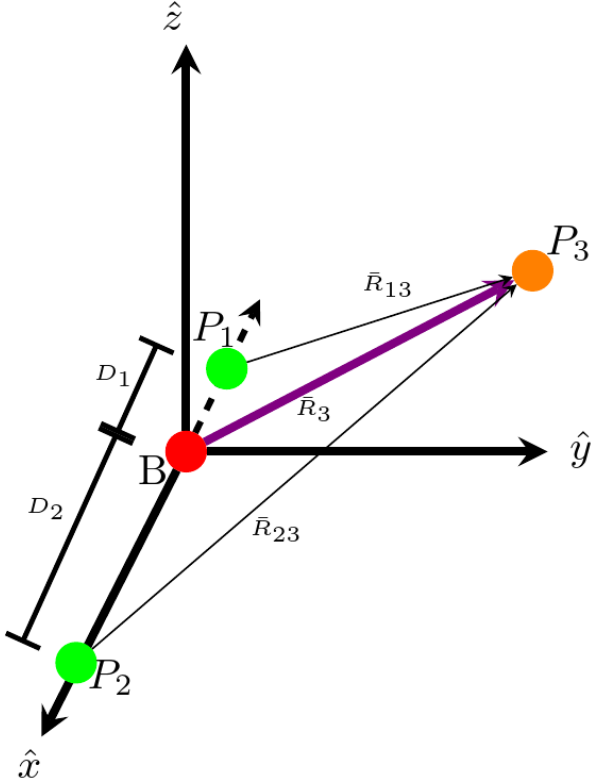


Figure 2.2. CR3BP important quantities in the rotational frames.

The analysis of the behavior of P_3 relies on the implementation of numerical approaches and the dynamical systems theory, thus, the Equations (2.8) to (2.10) are nondimensionalized. Nondimensionalization is advantageous as it minimizes round-off errors by converting the position and velocity states to the same order of magnitude, and the solutions are extrapolatable to a different primary system with similar characteristic quantities. Nondimensionalization of the equations of motion is accomplished by introducing the characteristic quantities of the system. The three characteristic quantities are the characteristic mass

(m^*) , characteristic length (l^*), and characteristic time (t^*), and they are mathematically described as follows,

$$m^* = m_1 + m_2 \quad (2.13)$$

$$l^* = D_1 + D_2 \quad (2.14)$$

$$t^* = \sqrt{\frac{l^{*3}}{\tilde{G}m^*}} \quad (2.15)$$

The characterisitc mass, m^* , gives rise to a helpful quantiy called CR3BP mass ratio (μ), and it is described as,

$$\mu = \frac{m_2}{m^*}; 1 - \mu = \frac{m_1}{m^*} \quad (2.16)$$

The characterisitc time, t^* , is specifically defined to yield a nondimensional value for the gravitational constant that is unity as well as a unity value for the nondimensional mean motion. The nondimensional form of the gravitational constant (\tilde{G}) and mean motion (\underline{N}) is presented below,

$$G = \tilde{G} \frac{m^* t^{*2}}{l^{*3}} = 1 \quad (2.17)$$

$$\underline{n} = \underline{N} t^2 = \sqrt{\frac{\tilde{G}m^*}{l^{*3}}} \sqrt{\frac{l^{*3}}{\tilde{G}m^*}} = 1 \quad (2.18)$$

In addition, the position vectors and distances in nondimensional units [nd] are evaluated as,

$$\bar{r}_j = \frac{\bar{R}_j}{l^*}; x = \frac{X_r}{l^*}; y = \frac{Y_r}{l^*}; z = \frac{Z_r}{l^*}; \quad (2.19)$$

Similarly, for time in [nd],

$$\tau = \frac{t}{t^*} \quad (2.20)$$

The velocity and acceleration quantities are related as,

$$\dot{x} = X'_r \frac{t^*}{l^*} \quad (2.21)$$

$$\ddot{x} = X''_r \frac{t^{*2}}{l^*} \quad (2.22)$$

It is apparent from the above equations that in this investigation, the time derivatives with respect to nondimensional time are represented through the dot notation. In addition, the position of the primaries from the barycenter are written in terms of μ and l^* by using the center of mass definition,

$$0\hat{x} = \frac{-m_1 D_1 + m_2 D_2}{m_1 + m_2} \hat{x} = (-(1 - \mu)D_1 + \mu D_2)\hat{x} \quad (2.23)$$

$$\implies D_1 = \mu l^*; D_2 = (1 - \mu)l^* \quad (2.24)$$

Using the definitions from Equations (2.17), (2.18), (2.20) to (2.22) and (2.24), the scalar differential equations Equations (2.8) to (2.10) in the nondimensional form are expressed as,

$$\hat{x} : \ddot{x} - 2\underbrace{n}_n \dot{y} - \underbrace{n^2}_n x = -\frac{(1 - \mu)(x + \mu)}{r_{13}^3} - \frac{\mu(x - 1 + \mu)}{r_{23}^3} \quad (2.25)$$

$$\hat{y} : \ddot{y} + 2\underbrace{n}_n \dot{x} - \underbrace{n^2}_n y = -\frac{(1 - \mu)y}{r_{13}^3} - \frac{\mu y}{r_{23}^3} \quad (2.26)$$

$$\hat{z} : \ddot{z} = -\frac{(1 - \mu)z}{r_{13}^3} - \frac{\mu z}{r_{23}^3} \quad (2.27)$$

where

$$r_{13} = [(x + \mu)^2 + y^2 + z^2]^{1/2} \quad (2.28)$$

$$r_{23} = [(x - 1 + \mu)^2 + y^2 + z^2]^{1/2} \quad (2.29)$$

Note that $\underbrace{n}_n = 1$ in the above formulation. The state history for the motion of P_3 is evaluated by numerically integrating Equations (2.25) to (2.27) given an initial position, velocity, and time-of-flight in the nondimensional units for a $P_1 - P_2$ system of known μ and l^* . A few reliable choices of numerical integration schemes for the CR3BP are variable

step Runge-Kutta 8(9) or Prince-Dormand 8(9) as mentioned by Folta et al. [43], or Runge-Kutta-Fehlberg 7(8) [44].

The equations of motion are alternatively expressed in terms of a pseudo-potential function. The pseduo-potential function that corresponds to Equations (2.25) to (2.27) is formulated as,

$$\Omega = \frac{x^2 + y^2}{2} + \frac{1 - \mu}{r_{13}} + \frac{\mu}{r_{23}} \quad (2.30)$$

The equations of motion are then represented using the pseudo-poential function as,

$$\hat{x} : \ddot{x} - 2\dot{y} = \Omega_x \quad (2.31)$$

$$\hat{y} : \ddot{y} + 2\dot{x} = \Omega_y \quad (2.32)$$

$$\hat{z} : \ddot{z} = \Omega_z \quad (2.33)$$

The compact form of the equations allows an integral of motion for the system to emerge in terms of the pseduo-potential function.

The global dynamics in the CR3BP are characterized by the equilibrium, periodic, and quasi-periodic solutions, as well as some chaotic behaviors. For the well-behaved structures, three sets of solutions are topologically represented as *n-dimensional* invariant tori, where equilibrium solutions are *0-dimensional* tori, periodic orbits are *1-dimensional* tori and quasi-periodic orbits are *n-dimensional* tori ($n \geq 2$) [45]. The three types of solutions are examined in this investigation in the increasing order of dimensionality.

2.3 Equilibrium Solutions

The equilibrium solutions are points where the P_3 is stationary, i.e. its velocity and acceleration are zero. These solutions are essential in computing higher-dimensional solutions. There are five equilibrium solutions associated with Equations (2.25) to (2.27), labeled the

Lagrange or libration points and all lie in the $\hat{x} - \hat{y}$ plane. The equilibrium solutions are solutions of the following equations, i.e., the reduced form of Equations (2.25) to (2.27),

$$x_{eq}(r_{13,eq}^3 r_{23,eq}^3) - (1 - \mu)(x_{eq} + \mu)r_{23,eq}^3 - \mu(x_{eq} - 1 + \mu)r_{13,eq}^3 = 0 \quad (2.34)$$

$$y_{eq}(r_{13,eq}^3 r_{23,eq}^3 - (1 - \mu)r_{23,eq}^3 - \mu r_{13,eq}^3) = 0 \quad (2.35)$$

$$z_{eq}((1 - \mu)r_{23,eq}^3 + \mu r_{13,eq}^3)r_{13,eq}^3 r_{23,eq}^3 = 0 \quad (2.36)$$

It is evident from Equation (2.36) that $z_{eq} = 0$ is its only physically feasible solution, so all the equilibrium solutions are planar. In addition, Equation (2.35) results in two feasible in-plane solutions: $y_{eq} = 0$ and $r_{13,eq} = r_{23,eq} = 1$. For $y_{eq} = 0$ case, Equation (2.34) further reduces to the following,

$$x_{eq}((x_{eq} + \mu)^3(x_{eq} - 1 + \mu)^3) - (1 - \mu)(x_{eq} + \mu)(x_{eq} - 1 + \mu)^3 - \mu(x_{eq} - 1 + \mu)(x_{eq} + \mu)^3 = 0 \quad (2.37)$$

This polynomial possess three roots and the solutions are denoted as the collinear libration points (L_1, L_2, L_3). For solutions off the x-axis, there are two solutions (L_4, L_5) and these are vertices of equilateral triangles formed by the two primaries and the solutions. The off-axis equilibrium solutions are then located at,

$$(x_{eq}, y_{eq}, z_{eq})_{L_4, L_5} = \left(\frac{1}{2} - \mu, \pm \frac{\sqrt{3}}{2}, 0\right) \quad (2.38)$$

The general location of the equilibrium solutions for any system appears in Figure 2.3. The Lagrange point locations vary significantly as a function of the mass ratio. This fact is illustrated by the location of the points for the Earth-Moon ($\mu = 1.2151 \times 10^{-2}$, $l^* = 3.8440 \times 10^5$ km) and Mars-Phobos ($\mu = 1.6606 \times 10^{-8}$, $l^* = 9.3760 \times 10^3$ km) system in Table 2.1.

2.4 Integral of Motion and Zero Velocity Surfaces

The familiar formulation of the CR3BP yields one known integral of motion, which is an energy-like quantity. The quantity is derived via the dot product between a rotating

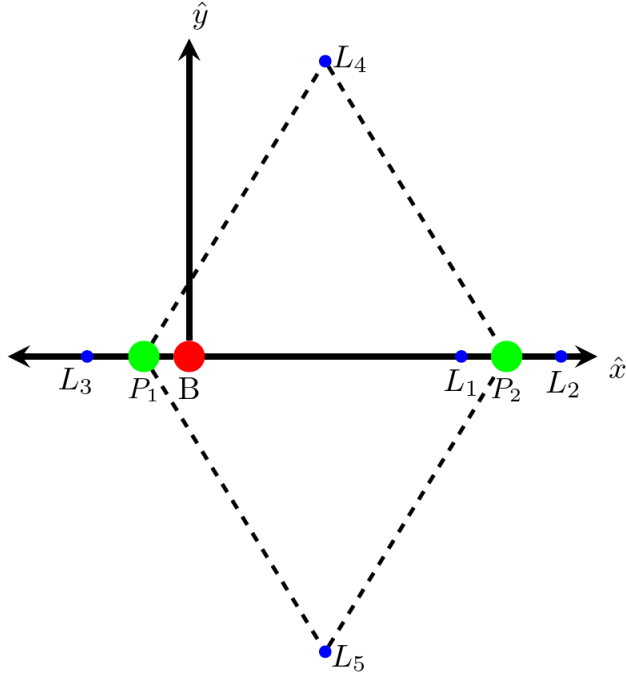


Figure 2.3. Location of the Lagrange points in the R frame

Table 2.1. Lagrange points of Earth-Moon and Mars-Phobos system in [nd] units

Lagrange Points	Earth-Moon	Mars-Phobos
$L_1(x,y,z)$	(0.83692, 0, 0)	(0.99823, 0, 0)
$L_2(x,y,z)$	(1.1557, 0, 0)	(1.0018, 0, 0)
$L_3(x,y,z)$	(-1.0051, 0, 0)	(-1.0000, 0, 0)
$L_4(x,y,z)$	(0.48785, 0.86603, 0)	(0.50000, 0.86603, 0)
$L_5(x,y,z)$	(0.48785, -0.86603, 0)	(0.50000, -0.86603, 0)

velocity vector and the scalar components of the vector differential equations of the model, Equations (2.31) to (2.33), similar to an energy quantity. The derivation proceeds from,

$$\dot{x}\ddot{x} + \dot{y}\ddot{y} + \dot{z}\ddot{z} = \dot{x}\Omega_x + \dot{y}\Omega_y + \dot{z}\Omega_z \quad (2.39)$$

The left side is the time derivative of the square of the velocity and the right side is equivalent to the total derivative of the pseudo-potential function. Thus, the above equation is alternatively written in terms of nondimensional time derivatives as,

$$\frac{d}{d\tau} \left(\frac{\dot{x}^2}{2} + \frac{\dot{y}^2}{2} + \frac{\dot{z}^2}{2} \right) = \frac{d\Omega}{d\tau} \quad (2.40)$$

Integration of the equation results in an integration constant termed the *Jacobi Constant* (JC), evaluated as follows,

$$JC = 2\Omega - (\dot{x}^2 + \dot{y}^2 + \dot{z}^2) \quad (2.41)$$

The existence of JC reduces the complexity of the system as it indicates that only five of the six states are linearly independent.

The *Zero Velocity Surfaces* (ZVS) is a concept that is useful in realizing the regions that bound the motion of a spacecraft. It is evident that the $\dot{x}^2 + \dot{y}^2 + \dot{z}^2$ expression in Equation (2.41) is the square of a rotating velocity vector, hence, it is rewritten as,

$$v^2 = 2\Omega - JC \quad (2.42)$$

Since the physical velocity cannot be imaginary, $2\Omega \geq JC$ must hold, thus, boundaries for available motion are revealed. The region of space that does not satisfy this inequality is labeled the *forbidden region*. The boundaries that reflect the surface of solutions for $2\Omega = JC$ is denoted the *Zero Velocity Surfaces* (ZVS), and the planar cross sections ($z=0$) are termed the *Zero Velocity Curves* (ZVC). Hence, the region enclosed by the ZVS is the *forbidden region*.

The ZVC and ZVS for two different JC values in the Earth-Moon system are visualized in Figures 2.4 and 2.5. It is meaningful to observe that there are three isolated regions for allowed motion for $JC = 3.20$ as apparent in Figure 2.4, and in Figure 2.5, for $JC = 3.01$ the $\hat{x} - \hat{y}$ plane is available except for some bounded areas near L_4 and L_5 . The ZVS at $JC = 3.20$ when $z=0$ clearly indicates that a spacecraft in the vicinity of P_1 or P_2 cannot leave the vicinity as the two regions are isolated. However, if the value of the JC is modified to at least the value that corresponds to L_1 , then the two regions are linked and the L_1 'gateway'

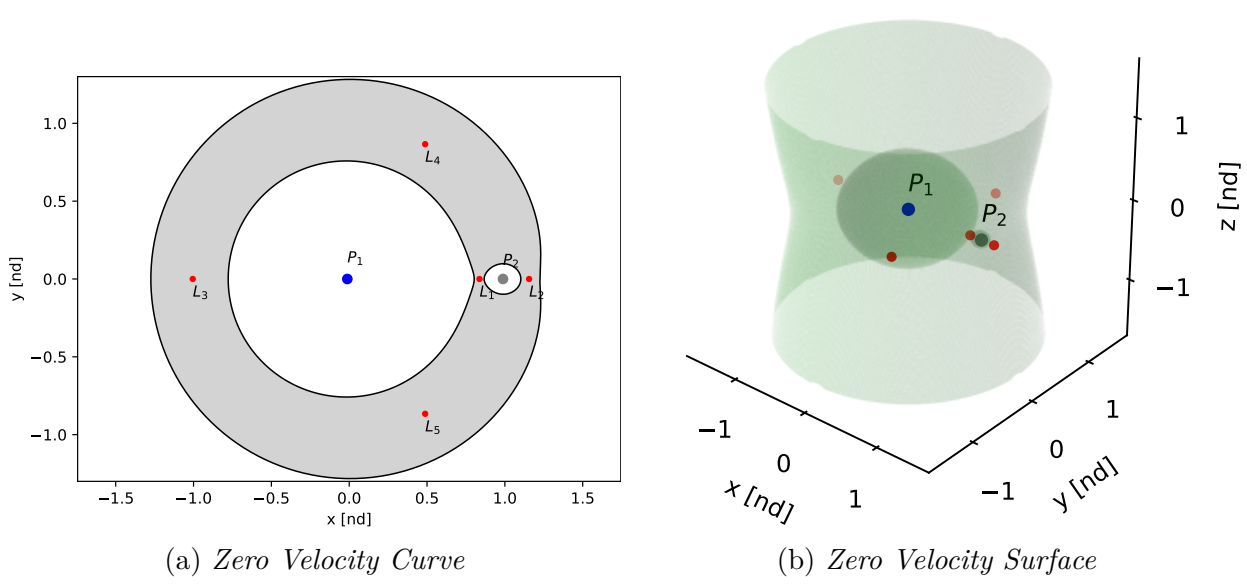


Figure 2.4. ZVC and ZVS for $JC = 3.20 > JC_{L_1}$ in the Earth-Moon system.

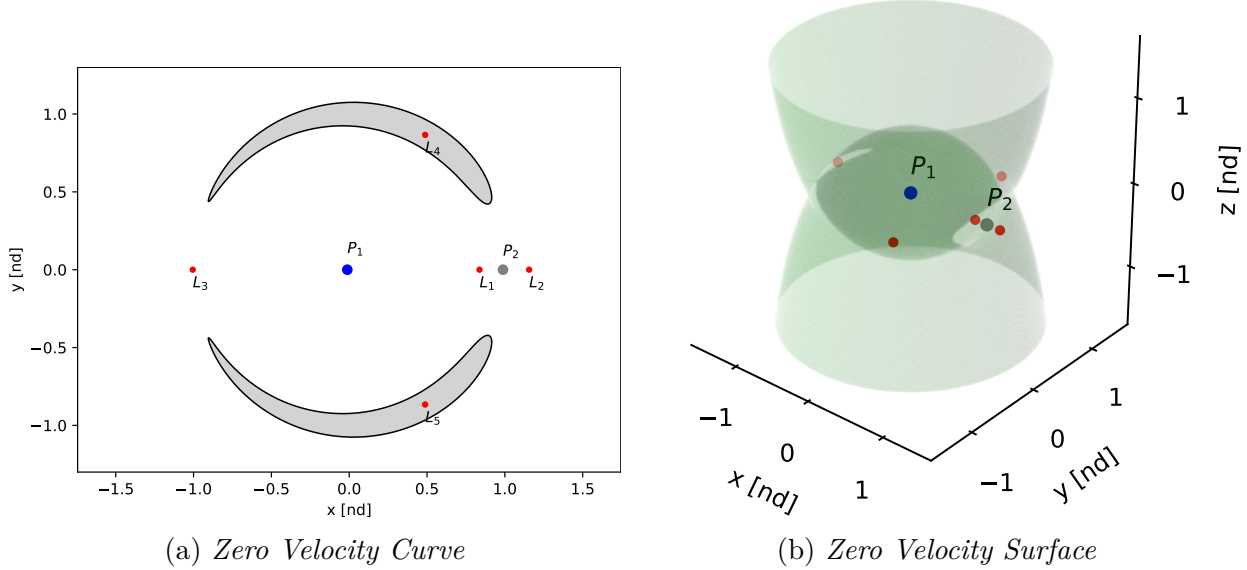


Figure 2.5. ZVC and ZVS for $JC_{L_{4,5}} > JC = 3.01 > JC_{L_3}$ in the Earth-Moon system.

opens, allowing access to a region near the other primary. The JC values corresponding to the 'gateways' between the different regions are visualized through ZVC and ZVS.

2.5 First-Order Linear Variational Equations of Motion

Despite the numerous assumptions made to the \mathfrak{N} -body problem to derive the CR3BP non-linear differential equations of motion, Equations (2.25) to (2.27), it is still a complex task to get any insight about the flows and compute the dynamical structures that exist in the system. Nonetheless, due to the presence of equilibrium solutions, it is advantageous to linearize the model around the equilibrium solutions to more straightforwardly understand the nearby innate flows, and to construct linear periodic and quasi-periodic orbits. The linear variational equations of motion are devised for a state \bar{x} in the vicinity of a Lagrange point (L_i) defined as,

$$\bar{x} = \bar{x}_{L_i} + \delta\bar{x} \quad (2.43)$$

The \bar{x}_{L_i} represents the position and velocity, *6-dimensional* state, of a Lagrange point and $\delta\bar{x}$ is a small perturbation about the Lagrange point, such that \bar{x} lies in the vicinity of \bar{x}_{L_i} . The linear analysis tools are useful in identifying analytical solutions about \bar{x}_{L_i} , assessing their Lyapunov stability, and characterizing nearby space using associated invariant manifolds.

The non-linear equations of motion for an autonomous system are generally represented as $\dot{\bar{x}} = \bar{f}(\bar{x})$ and for the five Lagrange points, $\dot{\bar{x}}_{L_i} = \bar{f}(\bar{x}_{L_i}) = 0$. The general form is expanded using the Taylor series expansion about \bar{x}_{L_i} as,

$$\dot{\bar{x}} = \dot{\bar{x}}_{L_i} + \delta\dot{\bar{x}} = \bar{f}(\bar{x}_{L_i}) + \left. \frac{\partial \bar{f}}{\partial \bar{x}} \right|_{\bar{x}_{L_i}} \delta\bar{x} + \dots \quad (2.44)$$

The higher-order terms are neglected to simplify the equation. It is reformulated in a time-independent matrix form, \mathbf{A}_{L_i} , as

$$\delta\dot{\bar{x}} \approx \left. \frac{\partial \bar{f}}{\partial \bar{x}} \right|_{\bar{x}_{L_i}} \delta\bar{x} = \mathbf{A}_{L_i} \delta\bar{x} \quad (2.45)$$

For CR3BP, the linear variational equations about the Lagrange points are of the following form in terms of the partial derivatives of the pseudo-potential,

$$\begin{bmatrix} \delta\dot{x} \\ \delta\dot{y} \\ \delta\dot{z} \\ \delta\ddot{x} \\ \delta\ddot{y} \\ \delta\ddot{z} \end{bmatrix} = \mathbf{A}_{L_i} \begin{bmatrix} \delta x \\ \delta y \\ \delta z \\ \delta\dot{x} \\ \delta\dot{y} \\ \delta\dot{z} \end{bmatrix} = \begin{bmatrix} 0 & 0 & 0 & 1 & 0 & 0 \\ 0 & 0 & 0 & 0 & 1 & 0 \\ 0 & 0 & 0 & 0 & 0 & 1 \\ \Omega_{xx,L_i} & \Omega_{xy,L_i} & \Omega_{xz,L_i} & 0 & 2 & 0 \\ \Omega_{yx,L_i} & \Omega_{yy,L_i} & \Omega_{yz,L_i} & -2 & 0 & 0 \\ \Omega_{zx,L_i} & \Omega_{zy,L_i} & \Omega_{zz,L_i} & 0 & 0 & 0 \end{bmatrix} \begin{bmatrix} \delta x \\ \delta y \\ \delta z \\ \delta\dot{x} \\ \delta\dot{y} \\ \delta\dot{z} \end{bmatrix} \quad (2.46)$$

The second-order form of the linear variational equation is represented as,

$$\hat{x} : \delta\ddot{x} - 2\delta\dot{y} = \frac{\partial^2 \Omega}{\partial x^2} \Big|_{\bar{x}_{L_i}} \delta x + \frac{\partial^2 \Omega}{\partial x \partial y} \Big|_{\bar{x}_{L_i}} \delta y + \frac{\partial^2 \Omega}{\partial x \partial z} \Big|_{\bar{x}_{L_i}} \delta z \quad (2.47)$$

$$\hat{y} : \delta\ddot{y} + 2\delta\dot{x} = \frac{\partial^2 \Omega}{\partial y \partial x} \Big|_{\bar{x}_{L_i}} \delta x + \frac{\partial^2 \Omega}{\partial y^2} \Big|_{\bar{x}_{L_i}} \delta y + \frac{\partial^2 \Omega}{\partial y \partial z} \Big|_{\bar{x}_{L_i}} \delta z \quad (2.48)$$

$$\hat{z} : \delta\ddot{z} = \frac{\partial^2 \Omega}{\partial z \partial x} \Big|_{\bar{x}_{L_i}} \delta x + \frac{\partial^2 \Omega}{\partial z \partial y} \Big|_{\bar{x}_{L_i}} \delta y + \frac{\partial^2 \Omega}{\partial z^2} \Big|_{\bar{x}_{L_i}} \delta z \quad (2.49)$$

The second-order partial derivatives of Ω are evaluated using the following,

$$\Omega_{xx} = 1 - \frac{1-\mu}{r_{13}^3} - \frac{\mu}{r_{23}^3} + \frac{3(1-\mu)(x+\mu)^2}{r_{13}^5} + \frac{3\mu(x-1+\mu)^2}{r_{23}^5} \quad (2.50)$$

$$\Omega_{yy} = 1 - \frac{1-\mu}{r_{13}^3} - \frac{\mu}{r_{23}^3} + \frac{3(1-\mu)y^2}{r_{13}^5} + \frac{3\mu y^2}{r_{23}^5} \quad (2.51)$$

$$\Omega_{zz} = -\frac{1-\mu}{r_{13}^3} - \frac{\mu}{r_{23}^3} + \frac{3(1-\mu)z^2}{r_{13}^5} + \frac{3\mu z^2}{r_{23}^5} \quad (2.52)$$

$$\Omega_{xy} = \Omega_{yx} = \frac{3(1-\mu)(x+\mu)y}{r_{13}^5} + \frac{3\mu(x-1+\mu)y}{r_{23}^5} \quad (2.53)$$

$$\Omega_{xz} = \Omega_{zx} = \frac{3(1-\mu)(x+\mu)z}{r_{13}^5} + \frac{3\mu(x-1+\mu)z}{r_{23}^5} \quad (2.54)$$

$$\Omega_{yz} = \Omega_{zy} = \frac{3(1-\mu)yz}{r_{13}^5} + \frac{3\mu yz}{r_{23}^5} \quad (2.55)$$

It is apparent that for the five Lagrange points, the value of $\Omega_{xz}, \Omega_{zx}, \Omega_{yz}, \Omega_{zy}$ are 0 and for the collinear points, the value of Ω_{xy}, Ω_{yx} are also 0. Since the coefficients of \mathbf{A}_{L_i} are constant,

a closed-form analytical solution exists for all the Lagrange points. The Equation (2.46) is reduced to,

$$\begin{bmatrix} \delta\dot{x} \\ \delta\dot{y} \\ \delta\dot{z} \\ \delta\ddot{x} \\ \delta\ddot{y} \\ \delta\ddot{z} \end{bmatrix} = \mathbf{A}_{L_i} \begin{bmatrix} \delta x \\ \delta y \\ \delta z \\ \delta\dot{x} \\ \delta\dot{y} \\ \delta\dot{z} \end{bmatrix} = \begin{bmatrix} 0 & 0 & 0 & 1 & 0 & 0 \\ 0 & 0 & 0 & 0 & 1 & 0 \\ 0 & 0 & 0 & 0 & 0 & 1 \\ \Omega_{xx,L_i} & \Omega_{xy,L_i} & 0 & 0 & 2 & 0 \\ \Omega_{yx,L_i} & \Omega_{yy,L_i} & 0 & -2 & 0 & 0 \\ 0 & 0 & \Omega_{zz,L_i} & 0 & 0 & 0 \end{bmatrix} \begin{bmatrix} \delta x \\ \delta y \\ \delta z \\ \delta\dot{x} \\ \delta\dot{y} \\ \delta\dot{z} \end{bmatrix} \quad (2.56)$$

It is important to note that the simplified form of \mathbf{A}_{L_i} suggests that the motion in the $\hat{x} - \hat{y}$ plane is decoupled from the out-of-plane motion. Hence, the in-plane and out-of-plane motions are analyzed separately.

The out-of-plane motion is defined by $\delta\ddot{z} - \Omega_{zz}\delta z = 0$ and $\Omega_{zz,L_i} < 0$. The analytical solution of the out-of-plane equation is the same as that of a simple harmonic oscillator and is described as,

$$\delta z(\tau) = \delta z_0 \cos(\omega_{\delta z}(\tau - \tau_0)) + \frac{\delta\dot{z}_0}{\omega_{\delta z}} \sin(\omega_{\delta z}(\tau - \tau_0)) \quad (2.57)$$

$$\delta\dot{z}(\tau) = -\delta z_0 \omega_{\delta z} \sin(\omega_{\delta z}(\tau - \tau_0)) + \delta\dot{z}_0 \cos(\omega_{\delta z}(\tau - \tau_0)) \quad (2.58)$$

Where:

$$\omega_{\delta z} = \sqrt{-\Omega_{zz,L_i}} \in \mathbb{R}$$

The identified solution allows for intuitive and simple computation of out-of-plane linear periodic orbits, as exemplified in Figure 2.6.

The in-plane analytical solution, similar to the out-of-plane solution, assists in the identification of the in-plane linear periodic orbits and their Lyapunov stability. The eigenfunction

of the in-plane equations of motion results in their analytical solution. The Jacobian for the in-plane motion is given by,

$$\mathbf{A}_{planar,L_i} = \begin{bmatrix} 0 & 0 & 1 & 0 \\ 0 & 0 & 0 & 1 \\ \Omega_{xx,L_i} & \Omega_{xy,L_i} & 0 & 2 \\ \Omega_{yx,L_i} & \Omega_{yy,L_i} & -2 & 0 \end{bmatrix} \quad (2.59)$$

The eigenvalues of \mathbf{A}_{planar,L_i} are computed by identifying the roots of the below characteristic polynomial,

$$\lambda^4 + (4 - \Omega_{xx,L_i} - \Omega_{yy,L_i})\lambda^2 + (\Omega_{xx,L_i}\Omega_{yy,L_i} - \Omega_{xy,L_i}^2) = 0 \quad (2.60)$$

The characteristic polynomial suggests that it has four roots (λ_i). For collinear Lagrange points, the polynomial is further simplified as $\Omega_{xy,L_i} = 0$, $\Omega_{xx,L_i} > 0$ and $\Omega_{yy,L_i} < 0$, and reframed as a quadratic equation by defining $\Lambda = \lambda^2$. The polynomial then takes the form,

$$\Lambda^2 + 2\beta_1\Lambda - \beta_2^2 = 0 \quad (2.61)$$

Where:

$$\begin{aligned} \beta_1 &= 2 - \frac{\Omega_{xx,L_i} + \Omega_{yy,L_i}}{2} \\ \beta_2^2 &= -\Omega_{xx,L_i}\Omega_{yy,L_i} \end{aligned}$$

The solution of the quadratic form of the polynomial is,

$$\Lambda_{1,2} = -\beta_1 \pm \sqrt{\beta_1^2 + \beta_2^2} \quad (2.62)$$

Using the values of $\Lambda_{1,2}$, the four roots are identified as,

$$\lambda_{1,2} = \pm\sqrt{|\Lambda_1|} \quad (2.63)$$

$$\lambda_{3,4} = \pm i\sqrt{|\Lambda_2|} \quad (2.64)$$

It is apparent that the collinear Lagrange points for in-plane motion have two real roots ($\lambda_{1,2}$) and two imaginary roots ($\lambda_{3,4}$). The existence of the two real roots of opposite signs suggests the presence of *1-dimensional* stable and unstable invariant subspaces, and the two imaginary roots suggest that the fixed point possesses a *2-dimensional* center subspace. Due to the existence of *2-dimensional* center subspace associated with the solutions, it is feasible to obtain in-plane linear periodic orbits. A similar method is applicable to the equilateral Lagrange points, however, their corresponding center manifolds are *4-dimensional*, so two distinct sets of in-plane linear periodic orbits exist around the L_4 and L_5 points.

The in-plane linear periodic orbits are realized by only exciting the center mode of the general analytical solution. The general solution for motion near the collinear equilibrium points in terms of eigenfunctions is expressed as,

$$\delta x(\tau) = A_1 e^{\lambda_1 \tau} + A_2 e^{\lambda_2 \tau} + A_3 e^{\lambda_3 \tau} + A_4 e^{\lambda_4 \tau} \quad (2.65)$$

$$\delta \dot{x}(\tau) = \lambda_1 A_1 e^{\lambda_1 \tau} + \lambda_2 A_2 e^{\lambda_2 \tau} + \lambda_3 A_3 e^{\lambda_3 \tau} + \lambda_4 A_4 e^{\lambda_4 \tau} \quad (2.66)$$

$$\delta y(\tau) = B_1 e^{\lambda_1 \tau} + B_2 e^{\lambda_2 \tau} + B_3 e^{\lambda_3 \tau} + B_4 e^{\lambda_4 \tau} \quad (2.67)$$

$$\delta \dot{y}(\tau) = \lambda_1 B_1 e^{\lambda_1 \tau} + \lambda_2 B_2 e^{\lambda_2 \tau} + \lambda_3 B_3 e^{\lambda_3 \tau} + \lambda_4 B_4 e^{\lambda_4 \tau} \quad (2.68)$$

Where:

$$B_i = \frac{\lambda_i - \Omega_{xx,L_i}}{2\lambda_i} A_i$$

A_i and B_i correspond to the coefficients of the terms related to the four λ_i values. The unstable and stable modes are negated by setting $A_1 = A_2 = 0$ and exciting the modes asso-

ciated with the imaginary eigenvalues. The first-order linear variational analytical solution for in-plane periodic orbits around the collinear Lagrange points are reduced to,

$$\delta x(\tau) = \delta x_0 \cos(s(\tau - \tau_0)) + \frac{\delta y_0}{\beta_3} \sin(s(\tau - \tau_0)) \quad (2.69)$$

$$\delta \dot{x}(\tau) = -s \delta x_0 \sin(s(\tau - \tau_0)) + \frac{s \delta y_0}{\beta_3} \cos(s(\tau - \tau_0)) \quad (2.70)$$

$$\delta y(\tau) = \delta y_0 \cos(s(\tau - \tau_0)) - \beta_3 \delta x_0 \sin(s(\tau - \tau_0)) \quad (2.71)$$

$$\delta \dot{y}(\tau) = -s \delta y_0 \sin(s(\tau - \tau_0)) - s \beta_3 \delta x_0 \cos(s(\tau - \tau_0)) \quad (2.72)$$

Where:

$$s = \beta_1 + \sqrt{\beta_1 + \beta_2}$$

$$\beta_3 = \frac{s^2 + \Omega_{xx}}{2s}$$

For a small value of δx_0 , a linear periodic orbit of period $2\pi/s$ is simulated and plotted in Figure 2.6.

The linear motion around the Lagrange points also sheds light on *2-dimensional* linear quasi-periodic orbits in their vicinity. A linear quasi-periodic orbit is constructed as a result of coupled in-plane and out-of-plane motion, such that $\omega_{\delta z}$ and s are incommensurate, as depicted in Figure 2.7. The linear periodic and quasi-periodic orbits computed through the analytical solutions of the first-order linear variational equations about the Lagrange points for small perturbations ($\delta \bar{x}$) inform the geometry, stability, and computation of their non-linear counterparts.

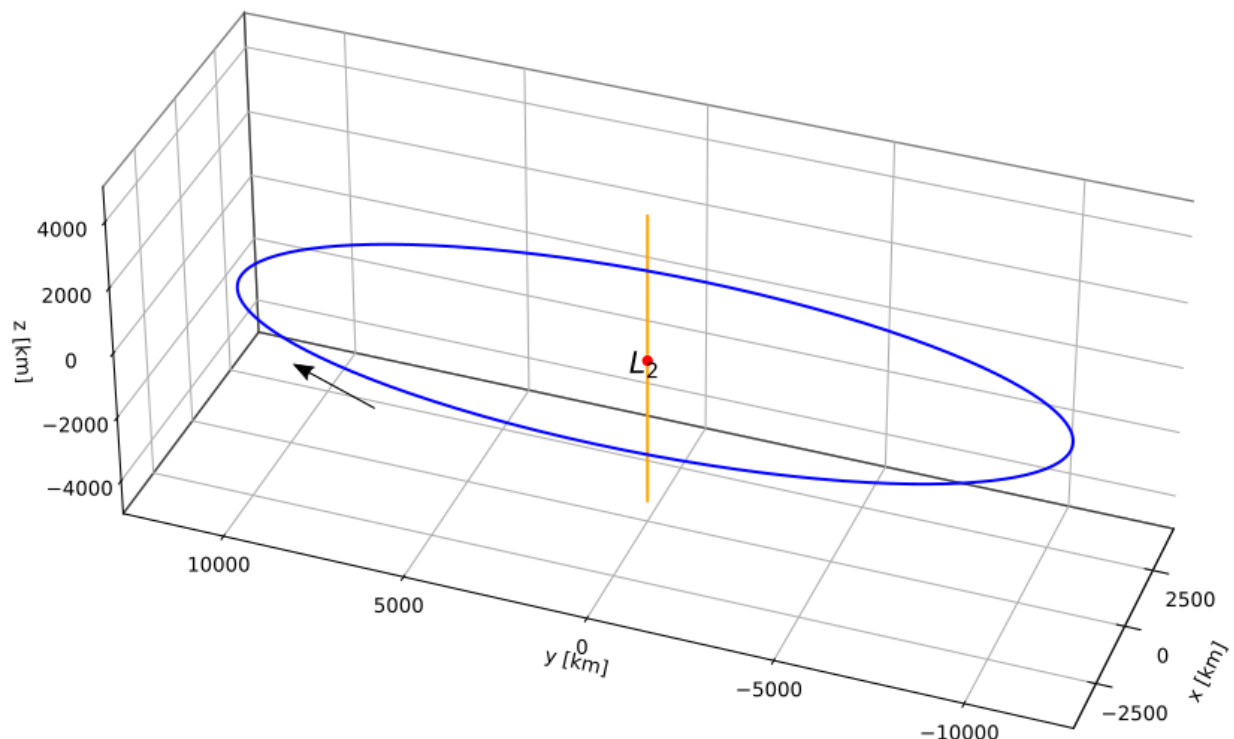
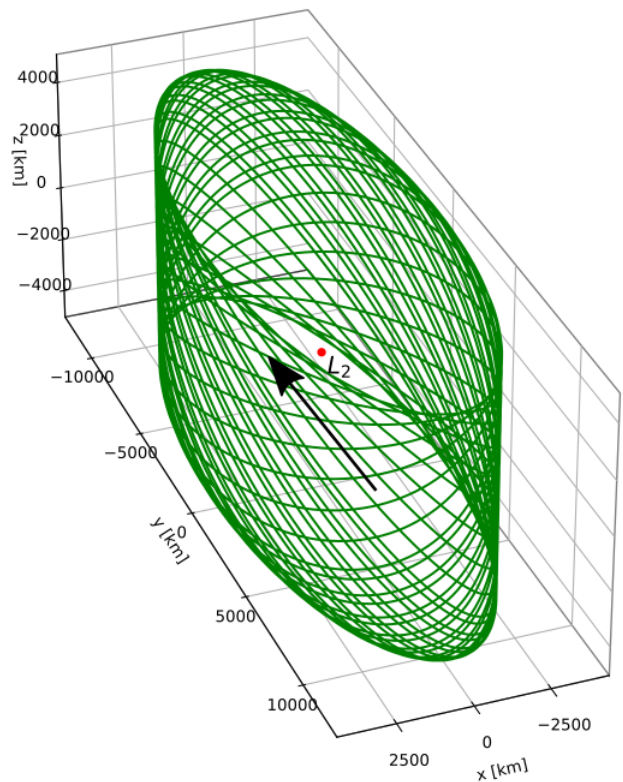
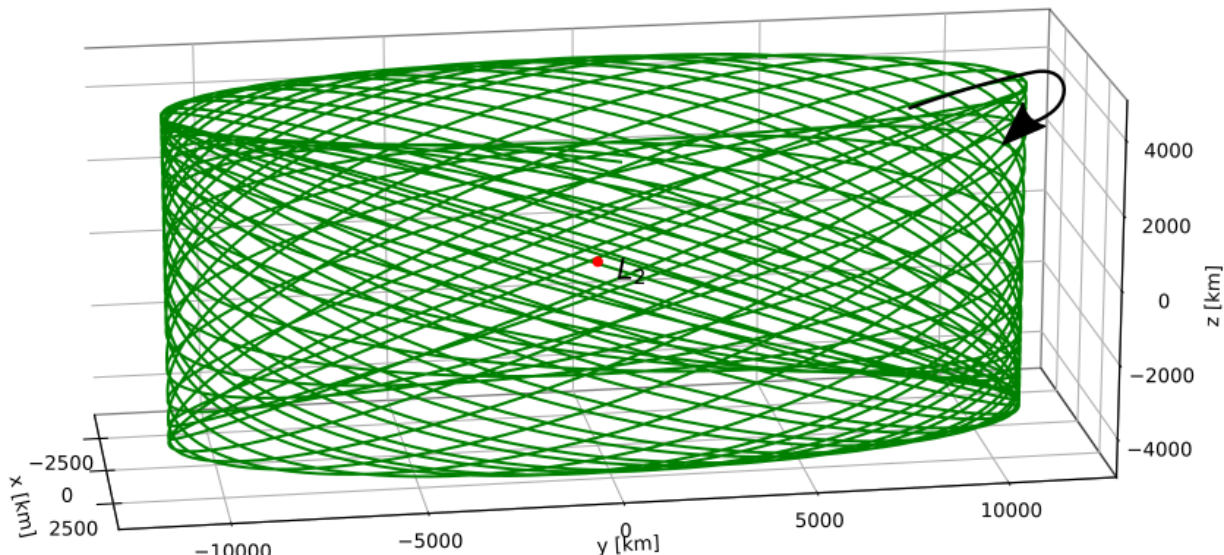


Figure 2.6. In-plane(blue) and out-of-plane(yellow) linear periodic orbits about the L_2 point in the Earth-Moon System.



(a) View 1



(b) View 2

Figure 2.7. Linear quasi-periodic orbit around the L_2 point in the Earth-Moon system.

3. NUMERICAL METHODS

The predicted dynamical behavior from the first-order linear variational equations around the five Lagrange points is not accurately extrapolatable to regions distant from these points. Therefore, sophisticated numerical tools are employed to acquire, expand upon, and analyze the linear flows and structures using the non-linear differential equations of the model, Equations (2.25) to (2.27). The concept of the State Transition Matrix (STM) is explored with an examination of several differential correction strategies. These strategies employ the multi-variate Newton-Raphson method to compute solutions with certain desired characteristics. Furthermore, two numerical continuation schemes are elucidated that enable the computation of a family of solutions for underconstrained problems.

3.1 State Transition Matrix

A State Transition Matrix linearly maps the effect of perturbations on an initial state to an upstream or downstream state from it. The matrix is advantageous in assessing the local behavior of the initial state, as well as in guiding a differential corrections process with an initial guess to a state with required characteristics. Consider a state of interest, $\bar{x}_k(\tau_0)$, and a small perturbation to it, $\delta\bar{x}(\tau_0)$. An estimated impact of any small $\delta\bar{x}(\tau_0)$ on $\bar{x}_k(\tau_0)$ propagated for τ is readily available if the STM from $\bar{x}_k(\tau_0)$ to its propagated state is known. The downstream effect of multiple small perturbations to a state is more computationally efficient to linearly approximate through an STM than individually integrating the multiple perturbed states and comparing them with the propagated initial state. These use cases of the STM make it an attractive choice for its use in spacecraft guidance, navigation, and control schemes.

The derivation of the STM for $\bar{x}_k(\tau)$ is similar to computing the first-order linear variational equations about the Lagrange points. The equivalent of Equation (2.45) for $\bar{x}_k(\tau)$ and $\delta\bar{x}(\tau)$ is of the form,

$$\delta\dot{\bar{x}}(\tau) \approx \left. \frac{\partial \bar{f}}{\partial x} \right|_{\bar{x}(\tau)} \delta\bar{x}(\tau) = \mathbf{A}(\tau) \delta\bar{x}(\tau) \quad (3.1)$$

The above equation is a system of linear time-varying differential equations and admits to a general solution expressed as,

$$\delta\bar{x}(\tau) = \Phi(\tau, \tau_0)\delta\bar{x}(\tau_0) \quad (3.2)$$

Where, $\Phi(\tau, \tau_0) = \frac{\partial\bar{x}(\tau)}{\partial\bar{x}(\tau_0)}$. The matrix Φ is called the *State Transition Matrix*. It is a 6×6 matrix and also represented as,

$$\Phi(\tau, \tau_0) = \begin{bmatrix} \frac{\partial x(\tau)}{\partial x(\tau_0)} & \frac{\partial x(\tau)}{\partial y(\tau_0)} & \frac{\partial x(\tau)}{\partial z(\tau_0)} & \frac{\partial x(\tau)}{\partial \dot{x}(\tau_0)} & \frac{\partial x(\tau)}{\partial \dot{y}(\tau_0)} & \frac{\partial x(\tau)}{\partial \dot{z}(\tau_0)} \\ \frac{\partial y(\tau)}{\partial x(\tau_0)} & \frac{\partial y(\tau)}{\partial y(\tau_0)} & \frac{\partial y(\tau)}{\partial z(\tau_0)} & \frac{\partial y(\tau)}{\partial \dot{x}(\tau_0)} & \frac{\partial y(\tau)}{\partial \dot{y}(\tau_0)} & \frac{\partial y(\tau)}{\partial \dot{z}(\tau_0)} \\ \frac{\partial z(\tau)}{\partial x(\tau_0)} & \frac{\partial z(\tau)}{\partial y(\tau_0)} & \frac{\partial z(\tau)}{\partial z(\tau_0)} & \frac{\partial z(\tau)}{\partial \dot{x}(\tau_0)} & \frac{\partial z(\tau)}{\partial \dot{y}(\tau_0)} & \frac{\partial z(\tau)}{\partial \dot{z}(\tau_0)} \\ \frac{\partial \dot{x}(\tau)}{\partial x(\tau_0)} & \frac{\partial \dot{x}(\tau)}{\partial y(\tau_0)} & \frac{\partial \dot{x}(\tau)}{\partial z(\tau_0)} & \frac{\partial \dot{x}(\tau)}{\partial \dot{x}(\tau_0)} & \frac{\partial \dot{x}(\tau)}{\partial \dot{y}(\tau_0)} & \frac{\partial \dot{x}(\tau)}{\partial \dot{z}(\tau_0)} \\ \frac{\partial \dot{y}(\tau)}{\partial x(\tau_0)} & \frac{\partial \dot{y}(\tau)}{\partial y(\tau_0)} & \frac{\partial \dot{y}(\tau)}{\partial z(\tau_0)} & \frac{\partial \dot{y}(\tau)}{\partial \dot{x}(\tau_0)} & \frac{\partial \dot{y}(\tau)}{\partial \dot{y}(\tau_0)} & \frac{\partial \dot{y}(\tau)}{\partial \dot{z}(\tau_0)} \\ \frac{\partial \dot{z}(\tau)}{\partial x(\tau_0)} & \frac{\partial \dot{z}(\tau)}{\partial y(\tau_0)} & \frac{\partial \dot{z}(\tau)}{\partial z(\tau_0)} & \frac{\partial \dot{z}(\tau)}{\partial \dot{x}(\tau_0)} & \frac{\partial \dot{z}(\tau)}{\partial \dot{y}(\tau_0)} & \frac{\partial \dot{z}(\tau)}{\partial \dot{z}(\tau_0)} \end{bmatrix} \quad (3.3)$$

It is evident that $\Phi(\tau_0, \tau_0) = \mathbf{I}_{6 \times 6}$, and serves as the initial condition for numerical integration of the STM. The time derivative of Equation (3.2) expressed in terms of Equation (3.1) admits to the following form,

$$\dot{\delta\bar{x}}(\tau) = \dot{\Phi}(\tau, \tau_0)\delta\bar{x}(\tau_0) = \mathbf{A}(\tau)\delta\bar{x}(\tau) = \mathbf{A}(\tau)\Phi(\tau, \tau_0)\delta\bar{x}(\tau_0) \quad (3.4)$$

The computation of $\mathbf{A}(\tau)$ is similar to that of \mathbf{A}_{L_i} in Equation (2.46) but at $\bar{x}_k(\tau)$. The following relationship is obtained from Equation (3.4) and describes 36 differential equations that are useful in the evaluation of $\Phi(\tau, \tau_0)$ at τ ,

$$\dot{\Phi}(\tau, \tau_0) = \mathbf{A}(\tau)\Phi(\tau, \tau_0) \quad (3.5)$$

It is common to integrate these differential equations with the 6 first-order non-linear equations of motion of CR3BP to obtain the state history of P_3 and the STM at each time step.

Furthermore, there are a few noteworthy properties of STM that are leveraged in differential correction schemes and are as follows,

$$\Phi(\tau_0, \tau) = \Phi^{-1}(\tau, \tau_0) \quad (3.6)$$

$$|\Phi(\tau, \tau_0)| = 1 \quad (3.7)$$

$$\Phi(\tau_2, \tau_0) = \Phi(\tau_2, \tau_1)\Phi(\tau_1, \tau_0) \quad (3.8)$$

Also, the STM serves as a valuable tool in stability analysis and approximation of the invariant manifolds associated with periodic and quasi-periodic orbits.

3.2 Differential Correction

Trajectories are often designed to possess specific characteristics or fulfill defined criteria, such as periodicity, quasi-periodicity, specific *JC* value, avoidance of eclipses, and more. Although an analytical solution isn't available for this model, the trajectory design problem is approached as a boundary value problem to generate trajectories with the desired behavior. Since the CR3BP is a continuous finite-dimensional dynamical system, the technique of differential correction is employed to solve this problem. A prominent method within this framework is the Newton-Raphson method, which offers efficient solutions due to its quadratic convergence property and its requirement of only one initial guess. A multi-dimensional form of Newton-Raphson, commonly known as the shooting method, is often favored for its ease of implementation. The method is qualitatively thought of as finding design variables that meet certain constraints given the initial guess of the design variables.

The Newton-Raphson method provides an iterative equation to refine the initial guess of design variables in order to achieve a solution that satisfies certain constraints up to a specified convergence tolerance. The main components of this method are the design variables and the constraints. Design variables, also referred to as free variables, represent

any state, time, or parameter that is functionally dependent on a constraint and is not fixed. A general design variable vector is a column vector of length n and represented as,

$$\bar{X} = \begin{bmatrix} X_1 \\ X_2 \\ \vdots \\ X_n \end{bmatrix} \quad (3.9)$$

Constraints are expressions that quantify desired trajectory characteristics. A constraint vector is set up as a column vector of length m and represented as,

$$\bar{F}(\bar{X}) = \begin{bmatrix} F_1(\bar{X}) \\ F_2(\bar{X}) \\ \vdots \\ F_m(\bar{X}) \end{bmatrix} \quad (3.10)$$

The convergence tolerance is dependent on the $P_1 - P_2$ system and the constraints. In this study, the solutions are iterated until $\|\bar{F}(\bar{X})\|_2 < 1e^{-12}$. The general form of the update equation is given as,

$$\bar{X}_{k+1} = \bar{X}_k - \mathbf{DF}(\bar{X}_k)^{-1} \bar{F}(\bar{X}_k) \quad (3.11)$$

Where, \bar{X}_k represents the design variable vector at the k^{th} iteration, $\bar{F}(\bar{X}_k)$ denotes the constraint vector evaluated at the k^{th} design variables, $\mathbf{DF}(\bar{X}_k)$ stands for the Jacobian matrix containing partial derivatives of constraints with respect to their dependent variables, and \bar{X}_{k+1} signifies the updated design variable vector. Constructing the Jacobian matrix $\mathbf{DF}(\bar{X})$ is challenging due to the multiple functional dependencies present in a $\bar{F}(\bar{X})$ vector, often compounded by the absence of analytical expressions for partial derivatives. While analytical derivatives are sought, numerical techniques are often employed to compute these partial derivatives when it is not feasible to identify the analytical expression due to the lack of understanding of the functional dependence of a constraint with a design variable. Alterna-

tively, when the computational complexity and cost associated with evaluating the analytical expression is higher than computing the derivatives through a numerical technique. In addition, the alternative methods assist in the validation of results obtained from a different technique. Three popular numerical approaches include: *automatic differentiation*, *symbolic differentiation* and *numerical differentiation*. Among numerical differentiation formulations, forward differentiation, backward differentiation, and complex-step differentiation [46] stand out as intuitive and reliable techniques. Regardless of how the Jacobian is computed, the shooting method enables the generation of trajectories with desired characteristics, given an initial guess.

The choice of the matrix inverse algorithm for computing the inverse of the Jacobian matrix, $\mathbf{DF}(\bar{X})^{-1}$, in Equation (3.11) depends on the shape of the $\mathbf{DF}(\bar{X})$ matrix. The length of the constraint (m) and design variable vector (n) instructs the size of the $\mathbf{DF}(\bar{X})$ ($m \times n$) matrix. However, at times, linearly dependent constraints are included in the constraint vector to alter the numerical behavior of the Newthon-Raphson method, which in turn changes the size of the Jacobian matrix but not the rank. It is apparent that three possibilities exist for the shape: $m = n$ (fully constrained), $m > n$ (overconstrained), and $m < n$ (underconstrained). The fully constrained system suggests the Jacobian is a square matrix, so $\mathbf{DF}(\bar{X})^{-1}$ is straightforward to compute, and a unique design vector satisfies the constraints. The overconstrained system does not have a solution but the least squares solution is found by using the projection theorem. The update equation Equation (3.11) is modified accordingly,

$$\bar{X}_{k+1} = \bar{X}_k - (\mathbf{DF}(\bar{X}_k)^T \mathbf{DF}(\bar{X}_k))^{-1} \mathbf{DF}(\bar{X}_k)^T \bar{F}(\bar{X}_k) \quad (3.12)$$

An underconstrained system has an $(n-m)$ -dimensional nullspace, resulting in infinitely many solutions forming an $(n-m)$ -family of solutions. A common approach is to find the minimum-norm solution closest to the initial guess, leading to the following update equation:

$$\bar{X}_{k+1} = \bar{X}_k - \mathbf{DF}(\bar{X}_k)^T (\mathbf{DF}(\bar{X}_k) \mathbf{DF}(\bar{X}_k)^T)^{-1} \bar{F}(\bar{X}_k) \quad (3.13)$$

In practice, Equations (3.12) and (3.13) are susceptible to numerical errors due to finite precision of computers. An alternate method to compute the $\mathbf{DF}(\bar{X})^{-1}$ is by employing Moore-Penrose pseudo-inverse method [47]. The differential corrections method introduced here is detailed in the following sections for its application in the trajectory design process.

3.2.1 Single Shooting

Single shooting involves a multi-dimensional Newton-Raphson approach for trajectory design, focusing on a single state within the \bar{X} vector that characterizes the trajectory. To illustrate the utilization of STM and differential correction, consider a trajectory design problem: crafting a trajectory from an initial state, \bar{x}_0 , to a desired point, (x_d, y_d, z_d) . The initial velocity components, $(\dot{x}_0, \dot{y}_0, \dot{z}_0)$, and time of flight, T , are variables, and the setup is depicted in Figure 3.1. The design variable and constraint vectors are formulated as,

$$\bar{X}_{ss} = \begin{bmatrix} \dot{x}_0 \\ \dot{y}_0 \\ \dot{z}_0 \\ T \end{bmatrix}; \bar{F}(\bar{X}_{ss}) = \begin{bmatrix} x_0(T) - x_d \\ y_0(T) - y_d \\ z_0(T) - z_d \end{bmatrix} \quad (3.14)$$

Given the underconstrained nature of this problem, there exist numerous solutions, and

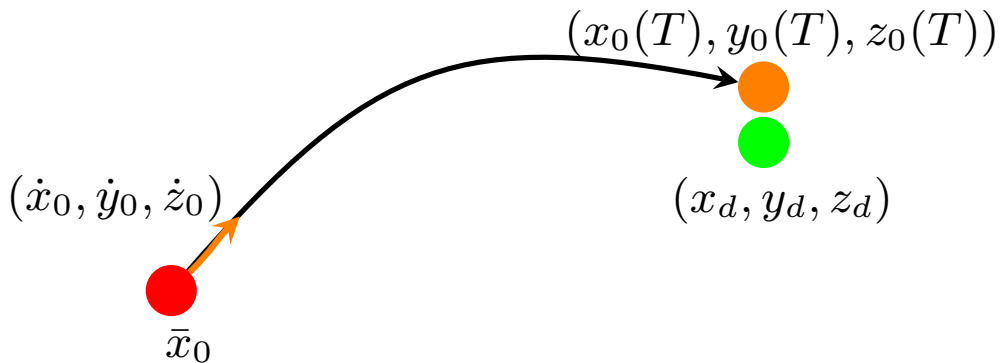


Figure 3.1. Single shooting method problem setup

the converged outcome depends on the initial guess. The Jacobian of the problem takes the form:

$$\mathbf{DF}(\bar{X}_{ss}) = \begin{bmatrix} \frac{\partial x_0(T)}{\partial \dot{x}_0} - 0 & \frac{\partial x_0(T)}{\partial \dot{y}_0} - 0 & \frac{\partial x_0(T)}{\partial \dot{z}_0} - 0 & \frac{\partial x_0(T)}{\partial T} - 0 \\ \frac{\partial y_0(T)}{\partial \dot{x}_0} - 0 & \frac{\partial y_0(T)}{\partial \dot{y}_0} - 0 & \frac{\partial y_0(T)}{\partial \dot{z}_0} - 0 & \frac{\partial y_0(T)}{\partial T} - 0 \\ \frac{\partial z_0(T)}{\partial \dot{x}_0} - 0 & \frac{\partial z_0(T)}{\partial \dot{y}_0} - 0 & \frac{\partial z_0(T)}{\partial \dot{z}_0} - 0 & \frac{\partial z_0(T)}{\partial T} - 0 \end{bmatrix} \quad (3.15)$$

The elements in the fourth column of $\mathbf{DF}(\bar{X}_{ss})$ are the velocity components at the downstream state. The elements in the first three columns are approximated by the STM elements corresponding to the linear variations in $(x_0(T), y_0(T), z_0(T))$ with respect to the variations in $(\dot{x}_0, \dot{y}_0, \dot{z}_0)$. The use of STM to compute the partial derivatives is accurate only for a short time of flight and insignificant non-linear terms. Assuming the (i,j) component of the STM is denoted as Φ_{ij} , the Jacobian matrix is expressed in terms of STM elements

$$\mathbf{DF}(\bar{X}_{ss}) = \begin{bmatrix} \Phi_{14} & \Phi_{15} & \Phi_{16} & \dot{x}_0(T) \\ \Phi_{24} & \Phi_{25} & \Phi_{26} & \dot{y}_0(T) \\ \Phi_{34} & \Phi_{35} & \Phi_{36} & \dot{z}_0(T) \end{bmatrix} \quad (3.16)$$

For a known initial guess of \bar{X}_{ss} , the update of the design vector is computed using Equation (3.11). After each update, the initial state and STM are repaginated and the process is repeated until the constraint vector meets a convergence tolerance. However, for onboard implementation of the method, the repagation of STM after each update might be avoided due to computational limitations. Nevertheless, the scheme still converges to a solution if the initial guess is in the solution basin. The design and constraint vector formulation for the single shooting method is extendable to the computation of periodic and quasi-periodic orbits.

3.2.2 Multiple Shooting

Multiple shooting builds on the logic of single shooting by breaking a trajectory into multiple segments and simultaneously targeting each segment to yield a continuous trajectory of desired attributes. There are a few scenarios where multiple shooting assists with

the convergence behavior numerical challenges that the single shooting method faces. The method is more robust in targeting a trajectory that either traverses through a sensitive dynamical region or has a long time of flight. In addition, the method is employed when the solution geometry needs to be more heavily biased to an initial guess geometry found using the minimum-norm formulation for an underconstrained problem. However, the multiple shooting method increases the computational complexity of solving a problem and encounters numerical challenges if too many segments are used in the formulation.

The method is set up by first discretizing a trajectory into multiple segments that are represented by nodes or initial states of each segment. There are multiple techniques to discretize the trajectory and the choice of the technique is based on the problem. Two common approaches include segmenting the trajectory into n equal time of flight segments, or placing more nodes within dynamically sensitive regions, possibly guided by a variable time numerical integration method. Thereafter, the nodes are added to the design variables and full-state continuity is imposed between the adjacent nodes. However, the exact formulation is problem-dependent, and other variations exist where only the position continuity between the nodes is sought or the time of flight is allowed to vary but the value is the same for all the segments.

The technique is elucidated by considering the problem defined in Section 3.2.1 but for a different scenario as depicted in Figure 3.2. The seemingly more complicated trajectory than in Figure 3.1 with an initial state (\bar{x}_0) and time of flight (T) is discretized into n segments as visualized in Figure 3.3. The design variable vector consists of the initial states and time

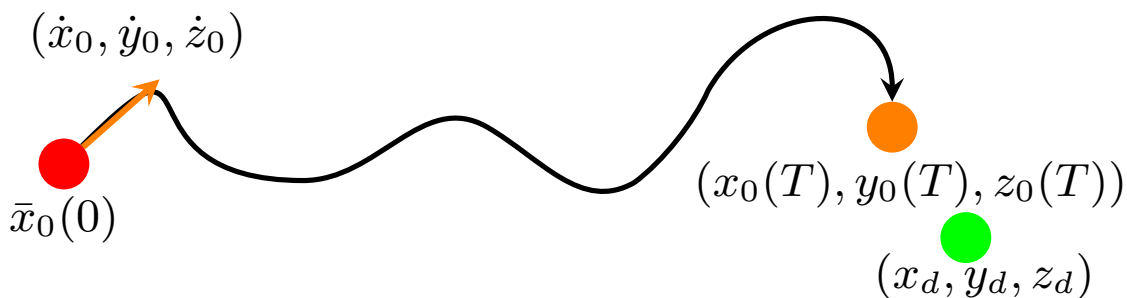


Figure 3.2. Multiple shooting method problem setup

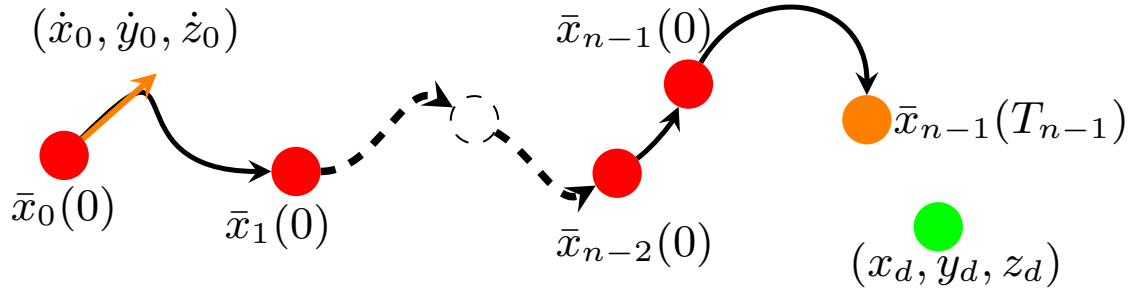


Figure 3.3. Multiple shooting method problem setup with n nodes

of flight of each node, except for the initial position of the first node. The constraint vector is made up of full-state continuity constraints between the nodes, as well as the position continuity constraint at the final state of the last node to the desired final position. The two vectors are thus expressed as,

$$\bar{X}_{ms} = \begin{bmatrix} \dot{x}_0 \\ \dot{y}_0 \\ \dot{z}_0 \\ \bar{x}_1 \\ \bar{x}_2 \\ \vdots \\ \bar{x}_{n-2} \\ \bar{x}_{n-1} \\ T_0 \\ T_1 \\ \vdots \\ T_{n-1} \end{bmatrix}; \bar{F}(\bar{X}_{ms}) = \begin{bmatrix} \bar{x}_0(T_0) - \bar{x}_1(0) \\ \bar{x}_1(T_1) - \bar{x}_2(0) \\ \vdots \\ \bar{x}_{n-2}(T_{n-2}) - \bar{x}_{n-1}(0) \\ x_{n-1}(T_{n-1}) - x_d \\ y_{n-1}(T_{n-1}) - y_d \\ z_{n-1}(T_{n-1}) - z_d \end{bmatrix} \quad (3.17)$$

The design vector is of length $(4 + 7(\mathbf{n}-1))$ and the constraint vector is of length $(6(\mathbf{n}-1)+3)$. The Jacobian matrix is constructed by leveraging STM, similar to the single shooting case, as shown below,

$$\mathbf{DF}(\bar{X}_{ms}) = \begin{bmatrix} \mathbf{DF}(\bar{X}_{ms})_x & \mathbf{DF}(\bar{X}_{ms})_T \end{bmatrix} \quad (3.18)$$

where,

$$\mathbf{DF}(\bar{X}_{ms})_x = \begin{bmatrix} \Phi_{i4}(T_0, 0) & \Phi_{i5}(T_0, 0) & \Phi_{i6}(T_0, 0) & -\mathbf{I}_{6 \times 6} & \mathbf{0}_{6 \times 6} & \dots & \mathbf{0}_{6 \times 6} & \mathbf{0}_{6 \times 6} \\ \bar{0}_{6 \times 1} & \bar{0}_{6 \times 1} & \bar{0}_{6 \times 1} & \Phi(T_1, T_0) & -\mathbf{I}_{6 \times 6} & \dots & \mathbf{0}_{6 \times 6} & \mathbf{0}_{6 \times 6} \\ \vdots & \vdots & \vdots & \ddots & \ddots & \ddots & \ddots & \ddots \\ \vdots & \vdots & \vdots & & \ddots & \ddots & \ddots & \ddots \\ \bar{0}_{6 \times 1} & \bar{0}_{6 \times 1} & \bar{0}_{6 \times 1} & \mathbf{0}_{6 \times 6} & \mathbf{0}_{6 \times 6} & \dots & \Phi(T_{n-2}, T_{n-3}) & -\mathbf{I}_{6 \times 6} \\ 0_{1 \times 1} & 0_{1 \times 1} & 0_{1 \times 1} & \bar{0}_{1 \times 6} & \bar{0}_{1 \times 6} & \dots & \bar{0}_{1 \times 6} & \Phi_{1j}(T_{n-1}, T_{n-2}) \\ 0_{1 \times 1} & 0_{1 \times 1} & 0_{1 \times 1} & \bar{0}_{1 \times 6} & \bar{0}_{1 \times 6} & \dots & \bar{0}_{1 \times 6} & \Phi_{2j}(T_{n-1}, T_{n-2}) \\ 0_{1 \times 1} & 0_{1 \times 1} & 0_{1 \times 1} & \bar{0}_{1 \times 6} & \bar{0}_{1 \times 6} & \dots & \bar{0}_{1 \times 6} & \Phi_{3j}(T_{n-1}, T_{n-2}) \end{bmatrix} \quad (3.19)$$

$$\mathbf{DF}(\bar{X}_{ms})_T = \begin{bmatrix} \dot{x}_0(T_0) & \bar{0}_{6 \times 1} & \dots & \bar{0}_{6 \times 1} \\ \bar{0}_{6 \times 1} & \dot{x}_1(T_1) & \dots & \bar{0}_{6 \times 1} \\ \vdots & \vdots & \ddots & \vdots \\ \vdots & \vdots & & \ddots \\ 0_{1 \times 1} & 0_{1 \times 1} & \dots & \dot{x}_{n-1}(T_{n-1}) \\ 0_{1 \times 1} & 0_{1 \times 1} & \dots & \dot{y}_{n-1}(T_{n-1}) \\ 0_{1 \times 1} & 0_{1 \times 1} & \dots & \dot{z}_{n-1}(T_{n-1}) \end{bmatrix} \quad (3.20)$$

Where, i corresponds to $[1,6]$ row components and j corresponds to $[1,6]$ column components of a STM. For a known initial guess, the problem is solved using the minimum-norm formulation, Equation (3.13), of the Newton-Raphson method as the presented formulation has a \mathbf{n} -dimensional nullspace. An intermediate step during the corrections process is depicted in Figure 3.4. Due to the expansive nullspace, it may be useful to incorporate additional constraints, such as an apse or altitude constraint, or to reduce the number of free variables by considering all the segments to have the same time of flight to better preserve the initial guess geometry during the correction process.

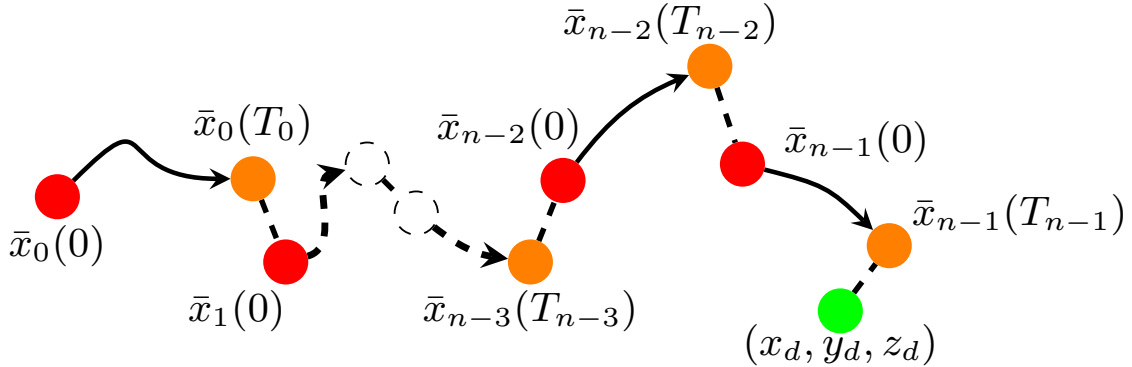


Figure 3.4. Multiple shooting method intermediate correction step

3.3 Numerical Continuation

A trajectory design problem is typically formulated as an underconstrained problem and often there is a need to realize the entire solution space. A shooting method delivers a point solution to an underconstrained problem, so to compute other solutions in the nullspace a numerical continuation technique is leveraged. The family of solutions is useful in determining bifurcations, if any exist, to understand how they are linked with other families of solutions, thereby improving the understanding of the chaotic dynamical environment. In addition, it assists in identifying significant changes to the trajectory geometry in the solution space as exemplified by Almanza-Soto [48]. The techniques are heavily relied upon to compute periodic orbit and quasi-periodic orbit families. There are a variety of numerical continuation techniques and two of them, Natural Parameter Continuation and Psuedo-Arclength Continuation, are discussed and employed in this investigation.

3.3.1 Natural Parameter Continuation

Natural Parameter Continuation (NPC) is an intuitive continuation method that relies on perturbing a design variable of a converged solution to construct a new solution using a shooting method, and the process is iterated to obtain a family of solutions. The method follows the predictor-corrector method logic, so the evolution of a design variable, referred to as the continuation parameter, is linearly predicted. A shooting method is leveraged to compute the value of other design variables for the predicted value of the continuation

parameter. Consider the trajectory design problem setup in Section 3.2.1, which illustrates the application of the single shooting method. The sample problem has a *1-dimensional* nullspace, which is parameterizable through any one of the design variables, $\dot{x}_0, \dot{y}_0, \dot{z}_0$ or T . The chosen design variable for parameterization of the nullspace is termed the continuation parameters, ζ . It is notable that alternative formulations of the problem exist, such that the design vector consists of an in-plane velocity angle, out-of-plane velocity angle, or Jacobi Constant, which can then be used as the continuation parameter. For a known solution of the problem, another solution is constructed by first selecting ζ , and a small perturbation, $\delta\zeta$, to ζ . The value of ζ is updated to be $\zeta + \delta\zeta$, and a new solution is computed using a shooting method for the updated ζ by not considering the continuation parameter as part of the design variable vector. This process is repeated till the end of the family or a desired solution is encountered.

The technique is easy to implement but it is not robust as it requires a *priori* insight into how the family evolves for a continuation parameter. It commonly breaks down near a turning point in the solution space. In addition, if NPC fails to compute a new solution then it cannot suggest if the failure is due to the lack of a family member or due to the choice of $\delta\zeta$ value. There are a few ideas that alleviate some of the problems that NPC suffers, such as changing the continuation parameter, updating the value of $\delta\zeta$ based on the slope information from previous solutions, using line search, or altering the initial guess for all the design variables for the next solution by including the slope information from previous solutions. Despite natural parameter continuation's ease of implementation and intuitive adaption of the differential corrections, it is not an effective tool for the continuation of complex solutions such as the continuation of quasi-periodic orbits.

3.3.2 Pseudo-Arclength Continuation

Pseudo-Arclength Continuation (PALC) is also a predictor-corrector continuation method and it was first proposed by H. Keller in 1977 [49]. The nullspace of the Jacobian, $\mathbf{DF}(\bar{X})$, predicts the next solution in a family, and the Newton-Raphson method is employed to correct the linearly predicted initial guess. A key benefit of this technique over NPC is that

it does not rely on the knowledge of how the solution space evolves, but rather on how the smooth arc of solutions appears in the vicinity of a known solution. A pseudo solution arc is computed by updating the value of the design vector of a valid solution by a null vector of $\mathbf{DF}(\bar{X})$ that is scaled by the choice of a step size. The predicted value of all the design variables makes it feasible to take larger continuation steps without sacrificing the differential correction accuracy compared to NPC. However, it is challenging to intuitively realize the step size, a dimensionless quantity, as it is a scaling factor for the null vector. Thus, the null vector is often normalized by a design variable to add a physical interpretation to the step size. A shooting method with an additional arclength constraint with the pseudo solution arc as the initial guess allows for the computation of a solution along the non-linear solution arc. The process is iterated till sufficient family members are computed.

The predictor step relies on the nullspace of the Jacobian, so the problem is formulated to comprise only *1-dimensional* nullspace to minimize any continuation direction ambiguity. In addition, if a bifurcation is encountered during the continuation process, then the continuation step size and direction are more carefully chosen to avoid traversing an unintended solution arc. The step-by-step implementation of the scheme is as follows,

1. Assume a solution \bar{X}_k^* for a constraint $\bar{F}(\bar{X}_k^*)$ with a known Jacobian matrix $\mathbf{DF}(\bar{X}_k^*)$.
2. The null vector of $\mathbf{DF}(\bar{X}_k^*)$ matrix at the current solution is evaluated as $\Delta\bar{X}_k^*$. The null vector may be normalized by a design variable to aid the intuition of step size.
3. The next solution with a step size, Δs , is predicted using the following and illustrated in Figure 3.5,

$$\bar{X}_{k+1} = \bar{X}_k^* + \Delta s \Delta\bar{X}_k^* \quad (3.21)$$

4. Adapt the *1-dimensional* nullspace underconstrained problem to ensure that the new solution is Δs arclength from the previous solution. This is achieved by augmenting the constraint vector ($\bar{F}(\bar{X}_{k+1})$) to include an arclength constraint presented below,

$$\bar{G}(\bar{X}_{k+1}) = \begin{bmatrix} \bar{F}(\bar{X}_{k+1}) \\ (\bar{X}_{k+1} - \bar{X}_k^*)^T \Delta \bar{X}_k^* - \Delta s \end{bmatrix} \quad (3.22)$$

The partial derivative of the arclength constraint is augmented to $\mathbf{DF}(\bar{X}_{k+1})$ to construct the Jacobian of the adapted fully constrained problem as,

$$\mathbf{DG}(\bar{X}_{k+1}) = \begin{bmatrix} \mathbf{DF}(\bar{X}_{k+1}) \\ (\Delta \bar{X}_k^*)^T \end{bmatrix} \quad (3.23)$$

5. Use a corrector, Newton-Raphon method, for \bar{X}_{k+1} with $\bar{G}(\bar{X}_{k+1})$ and $\mathbf{DG}(\bar{X}_{k+1})$ to obtain \bar{X}_{k+1}^* , which is a solution of $\bar{F}(\bar{X})$ and Δs arclength from \bar{X}_k^* .
6. The predicted step for the next solution is $\Delta \bar{X}_{k+1}^* + \Delta s \Delta \bar{X}_{k+1}^*$. Check that the step is in the intended direction, if not then change the sign of Δs , and check if the magnitude of Δs is appropriate. Line search may be used to modify the magnitude of the step size.
7. Compute \bar{X}_{k+2}^* using a corrector for the adapted fully constrained problem. If the solution fails to converge then identify if the null-space is *1-dimensional* and the elements of the null-vector are non-zero. An increase in the dimension of the nullspace indicates the existence of a bifurcation and a decrease in the dimension points to the end of the family.
8. Repeat the process till the end of the family or till a desired solution is constructed.

The continuation process alleviates some of the challenges that NPC encounters, such as continuation along a turning point. In addition, the method allows for larger continuation steps than NPC, as well as more insights into the evolution of the family based on the nullity of the Jacobian matrix. However, PALC is more computationally intensive and less intuitive

to comprehend than NPC. Furthermore, it requires a careful assessment of the step size and direction to avoid traversing an unintended bifurcation branch or wrapping back to the initial solution.

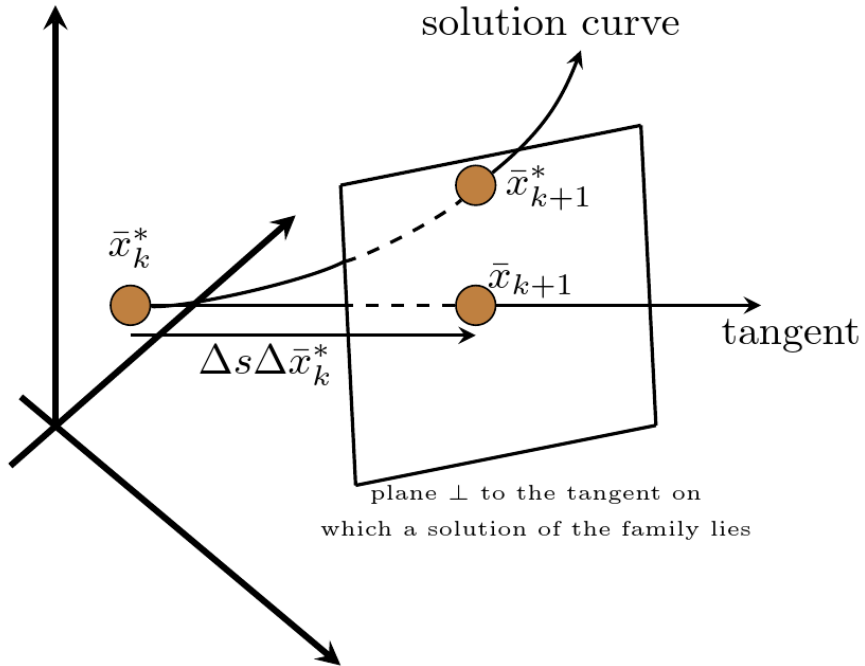


Figure 3.5. PALC predicted step schematic. Adapted from Keller [49].

4. PERIODIC ORBITS

Periodic orbits are dynamical structures that constitute of states that return to themselves after a finite period. These orbits are topologically interpreted as *1-dimensional* invariant tori embedded in the \mathbb{R}^6 phase space. The individual states of a periodic orbit are referred to as periodic solutions. Its repeatable geometry makes it an attractive choice for staging and hosting satellites and spacecrafts, as evident by their use in for Artemis 1 mission [11] and Solar and Heliospheric Observatory (SOHO) [50]. The understanding of periodic orbits and their associated hyperbolic invariant manifolds assist in characterizing part of the global dynamics and designing transfer trajectories, as exemplified by the Genesis mission [51]. Furthermore, their corresponding center manifolds enable the characterization and computation of quasi-periodic orbits. These orbits are a fundamental aspect of the preliminary trajectory design process because of the various benefits they offer.

The analytical solutions of the linearized variational equations around the Lagrange points, Section 2.5, highlight the existence of in-plane and out-of-plane periodic orbits around the Lagrange points. The following sections continue that discussion to elucidate the computation of periodic orbits in the non-linear model using the techniques presented in Chapter 3, as well as the characterization of the orbits and their associated invariant manifolds.

4.1 Targeting: Symmetry, Periodicity, and Phase Constraint

The CR3BP symmetry properties and the periodic nature of the periodic orbits facilitate their computation using a shooting method. The application of a shooting method requires an initial guess that is commonly computed from the analytical solutions of the linearized variational equations around the Lagrange points as presented in Section 2.5, from a relative two-body problem orbit around a primary [52], or found in the literature [53], [54]. After a periodic orbit is constructed, NPC or PALC is employed to construct the *1-dimensional* family of periodic orbits.

There are three types of symmetries in CR3BP that were first identified by Roy and Ovendon for defining the *Mirrior Theorem* [55]. Robin and Markellos [56] built on the idea of the *Mirrior Theorem* to formulate differential corrections algorithm for the construction

of periodic orbits that admit to the three types of symmetries. A brief discussion of how the different types of symmetries assist in the computation of symmetric periodic orbits is presented below:

1. *$\hat{x} - \hat{z}$ plane symmetry*: If P_3 crosses the $\hat{x} - \hat{z}$ plane perpendicularly twice then P_3 is in a periodic orbit. Consider an initial state that is perpendicular to the $\hat{x} - \hat{z}$ plane and represented by $\bar{x}_0 = [x_0, 0, z_0, 0, \dot{y}_0, 0]$. The symmetric behavior is employed to correct the initial state, such that the propagated initial state again crosses the plane perpendicularly. The resultant propagation time is half the period of the orbit, $\mathbb{P}/2$. The design and constraint vector for this kind of symmetry are,

$$\bar{X} = \begin{bmatrix} x_0 \\ z_0 \\ \dot{y}_0 \\ \mathbb{P}/2 \end{bmatrix}; \bar{F}(\bar{X}) = \begin{bmatrix} y(\mathbb{P}/2) - 0 \\ \dot{x}(\mathbb{P}/2) - 0 \\ \dot{z}(\mathbb{P}/2) - 0 \end{bmatrix} \quad (4.1)$$

After the successful computation of an initial state that satisfies the constraints, the targeted \bar{x}_0 state is propagated for the full period, \mathbb{P} , to generate the entire orbit. This symmetry property is useful in targeting periodic orbits, such as Lyapunov orbits, halo orbits, distant retrograde orbits, etc.

2. *\hat{x} axis symmetry*: If P_3 crosses the \hat{x} axis with $\dot{x} = 0$ twice then it is in a periodic orbit. This principle is leveraged for targeting an initial state on the \hat{x} axis, such that it again crosses the axis with $\dot{x} = 0$ after half the period of the orbit. The design and constraint vector for this setup with an initial state of type $\bar{x}_0 = [x_0, 0, 0, 0, \dot{y}_0, \dot{z}_0]$ are,

$$\bar{X} = \begin{bmatrix} x_0 \\ \dot{y}_0 \\ \dot{z}_0 \\ \mathbb{P}/2 \end{bmatrix}; \bar{F}(\bar{X}) = \begin{bmatrix} y(\mathbb{P}/2) - 0 \\ z(\mathbb{P}/2) - 0 \\ \dot{x}(\mathbb{P}/2) - 0 \end{bmatrix} \quad (4.2)$$

The targeted \bar{x}_0 state is thereafter propagated for one period to deliver the entire orbit. This symmetry property is beneficial in targeting the axial orbits.

3. *Double symmetry:* If P_3 traverses through both $\hat{x} - \hat{z}$ plane and \hat{x} axis perpendicularly twice then it is in a periodic orbit. It is apparent that either of the symmetry-based differential correction formulations, Equations (4.1) and (4.2), are useful in targeting a periodic orbit that is doubly symmetric. Alternatively, the two properties are combined for an initial state of type $\bar{x}_0 = [x_0, 0, 0, 0, \dot{y}_0, \dot{z}_0]$ to target a state that is a quarter period downstream. The design and constraint vectors for this symmetry are,

$$\bar{X} = \begin{bmatrix} x_0 \\ \dot{y}_0 \\ \dot{z}_0 \\ \mathbb{P}/4 \end{bmatrix}; \bar{F}(\bar{X}) = \begin{bmatrix} y(\mathbb{P}/4) - 0 \\ \dot{x}(\mathbb{P}/4) - 0 \\ \dot{z}(\mathbb{P}/4) - 0 \end{bmatrix} \quad (4.3)$$

The targeted \bar{x}_0 state is then propagated for the entire period to obtain the complete orbit. This symmetry property is advantageous in targeting vertical orbits.

The above targeting setups are modified based on the problem to leverage multiple shooting, or for computation of planar symmetric periodic orbits. The described formulations have a *1-dimensional* nullspace, so either of the two previously discussed continuation methods delivers a family of periodic orbits.

A general approach to computing any periodic orbit using a shooting method is by leveraging its periodic nature. This method is especially useful for the computation of asymmetric periodic orbits, such as the L_4 short-period orbits. A periodicity-constrained

corrector is defined to drive an initial guess to a solution that returns to itself after a finite period. The design and constraint vectors for the general setup are,

$$\bar{X} = \begin{bmatrix} x_0 \\ y_0 \\ z_0 \\ \dot{x}_0 \\ \dot{y}_0 \\ \dot{z}_0 \\ \mathbb{P} \end{bmatrix}; \bar{F}(\bar{X}) = \begin{bmatrix} x(\mathbb{P}) - x_0 \\ y(\mathbb{P}) - y_0 \\ z(\mathbb{P}) - z_0 \\ \dot{x}(\mathbb{P}) - \dot{x}_0 \\ \dot{y}(\mathbb{P}) - \dot{y}_0 \\ \dot{z}(\mathbb{P}) - \dot{z}_0 \end{bmatrix} \quad (4.4)$$

It is essential to note that the above formulation is numerically unstable as one of the rows of the corresponding Jacobian matrix is linearly dependent due to the existence of an integral of motion, JC . Thus, one of the state constraint is removed based on the application to avoid incorrectly inverting a rank-deficient Jacobian. It is straightforward to realize that while the general setup allows for the construction of any periodic orbit, the symmetry leveraging formulations require fewer computations to target a symmetric periodic orbit. The presented differential corrector, Equation (4.4), consists of a *2-dimensional* nullspace, i.e. the solutions along a periodic orbit and the solutions along the periodic orbit family. The construction of a periodic orbit family using the general setup and NPC is straightforward but for PALC a phase constraint is appended to the constraint vector to reduce the nullspace to *1-dimension*.

A phase constraint reduces the *2-dimensional* nullspace of the periodicity-constrained corrector, Equation (4.4), by fixing the phase of the initial state, which is unique in an orbit. The phase condition employed in AUTO [57] is leveraged in this investigation. The constraint and its partial derivative with respect to the initial state are mathematically expressed as,

$$F_{phase}(\bar{x}_{0,k+1}) = \langle \bar{x}_{0,k+1} - \bar{x}_{0,k}^*, \frac{d\bar{x}_{0,k}^*}{dt} \rangle - 0 = (\bar{x}_{0,k+1} - \bar{x}_{0,k}^*)^T \frac{d\bar{x}_{0,k}^*}{dt} \quad (4.5)$$

$$\frac{\partial F_{phase}(\bar{x}_{0,k+1})}{\partial \bar{x}_{0,k+1}} = \frac{d\bar{x}_{0,k}^*}{dt} \quad (4.6)$$

Where, $\bar{x}_{0,k}^*$ represents the initial state of a converged solution and $\bar{x}_{0,k+1}$ denotes the uncoverged initial state of the next family member. The phase constraint and its partial derivative are augmented to the constraint vector, Equation (4.4), and its Jacobian matrix respectively. The augmented formulation has a *1-dimensional* nullspace that allows for the application of PALC to construct a periodic orbit family. A number of family members of various periodic orbit families are constructed through the mentioned techniques and visualized in Figures 4.1(a), 4.2(a) and 4.3(a) and Chapter A. After the construction of periodic orbits, it is essential to characterize the orbits for an improved understanding of the solution space to assist with a mission design.

4.2 Monodromy Matrix and Stability

The behavior of a periodic orbit and the motion around it is described through the Lyapunov stability analysis and the exploration of associated invariant manifolds. A discrete linear transformation of a periodic solution back onto itself after one complete period under which the periodic solution is a fixed point is identified. The linear transformation allows for linear stability analysis of the fixed point through its eigenvalues. The linear mapping is formulated in terms of the STM of a desired state of the orbit to itself after one period, $\Phi(\tau + \mathbb{P}, \tau)$, and termed the *monodromy matrix*. The monodromy matrix is a symplectic matrix, so its eigenvalues exist as reciprocal pairs [58]. The eigenvalues of the monodromy matrix are the same for all the states along a periodic orbit. In addition, since CR3BP is a Hamiltonian system, thus, two of the eigenvalues are unity, and are referred to as the trivial unity pair [58]. The other two non-trivial eigenvalue pairs describe the stability of the orbit.

Since the monodromy matrix is a discrete-time linear mapping, hence, the stability information encapsulated by the eigenvalues is based on their locations with respect to the unit circle. An eigenvalue situated away from the unit circle indicates hyperbolic local dynamics, while an eigenvalue positioned on the unit circle signifies bounded motion along a higher-period or higher-dimensional orbit. The presence of another unity pair among the non-trivial eigenvalues signifies the periodic orbit as a potential bifurcation point within the orbit family.

A stability index is defined for the periodic orbits for the identification of family members with an additional center subspace that serves as an initial guess for the construction of quasi-periodic orbits. In addition, the index is helpful in realizing orbits that have associated hyperbolic invariant manifolds. There are multiple definitions of the stability index [53], [59] and the index is evaluated for the two non-trivial eigenvalue pairs. The index leveraged in this investigation is defined as,

$$\nu_i = \frac{1}{2} \left(|\lambda_i| + \frac{1}{|\lambda_i|} \right) \quad (4.7)$$

Where, ν_i corresponds to the stability index for λ_i , which is one of the eigenvalues within a pair. The indices for $i = 1$ and $i = 2$ pertain to the first and second non-trivial eigenvalue pairs, respectively. A value of ν_i equal to one for multiple adjacent orbit family members signals the presence of nearby higher-dimensional orbits. Whereas, a value of ν_i greater than one indicates the existence of associated hyperbolic invariant manifolds. The stability indices for a number of periodic orbit families are plotted in Figures 4.1(b), 4.2(b) and 4.3(b) and Chapter A. The family members with $\nu_{1,2} = 1$ and complex conjugate eigenvalue pair allow for the computation of quasi-periodic orbits.

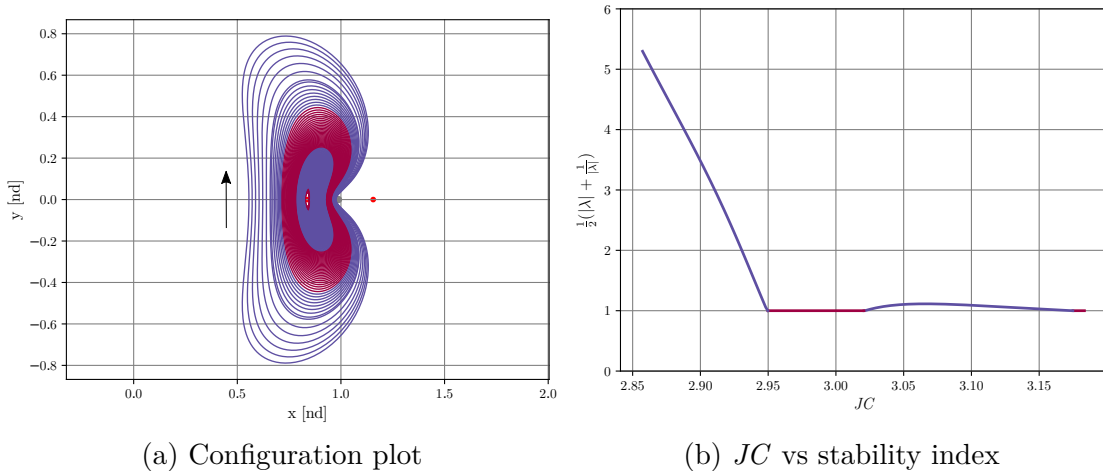


Figure 4.1. The L_1 Lyapunov orbit family members in the Earth-Moon system and stability index, where crimson: family members with atleast one non-trivial 2-dimensional center subspace

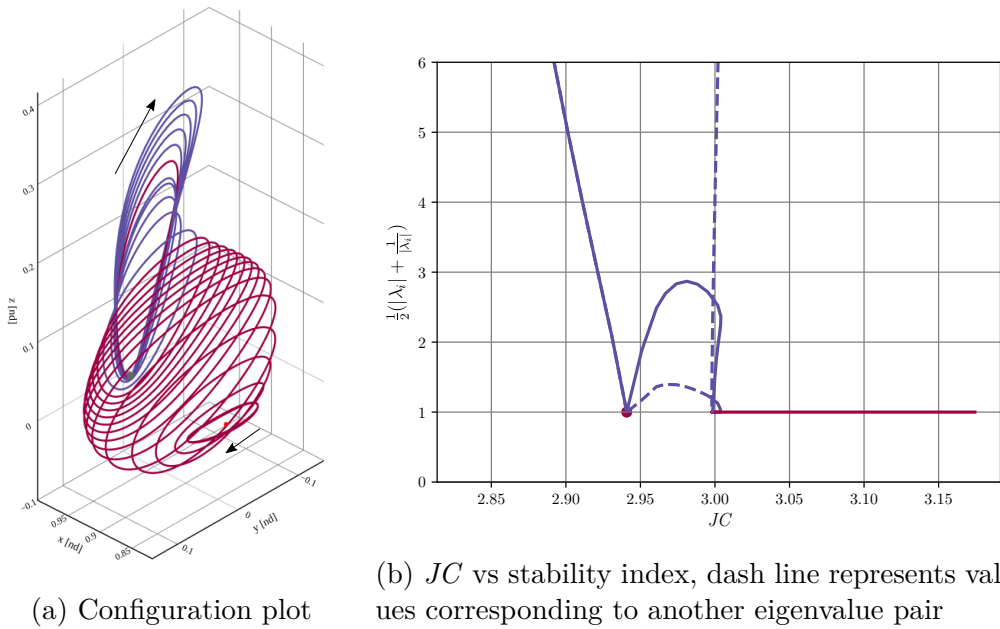


Figure 4.2. The northern L_1 halo orbit family members in the Earth-Moon system and stability index, where crimson: family members with atleast one non-trivial *2-dimensional* center subspace

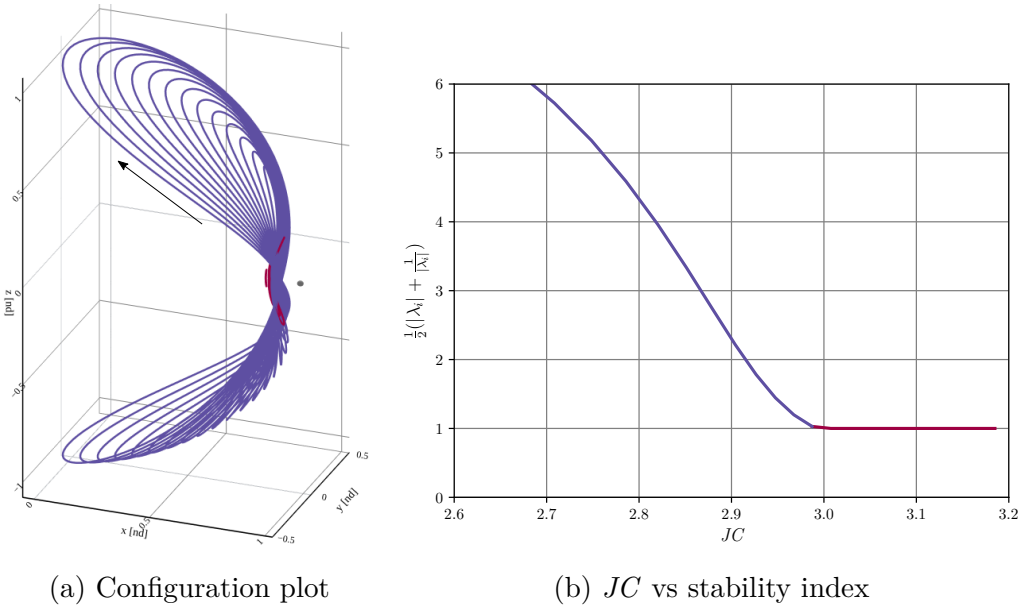


Figure 4.3. The L_1 vertical orbit family members in the Earth-Moon system and stability index, where crimson: family members with atleast one non-trivial *2-dimensional* center subspace

4.3 Hyperbolic Invariant Manifolds

The stable and unstable hyperbolic invariant manifolds corresponding to a periodic orbit play a crucial role in capturing the natural flow towards and away from the orbit. They are particularly valuable for designing transfer pathways between orbits based on the underlying dynamics. For a state of a periodic orbit, \bar{x}^* , the associated local stable/unstable, $W_{loc}^S(\bar{x}^*)$, $W_{loc}^U(\bar{x}^*)$, and global stable/unstable, $W^S(\bar{x}^*)$, $W^U(\bar{x}^*)$, manifolds are defined through the local and global stable/unstable manifolds that emanate from the periodic orbit. The theoretical framework governing the hyperbolic manifolds linked to periodic orbits is provided by the *Stable Manifold Theorem for Periodic Orbits* [60]. The global hyperbolic manifolds corresponding to an orbit are unique, smooth, and invariant.

The global stable/unstable invariant manifolds, $W^S(\Gamma)$, $W^U(\Gamma)$, associated with a periodic orbit are each a *2-dimensional* tube-like surfaces embedded in the *6-dimensional* phase space of CR3BP. Several researchers, including Swenson et al. [61], Gómez et al. [62], and Parker et al. [44] delve into the intricacies of the manifold topology in the context of trajectory design employing the CR3BP model. The hyperbolic trajectory arcs that make up the manifolds tend asymptotically towards or away from every point on the periodic orbit. Consequently, each point on a *2-dimensional* manifold is characterized by two parameters: the step-off location along the periodic orbit and the associated propagation time along the manifold arc originating from the step-off point. To approximate the global stable/unstable invariant manifolds, a discrete set of points is chosen along the periodic orbit. These points serve as origins for the manifold arcs, $W^S(\bar{x}^*)$, $W^U(\bar{x}^*)$, which collectively define the manifolds. The selection of these fixed point locations is tailored to effectively capture the orbit's extent and accurately estimate the characteristics of the manifold tube.

The local manifolds, $W_{loc}^S(\bar{x}^*)$, $W_{loc}^U(\bar{x}^*)$, associated with a fixed point are determined by perturbing the point along the stable/unstable eigenvectors, which are tangential to the

corresponding local manifolds. These eigenvectors are derived from the monodromy matrix of the fixed point. The computation of $W_{loc}^S(\bar{x}^*)$ and $W_{loc}^U(\bar{x}^*)$ involves the following expressions,

$$\bar{x}_U^* = \bar{x}^* \pm \epsilon \bar{v}_U \quad (4.8)$$

$$\bar{x}_S^* = \bar{x}^* \pm \epsilon \bar{v}_S \quad (4.9)$$

Where, \bar{x}^* represents a fixed point along the orbit, \bar{v}_S and \bar{v}_U are the stable and unstable eigenvectors respectively, and ϵ is a scaling factor. The resulting states \bar{x}_S^* and \bar{x}_U^* are local stable and unstable manifold approximations. Importantly, each local manifold $W_{loc}^S(\bar{x}^*)$ and $W_{loc}^U(\bar{x}^*)$ consists of two half-manifolds due to perturbations in the two directions of each of the eigenvectors. The scaling factor, ϵ , has no physical significance, thus, it is common to normalize the eigenvector by its position components for intuitive interpretation of the factor as a distance from \bar{x}^* . For enhanced clarity, Equations (4.8) and (4.9) are revised with normalized eigenvectors as,

$$\bar{x}_U^* = \bar{x}^* \pm \nabla \frac{\bar{v}_U}{\sqrt{v_{U,x}^2 + v_{U,y}^2 + v_{U,z}^2}} \quad (4.10)$$

$$\bar{x}_S^* = \bar{x}^* \pm \nabla \frac{\bar{v}_S}{\sqrt{v_{S,x}^2 + v_{S,y}^2 + v_{S,z}^2}} \quad (4.11)$$

Where, ∇ represents the step-off distance in terms of length units. The Equations (4.10) and (4.11) are leveraged for calculation of $W_{loc}^S(\bar{x}^*)$ and $W_{loc}^U(\bar{x}^*)$ for all the selected fixed points with the same value of ∇ . Subsequently, the local manifolds associated with the fixed points are propagated in backward and forward time for the construction of $W^S(\bar{x}^*)$, $W^U(\bar{x}^*)$ for each point. The collective set of the stable and unstable global manifold arcs approximate the global manifolds corresponding to a periodic orbit. Additionally, there exists a special subset of periodic orbits that possess stable/unstable spiral manifolds that are identified by the presence of stable/unstable complex conjugate eigenvalue pairs of the monodromy matrix of the orbit. The stable/unstable spiral manifolds are *3-dimensional* manifold tubes that are estimated through the method outlined by Bollinger [63] and in this investigation $\theta_{PO,spiral}$ angle represents the angle along the complex plane associated with a local unstable/stable

spiral manifold state. In general, the periodic orbits in this investigation are considered to not possess spiral modes, if otherwise noted. The two-half stable/unstable global manifolds associated with an L_1 Lyapunov and an L_1 halo orbit are approximated through the described technique and plotted in Figures 4.4 and 4.5.

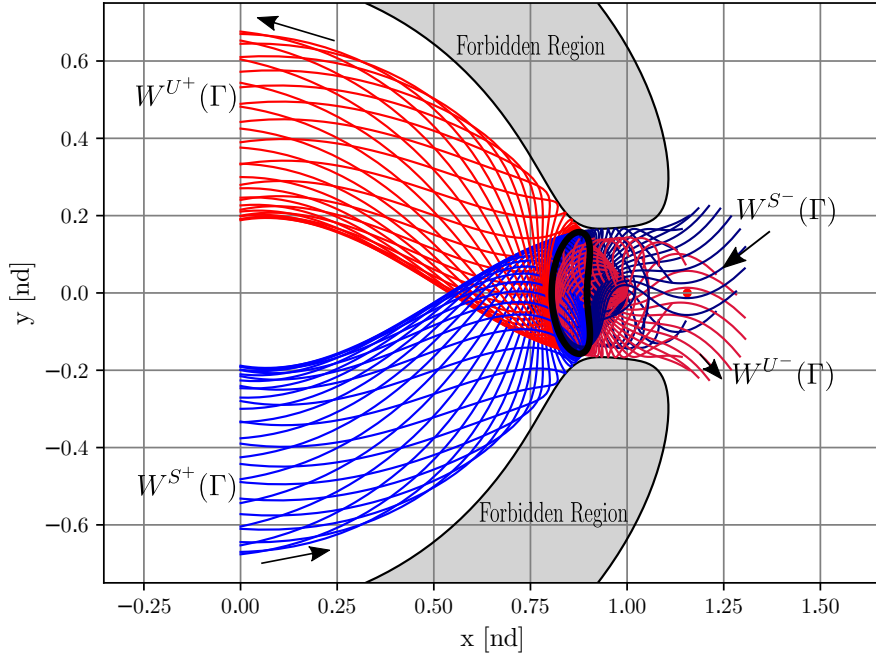


Figure 4.4. The stable and unstable global manifolds corresponding to an L_1 Lyapunov orbit

4.3.1 Effect of Varying Step-off Distance

The choice of the step-off distance, ∇ , for computation of the local manifolds, as described by Equations (4.10) and (4.11), depends on the characteristics of the primary system and is suggested to be within a certain order of magnitude rather than a specific value. The hyperbolic invariant manifolds are asymptotic in nature, they either approach or depart from the orbit in an infinite span of time. It is evident from Equations (4.10) and (4.11) that a smaller ∇ value yields a local manifold approximation that aligns more closely with the true manifold state. However, employing a smaller perturbation necessitates a longer propagation time for the departure of the local stable/unstable manifold state from the orbit in backward/forward time. Such extended propagation time worsens the approximation of

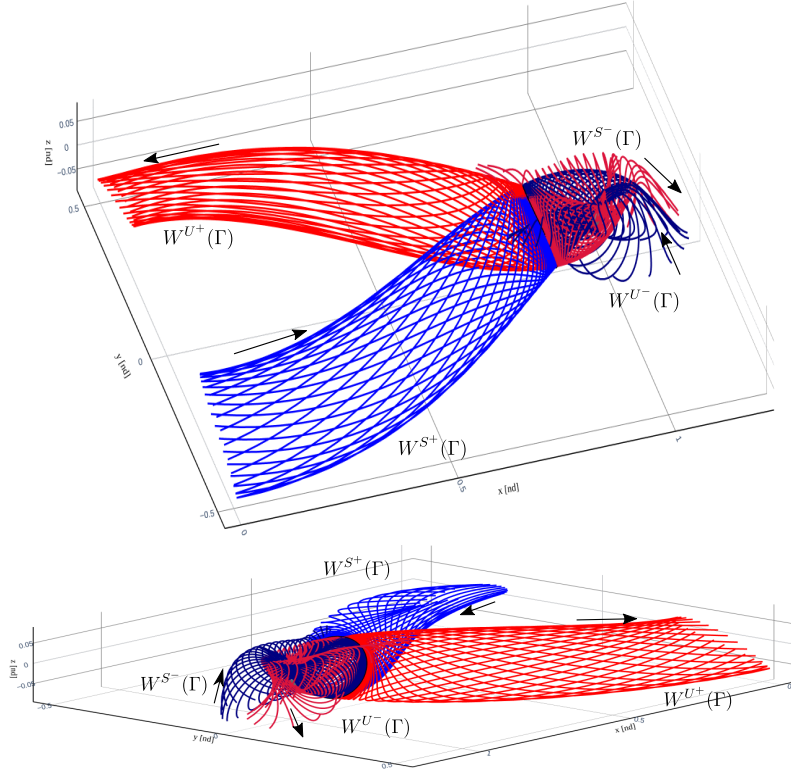


Figure 4.5. The stable and unstable global manifolds associated with an L_1 halo orbit

the global manifolds associated with an orbit due to the accumulation of numerical errors. Conversely, employing a larger ∇ value is not ideal, as it yields a poorer manifold state approximation. Parker et al. [44] suggest selecting a value of ∇ around 100 km for the Earth-Moon system and approximately 1000 km for the Sun-Earth system.

A stable/unstable eigenvector of a fixed point is transversal to the stable/unstable flow associated with an orbit as discussed by Gómez et al. [62]. Consider a fixed point, \bar{x}_1^* , on an orbit and a step-off distance, ∇_1 , as well as two other fixed points, \bar{x}_{1-}^* and \bar{x}_{1+}^* , on the same orbit in the vicinity of \bar{x}_1^* . The approximation of the unstable global manifold arc using the three fixed points and ∇_1 leads to three distinct unstable manifold arcs, $W^U(\bar{x}_1^*, \nabla_1)$, $W^U(\bar{x}_{1-}^*, \nabla_1)$, $W^U(\bar{x}_{1+}^*, \nabla_1)$. Due to the transversal nature of the manifold flow and the freedom to vary the step-off distance, it is feasible to numerically estimate $W^U(\bar{x}_{1-}^*, \nabla_1)$ and $W^U(\bar{x}_{1+}^*, \nabla_1)$ through \bar{x}_1^* as the fixed point and ∇_{1-} and ∇_{1+} as the step-off distance as illustrated in Figure 4.6. The $W^U(\bar{x}_1^*, \nabla_{1-})$ and $W^U(\bar{x}_1^*, \nabla_{1+})$ arcs are qualitatively the same as the $W^U(\bar{x}_{1-}^*, \nabla_1)$ and $W^U(\bar{x}_{1+}^*, \nabla_1)$ and have insignificant numerical

differences, if ∇_{1-} and ∇_{1+} are close to ∇_1 . This powerful realization assists in approximating a collection of global manifold arcs corresponding to an orbit through a single fixed point and an acceptable range of step-off distance. This strategy has been employed by Gómez et al. [62] and Howell et al. [64], [65] with a differential correction scheme to approximate a manifold arc that meets the desired time of flight and phase criteria.

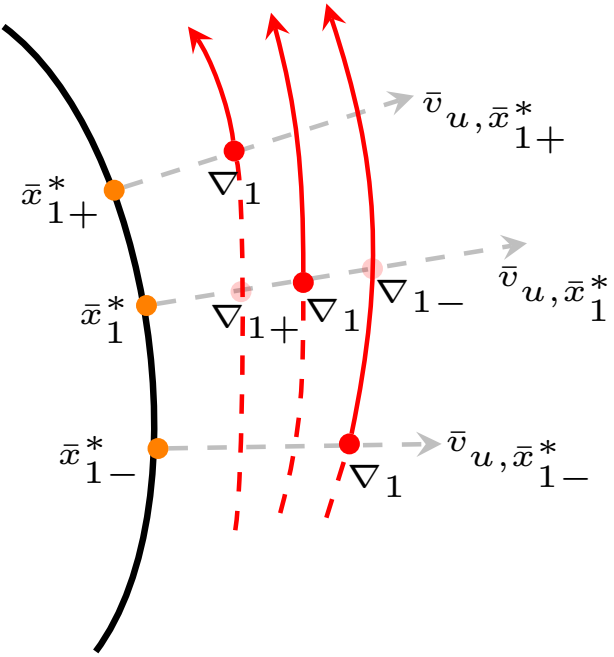


Figure 4.6. Effect of varying step-off distance to approximate unstable manifold arcs associated with nearby fixed points on a periodic orbit

5. QUASI-PERIODIC ORBITS

Quasi-periodic orbits (QPOs) are predictable solutions of the CR3BP and exist as invariant tori with *dimensionality* ≥ 2 , termed the quasi-periodic tori (QPT). The quasi-periodic solutions are challenging to construct due to their non-stationary and non-periodic behavior. The focus of this investigation is limited to *2-dimensional* QPOs that are defined by two fundamental frequencies that are not commensurate. A quasi-periodic torus or orbit represents a higher dimensional invariant torus, whereas a quasi-periodic trajectory refers to a discrete trajectory on the torus. The first-order linear variational equations about the collinear Lagrange points discussed in Section 2.5 showcase the existence of linear *2-dimensional* QPOs. An alternate approach is described for linear approximation of QPOs using a non-trivial *2-dimensional* center subspace associated with periodic orbits, if it exists. The higher dimensional orbits of the CR3BP are sought for the recognition of dynamical behaviors that are not captured by periodic orbits and lead to increased solution space for the purpose of trajectory design.

This chapter delves into the discussion of quasi-periodic behavior and relevant characteristics. Additionally, numerical techniques to construct a QPO and its two-parameter families are explored. Thereafter, the flow dynamics of the structures are described through Lyapunov stability and the associated stable/unstable hyperbolic invariant manifolds.

5.1 Characterization of Quasi-Periodic Behavior

The examination of the flow on a quasi-periodic torus is facilitated through a stroboscopic map. A periodic orbit appears as a fixed point on a stroboscopic map, while a quasi-periodic torus manifests as an unchanging closed curve on the map. A quasi-periodic trajectory's successive returns to a stroboscopic map are displayed as discrete points. If this trajectory is extended indefinitely, the discrete points coalesce to form a continuous curve known as the invariant curve. The QPO behavior is explored via the projection of the linear estimation of the non-trivial *2-dimensional* center subspace associated with a periodic orbit on a stroboscopic map. The approximation of the center manifolds follows a similar approach to that of the associated stable/unstable invariant manifolds, as elucidated in Section 4.3.

The stroboscopic map simplifies the representation of the center manifolds by reducing the motion on a torus to an invariant curve.

The linear dynamics in the center subspace associated with a periodic orbit are demonstrated by considering a sample orbit and employing a stroboscopic map. Consider an L_1 northern halo orbit in the Earth-Moon system with $JC = 3.10$ and Period = 12.10035 days. The orbit has a non-trivial *2-dimensional* center subspace with center eigenvalues as $\lambda_c = 0.29449 \pm 0.9557i$. A local center manifold state, \bar{x}_c^* , is approximated via the center eigenvector, \bar{v}_c , associated with λ_c , of the monodromy of a periodic orbit state. The approximation is governed by the following expression, which is similar to Equations (4.10) and (4.11),

$$\bar{x}_c^* = \bar{x}_{\text{PO}}^* + \nabla \frac{(\text{Re}[\bar{v}_c]\cos(\theta_c) - \text{Im}[\bar{v}_c]\sin(\theta_c))}{\sqrt{v_{c,x}^2 + v_{c,y}^2 + v_{c,z}^2}} \quad (5.1)$$

Where, \bar{x}_{PO}^* represents a state on the periodic orbit, ∇ denotes the step-off distance from the periodic orbit state (measured in unit length), $\text{Re}[\bar{v}_c]$ and $\text{Im}[\bar{v}_c]$ are the real and imaginary components of \bar{v}_c , and θ_c is an arbitrary angle $\in [0, 2\pi]$. It is apparent from Equation (5.1) that a center manifold approximation is not unique for a choice of step-off location and ∇ value, unlike for stable/unstable manifold approximation [45].

When a center manifold state is propagated for a single stroboscopic time period (equivalent to the period of the underlying periodic orbit), it returns to the vicinity of the initial state albeit shifted. The shift in a linear sense is realized in terms of rotation on a *6-dimensional* hypersphere spanned by the vectors: $\text{Re}[\bar{v}_c]$ and $-\text{Im}[\bar{v}_c]$. The angle of rotation of the center manifold state after one stroboscopic time period is linearly estimated by the argument of the complex center eigenvalue, as evaluated by the subsequent equation,

$$\rho^0 = \tan^{-1} \left(\frac{\text{Im}[\lambda_c]}{\text{Re}[\lambda_c]} \right) \quad (5.2)$$

where, $\text{Re}[\lambda_c]$ and $\text{Im}[\lambda_c]$ are the real and imaginary components of λ_c , respectively. To illustrate the aforementioned concepts, consider the apoapse state of the halo orbit as the step-off location, \bar{x}_{PO}^* , as plotted in Figure 5.1. A local center manifold state, $\bar{x}_{c,0}^*$, is approximated through Equation (5.1) with $\theta_c = 0$ rad and $\nabla = 100$ km, and it is propagated for one

stroboscopic period to yield $\bar{x}_{c,0}^*(\mathbb{P})$ state. The propagated state is theoretically known to lie on the invariant curve with an angular displacement of ρ^0 from the initial state. Another local center manifold state, \bar{x}_{c,ρ^0}^* , is evaluated using $\theta_c = \rho^0$ and $\nabla = 100$ km. The three center manifold states: $\bar{x}_{c,0}^*$, $\bar{x}_{c,0}^*(\mathbb{P})$, \bar{x}_{c,ρ^0}^* , as well as \bar{x}_{PO}^* lie on the same stroboscopic map and are presented in Figure 5.2 for clarity. This visualization demonstrates that the downstream center manifold state is displaced along the invariant curve with respect to the initial state, as well as being approximated by the \bar{x}_{c,ρ^0}^* state. However, due to the linear approximation of the manifold state, the two states do not perfectly coincide in the *6-dimensional* phase space. Consequently, a numerical algorithm is sought, that is capable of harnessing the quasi-periodic behavior to facilitate the construction of non-linear QPT.

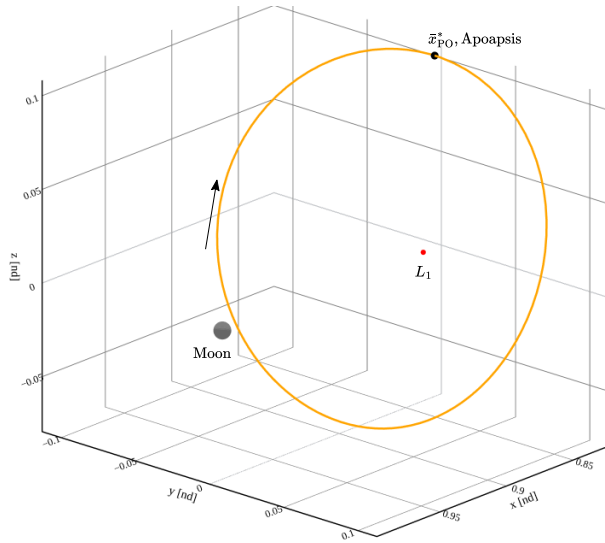
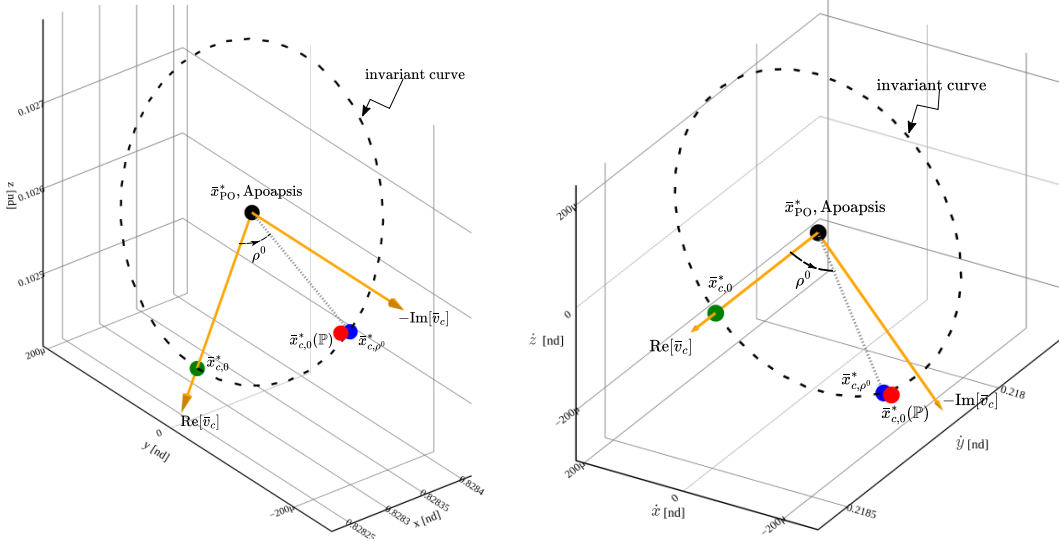


Figure 5.1. L_1 halo orbit in the Earth-Moon system, $JC = 3.10$ and its apoapse state.

The corrected non-linear *2-dimensional* QPT are characterized by two constant incommensurate frequencies, $[\omega_{T^0}, \omega_{\rho^0}]$. A phase state on the torus is alternatively parameterized by two angular variables, $[\theta_{T^0}, \theta_{\rho^0}] \in [0, 2\pi]^2$. The first frequency, referred to as the longitudinal frequency and symbolized as ω_{T^0} , is the rate of change of θ_{T^0} , and is defined by the stroboscopic time period as follows,

$$\omega_{T^0} = \frac{2\pi}{T^0} \quad (5.3)$$



(a) Configuration space plot

(b) Velocity space plot

Figure 5.2. Stroboscopic map about the apoapse state of an L_1 halo orbit in the Earth-Moon system, $JC = 3.10$.

The latitudinal frequency, $\omega_{\rho^0} = \dot{\theta}_{\rho^0}$, depends on the rotational angle and time period, and is evaluated as,

$$\omega_{\rho^0} = \frac{\rho^0}{T^0} = \frac{\rho^0 \omega_{T^0}}{2\pi} \quad (5.4)$$

The two frequencies are constant, hence, the two angular parameters evolve linearly with time, τ , and are straightforwardly given by,

$$\theta_{T^0}(\tau) = \theta_{T^0}(0) + \omega_{T^0}\tau \quad (5.5)$$

$$\theta_{\rho^0}(\tau) = \theta_{\rho^0}(0) + \omega_{\rho^0}\tau \quad (5.6)$$

It is essential that the the two frequencies are not commensurate, or else the motion degenerates to a periodic orbit. The above parameters, as depicted in Figure 5.3, assist in the succinct description of a QPO and a phase state on it.

The predictable nature of a center manifold state after the first return to a stroboscopic map assists in formulating an invariance constraint for the construction of QPT. Consider a

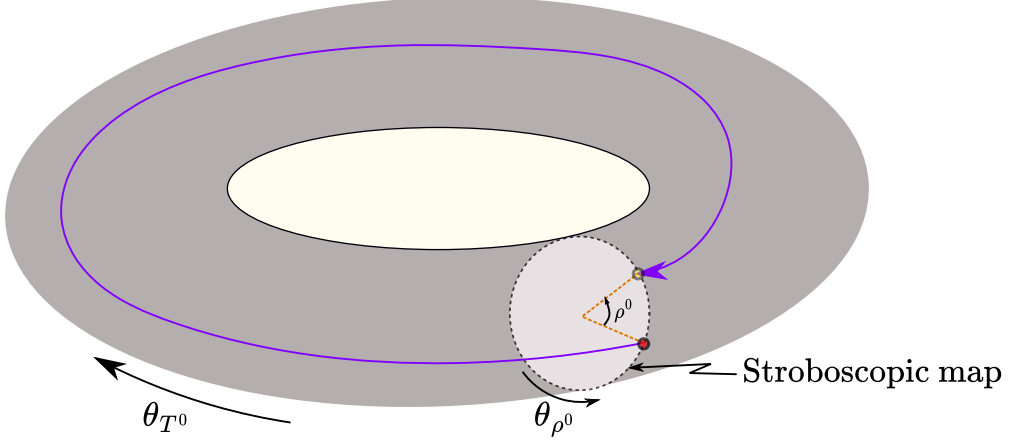


Figure 5.3. Phase states on a QPO defined by θ_{T^0} and θ_{ρ^0} angles.

phase state on the QPO with angular variables $\theta_{T^0}, \theta_{\rho^0}$ represented as $\bar{x}(\theta_{T^0}, \theta_{\rho^0})$. The three manifold states: $\bar{x}_{c,0}^*, \bar{x}_{c,0}^*(\mathbb{P}), \bar{x}_{c,\rho^0}^*$ are then rewritten in terms of the two angular variables as,

$$\bar{x}(0, 0) = \bar{x}_{c,0}^* \quad (5.7)$$

$$\bar{x}(2\pi, \rho^0) = \bar{x}_{c,0}^*(\mathbb{P}) \quad (5.8)$$

$$\bar{x}(0, \rho^0) = \bar{x}_{c,\rho^0}^* \quad (5.9)$$

There exists a rotation matrix, $\mathfrak{R}_{-\rho^0}$, that rotates a state by $-\rho^0$ along the invariant curve, the resulting state is expressed as,

$$\mathfrak{R}_{-\rho^0}\bar{x}(2\pi, \rho^0) = \bar{x}(2\pi, 0) = \bar{x}(0, 0) \quad (5.10)$$

It is evident from the above expression that it is feasible to recover the initial state, $\bar{x}_{c,0}^*$, by removing the rotation from the downstream state, $\bar{x}_{c,0}^*(\mathbb{P})$. This property is referred to as the invariance condition and is defined as a constraint for the application of differential corrections, represented as,

$$\mathfrak{R}_{-\rho^0}\bar{x}(2\pi, \rho^0) - \bar{x}(0, 0) = 0 \quad (5.11)$$

The formulation of $\mathfrak{R}_{-\rho^0}$ matrix is challenging, hence, an alternate strategy built on the described behavior is elucidated for computation of a rotation operator in the subsequent section for the construction of QPT.

5.2 Construction of *2-dimensional* Quasi-Periodic Tori

The GMOS algorithm is leveraged in this investigation for the construction of QPOs and the description of the algorithm is inspired by McCarthy [27]. An invariant torus is numerically constructed by targeting a discrete number of states that describe an invariant curve and satisfy the invariance condition. Akin to the discrete number of trajectories that are desired for the approximation of stable/unstable global manifolds associated with a periodic orbit, a discrete number of trajectories are required to numerically approximate an invariant torus. However, due to the predictable quasi-periodic behavior, the initial state representation of the discrete trajectories originating from the same invariant curve is sufficient to describe the torus. For the numerical implementation of the invariance condition, as exemplified in Equation (5.11), the constraint is reformulated to rely on a rotation operator that is evaluated using a truncated Fourier series representation of the states that describe a continuous invariant curve. The Fourier series approximation allows for an intuitive approach to rotate the states along the invariant curve by phase-shifting the associated Fourier coefficients and computing the phase space representation of the phase-shifted coefficients. A differential correction scheme is elucidated that iteratively refines multiple states to satisfy the invariance constraint by leveraging the truncated Fourier series for rotating states along the invariant curve.

A single shooting method for the construction of a QPO involves targeting multiple states simultaneously that lie on the same invariant curve, such that the states have the same rotation angle and stroboscopic time period. A continuous invariant curve is sampled with N states that are equally spaced for computing a Fourier series representation of the curve. The choice of N is dependent on the primary system, and the span of the invariant curve at the chosen step-off location. Based on heuristics, for the Earth-Moon system, a reasonable value of N is 35. The initial guess of the invariant curve states for the single

shooter is obtained via the linear approximation of the center subspace using Equation (5.1). For a chosen step-off location on a periodic orbit and ∇ value, the N states are obtained through a $1 \times N$ vector of equally spaced latitudinal angles defined as,

$$\bar{\theta}_{\rho^0} = \begin{bmatrix} 0 & \frac{2\pi}{N} & \dots & \frac{2\pi(N-2)}{N} & \frac{2\pi(N-1)}{N} \end{bmatrix}; \quad \theta_{\rho^0,i} = \frac{2\pi(i-1)}{N}, i = 1, 2, \dots, N \quad (5.12)$$

where, N is assumed to be an odd value. To increase the computational accuracy for the determination of the discrete states, the basepoint of the states is transformed from the barycenter of the system to the chosen step-off location. The states on the invariant curve are thus evaluated for $\bar{\theta}_{\rho^0}$ as,

$$\bar{u}_i^1 = \bar{x}_{c,i}^* - \bar{x}_{\text{PO}}^* = \nabla \frac{(\text{Re}[\bar{v}_c] \cos(\theta_{\rho^0,i}) - \text{Im}[\bar{v}_c] \sin(\theta_{\rho^0,i}))}{\sqrt{v_{c,x}^2 + v_{c,y}^2 + v_{c,z}^2}} \quad (5.13)$$

where, $\bar{u}_i^1 = [u_{x,i}^1 \ u_{y,i}^1 \ u_{z,i}^1 \ u_{\dot{x},i}^1 \ u_{\dot{y},i}^1 \ u_{\dot{z},i}^1]^T$ is the i^{th} state on the invariant curve. The design variable vector for the single shooting method using \bar{u}^1 states is of size $(6N + 2) \times 1$ and given as,

$$\bar{X} = \begin{bmatrix} \bar{u}_1^1 \\ \bar{u}_2^1 \\ \vdots \\ \bar{u}_{N-1}^1 \\ \bar{u}_N^1 \\ T^0 \\ \rho^0 \end{bmatrix} \quad (5.14)$$

The initial guess for T^0 comes from the period of the underlying periodic orbit and ρ^0 is obtained through Equation (5.2). The previously presented idea of invariance condition is

exploited for the construction of a non-linear constraint. The constraint vector is of length $6N$ and defined as,

$$\bar{F}(\bar{X}) = \begin{bmatrix} {}^{T^0,R}\bar{u}_1^1 - \bar{u}_1^1 \\ {}^{T^0,R}\bar{u}_2^1 - \bar{u}_2^1 \\ \vdots \\ {}^{T^0,R}\bar{u}_{N-1}^1 - \bar{u}_{N-1}^1 \\ {}^{T^0,R}\bar{u}_N^1 - \bar{u}_N^1 \end{bmatrix} \quad (5.15)$$

where, ${}^{T^0,R}\bar{u}_i^1$ denotes a state obtained after propagating \bar{u}_i^1 state till the next crossing of the stroboscopic map, denoted by ${}^{T^0}\bar{u}_i^1$ state, and then rotating ${}^{T^0}\bar{u}_i^1$ state by $-\rho^0$ around the curve. The GMOS algorithm relies on truncated Fourier series representation of all the ${}^{T^0}\bar{u}^1$ states for the evaluation of the invariance constraint.

A rotation operator for computation of the ${}^{T^0,R}\bar{u}^1$ states is devised through the truncated Fourier series representation of the ${}^{T^0}\bar{u}^1$ states. The discrete Fourier transform is employed to express the discrete states in terms of Fourier series coefficients, ${}^{T_0}\mathbf{C}_0$, through the following expression,

$${}^{T_0}\mathbf{C}_0 = (\mathbf{D})(\mathbf{T}^0\mathbf{U}) \quad (5.16)$$

Where, \mathbf{D} is the discrete Fourier transform operator of size $N \times N$ and $\mathbf{T}^0\mathbf{U}$ represents all the ${}^{T_0}\bar{u}^1$ states in a matrix form. The discrete Fourier transform (DFT) operator is independent of the choice of phase states. However, the application of the DFT operator is only valid for

the phase states that lie on a periodic curve and are equally spaced along the curve. The operator is defined as,

$$\mathbf{D} = \frac{1}{N} e^{-i\bar{k}^T \bar{\theta}_{\rho^0}} \quad (5.17)$$

$$= \frac{1}{N} \begin{bmatrix} e^{-i(-\frac{N-1}{2})0} & e^{-i(-\frac{N-1}{2})\frac{2\pi}{N}} & \dots & e^{-i(-\frac{N-1}{2})\frac{2\pi(N-1)}{N}} \\ \vdots & \vdots & & \vdots \\ e^{-i(-1)0} & e^{-i(-1)\frac{2\pi}{N}} & \dots & e^{-i(-1)\frac{2\pi(N-1)}{N}} \\ e^{-i(0)0} & e^{-i(0)\frac{2\pi}{N}} & \dots & e^{-i(0)\frac{2\pi(N-1)}{N}} \\ e^{-i(1)0} & e^{-i(1)\frac{2\pi}{N}} & \dots & e^{-i(1)\frac{2\pi(N-1)}{N}} \\ \vdots & \vdots & & \vdots \\ e^{-i(\frac{N-1}{2})0} & e^{-i(\frac{N-1}{2})\frac{2\pi}{N}} & \dots & e^{-i(\frac{N-1}{2})\frac{2\pi(N-1)}{N}} \end{bmatrix} \quad (5.18)$$

where, $\bar{\theta}_{\rho^0}$ is based on Equation (5.12) and \bar{k} for odd value of N is given as,

$$\bar{k} = \left[-\frac{N-1}{2} \quad \dots \quad -1 \quad 0 \quad 1 \quad \dots \quad \frac{N-1}{2} \right] \quad (5.19)$$

and $\mathbf{T}_0 \mathbf{U}$ matrix is expressed as,

$$\mathbf{T}_0 \mathbf{U} = \begin{bmatrix} T_0 \bar{u}_1^{1T} \\ T_0 \bar{u}_2^{1T} \\ \vdots \\ T_0 \bar{u}_{N-1}^{1T} \\ T_0 \bar{u}_N^{1T} \end{bmatrix} = \begin{bmatrix} T_0 u_{x,1}^1 & T_0 u_{y,1}^1 & T_0 u_{z,1}^1 & T_0 u_{\dot{x},1}^1 & T_0 u_{\dot{y},1}^1 & T_0 u_{\dot{z},1}^1 \\ T_0 u_{x,2}^1 & T_0 u_{y,2}^1 & T_0 u_{z,2}^1 & T_0 u_{\dot{x},2}^1 & T_0 u_{\dot{y},2}^1 & T_0 u_{\dot{z},2}^1 \\ \vdots & \vdots & \vdots & \vdots & \vdots & \vdots \\ T_0 u_{x,N-1}^1 & T_0 u_{y,N-1}^1 & T_0 u_{z,N-1}^1 & T_0 u_{\dot{x},N-1}^1 & T_0 u_{\dot{y},N-1}^1 & T_0 u_{\dot{z},N-1}^1 \\ T_0 u_{x,N}^1 & T_0 u_{y,N}^1 & T_0 u_{z,N}^1 & T_0 u_{\dot{x},N}^1 & T_0 u_{\dot{y},N}^1 & T_0 u_{\dot{z},N}^1 \end{bmatrix} \quad (5.20)$$

The computed Fourier coefficients are phase shifted by $-\rho^0$ and transformed back to the phase space to deliver the rotation operator and subsequently the $T^0, R \bar{u}^1$ states. The Fourier coefficients are phase-shifted straightforwardly by adding the desired phase to the phase of

the coefficients. It is numerically accomplished by employing a phase-shift operator, that is a $N \times N$ diagonal matrix, and defined for phase shift by $-\rho^0$ as,

$$\mathbf{Q}_{-\rho^0} = e^{-i\bar{k}\rho^0} \mathbf{I}_{N \times N} = \begin{bmatrix} e^{i(-\frac{N-1}{2})-\rho^0} & 0 & \dots & 0 \\ 0 & e^{i(-\frac{N-1}{2}+1)-\rho^0} & \dots & 0 \\ \vdots & \vdots & \ddots & \vdots \\ 0 & 0 & \dots & e^{i(\frac{N-1}{2})-\rho^0} \end{bmatrix} \quad (5.21)$$

where, $\mathbf{I}_{N \times N}$ is the identity matrix of size $N \times N$. An inverse DFT operator, which is the inverse of the DFT operator, transforms the phase-shifted coefficients to phase space. The above ideas are combined to formulate the following expression,

$$\mathbf{T}^0, \mathbf{R} \mathbf{U} = (\mathbf{D}^{-1} \mathbf{Q}_{-\rho^0} \mathbf{D})(\mathbf{T}^0 \mathbf{U}) = (\mathbf{R}_{-\rho^0})(\mathbf{T}^0 \mathbf{U}) \quad (5.22)$$

$$\implies \mathbf{R}_{-\rho^0} = \mathbf{D}^{-1} \mathbf{Q}_{-\rho^0} \mathbf{D} \quad (5.23)$$

Where, $\mathbf{T}^0, \mathbf{R} \mathbf{U}$ is the matrix representation of ${}^{T^0, R} \bar{\mathbf{u}}^1$ states, similar to the definition of $\mathbf{T}^0 \mathbf{U}$ in Equation (5.20) and $\mathbf{R}_{-\rho^0}$ signifies the rotation operator. The rotation operator is a real-valued matrix of size $N \times N$ and acts on the matrix form of the state vectors instead of an individual state vector. The devised $\mathbf{T}^0, \mathbf{R} \mathbf{U}$ matrix through the $\mathbf{R}_{-\rho^0}$ matrix assists in the evaluation of the invariance constraint as constructed in Equation (5.15). The differential corrections setup, Equations (5.14) and (5.15), has a *4-dimensional* null-space as it makes no assumption about the longitudinal and latitudinal phase of the states and since QPO exists as a biparameteric family. Nonetheless, the setup is adequate for the correction of a set of states that represent an invariant curve, which in turn describes a QPO.

The Jacobian matrix of the shooting method to construct a QPO is evaluated through numerical differentiation, as described in Chapter 3, or through analytical expressions. The partial derivatives of the single shooting method described by Equations (5.14) and (5.15) are represented as,

$$\mathbf{DF}(\bar{X}) = \left[\frac{\partial(\mathbf{T}^0, \mathbf{R} \bar{\mathbf{u}}^1 - \bar{\mathbf{u}}^1)}{\partial \bar{\mathbf{u}}^1} \quad \frac{\partial(\mathbf{T}^0, \mathbf{R} \bar{\mathbf{u}}^1 - \bar{\mathbf{u}}^1)}{\partial T^0} \quad \frac{\partial(\mathbf{T}^0, \mathbf{R} \bar{\mathbf{u}}^1 - \bar{\mathbf{u}}^1)}{\partial \rho^0} \right] \quad (5.24)$$

where, $\frac{\partial(\mathbf{T}^0, \mathbf{R}\bar{\mathbf{u}}^1 - \bar{\mathbf{u}}^1)}{\partial\bar{\mathbf{u}}^1}$ denotes the partial derivatives of the invariance constraint with respect to the initial states, $\frac{\partial(\mathbf{T}^0, \mathbf{R}\bar{\mathbf{u}}^1 - \bar{\mathbf{u}}^1)}{\partial T^0}$ symbolizes the partial derivatives of the invariance constraint with respect to the stroboscopic time period and $\frac{\partial(\mathbf{T}^0, \mathbf{R}\bar{\mathbf{u}}^1 - \bar{\mathbf{u}}^1)}{\partial\rho_0}$ signifies the partial derivatives of the invariance condition with respect to the rotation angle. The $\frac{\partial(\mathbf{T}^0, \mathbf{R}\bar{\mathbf{u}}^1 - \bar{\mathbf{u}}^1)}{\partial\bar{\mathbf{u}}^1}$ derivatives are analytically evaluated by leveraging the idea of STM, through the following expression,

$$\frac{\partial(\mathbf{T}^0, \mathbf{R}\bar{\mathbf{u}}^1 - \bar{\mathbf{u}}^1)}{\partial\bar{\mathbf{u}}^1} = \frac{\partial(\mathbf{T}^0, \mathbf{R}\bar{\mathbf{u}}^1)}{\partial\bar{\mathbf{u}}^1} - \frac{\partial(\bar{\mathbf{u}}^1)}{\partial\bar{\mathbf{u}}^1} = (\mathbf{R}_{-\rho^0} \otimes \mathbf{I})\tilde{\Phi} - \tilde{\mathbf{I}} = \mathbf{D}\mathbf{G}_{\text{qpo}} - \tilde{\mathbf{I}} \quad (5.25)$$

where, \mathbf{I} and $\tilde{\mathbf{I}}$ are identity matrices of size $N \times N$ and $6N \times 6N$ respectively, $\mathbf{R}_{-\rho^0}$ denotes the rotation operator as defined in Equation (5.23), \otimes signifies the Kronecker product operator, $\tilde{\Phi}$ represents a block diagonal matrix comprising of STMs of all the $T_0\bar{u}^1$ states with respect to all the \bar{u}^1 states, and $\mathbf{D}\mathbf{G}_{\text{qpo}}$ corresponds to a modified form of the STMs that defines a linear mapping under which the quasi-periodic states on the invariant curve are all fixed points. The block diagonal matrix of STMs, $\tilde{\Phi}$, is defined as,

$$\tilde{\Phi} = \begin{bmatrix} \Phi_1(T^0, 0) & \mathbf{0}_{6 \times 6} & \dots & \mathbf{0}_{6 \times 6} & \mathbf{0}_{6 \times 6} \\ \mathbf{0}_{6 \times 6} & \Phi_2(T^0, 0) & \dots & \mathbf{0}_{6 \times 6} & \mathbf{0}_{6 \times 6} \\ \vdots & \vdots & \ddots & \vdots & \vdots \\ \mathbf{0}_{6 \times 6} & \mathbf{0}_{6 \times 6} & \dots & \Phi_{N-1}(T^0, 0) & \mathbf{0}_{6 \times 6} \\ \mathbf{0}_{6 \times 6} & \mathbf{0}_{6 \times 6} & \dots & \mathbf{0}_{6 \times 6} & \Phi_N(T^0, 0) \end{bmatrix} \quad (5.26)$$

where, $\Phi_i(T^0, 0)$ is a STM of $T_0\bar{u}_i^1$ state with respect to the \bar{u}_i^1 state. The $\frac{\partial(\mathbf{T}^0, \mathbf{R}\bar{\mathbf{u}}^1 - \bar{\mathbf{u}}^1)}{\partial T^0}$ derivatives form a $6N \times 1$ vector represented as,

$$\frac{\partial(\mathbf{T}^0, \mathbf{R}\bar{\mathbf{u}}^1 - \bar{\mathbf{u}}^1)}{\partial T^0} = \begin{bmatrix} T_0, R\dot{\bar{u}}_1^1 \\ T_0, R\dot{\bar{u}}_2^1 \\ \vdots \\ T_0, R\dot{\bar{u}}_{N-1}^1 \\ T_0, R\dot{\bar{u}}_N^1 \end{bmatrix} \quad (5.27)$$

The ${}^{T_0,R}\dot{\bar{u}}^1$ states are evaluated through,

$${}^{T_0,R}\dot{\mathbf{U}} = (\mathbf{R}_{-\rho^0})({}^{T_0}\dot{\mathbf{U}}) \quad (5.28)$$

where, ${}^{T_0,R}\dot{\mathbf{U}}$ and ${}^{T_0}\dot{\mathbf{U}}$ are the $N \times 6$ matrix form of the ${}^{T_0,R}\dot{\bar{u}}^1$ and ${}^{T_0}\dot{\bar{u}}^1$ states, respectively. The ${}^{T_0}\dot{\bar{u}}^1$ states are the time derivatives of the ${}^{T_0}\bar{u}^1$ states. The last column of the Jacobian matrix, Equation (5.24), is analytically governed by the partial derivative of the phase-shift operator with respect to the rotation angle. The relationship in the matrix form is mathematically expressed as,

$$\frac{\partial(\mathbf{T}^0, \mathbf{R}\mathbf{U})}{\partial\rho^0} = \frac{\partial((\mathbf{D}^{-1}\mathbf{Q}_{-\rho^0}\mathbf{D})(\mathbf{T}^0\mathbf{U}))}{\partial\rho_0} = (\mathbf{D}^{-1}\frac{\partial(\mathbf{Q}_{-\rho^0})}{\partial\rho_0}\mathbf{D})(\mathbf{T}^0\mathbf{U}) \quad (5.29)$$

where, the partial derivative of $\frac{\partial(\mathbf{Q}_{-\rho^0})}{\partial\rho_0}$ is defined as,

$$\frac{\partial(\mathbf{Q}_{-\rho^0})}{\partial\rho_0} = \text{diag}[-i\bar{k}]e^{-i\bar{k}\rho^0} = \begin{bmatrix} \frac{N-1}{2}e^{i(-\frac{N-1}{2})-\rho^0} & 0 & \dots & 0 \\ 0 & (\frac{N-1}{2}+1)e^{i(-\frac{N-1}{2}+1)-\rho^0} & \dots & 0 \\ \vdots & \vdots & \ddots & \vdots \\ 0 & 0 & \dots & -\frac{N-1}{2}e^{i(\frac{N-1}{2})-\rho^0} \end{bmatrix} \quad (5.30)$$

The $\text{diag}[-i\bar{k}]$ matrix represents a diagonal matrix with $-i\bar{k}$ as the diagonal elements. After the evaluation of $\frac{\partial(\mathbf{T}^0, \mathbf{R}\mathbf{U})}{\partial\rho^0}$ matrix of size $N \times 6$, the elements are reshaped to a vector of shape $6N \times 1$ to define the $\frac{\partial(\mathbf{T}^0, \mathbf{R}\bar{\mathbf{u}}^1 - \bar{\mathbf{u}}^1)}{\partial\rho^0}$ partial. It is evident that the Jacobian matrix, Equation (5.24), is a dense matrix and it is feasible to evaluate the elements through the outlined analytical expressions. Due to the underconstrained nature of the problem, Equations (5.14) and (5.15), a minimum norm update is employed for refinement of the initial guess. For increased control over parameter selection for the construction of QPT, additional characteristic and phase constraints are appended to the shooting framework.

5.3 Biparametric Families of *2-dimensional* Quasi-Periodic Tori and Phase Constraints

The *2-dimensional* QPT exist as biparametric families of QPOs. The biparametric family members, which are a *2-dimensional* surface of solutions, are parameterized by either the two fundamental frequencies or through the stroboscopic time period and rotation angle as illustrated in Figure 5.4. However, for integer frequency ratios, the QPT degenerates to periodic orbits, hence, all the members are not smoothly connected. For methodical construction of the family members or a QPO of desired characteristics, it is advantageous to append a characteristic constraint to the previously constructed constraint vector of the shooting method that relies on the GMOS algorithm.

For orbit and transfer design purposes, often *1-dimensional* subsets of the biparametric family are sought with members that have a common characteristic, such as the stroboscopic time period, or rotation angle. Additionally, due to the multi-dimensional nature of the family of QPOs, it is feasible to obtain a set of QPOs with the same JC value as visualized in Figure 5.4(b). A family of QPOs with a specific stroboscopic time period or rotation angle is computed by constraining the chosen characteristic to be of a desired value. The *1-dimensional* iso-energy family members are determined by adding a constraint such that the average JC value of the states on an invariant curve is the same as a desired JC value. The three subsets of the family based on the three characteristics, stroboscopic time period, rotation angle, and JC value, are termed the constant mapping time, constant frequency ratio, and constant energy families, respectively, as shown in Figure 5.4(b). The characteristic constraint that is appended to Equation (5.15) and the associated partial derivatives with Equation (5.14) as the design vector are presented in Table 5.1. The JC_{avg} quantity is the average of the JC values of the N states on the invariant curve given by,

$$JC_{\text{avg}} = \frac{1}{N} \sum_{i=1}^N JC_i \quad (5.31)$$

Table 5.1. Characteristic constraints and their partial derivatives

Family type	F_{char}	$\frac{\partial F_{\text{char}}}{\partial \bar{u}^1}$	$\frac{\partial F_{\text{char}}}{\partial T^0}$	$\frac{\partial F_{\text{char}}}{\partial \rho^0}$
Constant mapping time	$T^0 - T_d^0$	$\mathbf{0}_{1 \times 6N}$	1	0
Constant frequency ratio	$\rho^0 - \rho_d^0$	$\mathbf{0}_{1 \times 6N}$	0	1
Constant energy	$JC_{\text{avg}} - JC_d$	$\frac{\partial \mathbf{JC}_{\text{avg}}}{\partial \bar{u}^1}$	0	0

where, JC_i is the JC value of the $\bar{x}_{c,i}^*$ state, which was defined as the barycentered rotating frame analog of the \bar{u}_i^1 state in the Equation (5.13). The $\frac{\partial \mathbf{JC}_{\text{avg}}}{\partial \bar{u}^1}$ partial derivatives are expressed as,

$$\frac{\partial \mathbf{JC}_{\text{avg}}}{\partial \bar{u}^1} = \frac{1}{N} \begin{bmatrix} \frac{\partial JC_1}{\partial \bar{u}_1^1} & \frac{\partial JC_2}{\partial \bar{u}_2^1} & \cdots & \frac{\partial JC_N}{\partial \bar{u}_N^1} \end{bmatrix} \quad (5.32)$$

The $\frac{\partial JC_i}{\partial \bar{u}_i^1}$ is evaluated through the following equation,

$$\frac{\partial JC_i}{\partial \bar{u}_i^1} = [2\Omega_{x,i} \quad 2\Omega_{y,i} \quad 2\Omega_{z,i} \quad -2\dot{x}_i \quad -2\dot{y}_i \quad -2\dot{z}_i] \quad (5.33)$$

where, $\Omega_{x,i}$, $\Omega_{y,i}$ and $\Omega_{z,i}$ are the partial derivatives of the pseudo-potential function that are evaluated for $\bar{x}_{c,i}^*$ state through the Equations (2.31) to (2.33). The process of computation of the *1-dimensional* subset of the family begins by determining a periodic orbit of the desired characteristic. Subsequently, a QPO is constructed by leveraging the linear approximation of the invariant curve around the chosen periodic orbit with the selected characteristic constraint. Thereafter, a numerical continuation technique is leveraged to obtain additional members of the *1-dimensional* characteristic constrained family.

The *1-dimensional* family of QPOs with a common characteristic is constructed via PALC, Section 3.3.2, and requires two additional phase constraints. The single shooting formulation, Equations (5.14) and (5.15), with a characteristic constraint, Table 5.1, comprises of a *3-dimensional* null-space, hence, the addition of two-phase constraints to the setup guarantees that the solutions of the modified shooting method correspond to unique orbits. It is feasible to employ NPC, Section 3.3.1, with T^0 or ρ^0 as the continuation param-

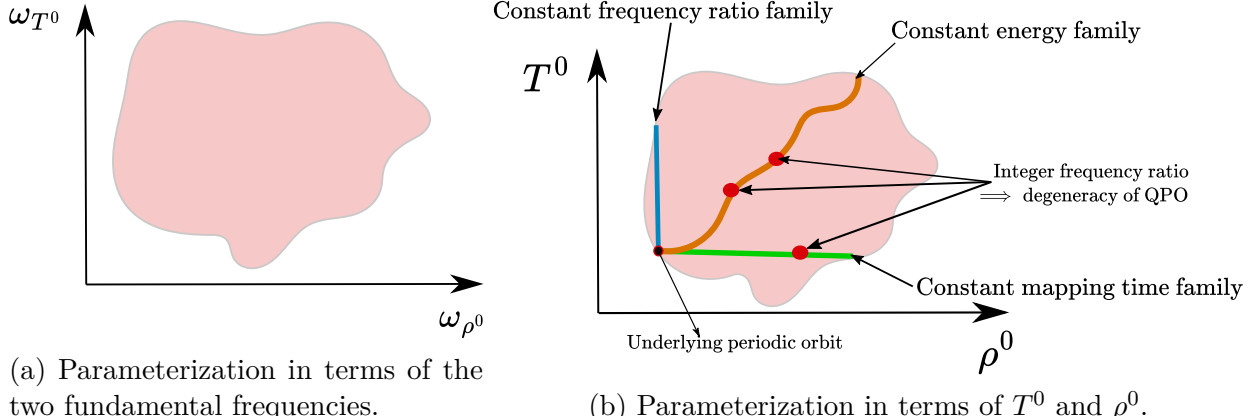


Figure 5.4. Schematic of a *2-dimensional* solution surface representing the biparametric family of QPOs.

eter, or JC_{avg} by reformulation of the shooting method. However, the continuation process is more challenging due to the lack of a *priori* knowledge of the evolution of the family. Hence, PALC is the preferred method for the construction of the *1-dimensional* subset of the QPOs. A rudimentary phase constraint may be implemented by fixing the y-position of \bar{u}_1^1 state initialized with an apse state as the step-off location of a $\hat{x} - \hat{z}$ plane-symmetric periodic orbit. However, for a more generalized formulation two phase constraints, akin to the phase constraint described for a periodic orbit Section 4.1, as defined by Schilder et al. [66] and Olikara et al. [26] are incorporated to the shooting method. The first phase constraint preserves the latitudinal angle of the states on the invariant curve during the continuation process and the second phase constraint fixes the longitudinal angle of the invariant curve around the torus. The constraints are defined as,

$$F_{\theta_{\rho^0}} = (\bar{\mathbf{u}}^1 - \tilde{\mathbf{u}}^1)^T \left(\frac{\partial \tilde{\mathbf{u}}^1}{\partial \theta_{\rho^0}} \right) = 0 \quad (5.34)$$

$$F_{\theta_{T^0}} = (\bar{\mathbf{u}}^1 - \tilde{\mathbf{u}}^1)^T \left(\frac{\partial \tilde{\mathbf{u}}^1}{\partial \theta_{T^0}} \right) = 0 \quad (5.35)$$

where, $F_{\theta_{\rho^0}}$ and $F_{\theta_{T^0}}$ are the latitudinal and longitudinal phase constraints, respectively. The $\bar{\mathbf{u}}^1$ represents the \bar{u}^1 states that are stacked vertically to form a $6N \times 1$ vector, $\tilde{\mathbf{u}}^1$ is similar to $\bar{\mathbf{u}}^1$ but constructed using \tilde{u}^1 states, that denote the invariant curve states of a previously converged family member. The $\frac{\partial \tilde{\mathbf{u}}^1}{\partial \theta_{\rho^0}}$ and $\frac{\partial \tilde{\mathbf{u}}^1}{\partial \theta_{T^0}}$ are $6N \times 1$ vectors that signify the partial

derivatives of the $\tilde{\mathbf{u}}^1$ with respect to the latitudinal and longitudinal angles, respectively. The $\bar{\mathbf{u}}^1$ in the expanded form appears as,

$$\bar{\mathbf{u}}^1 = \begin{bmatrix} \bar{u}_{x,1}^1 \\ \bar{u}_{y,1}^1 \\ \bar{u}_{z,1}^1 \\ \bar{u}_{\dot{x},1}^1 \\ \bar{u}_{\dot{y},1}^1 \\ \bar{u}_{\dot{z},1}^1 \\ \vdots \\ \bar{u}_{x,N}^1 \\ \bar{u}_{y,N}^1 \\ \bar{u}_{z,N}^1 \\ \bar{u}_{\dot{x},N}^1 \\ \bar{u}_{\dot{y},N}^1 \\ \bar{u}_{\dot{z},N}^1 \end{bmatrix} \quad (5.36)$$

The $\frac{\partial \tilde{\mathbf{u}}^1}{\partial \theta_{\rho^0}}$ vector is a reshaped form of a $N \times 6$ matrix that is evaluated through the following expression,

$$\frac{\partial \tilde{\mathbf{U}}^1}{\partial \theta_{\rho^0}} = (\text{diag}[i\bar{k}]e^{i\bar{k}^T \bar{\theta}_{\rho^0}})^T (\tilde{\mathbf{C}}_0) \quad (5.37)$$

where, $\text{diag}[ik]$ is a diagonal matrix with ik as the diagonal elements, $\tilde{\mathbf{C}}_0$ signifies the Fourier coefficients of the \tilde{u}^1 states, and the $e^{i\bar{k}^T \bar{\theta}_{\rho^0}}$ matrix is defined as,

$$e^{i\bar{k}^T \bar{\theta}_{\rho^0}} = \begin{bmatrix} e^{i(-\frac{N-1}{2})0} & e^{i(-\frac{N-1}{2})\frac{2\pi}{N}} & \dots & e^{i(-\frac{N-1}{2})\frac{2\pi(N-1)}{N}} \\ \vdots & \vdots & & \vdots \\ e^{i(-1)0} & e^{i(-1)\frac{2\pi}{N}} & \dots & e^{i(-1)\frac{2\pi(N-1)}{N}} \\ e^{i(0)0} & e^{i(0)\frac{2\pi}{N}} & \dots & e^{i(0)\frac{2\pi(N-1)}{N}} \\ e^{i(1)0} & e^{i(1)\frac{2\pi}{N}} & \dots & e^{i(1)\frac{2\pi(N-1)}{N}} \\ \vdots & \vdots & & \vdots \\ e^{i(\frac{N-1}{2})0} & e^{i(\frac{N-1}{2})\frac{2\pi}{N}} & \dots & e^{i(\frac{N-1}{2})\frac{2\pi(N-1)}{N}} \end{bmatrix} \quad (5.38)$$

which is similar to Equation (5.18). The $\frac{\partial \tilde{\mathbf{u}}^1}{\partial \theta_{T^0}}$ partial derivative is analytically represented as,

$$\frac{\partial \tilde{\mathbf{u}}^1}{\partial \theta_{T^0}} = \frac{\tilde{T}^0}{2\pi} \left(\frac{\partial \tilde{\mathbf{u}}^1}{\partial \tau} - \frac{\tilde{\rho}^0}{\tilde{T}^0} \frac{\partial \tilde{\mathbf{u}}^1}{\partial \theta_{\rho^0}} \right) \quad (5.39)$$

where, \tilde{T}^0 and $\tilde{\rho}^0$ denote the stroboscopic time period and rotation angle of the previously converged invariant curve states, \tilde{u}^1 . The $\frac{\partial \tilde{\mathbf{u}}^1}{\partial \tau}$ comprises of the time derivates of \tilde{u}^1 states formulated as a $6N \times 1$ vector and $\frac{\partial \tilde{\mathbf{u}}^1}{\partial \theta_{\rho^0}}$ is the reshaped form of the matrix given by Equation (5.37). The two-phase constraints do not rely on the stroboscopic time period and rotation angle, and their partial derivatives with respect to the \bar{u}^1 states are expressed as,

$$\frac{\partial F_{\theta_{\rho^0}}}{\partial \bar{\mathbf{u}}^1} = \frac{\partial \tilde{\mathbf{u}}^1}{\partial \theta_{\rho^0}} \quad (5.40)$$

$$\frac{\partial F_{\theta_{T^0}}}{\partial \bar{\mathbf{u}}^1} = \frac{\partial \tilde{\mathbf{u}}^1}{\partial \theta_{T^0}} \quad (5.41)$$

The constraint vector presented in Equation (5.15) along with the F_{char} and the phase constraints is rewritten as,

$$\bar{F}(\bar{X}) = \begin{bmatrix} T^0, R \bar{u}_1^1 - \bar{u}_1^1 \\ T^0, R \bar{u}_2^1 - \bar{u}_2^1 \\ \vdots \\ T^0, R \bar{u}_{N-1}^1 - \bar{u}_{N-1}^1 \\ T^0, R \bar{u}_N^1 - \bar{u}_N^1 \\ F_{\text{char}} \\ F_{\theta_{\rho^0}} \\ F_{\theta_{T^0}} \end{bmatrix} \quad (5.42)$$

and the corresponding Jacobian matrix with Equation (5.14) as the design vector is,

$$\mathbf{DF}(\bar{X}) = \begin{bmatrix} \frac{\partial(T^0, R \bar{u}^1 - \bar{u}^1)}{\partial \bar{u}^1} & \frac{\partial(T^0, R \bar{u}^1 - \bar{u}^1)}{\partial T^0} & \frac{\partial(T^0, R \bar{u}^1 - \bar{u}^1)}{\partial \rho^0} \\ \frac{\partial F_{\text{char}}}{\partial \bar{u}^1} & \frac{\partial F_{\text{char}}}{\partial T^0} & \frac{\partial F_{\text{char}}}{\partial \rho^0} \\ \frac{\partial F_{\theta_{\rho^0}}}{\partial \bar{u}^1} & 0 & 0 \\ \frac{\partial F_{\theta_{T^0}}}{\partial \bar{u}^1} & 0 & 0 \end{bmatrix} \quad (5.43)$$

The modified shooting method has a *1-dimensional* null-space and PALC allows for a robust method to generate a subset of the biparameteric family comprising of members with a common characteristic.

The described shooting method is demonstrated for the construction of a subset of L_2 southern quasi-halo orbits, L_1 quasi-Lyapunov orbits, and L_4 quasi-axial orbits. A constant mapping time family of L_2 southern quasi-halo orbits is generated by leveraging a L_2 southern halo orbit ($JC=3.04649$, $T^0=6.56235$ days) for identifying an initial guess, constraining the stroboscopic time period of the QPOs to be the same as the chosen halo orbit, and employing PALC for numerical continuation. The JC_{avg} values of the family members are plotted as a function of the ρ^0 values, along with three family members in Figure 5.5 and an initial guess for a family member is provided in Table B.1. Similarly, a constant frequency ratio family of L_1 quasi-Lyapunov orbits is obtained via the implementation of the shooting method with

an initial guess from an L_1 Lyapunov orbit ($JC=3.17745$, $T^0=11.86024$ days), constricting the rotation angle of the QPOs to be the same as the periodic orbit and leveraging PALC for continuation along the *1-dimensional* null-space. The evolution of T^0 and JC_{avg} values along the family, as well as three family members, are visualized in Figure 5.6, and an initial guess for a family member is included in Table B.2. The constant energy family is illustrated through the L_4 quasi-axial orbits that are constructed through an initial guess from an L_4 axial orbit ($JC=1.97268$, $T^0=27.33317$ days), and enforcing the average JC value of the invariant curve states of the QPOs to be the same as the JC of the underlying orbit. The family members are parameterized via the T^0 and ρ^0 values, and three QPT of the family are depicted in Figure 5.7. The GMOS algorithm allows for an intuitive framework to construct QPOs and their biparameteric family. However, the scheme does not require the two fundamental frequencies of a QPO to be incommensurate, thus, the states of an invariant curve may inadvertently converge to a periodic orbit during the continuation process. Since the biparameteric family of QPOs is not smooth, it is favorable to leverage the constant frequency ratio subset to characterize the *2-dimensional* family to avoid encountering integer frequency ratios [67]. Alternatively, it is feasible to continue across an integer frequency ratio by updating the direction of family continuation by changing the characteristic constraint.

5.3.1 Multiple Shooting for the Construction of Quasi-Periodic Tori

A multiple shooting strategy offers a robust framework to construct a QPO with a long stroboscopic time period or if the torus traverses through a dynamically sensitive region. The multiple shooting technique builds on the single shooting method, Equations (5.14) and (5.42), and leverages the idea presented in Section 3.2.2. The scheme relies on discretizing the N trajectories emanating from the same invariant curve into M segments with equal flight time as illustrated for $M = 3$ case in Figure 5.8. While the multiple shooter formulation is more computationally expensive compared to the single shooter method, it enables the construction of QPOs that are otherwise challenging to compute, primarily due to the long stroboscopic time period.

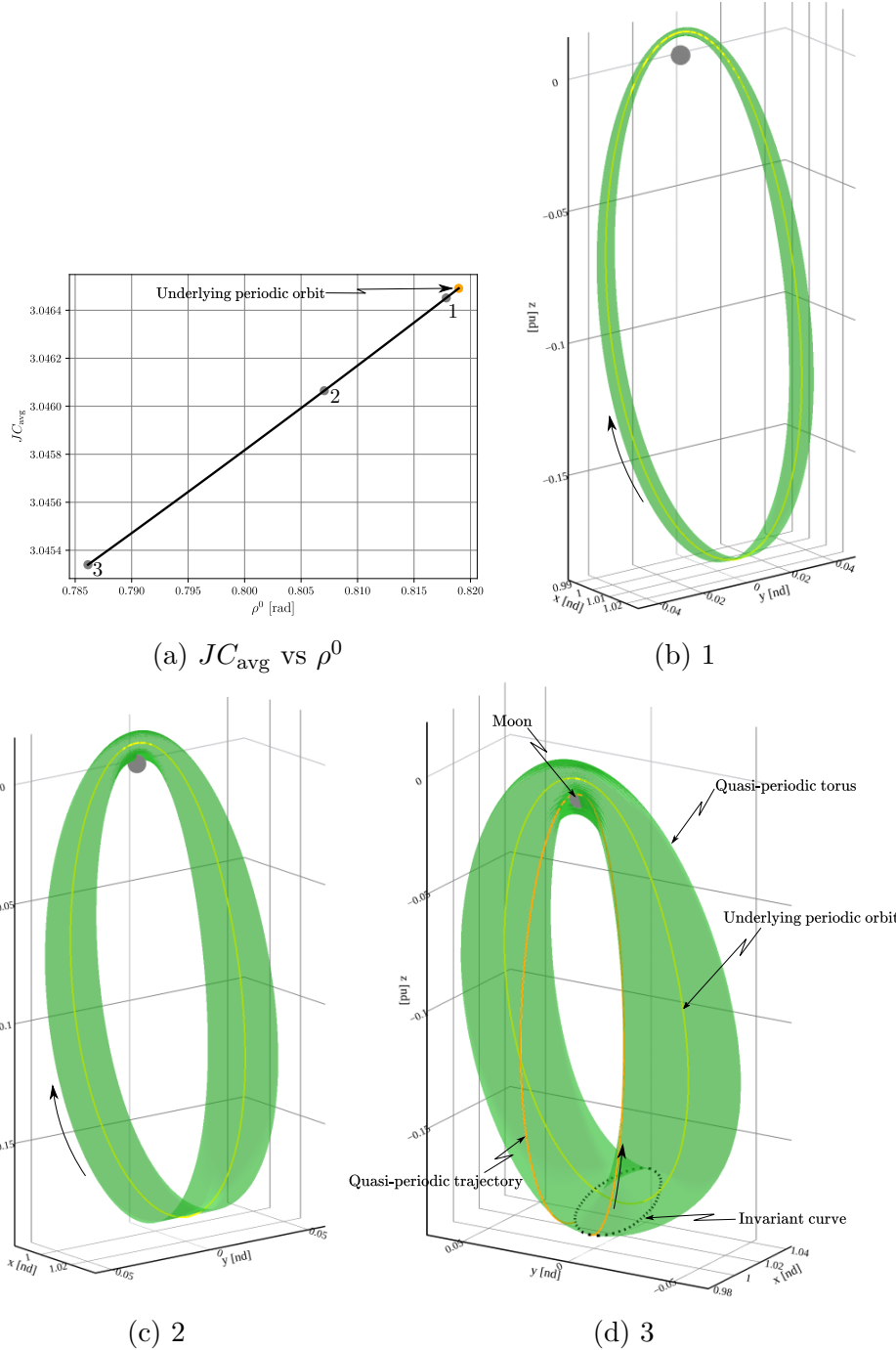


Figure 5.5. A constant mapping time family with $T^0=6.56235$ days originating from an L_2 southern halo orbit ($JC=3.04649$, $T^0=6.56235$ days) in the Earth-Moon system. Three QPT, as identified in the JC_{avg} vs ρ^0 plot, are visualized in the configuration space.

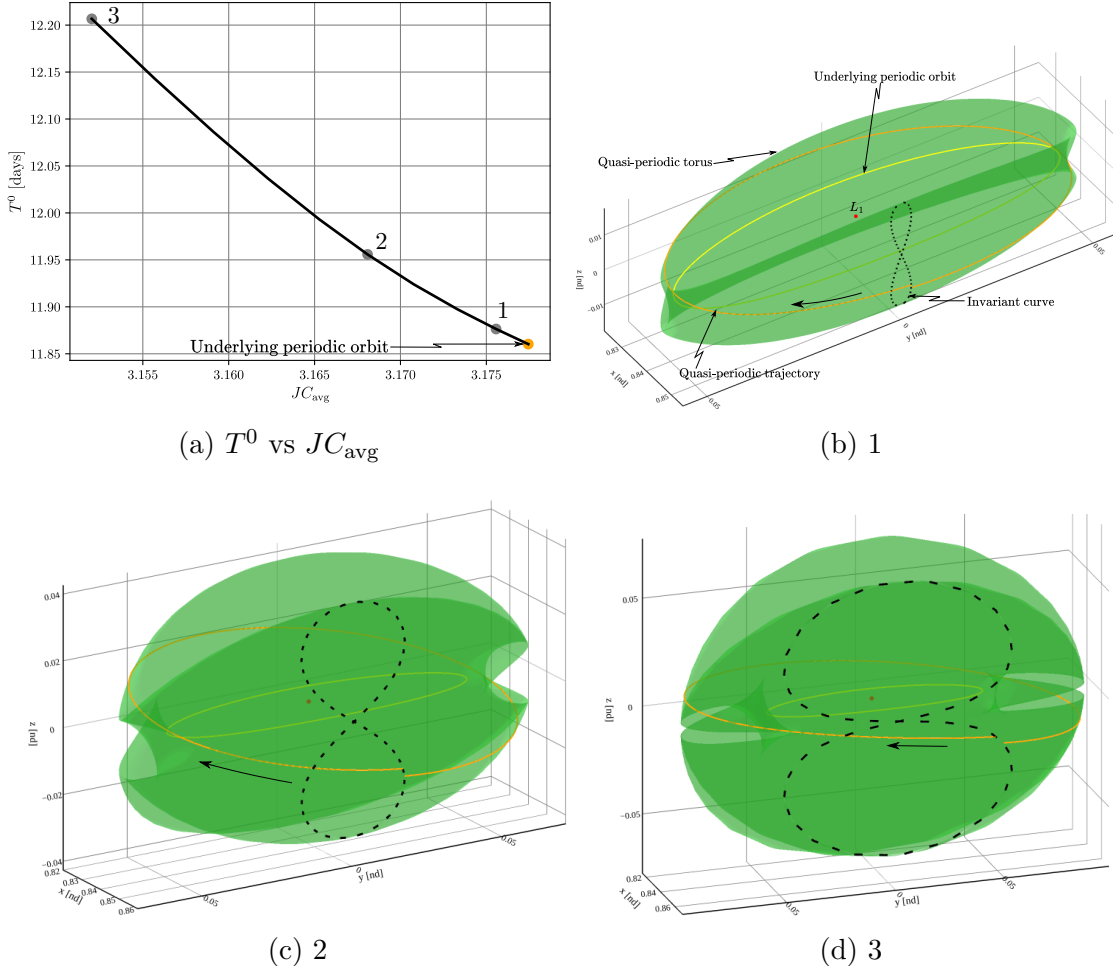


Figure 5.6. A constant frequency ratio family with $\rho^0=0.08385$ rad emanating from an L_1 Lyapunov orbit ($JC=3.17745$, $T^0=11.86024$ days) in the Earth-Moon system. Three QPT, as identified in the T^0 vs JC_{avg} plot, are shown in the configuration space.

The design vector of the multiple shooter method incorporates the N states of each of the M curves, along with the rotation angle and propagation time between the curves. The constraint vector consists of full state continuity constraints between states of an invariant curve and the propagated states of a previous curve, much like the sample case in Section 3.2.2, except for the states that return to the initial curve as depicted in Figure 5.8. The invariance condition is enforced for states that return to the initial invariant curve. Due to the equal propagation time formulation between intermediate invariant curves, the time period is represented as $T_M^0 = \frac{T^0}{M}$. Similar to the single shooting method, the characteristic constraint

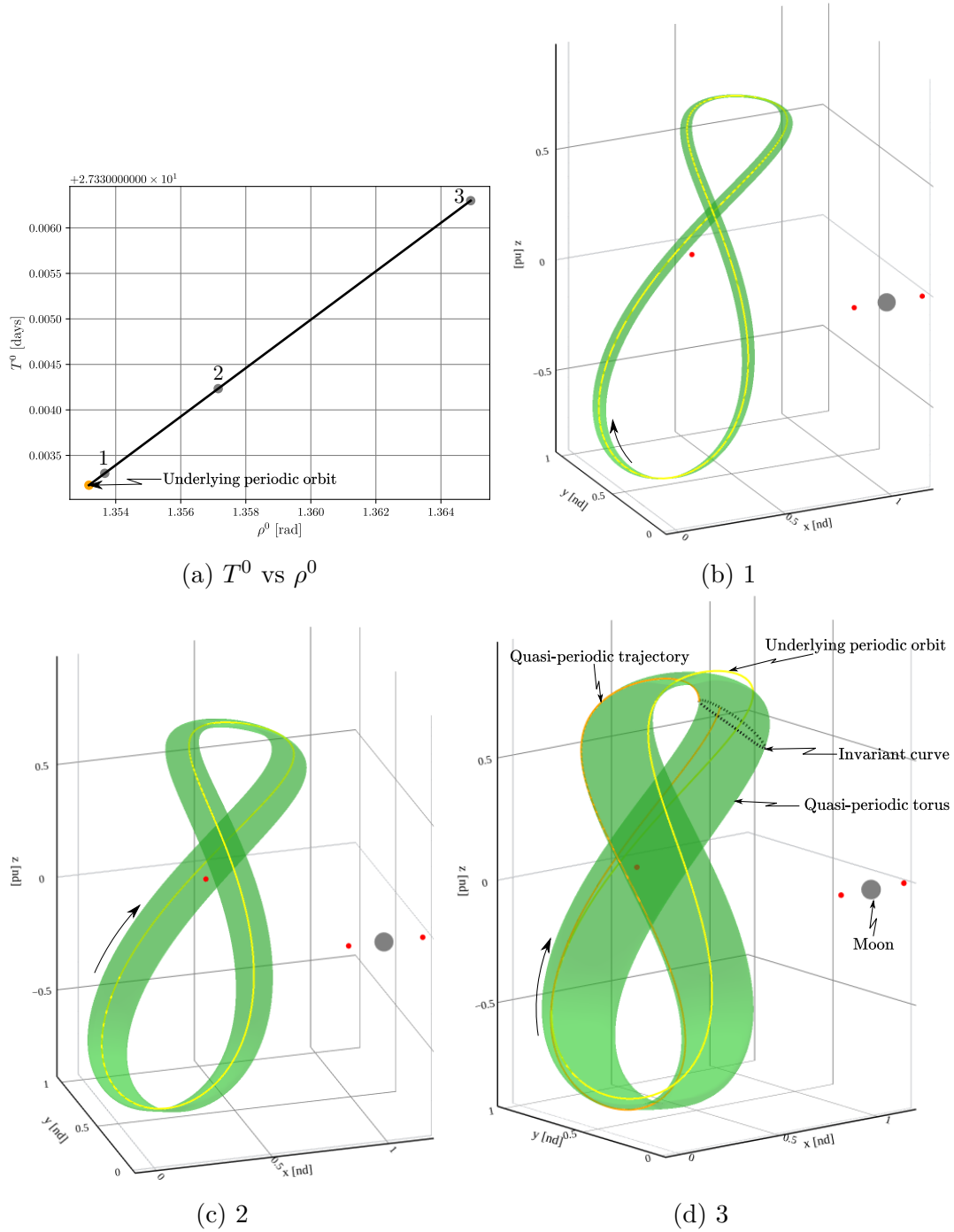


Figure 5.7. A constant energy family with $JC_{\text{avg}}=1.97268$ originating from an L_4 axial orbit ($JC=1.97268$, $T^0=27.33317$ days) in the Earth-Moon system. Three QPT, as identified in the T^0 vs ρ^0 plot, are depicted in the configuration space.

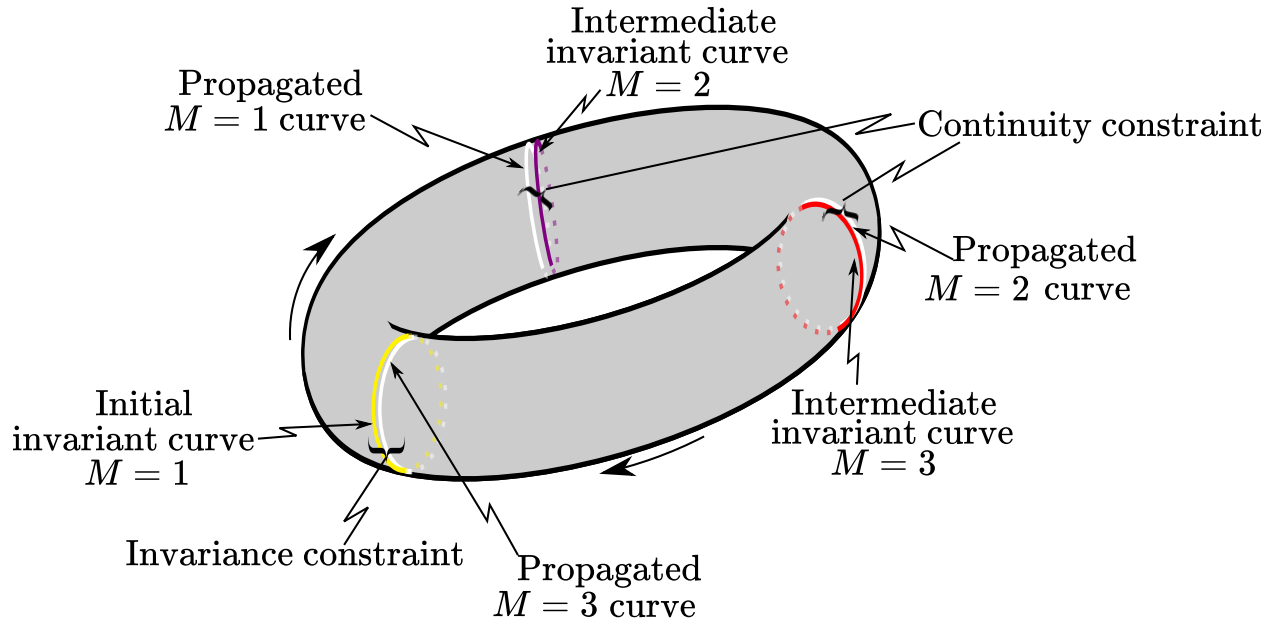


Figure 5.8. Multiple shooting schematic for construction of QPT.

and the two-phase constraints are incorporated to bound the behavior of the states of the initial invariant curve. The design vector for the multiple shooting method is written as,

$$\bar{X} = \begin{bmatrix} \bar{u}_1^1 \\ \bar{u}_2^1 \\ \vdots \\ \bar{u}_{N-1}^1 \\ \bar{u}_N^1 \\ \bar{u}_1^2 \\ \bar{u}_2^2 \\ \vdots \\ \bar{u}_1^M \\ \vdots \\ \bar{u}_N^M \\ T_M^0 \\ \rho^0 \end{bmatrix} \quad (5.44)$$

where, \bar{u}_i^j state represents the i^{th} 6-dimensional state vector along the j^{th} invariant curve.

The modified constraint vector is expressed as,

$$\bar{F}(\bar{X}) = \begin{bmatrix} T_M^0 \bar{u}_1^1 - \bar{u}_1^2 \\ T_M^0 \bar{u}_2^1 - \bar{u}_2^2 \\ \vdots \\ T_M^0 \bar{u}_N^1 - \bar{u}_N^2 \\ \vdots \\ T_M^0 \bar{u}_{N-1}^{M-1} - \bar{u}_{N-1}^M \\ T_M^0 \bar{u}_N^{M-1} - \bar{u}_N^M \\ T_M^0, R \bar{u}_1^M - \bar{u}_1^1 \\ T_M^0, R \bar{u}_2^M - \bar{u}_2^1 \\ \vdots \\ T_M^0, R \bar{u}_{N-1}^M - \bar{u}_{N-1}^1 \\ T_M^0, R \bar{u}_N^M - \bar{u}_N^1 \\ F_{\text{char}} \\ F_{\theta_{\rho^0}} \\ F_{\theta_{T^0}} \end{bmatrix} \quad (5.45)$$

where, $T_M^0 \bar{u}_i^j$ state is obtained by propagating \bar{u}_i^j state for T_M^0 period, and $T_M^0, R \bar{u}_i^j$ state is computed through the rotation operator and $T_M^0 \bar{u}_i^j$ state as elucidated for the single shooting

method. The Jacobian matrix for the multiple shooting method, Equations (5.44) and (5.45), is evaluated using the following expression,

$$\mathbf{DF}(\bar{X}) = \begin{bmatrix} & \underbrace{\tilde{\Phi}}_{\left[\begin{array}{c} \\ \\ \end{array} \right]} & & \left[\begin{array}{c} \frac{\partial(\mathbf{T}_M^0 \bar{\mathbf{u}})}{\partial T_M^0} \\ \frac{\partial(\mathbf{T}_M^0, \mathbf{R} \bar{\mathbf{u}}^M - \bar{\mathbf{u}}^1)}{\partial \bar{\mathbf{u}}^M} \end{array} \right] & \left[\begin{array}{c} \mathbf{0}_{6N(M-1) \times 1} \\ \frac{\partial(\mathbf{T}_M^0, \mathbf{R} \bar{\mathbf{u}}^M)}{\partial \rho^0} \end{array} \right] \\ \left[\begin{array}{c} -\tilde{\mathbf{I}} \\ \mathbf{0}_{N \times 6N(M-2)} \end{array} \right] & \left[\begin{array}{c} \frac{\partial(\mathbf{T}_M^0, \mathbf{R} \bar{\mathbf{u}}^M - \bar{\mathbf{u}}^1)}{\partial \bar{\mathbf{u}}^M} \\ \mathbf{0}_{N \times 6N(M-1)} \\ \mathbf{0}_{N \times 6N(M-1)} \\ \mathbf{0}_{N \times 6N(M-1)} \end{array} \right] & \left[\begin{array}{c} \frac{\partial(\mathbf{T}_M^0)}{\partial T_M^0} \\ \frac{\partial(\mathbf{T}_M^0, \mathbf{R} \bar{\mathbf{u}}^M)}{\partial \partial T_M^0} \\ 0 \\ 0 \end{array} \right] & \left[\begin{array}{c} \frac{\partial F_{\text{char}}}{\partial \bar{\mathbf{u}}^1} \\ \frac{\partial F_\theta}{\partial \bar{\mathbf{u}}^1} \\ \frac{\partial F_{\theta, T^0}}{\partial \bar{\mathbf{u}}^1} \end{array} \right] & \left[\begin{array}{c} \frac{\partial F_{\text{char}}}{\partial \partial \rho^0} \\ 0 \\ 0 \end{array} \right] \end{bmatrix} \quad (5.46)$$

where, $\underbrace{\tilde{\Phi}}$ matrix comprises of the partial derivates of the full state continuity constraints with respect to the state vectors. The $\underbrace{\tilde{\Phi}}$ matrix is defined as,

$$\underbrace{\tilde{\Phi}}_{\left[\begin{array}{ccccc} \tilde{\Phi}^1(T_M^0, 0) & -\tilde{\mathbf{I}} & \mathbf{0}_{6 \times 6} & \dots & \mathbf{0}_{6 \times 6} & \mathbf{0}_{6N \times 6N} \\ \mathbf{0}_{6N \times 6N} & \tilde{\Phi}^2(T_M^0, 0) & -\tilde{\mathbf{I}} & \dots & \mathbf{0}_{6N \times 6N} & \mathbf{0}_{6N \times 6N} \\ \vdots & \vdots & \vdots & \ddots & \vdots & \vdots \\ \mathbf{0}_{6N \times 6N} & \mathbf{0}_{6N \times 6N} & \mathbf{0}_{6 \times 6} & \dots & \tilde{\Phi}^{M-1}(T_M^0, 0) & -\tilde{\mathbf{I}} \end{array} \right]} \quad (5.47)$$

and the $\tilde{\Phi}^j$ denotes the block diagonal matrix of STMs of the j^{th} intermediate invariant curve, which is similar to Equation (5.26), is represented as,

$$\tilde{\Phi}^j = \left[\begin{array}{ccccc} \Phi_1^j(T_M^0, 0) & \mathbf{0}_{6 \times 6} & \dots & \mathbf{0}_{6 \times 6} & \mathbf{0}_{6 \times 6} \\ \mathbf{0}_{6 \times 6} & \Phi_2^j(T_M^0, 0) & \dots & \mathbf{0}_{6 \times 6} & \mathbf{0}_{6 \times 6} \\ \vdots & \vdots & \ddots & \vdots & \vdots \\ \mathbf{0}_{6 \times 6} & \mathbf{0}_{6 \times 6} & \dots & \Phi_{N-1}^j(T_M^0, 0) & \mathbf{0}_{6 \times 6} \\ \mathbf{0}_{6 \times 6} & \mathbf{0}_{6 \times 6} & \dots & \mathbf{0}_{6 \times 6} & \Phi_N^j(T_M^0, 0) \end{array} \right] \quad (5.48)$$

The $\frac{\partial(\mathbf{T}_M^0 \bar{\mathbf{u}})}{\partial T_M^0}$ partial derivatives are the time derivatives of N states along the M curves propagated by T_M^0 and are written as,

$$\frac{\partial(\mathbf{T}_M^0 \bar{\mathbf{u}})}{\partial T_M^0} = \begin{bmatrix} T_M^0 \dot{\bar{u}}_1^1 \\ T_M^0 \dot{\bar{u}}_2^1 \\ \vdots \\ T_M^0 \dot{\bar{u}}_{N-1}^1 \\ T_M^0 \dot{\bar{u}}_N^1 \\ T_M^0 \dot{\bar{u}}_1^2 \\ T_M^0 \dot{\bar{u}}_2^2 \\ \vdots \\ T_M^0 \dot{\bar{u}}_1^M \\ \vdots \\ T_M^0 \dot{\bar{u}}_N^M \end{bmatrix} \quad (5.49)$$

The partial derivatives of the invariance constraint with respect to the \bar{u}^1 states are evaluated as,

$$\frac{\partial(\mathbf{T}_M^0, \mathbf{R} \bar{\mathbf{u}}^M - \bar{\mathbf{u}}^1)}{\partial \bar{\mathbf{u}}^M} = (\mathbf{R}_{-\rho^0} \otimes \mathbf{I}) \tilde{\Phi}^M(T_M^0, 0) \quad (5.50)$$

The remaining partial derivatives are computed in the same manner as that for the single shooting method. The $\frac{\partial(\mathbf{T}_M^0, \mathbf{R} \bar{\mathbf{u}}^M)}{\partial T_M^0}$ and $\frac{\partial(\mathbf{T}_M^0, \mathbf{R} \bar{\mathbf{u}}^M)}{\partial \rho^0}$ parital derivates are computed via Equation (5.27) and Equation (5.28), respectively. The partial deriviates of the characteristic constraints are evaluated using the expressions in Table 5.1 and partial derivates of the phase constraints are given by Equations (5.40) and (5.41). The multiple shooting formulation has a *1-dimensional* null-space, so PALC is leveraged for the continuation along the characteristic constraint families.

5.4 Stability and Hyperbolic Manifolds

For the application of QPT for orbit and transfer trajectory design, it is vital to know their stability properties and the innate flow towards and away from the orbits. The Lyapunov stability of a QPO is assessed via a linear mapping, akin to the monodromy matrix for the periodic orbits, under which the states on an invariant curve return to the initial states after propagating them for one stroboscopic time period. This transformation is a byproduct of the implementation of the GMOS algorithm, Equation (5.25), and is evaluated via the following expression,

$$\mathbf{DG}_{\text{qpo}} = (\mathbf{R}_{-\rho^0} \otimes \mathbf{I}) \tilde{\Phi}(T^0, 0) \quad (5.51)$$

where, $\mathbf{R}_{-\rho^0}$ is the rotation operator as described by Equation (5.23) and $\tilde{\Phi}(T^0, 0)$ represents a block diagonal matrix comprising of STMs of all the ${}^{T_0}\bar{u}^1$ states with respect to all the \bar{u}^1 states. The \mathbf{DG}_{qpo} matrix, size $6N \times 6N$, is the linear mapping that renders the states on the invariant curve as fixed points. The eigenanalysis of the \mathbf{DG}_{qpo} matrix describes the stability properties of a QPO, as well as, allows for a first-order approximation of the associated hyperbolic invariant manifolds.

The $6N$ eigenvalues of the \mathbf{DG}_{qpo} matrix are reducible to 6 eigenvalues of a Floquet matrix representation of \mathbf{DG}_{qpo} as elucidated by Jorba [68]. The 6 eigenvalues succinctly describe the stability information of a QPO. The spectrum of 6 eigenvalues when plotted on a complex plane appears as six origin-centered concentric circles and the radius of each circle captures the magnitude of the eigenvalues as illustrated in Figure 5.9. The eigenvalues of the Floquet matrix and a theoretically accurate \mathbf{DG}_{qpo} matrix are related as,

$$\underbrace{\lambda_i}_{\mathbb{W}_i} = \mathbb{W}_i e^{-i\bar{k}\rho^0} \quad (5.52)$$

where, \mathbb{W}_i represents the i^{th} eigenvalue of the floquet matrix for $i = 1, 2, \dots, 6$ and $\underbrace{\lambda_i}_{\mathbb{W}_i}$ denotes the i^{th} spectrum of eigenvalues of a theoretically accurate \mathbf{DG}_{qpo} . The Floquet matrix eigenvalues are approximated as the positive eigenvalues with no imaginary component along each of the concentric circles. If a positive real-valued eigenvalue is not present in each of

the six circles then the accuracy of the eigenvalue spectrum is improved by reconstructing the QPO with increased resolution of the invariant curve or the number of intermediate curves leveraged for multiple shooting. The \mathbb{W}_i 's exist as reciprocal pairs since the model is a Hamiltonian system. Amongst the three reduced eigenvalue pairs, two pairs are unity and the third pair, if hyperbolic, hints at the presence of associated stable/unstable manifolds.

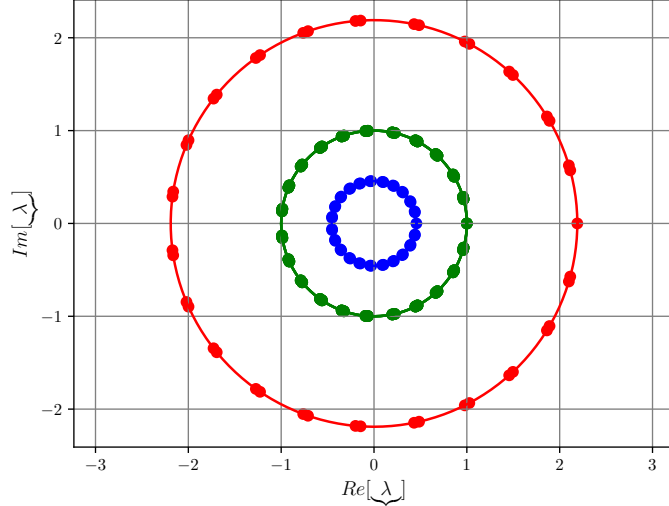


Figure 5.9. The spectrum of eigenvalues of \mathbf{DG}_{qpo} of the QPO depicted in Figure 5.6(c).

The global stable and unstable invariant manifolds associated with a QPO each form a *3-dimensional* phase space surface, and are approximated through a similar method as described for periodic orbits, Section 4.3. If a \mathbb{W}_i , chosen from λ_i , is of magnitude greater than 1 then its corresponding real-valued $6N$ eigenvector, computed through the eigenanalysis of the \mathbf{DG}_{qpo} , is transversal to the unstable manifolds associated with the QPO. Similarly, the real-valued eigenvector corresponding to $\mathbb{W}_i < 1$, is transversal to the stable manifolds linked to the QPO. The stable/unstable $6N$ eigenvector consists of eigenvectors corresponding to

the N states that represent an invariant curve and are leveraged for computation of \mathbf{DG}_{qpo} . The stable and unstable eigenvectors are expressed as,

$$\text{qpo} \bar{v}_S = \begin{bmatrix} \text{qpo} \bar{v}_{S,1} \\ \text{qpo} \bar{v}_{S,2} \\ \vdots \\ \text{qpo} \bar{v}_{S,N-1} \\ \text{qpo} \bar{v}_{S,N} \end{bmatrix}; \quad \text{qpo} \bar{v}_U = \begin{bmatrix} \text{qpo} \bar{v}_{U,1} \\ \text{qpo} \bar{v}_{U,2} \\ \vdots \\ \text{qpo} \bar{v}_{U,N-1} \\ \text{qpo} \bar{v}_{U,N} \end{bmatrix} \quad (5.53)$$

where, $\text{qpo} \bar{v}_S$ and $\text{qpo} \bar{v}_U$ represent the $6N$ stable and unstable eigenvector, repectively, and $\text{qpo} \bar{v}_{S,i}$ and $\text{qpo} \bar{v}_{U,i}$ signify the stable and unstable eigenvector associated with the \bar{u}_i^1 state. The local stable/unstable manifolds associated with an invariant curve, sampled using \bar{u}^1 states, are approximated as,

$$\text{qpo} \bar{x}_{S,i}^* = \bar{x}_{\text{PO}}^* + \bar{u}_i^1 \pm \nabla \frac{\text{qpo} \bar{v}_{S,i}}{\sqrt{\text{qpo} v_{S,i,x}^2 + \text{qpo} v_{S,i,y}^2 + \text{qpo} v_{S,i,z}^2}} \quad (5.54)$$

$$\text{qpo} \bar{x}_{U,i}^* = \bar{x}_{\text{PO}}^* + \bar{u}_i^1 \pm \nabla \frac{\text{qpo} \bar{v}_{U,i}}{\sqrt{\text{qpo} v_{U,i,x}^2 + \text{qpo} v_{U,i,y}^2 + \text{qpo} v_{U,i,z}^2}} \quad (5.55)$$

where, $\text{qpo} \bar{x}_{S,i}^*$ and $\text{qpo} \bar{x}_{U,i}^*$ denote the local stable and unstable manifold approximation associated with the \bar{u}_i^1 state. This procedure is repeated to approximate the local hyperbolic manifold states corresponding to other invariant curves around the torus. The collection of unstable local manifold states linked to various invariant curves, serves as an estimate of the unstable local manifold associated with a QPO. These unstable local manifold states when propagated in forward time approximate the global unstable manifold corresponding to a QPO as illustrated in Figure 5.10. The global stable manifold associated with a QPO is estimated by propagating the stable local manifold states corresponding to various invariant curves around the torus in backward time. Each state on the *3-dimensional* global invariant manifolds is parameterized via the two-phase angles $[\theta_{T^0}, \theta_{\rho^0}]$ that describe the step-off location on the torus and the propagation time along the manifold. The global stable/unstable manifolds associated with a QPO is higher dimensional than the global sta-

ble/unstable manifolds corresponding to a periodic orbit, thus, assisting in characterizing a greater hypervolume of the phase space.

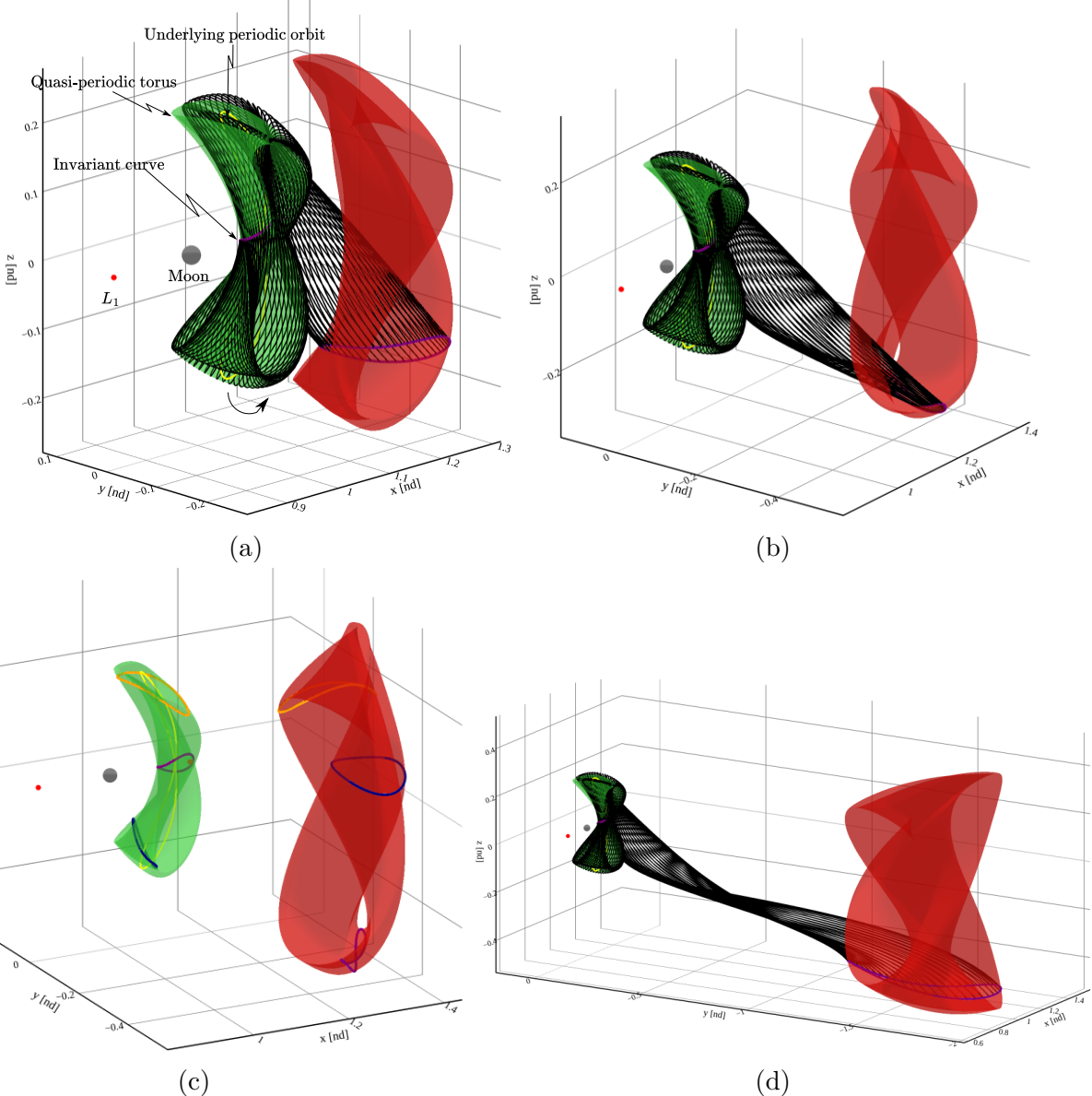


Figure 5.10. Approximation of positive-half global unstable manifold associated with an L_2 quasi-vertical orbit ($JC_{\text{avg}} = 3.04647$, $T^0 = 16.82590$ days) in the Earth-Moon system. The global unstable manifold trajectories(black) associated with $N = 55$ states, for $\nabla = 50$ km, emanating from an invariant curve(purple) are depicted in the plots. Additionally, the surface of manifold states(red) generated at 19.95786 days, 23.0283 days, and 30.39736 days along the manifold are visualized in Figures 5.10(a), 5.10(b) and 5.10(d), respectively. The evolution of manifold states corresponding to three invariant curves(purple, orange, navy) at 0 days and 23.0283 days along the manifold are depicted in Figure 5.10(c).

6. END-TO-END TRANSFER DESIGN FRAMEWORK

A framework is described that incorporates periodic/quasi-periodic orbits, along with their associated stable and unstable manifolds to inform the construction of transfer pathways between periodic orbits. The departure and arrival orbits are assumed to lie in the interior region of the cislunar space, i.e. in the proximity of the Moon. Two different classes of transfers are uncovered through the intermediate dynamical structures: interior-type and exterior-type transfers. The interior-type transfer geometries remain close to the Moon for the entirety of the transfer. The construction of the pathways is decomposed into the design of three segments that link the departure and arrival orbit as depicted in Figure 6.1. The exterior-type connections originate from the departure orbit in the interior region of the primary system, employ an impulsive maneuver on the far side of the Earth, and return to the arrival orbit in the vicinity of the Moon. This class of transfers is designed by stitching six segments that are described by two intermediate orbits as illustrated in Figure 6.2. Both types of transfers require a departure and arrival maneuver, and exterior-type transfers employ an additional maneuver on the far-side of the Earth as mentioned in Figures 6.1 and 6.2. To demonstrate the framework, a number of intermediate periodic and quasi-periodic orbits along with their associated stable and unstable manifolds are selected to compute low-maneuver cost and reasonable Time of Flight (TOF) highways. The subsequent sections provide a systematic framework for the computation of the various segments of the two transfer types, as well as techniques to link the segments to generate end-to-end transfers. The resultant geometries are characterized by the intermediate orbits selected to inform the design of the segments.

6.1 Departure and Arrival Periodic Orbits

For the transfer design problem of focus, a sample case is the design of transfers between an L_2 9:2 synodic resonant NRHO and a planar Moon-centered DRO. The dimensionality of the problem is reduced by selecting the two orbits with the same JC value. The initial conditions and relevant parameters of the selected departure and arrival orbit are presented in Table 6.1, and the two orbits are visualized in Figure 6.3. The stability indices of the

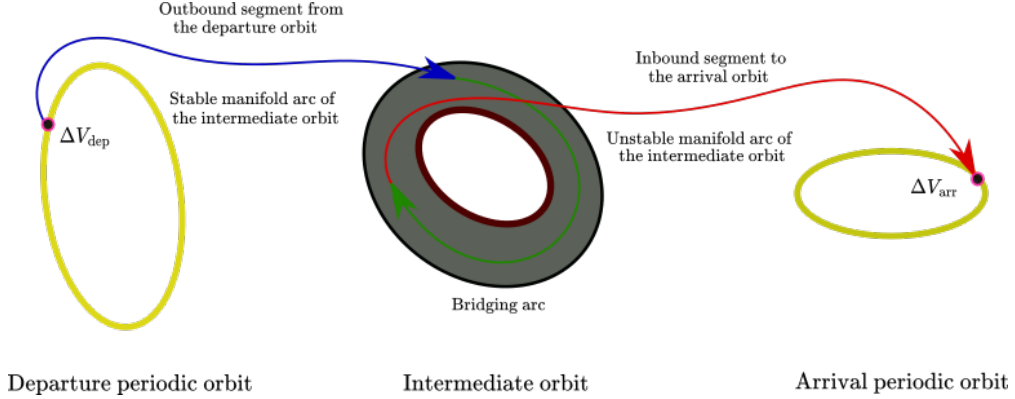


Figure 6.1. Interior-type end-to-end transfer schematic.

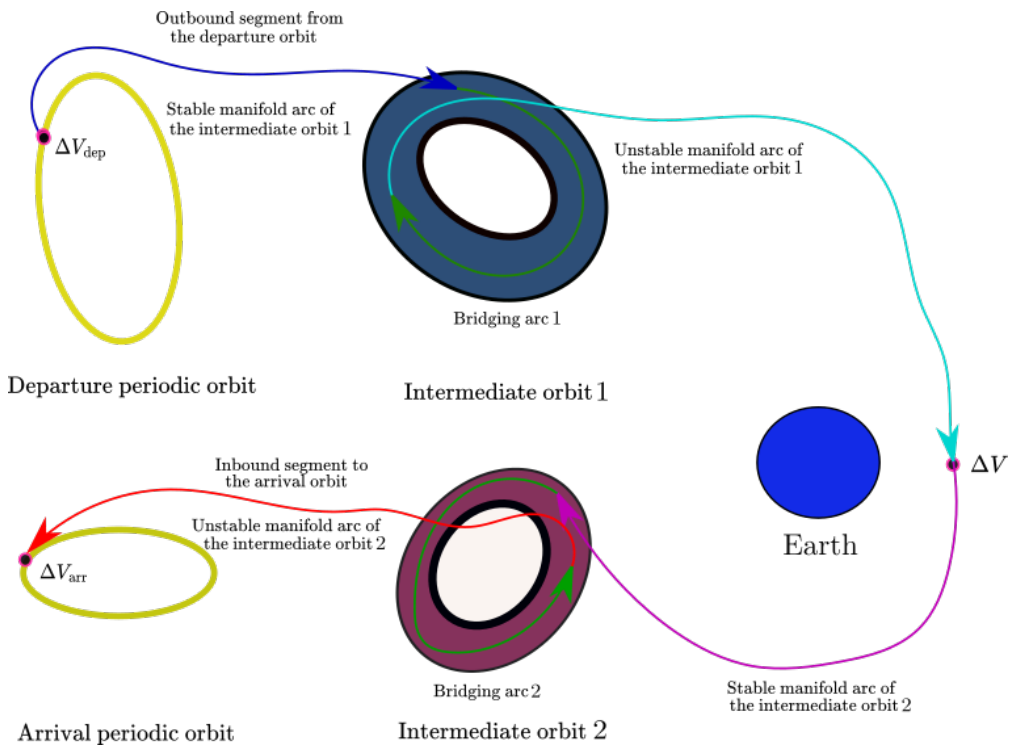


Figure 6.2. Exterior-type end-to-end transfer schematic.

NRHO signal the lack of useful associated stable/unstable manifolds. The DRO at the same JC value as the L_2 9:2 NRHO does not possess a hyperbolic stable/unstable subspace. A common metric employed in approximating the lowest transfer cost between two orbits is the theoretical minimum ΔV (TMDV) [69], [70]. The TMDV metric assumes that the orbits possess innate flows away and towards the orbit and require a single impulsive maneuver to

overcome the velocity discontinuity between the flow of the two orbits. Since the departure and arrival orbits are at the same energy level, the TMDV evaluates to 0 m/s. However, the absence of stable/unstable manifolds associated with the DRO necessitates an insertion maneuver. The innate absence of natural flows away and towards the departure and arrival orbits, coupled with the inherent difference in geometry motivates the use of intermediate dynamical structures to inform the transfer design process.

Table 6.1. Initial conditions, period, JC value and stability indices of an L_2 9:2 southern NRHO and a DRO.

Orbit	x_0 [nd]	z_0 [nd]	\dot{y}_0 [nd]	\mathbb{P} [nd]	JC	ν_1	ν_2
L_2 9:2 southern NRHO	1.02203	-0.18210	-0.10327	1.51120	3.04649	1	1.32301
DRO	0.91009	0	0.48639	1.08309	3.04649	1	1

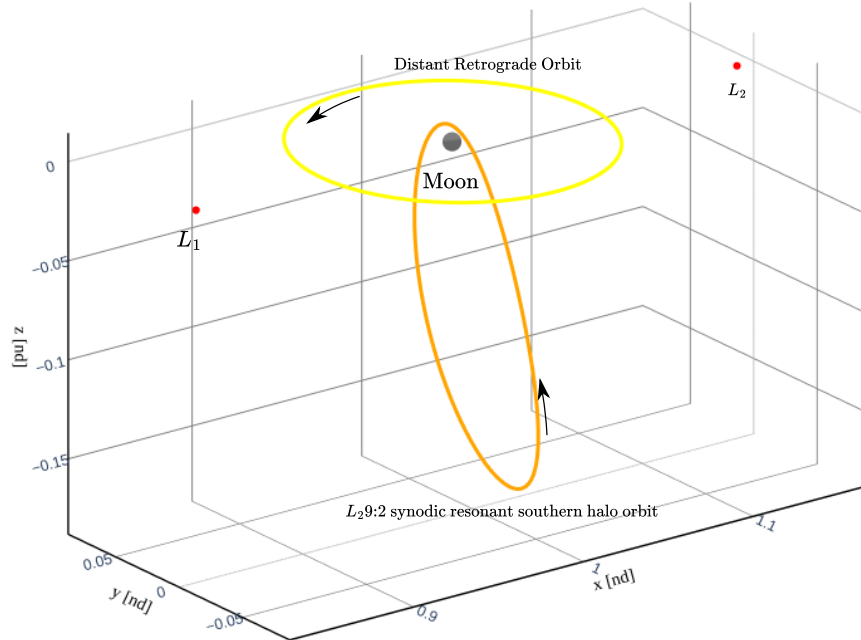


Figure 6.3. An L_2 9:2 NRHO (orange) and a DRO (yellow).

6.2 Intermediate Dynamical Structures

A number of intermediate periodic and quasi-periodic orbits are selected for demonstration of the proposed transfer design framework and assessment of local solution basins. The

intermediate orbits are selected to possess the same JC value as the departure/arrival orbit and useful stable/unstable invariant manifolds. Consequently, the departure and arrival maneuvers are only required to accomplish a change in geometry and no component is needed for a change in the energy level. The intermediate periodic orbits employed in this investigation are L_2 vertical, L_2 southern halo, L_2 southern P2HO₁, L_2 southern P2HO₂, planar 3:4 sidereal Resonant Periodic Orbit (RPO) and Distant Prograde Orbit (DPO). The initial conditions, period, JC value, and the stability indices of the candidate periodic orbits are presented in Table 6.2, and the orbits are plotted in Figures 6.4 and 6.5. It is evident from Table 6.2 that all the selected intermediate periodic orbits possess useful stable/unstable manifolds and P2HO₁ orbit comprises of spiral stable/unstable manifolds. A 3:4 RPO and DPO are employed only as the second intermediate orbit for exterior-type transfer design. For a specific energy, QPOs exist as a *1-dimensional* constant energy family. Hence, the *5-dimensional* solution space offered by the stable/unstable manifolds associated with a QPO family is reduced to *4-dimensional* manifolds corresponding to a constant energy family of QPOs. A QPO along two families: L_2 quasi-vertical orbits and L_2 quasi-P2HO₂ orbits, as depicted in Figures 6.6 and 6.7, inform the construction of end-to-end transfers. With the noted exception of a 3:4 RPO and a DPO, all the other selected intermediate orbits assist in uncovering interior-type and exterior-type pathways between the selected departure and arrival orbits.

Table 6.2. Initial conditions, period, JC value, and stability indices of the selected intermediate periodic orbits.

Orbit	x_0 [nd]	z_0 [nd]	\dot{y}_0 [nd]	\mathbb{P} [nd]	JC	ν_1	ν_2
L_2 vertical	1.05442	-0.19361	0.08128	3.87705	3.04649	1	303.83937
L_2 southern halo	1.13300	-0.17303	-0.22516	3.04091	3.04649	1	44.05357
L_2 southern P2HO ₁	0.94057	-0.15440	-0.18893	5.25489	3.04649	33.52874	33.52874
L_2 southern P2HO ₂	1.02578	0.059137	0.50201	4.20255	3.04649	1	45.64766
Planar 3:4 RPO	0.97615	0	1.40837	16.86499	3.04649	1	228.36123
DPO	1.02731	0	0.72419	4.50999	3.04649	1	619.95934

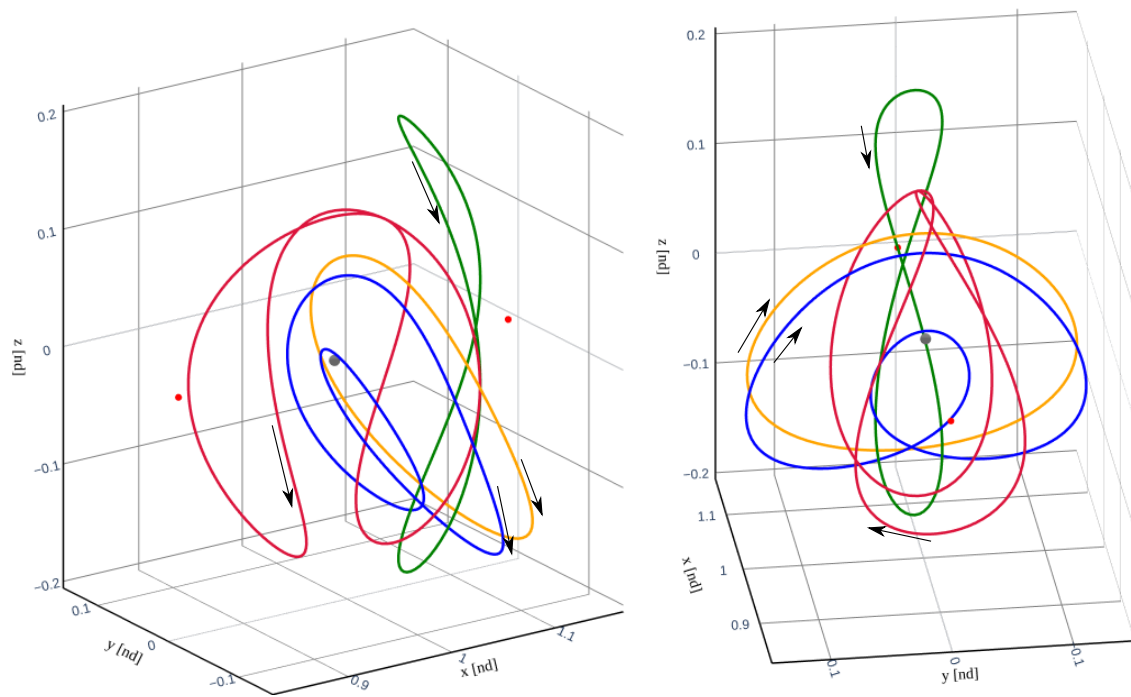


Figure 6.4. An L_2 vertical (green), L_2 southern halo (orange), L_2 southern P2HO₁ (crimson), L_2 southern P2HO₂ (navy) at the same JC value as an L_2 9:2 NRHO.

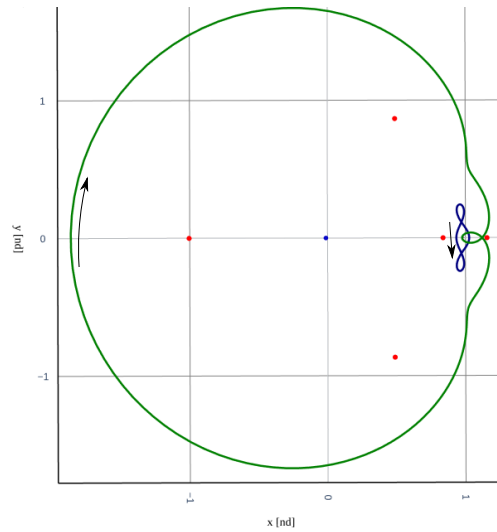


Figure 6.5. A planar 3:4 RPO (green) and a DPO (navy) at the same JC value as an L_2 9:2 NRHO

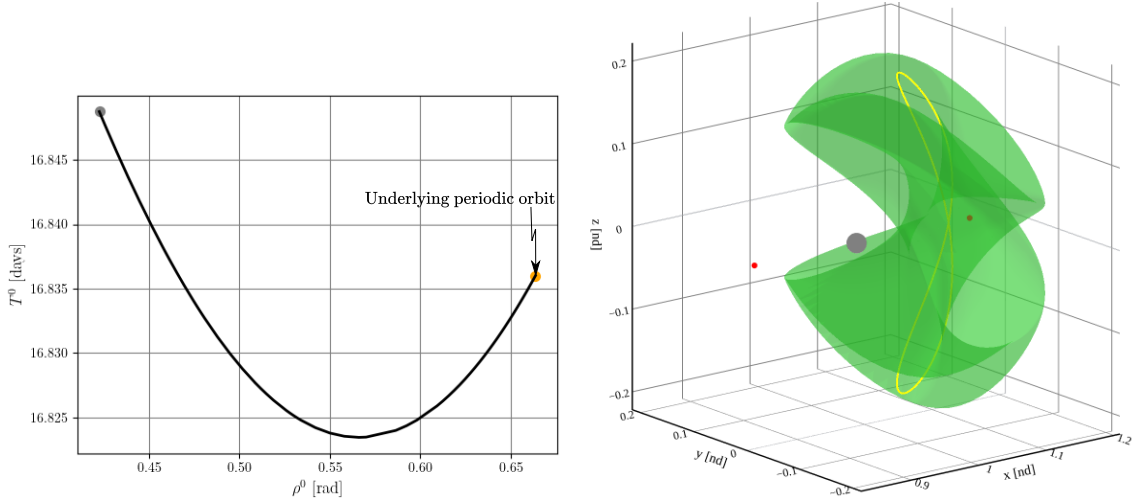


Figure 6.6. A constant energy family of L_2 quasi-vertical orbits with $J_C = 3.04649$. Plot of the evolution of ρ^0 and T^0 values of the QPOs along the family and a member (green) with $\rho^0 = 0.42259$ rad, as well as the underlying periodic orbit (yellow).

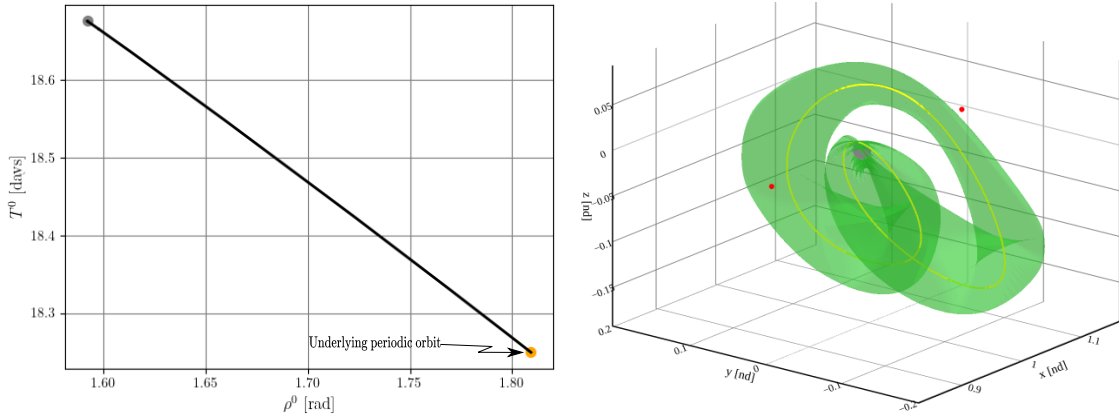


Figure 6.7. A constant energy family of L_2 quasi-P2HO₂ orbits with $J_C = 3.04649$. Plot of the evolution of ρ^0 and T^0 values of the QPOs along the family and a member (green) with $\rho^0 = 1.59184$ rad, as well as the underlying periodic orbit (yellow).

6.3 Inbound Segment to the Arrival Orbit

The design of an inbound segment to the arrival periodic orbit from an intermediate orbit is informed by the unstable manifold associated with the intermediate orbit. The step-by-step approach of the construction of a position continuous segment is as follows:

1. Identify the discrete unstable manifold arcs that cross near the arrival orbit states.
2. Employ a shooting method to construct manifold-constrained position continuous transfer arcs that require a single impulsive maneuver to insert into the arrival orbit.
3. If the constructed solution exists as a local family of solutions, generate the family of solutions through a numerical continuation technique.

This method is demonstrated for two intermediate orbits: an L_2 vertical and an L_2 quasi-vertical orbit in the following sections.

6.3.1 Initial Guess Generation

The identification of the potential candidate pathways seeds from the determination of the unstable manifold arcs that cross near an arrival periodic orbit. A popular technique to locate the crossings of the manifold arcs in the vicinity of an arrival orbit is to employ a Poincaré map [12], [27]. However, this approach is restrictive as often an arrival periodic orbit does not lie along a low dimensional hyperplane that defines a Poincaré map, hence, only a few states of the orbit are captured by the map. An alternate approach relies on defining a continuous representation of an arrival orbit and leverages an events function to determine the first nearby crossings of the manifold arcs with arrival orbit states. The continuous representation of a DRO is formulated through two cubic spline functions with the x position component of the periodic orbit states as the independent variable. Each spline function captures one-half of the orbit as illustrated in Figure 6.8. The events function is formulated to terminate the propagation of a manifold arc when the position discontinuity between a manifold state and an arrival periodic orbit state, which is evaluated using the spline function for the x position of the manifold state, is within an acceptable tolerance. The resultant event states suffice as the initial guess for the construction of single impulsive maneuver transfer arcs.

The initial guess for the transfer arcs that leverage the *2-dimensional* unstable manifold corresponding to a periodic orbit is obtained through the aforementioned events function

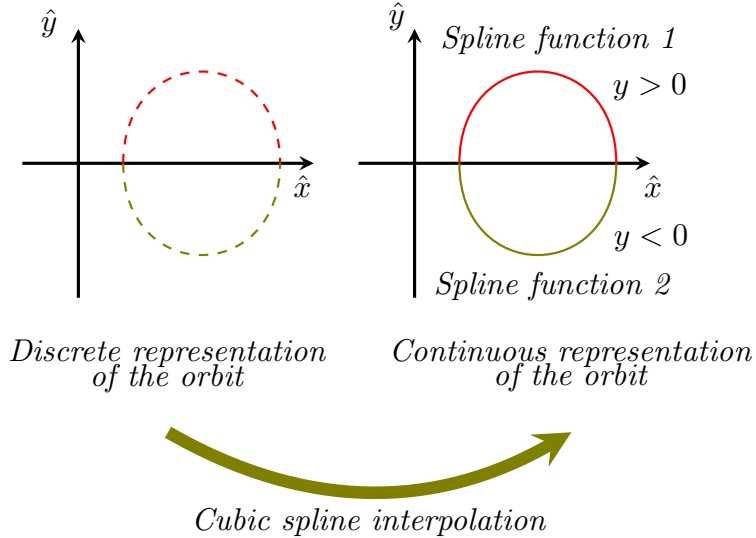


Figure 6.8. Continuous representation of the DRO of interest is generated through two cubic spline interpolation functions with x position as the independent variable.

method. The global manifold associated with a periodic orbit is approximated via the technique described in Section 4.3 for a constant step-off factor. A position discontinuity tolerance of 4000 km is used for the events function. The obtained manifold states are filtered down to options that have an initial velocity discontinuity of less than 700 m/s for the identification of low-cost geometries. The resultant event states for an L_2 vertical orbit are depicted in Figure 6.9. It is apparent from the plot that three local basins of solutions exist for the first crossings of the manifolds emanating from an L_2 vertical orbit. In addition, due to the $\hat{x} - \hat{y}$ plane symmetry of an L_2 vertical orbit and a DRO, each solution basin comprises of geometries that are mirror configurations about the plane. Subsequently, a shooting method is employed to construct position continuous transfer arcs that lie on the unstable manifold associated with the intermediate periodic orbit.

The 4-dimensional unstable manifold associated with the constant energy family of a QPO complicates the identification of an initial guess due to the high dimensionality of the solution space. To reduce the extent of the solution space, a QPO along the constant energy family is sought that delivers significantly different transfer options than the underlying periodic orbit. Consequently, it is vital to realize how the position and velocity discontinuities

between the potential candidate manifold states associated with an intermediate QPO and their nearest arrival orbit states evolve with the QPO family members along the constant energy family. Consider a member of the constant energy family of the L_2 quasi-vertical orbit with $\rho^0=0.42259$ rad as visualized in Figure 6.6. The *3-dimensional* unstable global manifold associated with a quasi-vertical orbit is estimated via the scheme elucidated in Section 5.4. The initial guess of the manifold arcs generated through the events function strategy is plotted in Figure 6.10. Due to the higher dimensionality of the manifold corresponding to a QPO than a periodic orbit, it is evident that many more solutions exist for manifold arcs associated with an L_2 quasi-vertical orbit than its underlying periodic orbit.

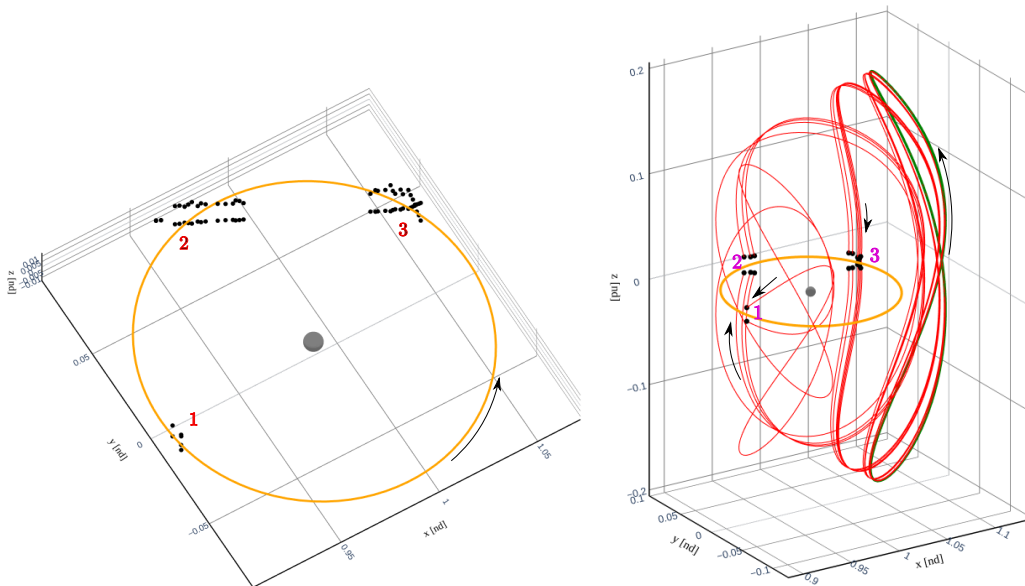


Figure 6.9. Unstable manifold states (black) and manifold arcs (red) associated with an L_2 vertical orbit (green) that cross near a DRO (orange).

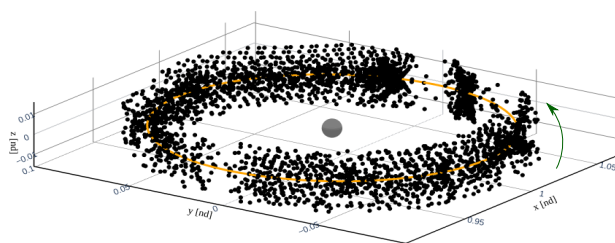


Figure 6.10. Unstable manifold states (black) associated with an L_2 quasi-vertical orbit ($\rho^0 = 0.42259$ rad) that cross near a DRO (orange).

An alternate visualization technique to Figure 6.10 is presented to allow for a more intuitive assessment of the initial guess. Additionally, the visualization strategy assists in the comparison of the position and velocity discontinuities of the manifolds corresponding to different QPOs along a constant energy family with the arrival orbit states. The proposed visualization method relies on parameterizing the candidate manifold states based on the angular variables that describe the manifold step-off location on the QPO. The longitudinal location of the step-off state is identified by θ_{T^0} angle as defined in Section 5.1. The latitudinal angle of the step-off state is specified by an Ω_{ρ^0} angle, instead of the θ_{ρ^0} angle as outlined in Section 5.1. The modified latitudinal angle, Ω_{ρ^0} , is defined such that all the states on a quasi-periodic trajectory propagated for one stroboscopic time period are denoted by the latitudinal angle of the initial state of the quasi-periodic trajectory. The traditional latitudinal angle, θ_{ρ^0} , evolves with the propagation time along a QPO as defined in Equation (5.6). However, the Ω_{ρ^0} angle is constant for all the states that are one revolution downstream of the initial state. The key advantage of the modified latitudinal angle is that it preserves information about the natural flow of motion along a QPO for one revolution of the torus. After every revolution of the quasi-periodic trajectory around the torus, the Ω_{ρ^0} angle is updated by the rotation angle, ρ^0 . The initial guess states, depicted in Figure 6.10, are represented by the longitudinal angle and the modified latitudinal angle parameterization of the step-off location of the manifold states and colored by the position and velocity discontinuity with the arrival orbit states at the x position of the manifold states in Figure 6.11.

The relationship between the position and velocity discontinuities of the initial guess and the evolution of the QPOs along the constant energy family is uncovered through the visualization method illustrated in Figure 6.11. The position and velocity discontinuities of the initial guess generated through the unstable manifolds associated with L_2 quasi-vertical orbits of $\rho^0 = 0.51490, 0.60913$ and 0.64859 rad are presented in Figures 6.12 to 6.14, respectively. It is apparent from Figures 6.11 to 6.14 that there is a gradual decrease in the velocity discontinuities as the QPOs are continued along the constant energy family, marked by the decrease in the rotation angle of the orbits. Hence, the quasi-vertical orbit with the smallest rotation angle amongst the generated family members is employed for the construction of the inbound segment to the arrival orbit, i.e. the quasi-vertical orbit with

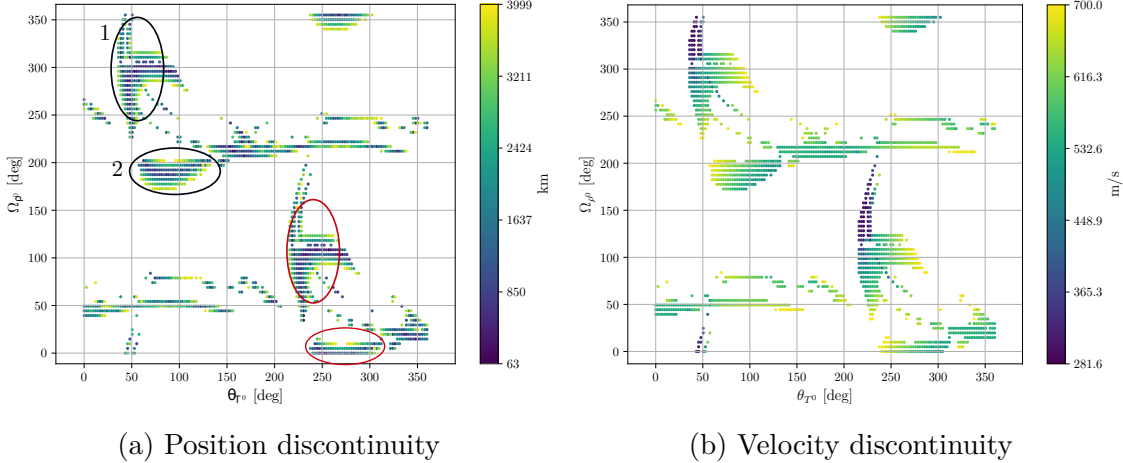


Figure 6.11. Position and velocity discontinuities between the unstable manifold states associated with an L_2 quasi-vertical orbit ($\rho^0 = 0.42259$ rad) and the corresponding nearest arrival orbit states.

$\rho^0 = 0.42259$ rad. The unstable manifold associated with the selected orbit hints at two candidate basins of solutions as highlighted by the black curves in Figure 6.11. Similar to the L_2 vertical orbit scenario, the candidate solutions in the regions marked by red curves are mirror configurations of the solutions in the regions highlighted by the black curves due to the inherent $\hat{x} - \hat{y}$ plane symmetry of the QPO and the arrival orbit. The identified manifold states corresponding to the quasi-vertical orbit with $\rho^0 = 0.42259$ rad suffice as the initial guess for the corrections process.

6.3.2 Differential Correction

Differential corrections schemes are formulated to leverage the identified initial guess to design transfer arcs that lie on the manifold corresponding to the intermediate periodic and quasi-periodic orbits. The transfer arcs are corrected for position continuity with the arrival periodic orbit and constraint to lie on the unstable manifold associated with the intermediate orbit. The insertion location along the arrival orbit, the time of flight of the transfer arc, and the location of the step-off state on the intermediate orbit that approximates the manifold arc are allowed to vary during the corrections process. Consequently, a single impulsive

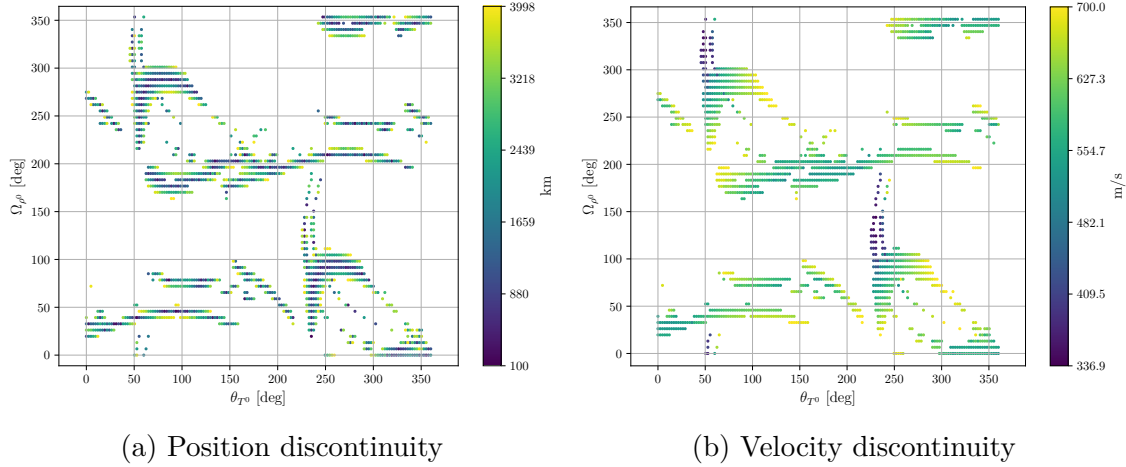


Figure 6.12. Position and velocity discontinuities between the manifold states corresponding with an L_2 quasi-vertical orbit ($\rho^0 = 0.51490$ rad) and the corresponding nearest arrival orbit states.

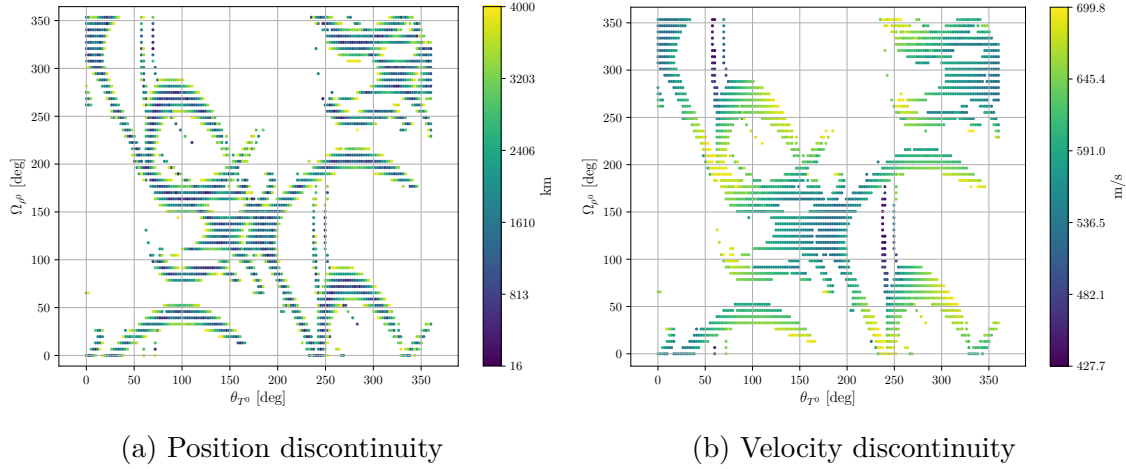


Figure 6.13. Position and velocity discontinuities between the manifold states corresponding with an L_2 quasi-vertical orbit ($\rho^0 = 0.60913$ rad) and the corresponding nearest arrival orbit states.

maneuver is required to overcome the velocity discontinuity at the crossing of the transfer arc and the arrival orbit.

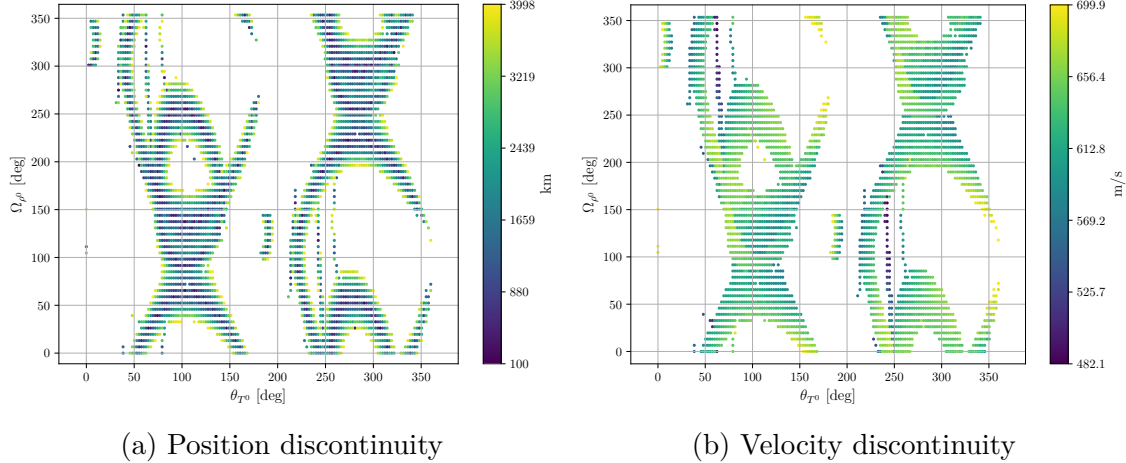


Figure 6.14. Position and velocity discontinuities between the manifold states corresponding with an L_2 quasi-vertical orbit ($\rho^0 = 0.64859$ rad) and the corresponding nearest arrival orbit states.

The initial guess from the manifolds corresponding to an intermediate periodic orbit results in locally unique solutions. For the refinement of the initial guess, the following design and constraint vector are employed,

$$\bar{X} = \begin{bmatrix} \mathbb{T} \\ \tau_{\text{arr}} \\ \tau_{\text{int}} \end{bmatrix}; \quad \bar{F}(\bar{X}) = \begin{bmatrix} {}_u x_{\tau_{\text{int}}}^{\mathbb{T}} - x_{\text{arr}}^{\tau_{\text{arr}}} \\ {}_u y_{\tau_{\text{int}}}^{\mathbb{T}} - y_{\text{arr}}^{\tau_{\text{arr}}} \\ {}_u z_{\tau_{\text{int}}}^{\mathbb{T}} - z_{\text{arr}}^{\tau_{\text{arr}}} \end{bmatrix} \quad (6.1)$$

where, \mathbb{T} denotes the flight time of the manifold arc, τ_{arr} and τ_{int} signify the propagation time along an arrival periodic orbit and intermediate periodic orbit, respectively. The $x_{\text{arr}}^{\tau_{\text{arr}}}$, $y_{\text{arr}}^{\tau_{\text{arr}}}$, and $z_{\text{arr}}^{\tau_{\text{arr}}}$ elements are the x , y and z positions of an arrival orbit state that is computed by propagating an initial arrival orbit state, \bar{x}_{arr} , for time τ_{arr} . The ${}_u x_{\tau_{\text{int}}}^{\mathbb{T}}$, ${}_u y_{\tau_{\text{int}}}^{\mathbb{T}}$ and ${}_u z_{\tau_{\text{int}}}^{\mathbb{T}}$ components represent the x , y and z positions of an unstable manifold state, ${}_u \bar{x}_{\tau_{\text{int}}}^{\mathbb{T}}$, associated with an intermediate periodic orbit. The ${}_u \bar{x}_{\tau_{\text{int}}}^{\mathbb{T}}$ state is computed by propagating a local

unstable manifold state, ${}_u\bar{x}_{\tau_{\text{int}}}$, for time \mathbb{T} . The local manifold state, ${}_u\bar{x}_{\tau_{\text{int}}}$, is approximated through the following expression,

$${}_u\bar{x}_{\tau_{\text{int}}} = \bar{x}_{\tau_{\text{int}}} + \nabla_u \frac{\Phi_{\tau_{\text{int}}} \bar{v}_u}{\sqrt{(\Phi_{\tau_{\text{int}}} \bar{v}_u)^T (\Phi_{\tau_{\text{int}}} \bar{v}_u)}} \quad (6.2)$$

where, $\bar{x}_{\tau_{\text{int}}}$ denotes a step-off state on an intermediate periodic orbit that lies τ_{int} downstream an initial state on the periodic orbit, ∇_u represents a step-off factor (dimensionless), \bar{v}_u corresponds to a 6×1 unstable eigenvector associated with the initial state of an intermediate orbit, and $\Phi_{\tau_{\text{int}}}$ is the STM that maps the first-order effect of variations in the initial state of an orbit to $\bar{x}_{\tau_{\text{int}}}$ state. The manifod step-off factor is assumed to be constant during the differential corrections process. The Jacobian matrix of the differential corrections scheme is given by,

$$\mathbf{DF}(\bar{X}) = \begin{bmatrix} {}_u\dot{x}_{\tau_{\text{int}}}^{\mathbb{T}} & -\dot{x}_{\text{arr}}^{\tau_{\text{arr}}} & \frac{\partial({}_u\bar{x}_{\tau_{\text{int}}}^{\mathbb{T}})}{\partial\tau_{\text{int}}} \\ {}_u\dot{y}_{\tau_{\text{int}}}^{\mathbb{T}} & -\dot{y}_{\text{arr}}^{\tau_{\text{arr}}} & \frac{\partial({}_u\bar{y}_{\tau_{\text{int}}}^{\mathbb{T}})}{\partial\tau_{\text{int}}} \\ {}_u\dot{z}_{\tau_{\text{int}}}^{\mathbb{T}} & -\dot{z}_{\text{arr}}^{\tau_{\text{arr}}} & \frac{\partial({}_u\bar{z}_{\tau_{\text{int}}}^{\mathbb{T}})}{\partial\tau_{\text{int}}} \end{bmatrix} \quad (6.3)$$

The first and the second column of the Jacobian matrix are the velocity components of ${}_u\bar{x}_{\tau_{\text{int}}}^{\mathbb{T}}$ and $\bar{x}_{\text{arr}}^{\tau_{\text{arr}}}$, respectively. The elements in the third column correspond to the variation in the position of the downstream manifold state with respect to the change in the step-off location on the intermediate periodic orbit. The partial derivative of the change in downstream manifold state with respect to τ_{int} is expressed as,

$$\frac{\partial({}_u\bar{x}_{\tau_{\text{int}}}^{\mathbb{T}})}{\partial\tau_{\text{int}}} = \phi_M(\mathbb{T}, 0) \frac{\partial({}_u\bar{x}_{\tau_{\text{int}}})}{\partial\tau_{\text{int}}} \quad (6.4)$$

where, $\phi_M(\mathbb{T}, 0)$ is an STM that captures the impact of change in ${}_u\bar{x}_{\tau_{\text{int}}}$ state on the ${}_u\bar{x}_{\tau_{\text{int}}}^{\mathbb{T}}$ state. The derivative of ${}_u\bar{x}_{\tau_{\text{int}}}$ with respect to τ_{int} is written as,

$$\frac{\partial({}_u\bar{x}_{\tau_{\text{int}}})}{\partial\tau_{\text{int}}} = \dot{\bar{x}}_{\tau_{\text{int}}} + \nabla_u \left(\frac{\dot{\Phi}_{\tau_{\text{int}}} \bar{v}_u}{\sqrt{(\Phi_{\tau_{\text{int}}} \bar{v}_u)^T (\Phi_{\tau_{\text{int}}} \bar{v}_u)}} - \frac{\Phi_{\tau_{\text{int}}} \bar{v}_u ((\dot{\Phi}_{\tau_{\text{int}}} \bar{v}_u)^T (\Phi_{\tau_{\text{int}}} \bar{v}_u) + (\Phi_{\tau_{\text{int}}} \bar{v}_u)^T (\dot{\Phi}_{\tau_{\text{int}}} \bar{v}_u))}{2((\Phi_{\tau_{\text{int}}} \bar{v}_u)^T (\Phi_{\tau_{\text{int}}} \bar{v}_u))^{\frac{3}{2}}} \right) \quad (6.5)$$

where, $\dot{\Phi}_{\tau_{\text{int}}}$ is the time derivative of matrix $\Phi_{\tau_{\text{int}}}$. The partial derivatives in the third column of the Jacobian matrix, Equation (6.3), are the first three components of Equation (6.4). The shooting method, Equation (6.1), is fully constrained, hence, the initial guess from a manifold arc of an intermediate periodic orbit leads to a unique solution. If the selected intermediate periodic orbit possesses unstable/stable spiral manifolds, then the differential corrections scheme is adapted to allow for the refinement of the $\theta_{PO,\text{spiral}}$ angle, as defined in Section 4.3. The angle along the spiral complex plane, $\theta_{PO,\text{spiral}}$, is appended to the design vector Equation (6.1). The partial derivative of the constraint vector with respect to the $\theta_{PO,\text{spiral}}$ angle are the first three elements of the following expression,

$$\frac{\partial(u\bar{x}_{\tau_{\text{int}}}^T)}{\partial\theta_{PO,\text{spiral}}} = \boldsymbol{\phi}_M(\mathbb{T}, 0)\nabla_u\Phi_{\tau_{\text{int}}} \left(\frac{-\text{Re}[\bar{v}_u]\sin(\theta_{PO,\text{spiral}}) - \text{Im}[\bar{v}_u]\cos(\theta_{PO,\text{spiral}})}{\sqrt{(\Phi_{\tau_{\text{int}}}\bar{v}_u)^T(\Phi_{\tau_{\text{int}}}\bar{v}_u)}} \right) \quad (6.6)$$

The described shooting method, Equation (6.1), is employed for the construction of three transfer arcs that originate near an L_2 vertical orbit and require a maneuver to insert into a DRO through the initial guess identified in Figure 6.9. The resultant geometries are visualized in Figure 6.15 and the associated maneuver costs, as well as the flight times are mentioned in Table 6.3.

Table 6.3. Maneuver costs and times of flight of the three transfer options, depicted in Figure 6.15, constructed with an L_2 vertical orbit as the intermediate orbit.

Transfer arc	ΔV_{arr} (m/s)	TOF (days)
1	644.335	19.690
2	638.378	17.052
3	535.494	29.901

For the construction of transfer arcs that leverage the unstable manifold associated with an intermediate QPO, the aforementioned differential scheme is modified to account for the

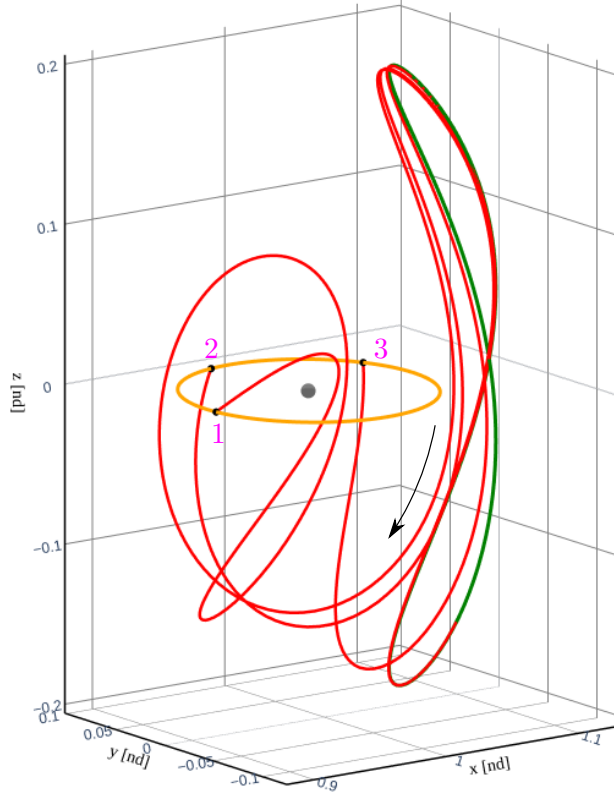


Figure 6.15. Three converged inbound segments (red) to the DRO (orange) informed by the initial guess generated through an L_2 vertical orbit (green). The transfer arcs require a single impulsive maneuver (black) to overcome the velocity discontinuity with the arrival orbit. The maneuver costs and flight times are tabulated in Table 6.3.

higher dimensionality of the unstable manifold associated with a QPO than a periodic orbit.

The design and constraint vectors are formulated as,

$$\bar{X} = \begin{bmatrix} \mathbb{T} \\ \tau_{\text{arr}} \\ \tau_{\text{int}} \\ \Omega_{\rho^0} \end{bmatrix}; \quad \bar{F}(\bar{X}) = \begin{bmatrix} u x_{\tau_{\text{int}}, \Omega_{\rho^0}}^{\mathbb{T}} - x_{\text{arr}}^{\tau_{\text{arr}}} \\ u y_{\tau_{\text{int}}, \Omega_{\rho^0}}^{\mathbb{T}} - y_{\text{arr}}^{\tau_{\text{arr}}} \\ u z_{\tau_{\text{int}}, \Omega_{\rho^0}}^{\mathbb{T}} - z_{\text{arr}}^{\tau_{\text{arr}}} \end{bmatrix} \quad (6.7)$$

The elements of the design and constraint vector are defined in a similar manner as Equation (6.1). In the design vector, \mathbb{T} denotes the time of flight along a manifold arc and τ_{arr} corresponds to the propagation time along an arrival periodic orbit from an initial state, \bar{x}_{arr} ,

on the orbit. The last two elements of the design vector, τ_{int} and Ω_{ρ^0} represent the step-off state, $\bar{x}_{\tau_{\text{int}}, \Omega_{\rho^0}}$, on an intermediate QPO that approximates a local unstable manifold state. Specifically, τ_{int} denotes the propagation time along a QPO from an initial invariant curve to the invariant curve on which the step-off location lies and Ω_{ρ^0} represents the modified latitudinal angle of the step-off location. The ${}_u x_{\tau_{\text{int}}, \Omega_{\rho^0}}^{\mathbb{T}}$, ${}_u y_{\tau_{\text{int}}, \Omega_{\rho^0}}^{\mathbb{T}}$ and ${}_u z_{\tau_{\text{int}}, \Omega_{\rho^0}}^{\mathbb{T}}$ components represent the x , y and z positions of an unstable manifold state, ${}_{u\bar{x}}^{\mathbb{T}}_{\tau_{\text{int}}, \Omega_{\rho^0}}$, associated with an intermediate QPO. The ${}_{u\bar{x}}^{\mathbb{T}}_{\tau_{\text{int}}, \Omega_{\rho^0}}$ state is computed by propagating a local unstable manifold state, ${}_{u\bar{x}}_{\tau_{\text{int}}, \Omega_{\rho^0}}$, for time \mathbb{T} . The local manifold state, ${}_{u\bar{x}}_{\tau_{\text{int}}, \Omega_{\rho^0}}$, is approximated through the following expression,

$${}_{u\bar{x}}_{\tau_{\text{int}}, \Omega_{\rho^0}} = \bar{x}_{\tau_{\text{int}}, \Omega_{\rho^0}} + \nabla_u \frac{\Phi_{\tau_{\text{int}}, \Omega_{\rho^0}} \bar{v}_u}{\sqrt{(\Phi_{\tau_{\text{int}}, \Omega_{\rho^0}} \bar{v}_u)^T (\Phi_{\tau_{\text{int}}, \Omega_{\rho^0}} \bar{v}_u)}} \quad (6.8)$$

where, ∇_u signifies the step-off factor, \bar{v}_u is a 6×1 unstable eigenvector associated with a state on a QPO on an initial curve at Ω_{ρ^0} angle, and $\Phi_{\tau_{\text{int}}, \Omega_{\rho^0}}$ is the STM propagated from an initial state on a QPO to $\bar{x}_{\tau_{\text{int}}, \Omega_{\rho^0}}$. The step-off factor is assumed to be constant during the differential corrections process. The Jacobian matrix for Equation (6.7) is formulated as,

$$\mathbf{DF}(\bar{X}) = \begin{bmatrix} {}_{u\dot{x}}^{\mathbb{T}}_{\tau_{\text{int}}, \Omega_{\rho^0}} & -\dot{x}_{\text{arr}}^{\tau_{\text{arr}}} & \frac{\partial({}_{u x}_{\tau_{\text{int}}, \Omega_{\rho^0}}^{\mathbb{T}})}{\partial \tau_{\text{int}}} & \frac{\partial({}_{u x}_{\tau_{\text{int}}, \Omega_{\rho^0}}^{\mathbb{T}})}{\partial \Omega_{\rho^0}} \\ {}_{u\dot{y}}^{\mathbb{T}}_{\tau_{\text{int}}, \Omega_{\rho^0}} & -\dot{y}_{\text{arr}}^{\tau_{\text{arr}}} & \frac{\partial({}_{u y}_{\tau_{\text{int}}, \Omega_{\rho^0}}^{\mathbb{T}})}{\partial \tau_{\text{int}}} & \frac{\partial({}_{u y}_{\tau_{\text{int}}, \Omega_{\rho^0}}^{\mathbb{T}})}{\partial \Omega_{\rho^0}} \\ {}_{u\dot{z}}^{\mathbb{T}}_{\tau_{\text{int}}, \Omega_{\rho^0}} & -\dot{z}_{\text{arr}}^{\tau_{\text{arr}}} & \frac{\partial({}_{u z}_{\tau_{\text{int}}, \Omega_{\rho^0}}^{\mathbb{T}})}{\partial \tau_{\text{int}}} & \frac{\partial({}_{u z}_{\tau_{\text{int}}, \Omega_{\rho^0}}^{\mathbb{T}})}{\partial \Omega_{\rho^0}} \end{bmatrix} \quad (6.9)$$

where, the first and second column elements are the velocity components of the propagated manifold state and the downstream arrival orbit state. The third and fourth column comprises of the partial derivatives of the downstream manifold state with respect to the

τ_{int} and Ω_{ρ^0} , respectively. These two partial derivatives are analytically evaluated through expressions similar to the ones derived by McCarthy et al. [27], [36] and written as,

$$\frac{\partial \left({}_u \bar{x}_{\tau_{\text{int}}, \Omega_{\rho^0}}^{\mathbb{T}} \right)}{\partial \tau_{\text{int}}} = \boldsymbol{\phi}_M(\mathbb{T}, 0) \frac{\partial \left({}_u \bar{x}_{\tau_{\text{int}}, \Omega_{\rho^0}} \right)}{\partial \tau_{\text{int}}} \quad (6.10)$$

$$\frac{\partial \left({}_u \bar{x}_{\tau_{\text{int}}, \Omega_{\rho^0}}^{\mathbb{T}} \right)}{\partial \Omega_{\rho^0}} = \boldsymbol{\phi}_M(\mathbb{T}, 0) \frac{\partial \left({}_u \bar{x}_{\tau_{\text{int}}, \Omega_{\rho^0}} \right)}{\partial \Omega_{\rho^0}} \quad (6.11)$$

The $\boldsymbol{\phi}_M(\mathbb{T}, 0)$ matrix is an STM that maps the first-order linear variations of the ${}_u \bar{x}_{\tau_{\text{int}}, \Omega_{\rho^0}}$ state to a downstream state at time \mathbb{T} . The expanded form of $\frac{\partial \left({}_u \bar{x}_{\tau_{\text{int}}, \Omega_{\rho^0}} \right)}{\partial \tau_{\text{int}}}$ is expressed as,

$$\begin{aligned} \frac{\partial \left({}_u \bar{x}_{\tau_{\text{int}}, \Omega_{\rho^0}} \right)}{\partial \tau_{\text{int}}} &= \dot{\bar{x}}_{\tau_{\text{int}}, \Omega_{\rho^0}} + \nabla_u \left(\frac{\dot{\Phi}_{\tau_{\text{int}}, \Omega_{\rho^0}} \bar{v}_u}{\sqrt{(\Phi_{\tau_{\text{int}}, \Omega_{\rho^0}} \bar{v}_u)^T (\Phi_{\tau_{\text{int}}, \Omega_{\rho^0}} \bar{v}_u)}} \right. \\ &\quad - \frac{\Phi_{\tau_{\text{int}}, \Omega_{\rho^0}} \bar{v}_u (\dot{\Phi}_{\tau_{\text{int}}, \Omega_{\rho^0}} \bar{v}_u)^T (\Phi_{\tau_{\text{int}}, \Omega_{\rho^0}} \bar{v}_u)}{2((\Phi_{\tau_{\text{int}}, \Omega_{\rho^0}} \bar{v}_u)^T (\Phi_{\tau_{\text{int}}, \Omega_{\rho^0}} \bar{v}_u))^{\frac{3}{2}}} \\ &\quad \left. - \frac{\Phi_{\tau_{\text{int}}, \Omega_{\rho^0}} \bar{v}_u (\Phi_{\tau_{\text{int}}, \Omega_{\rho^0}} \bar{v}_u)^T (\dot{\Phi}_{\tau_{\text{int}}, \Omega_{\rho^0}} \bar{v}_u)}{2((\Phi_{\tau_{\text{int}}, \Omega_{\rho^0}} \bar{v}_u)^T (\Phi_{\tau_{\text{int}}, \Omega_{\rho^0}} \bar{v}_u))^{\frac{3}{2}}} \right) \end{aligned} \quad (6.12)$$

The above equation is similar to the one derived for an intermediate periodic orbit in Equation (6.5). The partial derivative $\frac{\partial \left({}_u \bar{x}_{\tau_{\text{int}}, \Omega_{\rho^0}} \right)}{\partial \Omega_{\rho^0}}$ is written as,

$$\frac{\partial \left({}_u \bar{x}_{\tau_{\text{int}}, \Omega_{\rho^0}} \right)}{\partial \Omega_{\rho^0}} = \frac{\partial \left(\bar{x}_{\tau_{\text{int}}, \Omega_{\rho^0}} \right)}{\partial \Omega_{\rho^0}} + \nabla_u \frac{\partial \left(\Phi_{\tau_{\text{int}}, \Omega_{\rho^0}} \bar{v}_u \left(\sqrt{(\Phi_{\tau_{\text{int}}, \Omega_{\rho^0}} \bar{v}_u)^T (\Phi_{\tau_{\text{int}}, \Omega_{\rho^0}} \bar{v}_u)} \right)^{-1} \right)}{\partial \Omega_{\rho^0}} \quad (6.13)$$

It is evident that the above partial derivative requires the computation of $\frac{\partial \left(\Phi_{\tau_{\text{int}}, \Omega_{\rho^0}} \right)}{\partial \Omega_{\rho^0}}$, which is challenging due to the lack of an analytical expression as noted by McCarthy et al. [27], [36]. A different method is adopted to evaluate Equation (6.13) that relies on the construction

of an unstable eigenvector spectrum of the invariant curve on which $\bar{x}_{\tau_{\text{int}}, \Omega_{\rho^0}}$ state lies. The partial derivative, Equation (6.13), is rewritten as,

$$\frac{\partial \left({}_u \bar{x}_{\tau_{\text{int}}, \Omega_{\rho^0}} \right)}{\partial \Omega_{\rho^0}} = \frac{\partial \left(\bar{x}_{\tau_{\text{int}}, \Omega_{\rho^0}} \right)}{\partial \Omega_{\rho^0}} + \nabla_u \frac{\partial \left(\bar{w}_u \left(\sqrt{\bar{w}_u^T \bar{w}_u} \right)^{-1} \right)}{\partial \Omega_{\rho^0}} \quad (6.14)$$

$$= \frac{\partial \left(\bar{x}_{\tau_{\text{int}}, \Omega_{\rho^0}} \right)}{\partial \Omega_{\rho^0}} + \nabla_u \left(\frac{\frac{\partial \bar{w}_u}{\partial \Omega_{\rho^0}}}{\sqrt{\bar{w}_u^T \bar{w}_u}} \right. \\ \left. - \frac{\bar{w}_u \left(\left(\frac{\partial \bar{w}_u}{\partial \Omega_{\rho^0}} \right)^T \bar{w}_u + \bar{w}_u^T \frac{\partial \bar{w}_u}{\partial \Omega_{\rho^0}} \right)}{2(\bar{w}_u^T \bar{w}_u)^{\frac{3}{2}}} \right) \quad (6.15)$$

where, $\bar{w}_u = \Phi_{\tau_{\text{int}}, \Omega_{\rho^0}} \bar{v}_u$ is an unstable eigenvector corresponding to the step-off state, $\bar{x}_{\tau_{\text{int}}, \Omega_{\rho^0}}$. The derivative of the step-off state with respect to Ω_{ρ^0} is given as,

$$\frac{\partial \left(\bar{x}_{\tau_{\text{int}}, \Omega_{\rho^0}} \right)}{\partial \Omega_{\rho^0}} = \text{diag}[i\bar{k}] e^{i\bar{k}\Omega_{\rho^0}} \mathbf{C}_0 \quad (6.16)$$

Recall, \bar{k} is defined in Equation (5.19), and \mathbf{C}_0 matrix comprises the Fourier coefficients corresponding to the states that describe the initial invariant curve on the QPO, similar to Equation (5.16). The partial derivative of the unstable eigenvector with respect to the modified latitudinal angle in Equation (6.15) is evaluated using the Fourier coefficients of the unstable eigenvector spectrum associated with the invariant curve of the intermediate QPO that comprises of $\bar{x}_{\tau_{\text{int}}, \Omega_{\rho^0}}$ state,

$$\frac{\partial \bar{w}_u}{\partial \Omega_{\rho^0}} = \text{diag}[i\bar{k}] e^{i\bar{k}\Omega_{\rho^0}} \mathbf{C}_u \quad (6.17)$$

The \mathbf{C}_u matrix consists of the Fourier coefficients of the unstable eigenvector spectrum and is computed through the following,

$$\mathbf{C}_u = \mathbf{D} \mathbf{W}_u \quad (6.18)$$

where, \mathbf{D} denotes the DFT operator as defined in Equation (5.18), and \mathbf{V}_u matrix comprises of the unstable eigenvectors of the states that approximate the invariant curve, which is τ_{int} downstream from the initial invariant curve, and it is structured similar to Equation (5.20). The downstream eigenvector spectrum is computed through the block diagonal STM, $\tilde{\Phi}(\tau_{\text{int}}, 0)$, which is similar to Equation (5.26), and unstable eigenvector spectrum of the initial invariant curve, \mathbf{V}_u , through the following expression,

$$\mathbf{W}_u = \tilde{\Phi}(\tau_{\text{int}}, 0)\mathbf{V}_u \quad (6.19)$$

The shooting method to construct transfer arcs by leveraging the unstable manifolds corresponding to an intermediate QPO, Equation (6.7), consists of a *1-dimensional* null-space, hence, the transfer arcs exist as local *1-parameter* family of solutions. After the determination of a solution through the minimum norm update, the local family of solutions is generated through one of the numerical continuation techniques discussed in Sections 3.3.1 and 3.3.2. This scheme is employed for the construction of the local families of solutions with the selected L_2 quasi-vertical orbit as the intermediate orbit and the initial guess identified in Figure 6.11. Two distinct families of solutions in region 1, as highlighted in Figure 6.11, and its mirror configuration about the $\hat{x} - \hat{y}$ plane are constructed and represented in Figure 6.16. The solutions obtained through the initial guess in region 2, as marked in Figure 6.11, lead to higher maneuver cost transfers and multiple members of the local family traverse through the surface of the Moon. Hence, they are not represented in Figure 6.16. A few members of the families marked by 1' and 2 as depicted in Figure 6.16 are visualized in the configuration space in Figure 6.17. It is apparent that the manifold arcs corresponding to the selected L_2 quasi-vertical orbit offer many more solution geometries and lower maneuver cost transfers than the three geometries constructed via the manifolds associated with an L_2 vertical orbit. The presented shooting methods are extendable to multiple shooting methods that leverage multiple nodes along the manifold arc and the periodic/quasi-periodic trajectory along an intermediate periodic/quasi-periodic orbit.

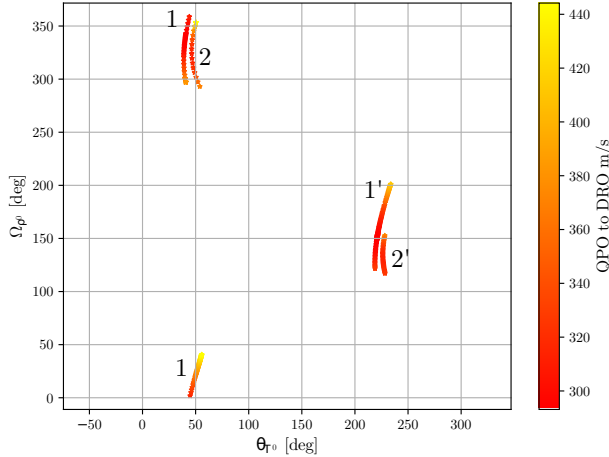
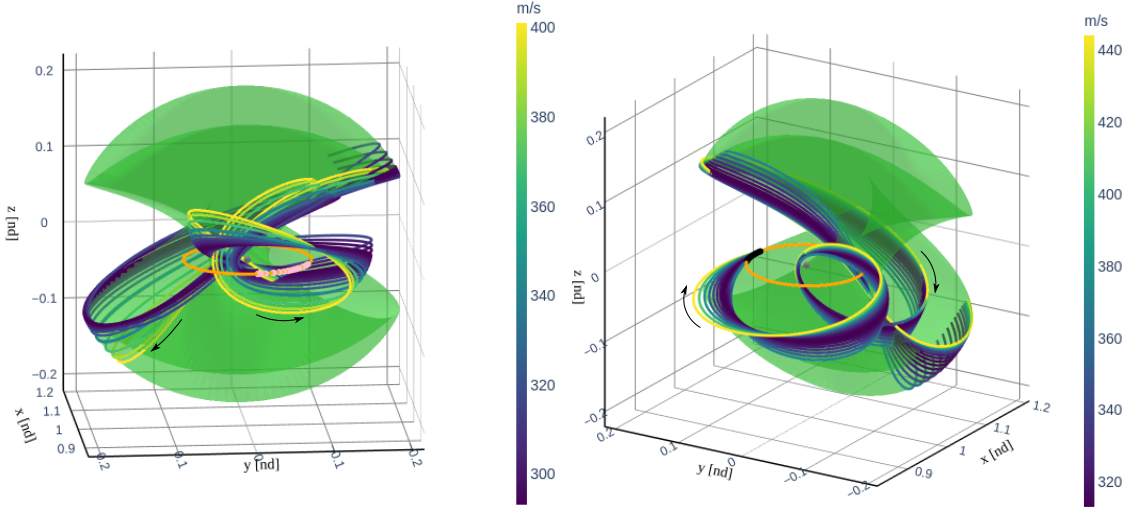


Figure 6.16. Differential corrected inbound segments to the arrival orbit constructed through the initial guess obtained in Figure 6.11. The solutions in the local basins 1' and 2' are mirror configurations of the options in local basins 1 and 2 about the $\hat{x} - \hat{y}$ plane.

6.4 Outbound Segment from the Departure Orbit

The outbound segment from the departure orbit to an intermediate orbit is constructed via the stable manifold arcs of the corresponding intermediate orbit. The procedure to identify candidate manifold arcs corresponding to an intermediate orbit that cross near the vicinity of the departure orbit employs the initial guess generation strategy discussed in Section 6.3.1. A continuous representation of the departure orbit, L_2 NRHO, is obtained through two cubic spline interpolation functions with the x position of the orbit states as the independent variable, as illustrated in Figure 6.8. An events function is formulated to terminate the propagation of the stable manifold arcs when the manifold states approach the departure orbit within a certain distance. The identified manifold states are differentially corrected through schemes similar to Section 6.3.2. The shooting methods in Equations (6.1) and (6.7) are altered such that the downstream stable manifold states are position continuous with the departure orbit state, and the flight time for stable manifold states is negative. The differential corrections scheme that leverages the stable manifolds associated with an intermediate periodic orbit is fully determined, whereas the one that employs the manifolds corresponding to an intermediate QPO comprises of a *1-dimensional* null-space.



(a) Solutions of the local basin 1'

(b) Solutions of the local basin 2

Figure 6.17. Transfer geometries corresponding to the local basin 1' and 2 as highlighted in Figure 6.16. The local solutions generated with an L_2 quasi-vertical orbit (green) as the intermediate orbit require a single maneuver (pink) to overcome the velocity discontinuity with the arrival orbit state (orange). The time of flight of the transfer arcs plotted above ranges from 26.8 to 28.1 days.

An L_2 vertical and L_2 quasi-vertical orbit with $\rho^0 = 0.42259$ rad are selected as the intermediate orbits to demonstrate the construction of the outbound segment from an L_2 NRHO. The initial guess identification strategy and differential corrections scheme uncover two outbound segments from an NRHO to an L_2 vertical orbit as plotted in Figure 6.18 with transfer costs outlined in Table 6.4. For an L_2 quasi-vertical orbits, the candidate manifold states are depicted in Figure 6.19. The initial guesses are differentially corrected and PALC is employed to generate local families of solutions. The local families of solutions that remain outside the surface of the Moon are represented in Figure 6.20 and plotted in the configuration space in Figure 6.21. The constructed outbound segments assist in the computation of interior-type and exterior-type end-to-end transfer geometries.

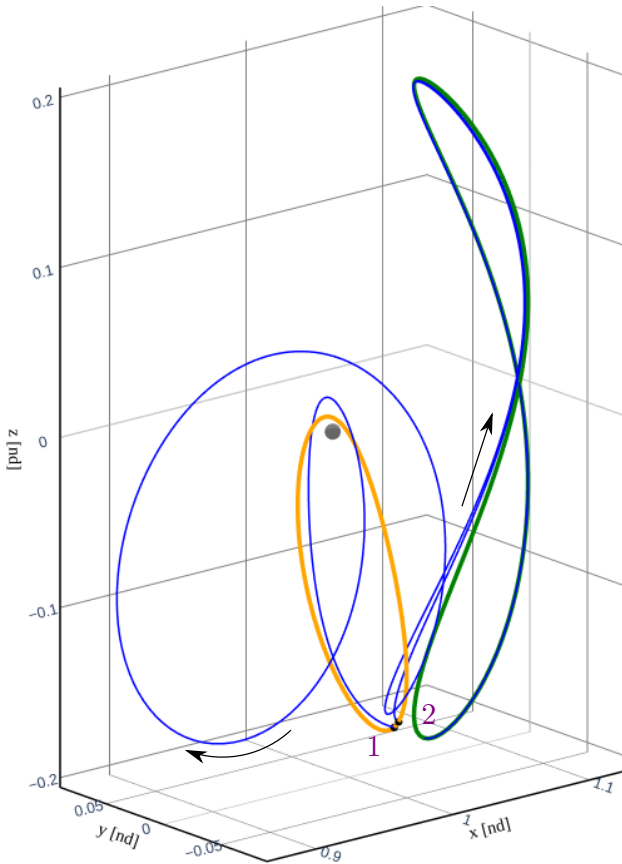


Figure 6.18. Two converged outbound segments (blue) from an NRHO (orange) informed by the initial guess generated through an L_2 vertical orbit (green). The transfer arcs require a single impulsive maneuver (black) to overcome the velocity discontinuity with the departure orbit. The maneuver costs and flight times are tabulated in Table 6.4.

Table 6.4. Maneuver costs and times of flight of the two transfer options, depicted in Figure 6.18, constructed with an L_2 vertical orbit as the intermediate orbit.

Transfer arc	ΔV_{dep} (m/s)	TOF (days)
1	275.097	15.278
2	197.810	30.879

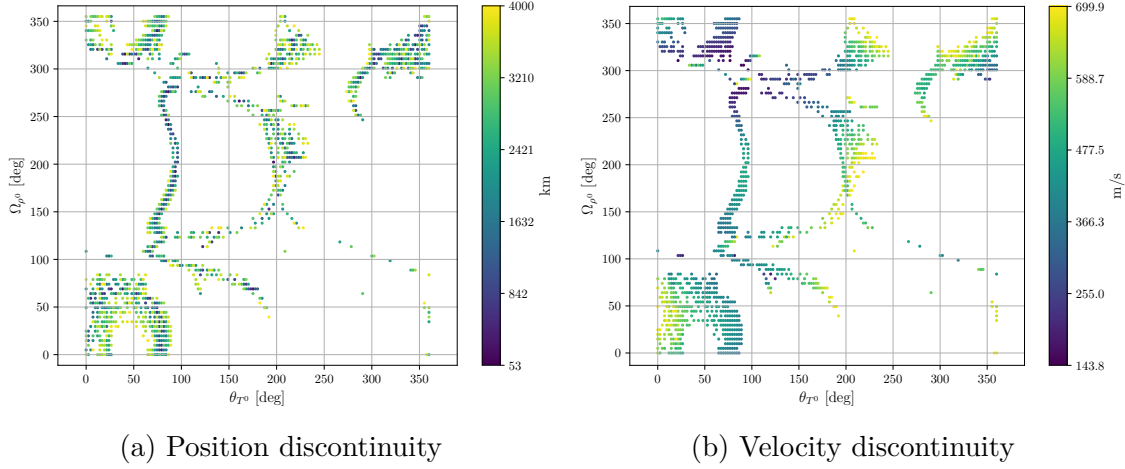


Figure 6.19. Position and velocity discontinuities between the stable manifold states associated with an L_2 quasi-vertical orbit ($\rho^0 = 0.42259$ rad) and the corresponding nearest departure orbit states.

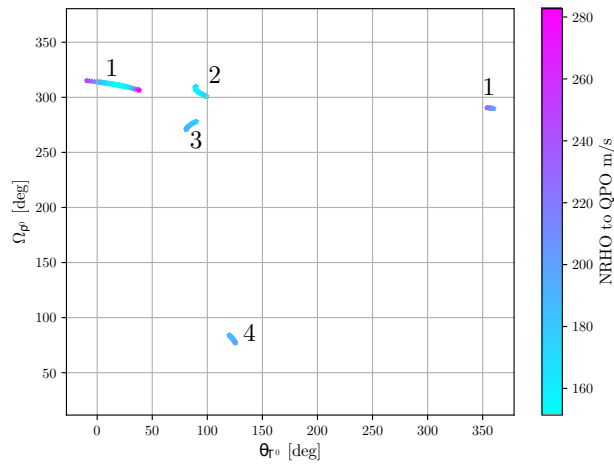


Figure 6.20. Differential corrected inbound segments to the arrival orbit constructed through the initial guess obtained in Figure 6.19 with an L_2 quasi-vertical orbit as the intermediate orbit .

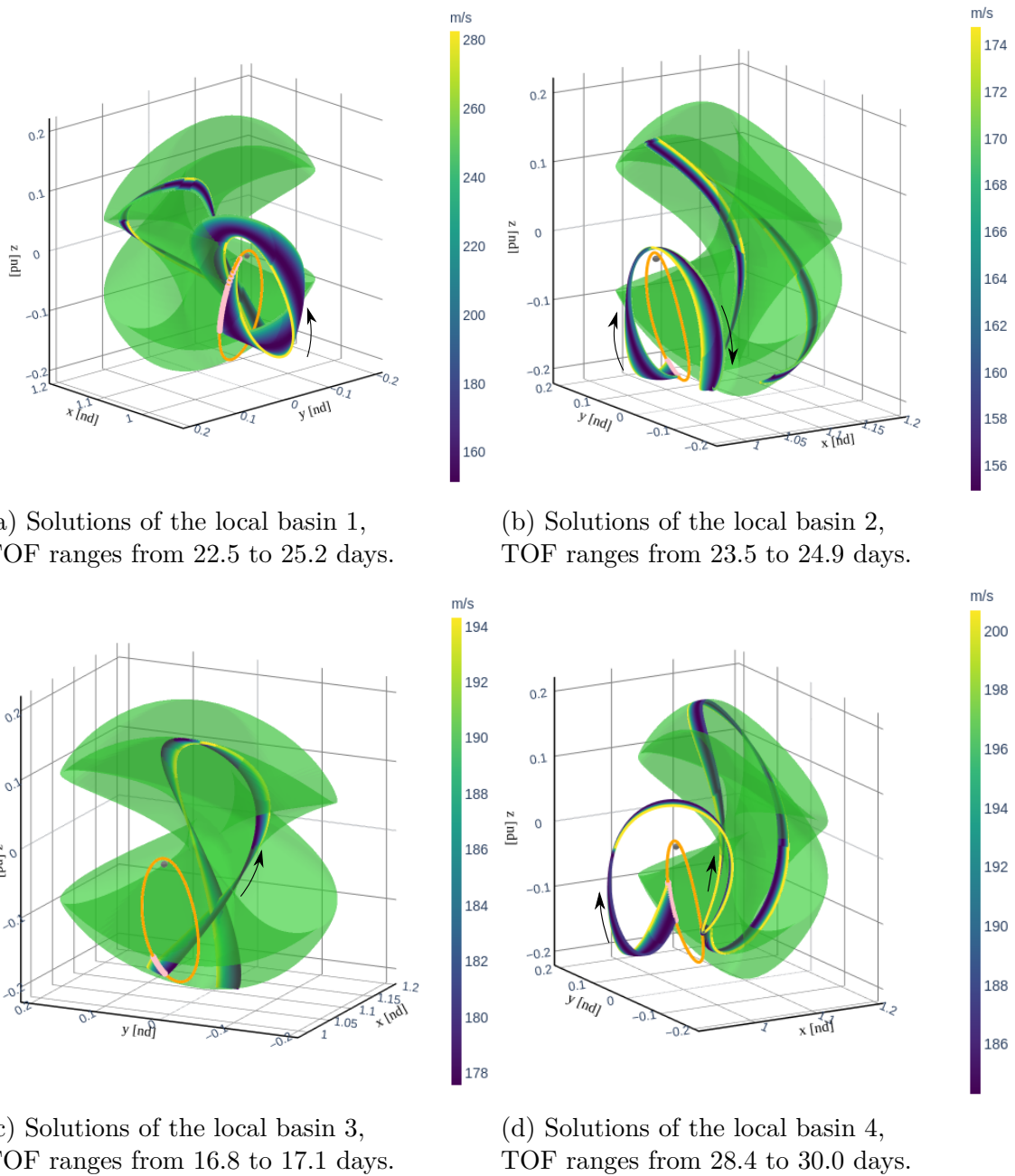


Figure 6.21. Transfer geometries corresponding to the local basin 1, 2, 3, and 4 as highlighted in Figure 6.20. The local solutions generated with an L_2 quasi-vertical orbit (green) as the intermediate orbit require a single maneuver (pink) to overcome the velocity discontinuity with the departure orbit state (orange).

6.5 Interior-type Transfers

The interior-type pathways between the departure periodic and arrival periodic orbit are generated by stitching an outbound segment from a departure orbit, a bridging arc, and an inbound segment to the arrival orbit. The construction of the three segments is informed by the stable and unstable manifolds associated with an intermediate orbit, as well as a trajectory arc on the intermediate orbit. The inbound and outbound geometries are generated through the initial guess and differential corrections strategy outlined in Section 6.3 and Section 6.4, respectively. The procedure to construct the bridging arc for an intermediate periodic/quasi-periodic orbit is defined in the following subsections. The three segments are differentially corrected for end-to-end full state continuity, such that the resultant pathway only requires a departure maneuver at a departure orbit state to jump onto the pathway and a maneuver to insert into the arrival orbit as depicted in Figure 6.1. The time of flight of the manifold arc, as well as the departure and arrival location on the departure and arrival periodic orbits, are allowed to vary during the corrections process. Subsequently, the constructed trajectories seed as an initial guess for the identification of locally mass-optimal solutions.

6.5.1 Intermediate Periodic Orbits

It is feasible to connect any inbound and outbound segment constructed by employing the stable and unstable manifold arcs associated with an intermediate periodic orbit through a bridging arc. An initial guess for a bridging arc is constructed by flowing the stable manifold state associated with the outbound segment from the departure orbit forward in time till the arc reaches the vicinity of the initial state of the inbound segment to the arrival orbit. The propagation time along an intermediate periodic orbit from a stable manifold to an unstable manifold step-off location, associated with the initial state of an outbound and inbound segment, respectively, approximates the flight time of the bridging arc. An estimate for the bridging arc flight time is computed as,

$$\mathfrak{T}_{\text{PO}} = \text{mod}(\mathbb{P}_{\text{int}} + \tau_{\text{int,arr}} - \tau_{\text{int,dep}}, \quad \mathbb{P}_{\text{int}}) \quad (6.20)$$

where, \mathfrak{T}_{PO} denotes the approximate flight time of the bridging arc, \mathbb{P}_{int} represents the period of an intermediate periodic orbit, $\tau_{\text{int,arr}}$ and $\tau_{\text{int,dep}}$ represent the propagation time from an initial state on the intermediate orbit till the unstable and stable manifold step-off locations. The modulo operator, mod, ensures that the bridging arc flight time does not exceed the period of the intermediate orbit. The initial guess for the bridging arc is full-state continuous with the outbound segment from the departure orbit as it is constructed by forward propagating the stable manifold state, ${}_s\bar{x}_{\tau_{\text{int,dep}}}$, for time \mathfrak{T}_{PO} . However, the downstream state on the bridging arc at time \mathfrak{T}_{PO} is discontinuous but in the vicinity of ${}_u\bar{x}_{\tau_{\text{int,arr}}}$ state. A differential correction scheme as elucidated for the construction of interior-type end-to-end transfer is employed to overcome the discontinuity between the bridging arc and ${}_u\bar{x}_{\tau_{\text{int,arr}}}$ state to result in a full-state continuous pathway that connects the departure and arrival orbit in the configuration space.

The aforementioned procedure uncovers end-to-end transfer options informed by the stable and unstable manifold arcs associated with an L_2 vertical, an L_2 southern halo, a P2HO₁ and a P2HO₂ orbit. The outbound and inbound segments generated through the manifolds associated with an L_2 vertical orbit are cataloged in Figures 6.15 and 6.18. The method leveraged to construct inbound and outbound segments through an L_2 vertical orbit as outlined in Sections 6.3 and 6.4 is employed for other intermediate periodic orbits of interest. The resultant solutions associated with an L_2 southern halo, a P2HO₁ and a P2HO₂ orbit are depicted in Figures 6.22 to 6.24 and the associated maneuver costs and flight times are provided in Tables 6.5 to 6.10. The end-to-end transfer geometries are constructed by pairing any inbound and outbound segment constructed through a common intermediate periodic orbit. The lowest maneuver cost inbound and outbound segments computed by each of the four selected intermediate periodic orbit are linked to obtain the corrected end-to-end transfers presented in Figure 6.25. The described framework allows for the selection of any inbound and outbound segment constructed via a common intermediate periodic orbit to generate two maneuver end-to-end transfer arcs.

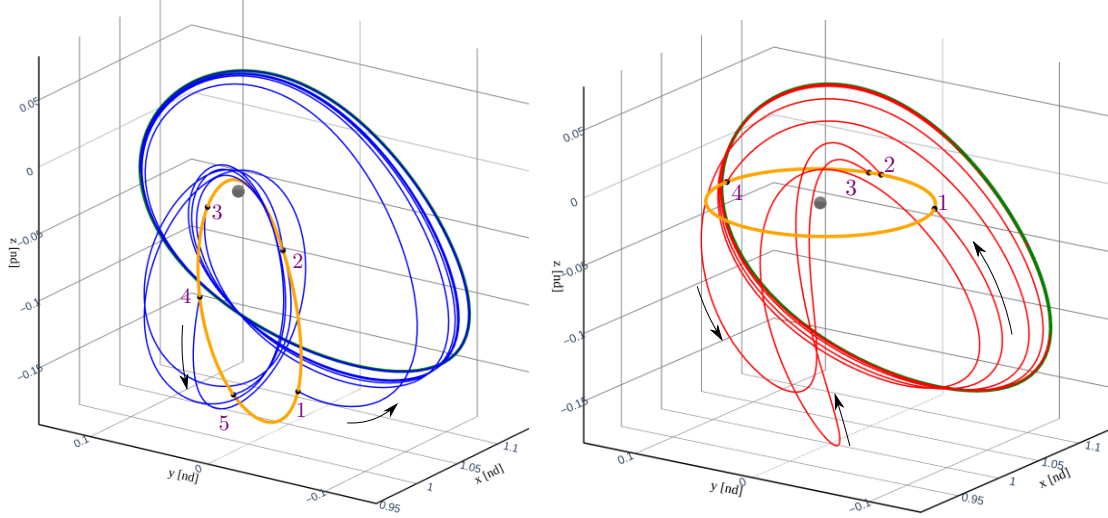


Figure 6.22. Five converged outbound segments (blue) from an L_2 NRHO (orange) and four inbound segments (red) to a DRO (orange) informed by the initial guess generated through an L_2 southern halo orbit (green). The transfer arcs require a single impulsive maneuver (black) to overcome the velocity discontinuity with the departure/arrival orbit. The departure and arrival maneuver costs and flight times are tabulated in Table 6.5 and Table 6.6, respectively.

Table 6.5. Maneuver costs and times of flight of the outbound transfer options, depicted in Figure 6.22(a), constructed with an L_2 southern halo orbit as the intermediate orbit.

Transfer arc	ΔV_{dep} (m/s)	TOF (days)
1	342.742	21.117
2	108.308	29.615
3	179.463	22.550
4	101.231	33.768
5	211.538	24.390

Table 6.6. Maneuver costs and times of flight of the inbound transfer options, depicted in Figure 6.22(b), constructed with an L_2 southern halo orbit as the intermediate orbit.

Transfer arc	ΔV_{arr} (m/s)	TOF (days)
1	694.607	17.916
2	641.154	23.705
3	611.532	27.148
4	646.734	17.979

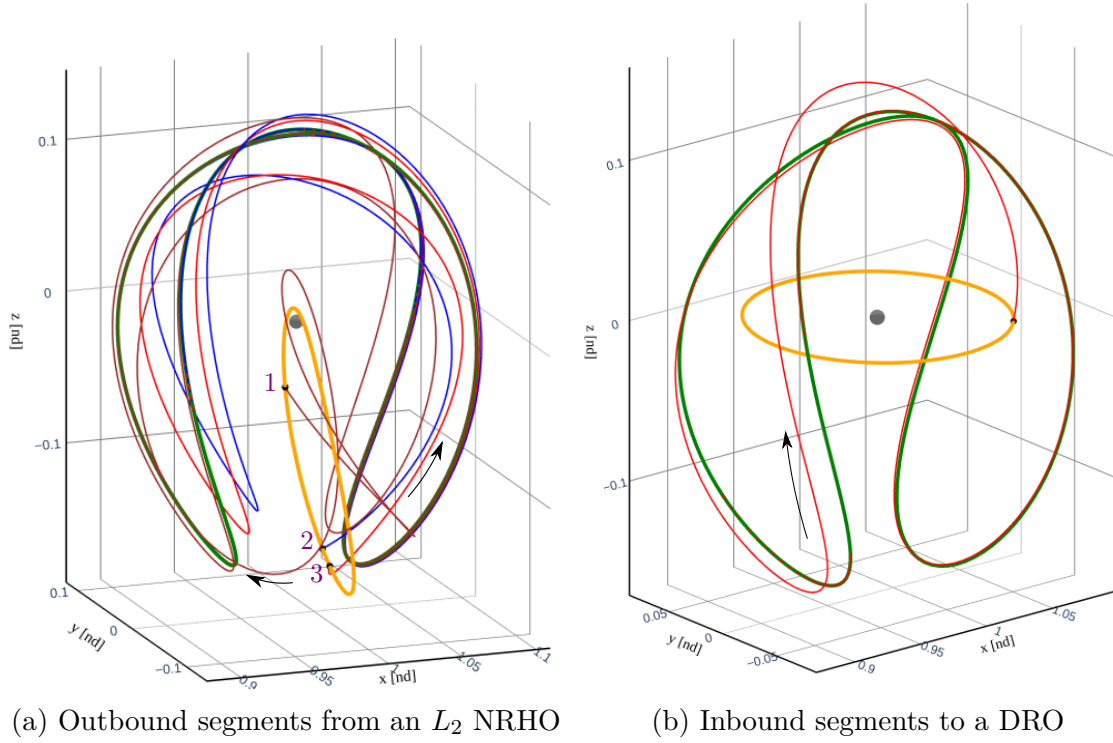


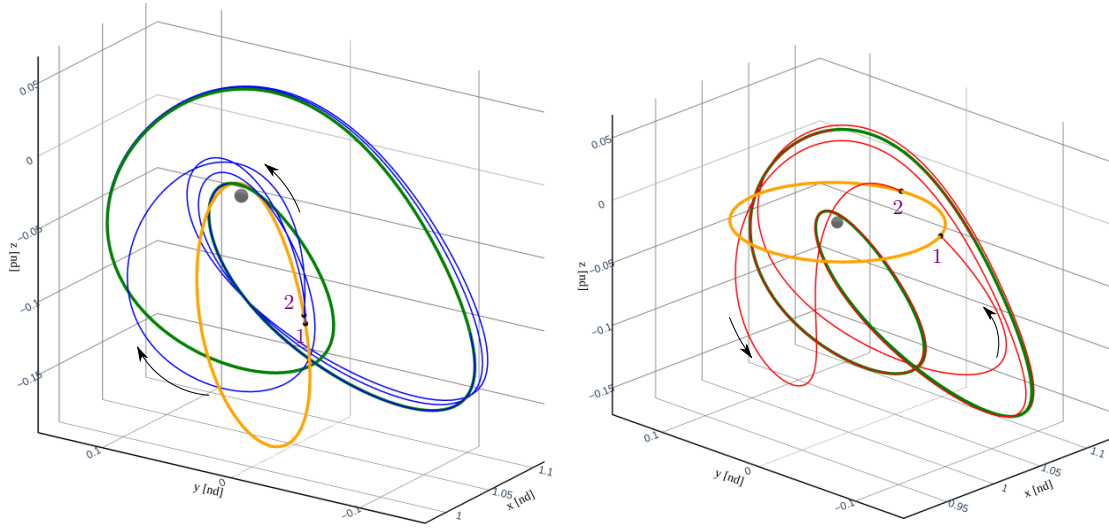
Figure 6.23. Two converged outbound segments (red, blue) from an L_2 NRHO and an inbound segment to a DRO (orange) informed by the initial guess generated through an L_2 P2HO₁ orbit (green). The transfer arcs require a single impulsive maneuver (black) to overcome the velocity discontinuity with the departure/arrival orbit. The departure and arrival maneuver costs and flight times are tabulated in Table 6.7 and Table 6.8, respectively.

Table 6.7. Maneuver costs and times of flight of the outbound transfer options, depicted in Figure 6.23(a), constructed with an L_2 P2HO₁ orbit as the intermediate orbit.

Transfer arc	ΔV_{dep} (m/s)	TOF (days)
1	272.479	50.711
2	280.325	47.761
2	204.387	40.953

Table 6.8. Maneuver costs and times of flight of the inbound transfer options, depicted in Figure 6.23(b), constructed with an L_2 P2HO₁ orbit as the intermediate orbit.

Transfer arc	ΔV_{arr} (m/s)	TOF (days)
1	639.140	33.531



(a) Outbound segments from the L_2 NRHO

(b) Inbound segments to the DRO

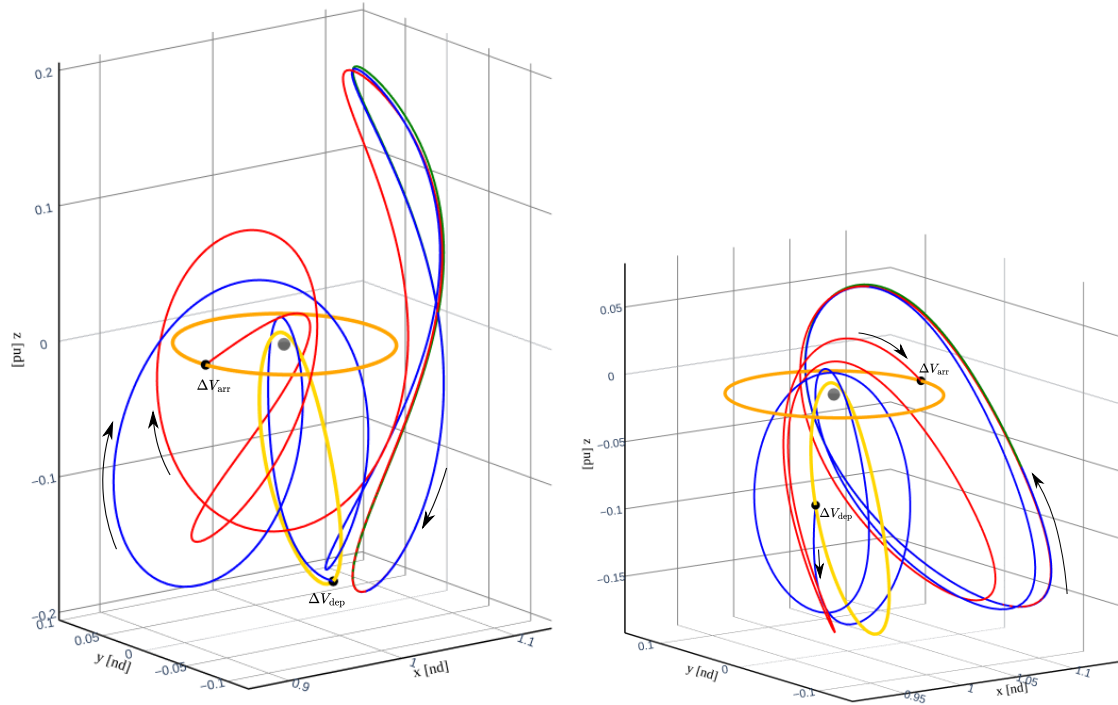
Figure 6.24. Two converged outbound segments (blue) from an L_2 NRHO (orange) and two inbound segments (red) to the DRO (orange) informed by the initial guess generated through an L_2 P2HO₂ orbit (green). The transfer arcs require a single impulsive maneuver (black) to overcome the velocity discontinuity with the departure/arrival orbit. The departure and arrival maneuver costs and flight times are tabulated in Table 6.9 and Table 6.10, respectively.

Table 6.9. Maneuver costs and times of flight of the outbound transfer options, depicted in Figure 6.24(a), constructed with an L_2 P2HO₂ orbit as the intermediate orbit.

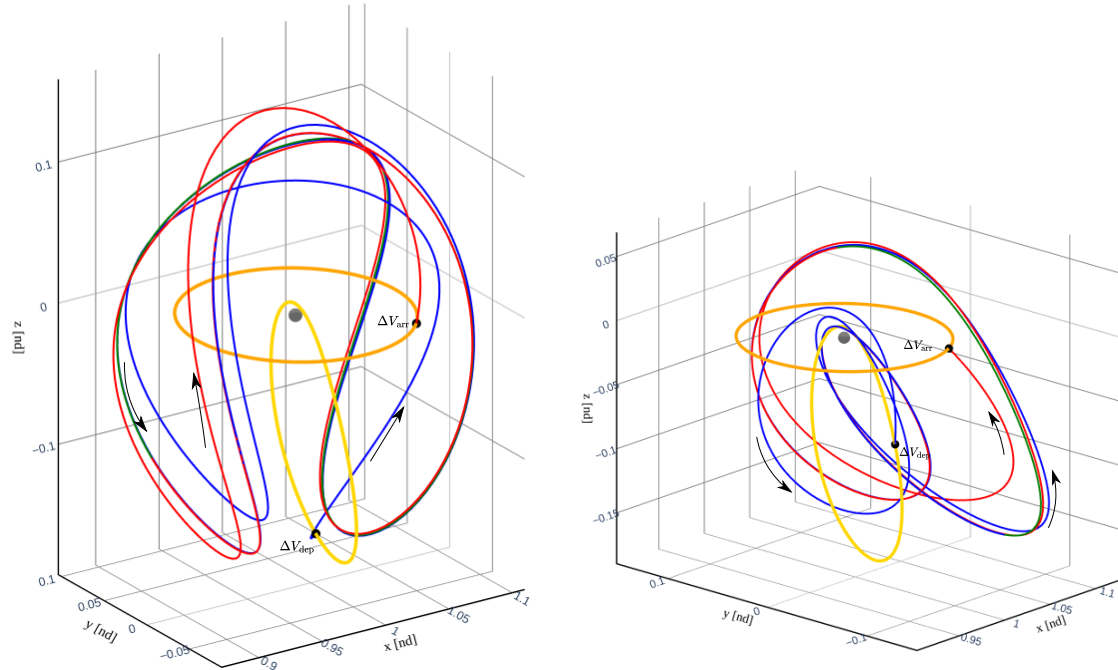
Transfer arc	ΔV_{dep} (m/s)	TOF (days)
1	119.847	26.813
2	103.394	30.331

Table 6.10. Maneuver costs and times of flight of the inbound transfer options, depicted in Figure 6.24(b), constructed with an L_2 P2HO₂ orbit as the intermediate orbit.

Transfer arc	ΔV_{arr} (m/s)	TOF (days)
1	669.800	27.708
2	602.450	28.380



(a) Informed by an L_2 vertical orbit, $\Delta V_{\text{tot}} = \Delta V_{\text{dep}} + \Delta V_{\text{arr}} = 197.810 + 535.494 = 733.304$ m/s, TOF = 75.745 days
(b) Informed by an L_2 southern halo orbit, $\Delta V_{\text{tot}} = \Delta V_{\text{dep}} + \Delta V_{\text{arr}} = 101.233 + 611.532 = 712.765$ m/s, TOF = 67.571 days



(c) Informed by an L_2 P2HO₁ orbit, $\Delta V_{\text{tot}} = \Delta V_{\text{dep}} + \Delta V_{\text{arr}} = 204.362 + 639.492 = 843.853$ m/s, TOF = 88.742 days
(d) Informed by an L_2 P2HO₂ orbit, $\Delta V_{\text{tot}} = \Delta V_{\text{dep}} + \Delta V_{\text{arr}} = 103.387 + 602.444 = 708.831$ m/s, TOF = 64.946 days

Figure 6.25. Interior-type end-to-end transfers informed by intermediate periodic orbits. The blue, green and red colored portions of the full-state continuous trajectory are post differential correction remanants of the initial guess of the three segments.

6.5.2 Intermediate Quasi-Periodic Orbits

For the construction of a low maneuver cost and reasonable TOF end-to-end transfer, select inbound and outbound segments designed through the unstable and stable manifold arcs associated with an intermediate QPO are stitched together by leveraging the natural flow along the QPO. The non-repeatable nature of the QPOs narrows the selection of inbound and outbound arcs to options with an initial inbound state that lies in the immediate upstream or downstream of a final outbound segment state. The angular variable representation of the step-off location of the stable and unstable manifold arcs that define the outbound segment and inbound segment, respectively, assist in the identification of segment pairings that are linked by a short TOF bridging arc. A strategy is devised to design a bridging arc informed by the innate flow of the intermediate QPO to connect an inbound and outbound segment.

The construction of a bridging arc is elucidated by considering an L_2 quasi-vertical orbit, $\rho = 0.4559$ rad = 26.1211 deg, as the intermediate QPO. Consider $\bar{x}_{\text{int,dep}}$ and $\bar{x}_{\text{int,arr}}$ states represent the step-off location of the stable and unstable manifold arcs that define the outbound segment and inbound segment, respectively. A $\bar{x}_{\text{int,arr}}$ state that lies in the vicinity of the immediate downstream of a $\bar{x}_{\text{int,dep}}$ state assists in the construction of a desirable bridging arc. The differentially corrected families of inbound and outbound segments computed via the manifold arcs associated with a quasi-vertical orbit, Figures 6.16 and 6.21, are overlaid on a single plot, as depicted in Figure 6.26, for the identification of suitable segment pairings, $\bar{x}_{\text{int,dep}}$ and $\bar{x}_{\text{int,arr}}$ state. It is evident from Figure 6.26 that the states: $\bar{x}_{\text{int,dep}}$ and $\bar{x}_{\text{int,arr}}$ are parameterizable as $(\theta_{T^0,\text{dep}}, \Omega_{\rho^0,\text{dep}})$ and $(\theta_{T^0,\text{arr}}, \Omega_{\rho^0,\text{arr}})$, respectively. The candidate $\bar{x}_{\text{int,dep}}$ and $\bar{x}_{\text{int,arr}}$ states are identified by leveraging the following expression,

$$\Omega_{\rho^0,\text{arr}} \approx \text{mod}(\Omega_{\rho^0,\text{dep}} + n_{\text{rev}}\rho^0, 2\pi) \quad (6.21)$$

where, n_{rev} is a positive integer number that represents the number of revolutions around a QPO that an $\bar{x}_{\text{int,dep}}$ state is propagated to attain the desirable $\Omega_{\rho^0,\text{arr}}$ value. The selection of $\bar{x}_{\text{int,dep}}$ and $\bar{x}_{\text{int,arr}}$ states parameterized by $\Omega_{\rho^0,\text{dep}}$ and $\Omega_{\rho^0,\text{arr}}$, respectively, is biased to

satisfy the Equation (6.21) with a small value of n_{rev} to uncover a bridging arc with a short TOF. For an identified value of n_{rev} , the TOF of the bridging arc is estimated as,

$$\tau_{QPO} = \frac{T^0}{2\pi}(\theta_{T^0, \text{arr}} - \theta_{T^0, \text{dep}}) + n_{rev}T^0 \quad (6.22)$$

where, τ_{QPO} denotes the TOF of the bridging arc. For a quasi-vertical orbit, a pair of $\bar{x}_{\text{int},\text{dep}}$ and $\bar{x}_{\text{int},\text{arr}}$ are selected and the two states are linked by a bridging arc with $n_{rev} = 1$ as illustrated in Figure 6.26. An initial guess for the bridging arc is formulated by propagating a stable manifold state associated with the $\bar{x}_{\text{int},\text{dep}}$ state, $s\bar{x}_{\text{int},\text{dep}}$, forward in time for τ_{QPO} . The resultant outbound segment, bridging arc, and inbound segment are differentially corrected, by employing the aforementioned scheme, in order to obtain a full-state continuous end-to-end transfer arc. The shooting method reveals an interior-type transfer plotted in Figure 6.27 for the selected segments designed through a quasi-vertical orbit.

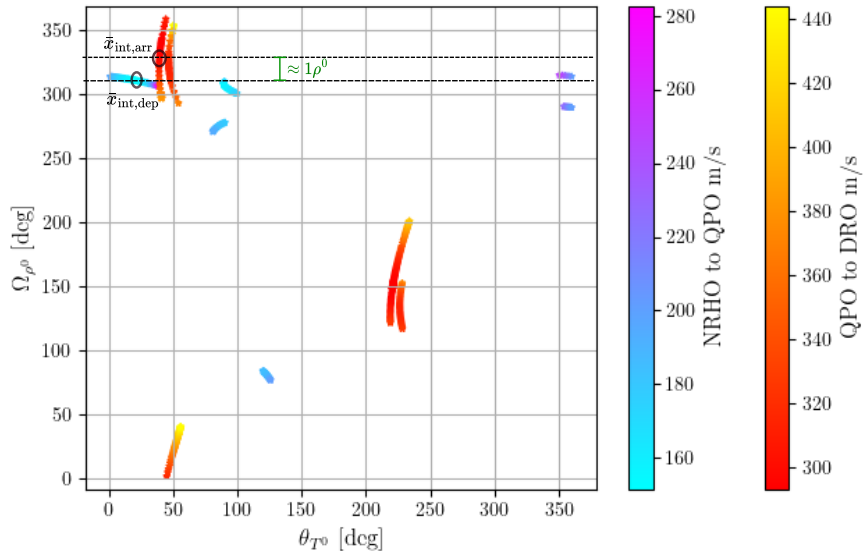


Figure 6.26. Angular variable representation of stable and unstable manifold step-off locations corresponding to families of differentially corrected outbound and inbound segments constructed through an L_2 quasi-vertical orbits. A candidate $\bar{x}_{\text{int},\text{arr}}$ state is identified that lies 1 revolution of the intermediate QPO downstream from a $\bar{x}_{\text{int},\text{dep}}$ state.

An alternate approach to design end-to-end transfer is employed if a short TOF bridging arc does not exist and a $\bar{x}_{\text{int},\text{arr}}$ state lies in the immediate upstream of a $\bar{x}_{\text{int},\text{dep}}$ state.

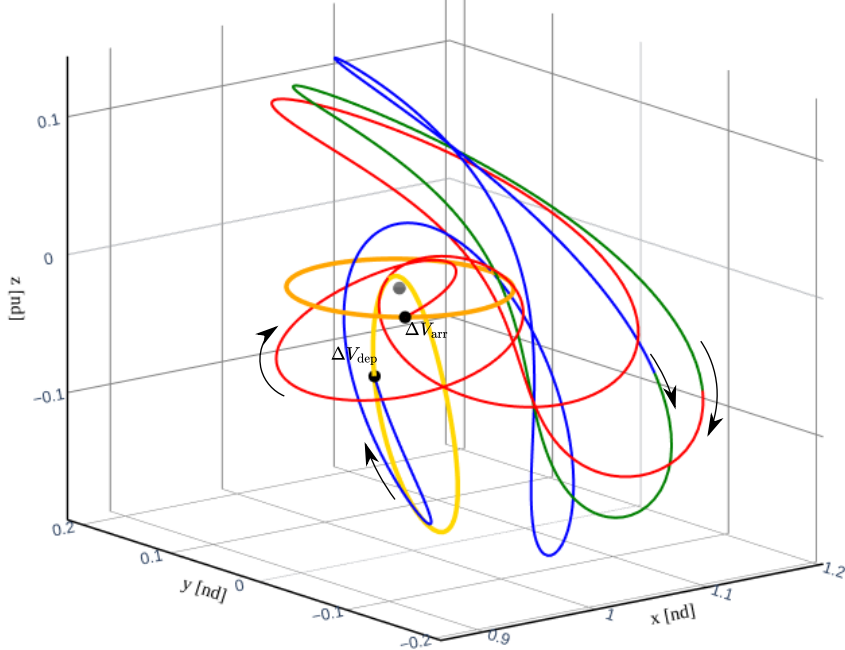


Figure 6.27. Interior-type end-to-end transfer informed by an L_2 quasi-vertical orbit. The blue, green, and red colored portions of the full-state continuous trajectory are post differential correction remanants of the initial guess of the three segments, $\Delta V_{\text{tot}} = \Delta V_{\text{dep}} + \Delta V_{\text{arr}} = 153.213 + 292.010 = 445.223$ m/s, TOF = 69.938 days

Consider an L_2 quasi-P2HO₂ orbit, $\rho^0 = 1.59185$ rad = 91.20624 deg and $T^0 = 18.67584$ days, as visualized in Figure 6.7. Outbound segments from the departure orbit and inbound segments to the arrival orbit informed by the manifold arcs associated with a quasi-P2HO₂ orbit are constructed through the procedures described in Sections 6.3 and 6.4. A few families of differentially corrected segments that maintain a preilune distance greater than the radius of the Moon are depicted in Figure 6.28. It is apparent that no $\bar{x}_{\text{int},\text{arr}}$ state lies within three revolutions ≈ 56.025 days of a trajectory propagated forward from $\bar{x}_{\text{int},\text{dep}}$. Hence, a short TOF bridging arc is complicated to construct, however, a $\bar{x}_{\text{int},\text{arr}}$ state as identified in Figure 6.28 lies in the vicinity of a quasi-periodic trajectory generated by back propagating $\bar{x}_{\text{int},\text{dep}}$ for a single revolution. The outbound and inbound segments corresponding to the selected $\bar{x}_{\text{int},\text{dep}}$ and $\bar{x}_{\text{int},\text{dep}}$ states are visualized in Figure 6.29. It is evident from the Figure 6.29 that the two segments follow along a common pathway as the outbound segment approaches the QPO and inbound segment departs the QPO. Hence, it is feasible

to connect the segments by modifying the TOF of the segments, such that the end state of the outbound segment lies in the vicinity of the initial state of the inbound segment. The computation of the end-to-end transfer in this scenario does not require a bridging arc and the aforementioned differential corrections scheme to obtain a continuous pathway that links the departure and arrival orbit is employed to construct the transfer geometry informed by a quasi-P2HO₂ orbit as plotted in Figure 6.30. Unlike the outbound and inbound segments designed via an intermediate periodic orbit, it is infeasible to determine maneuver-free short TOF bridging arc to link any outbound and with any inbound segment constructed through an intermediate QPO. Nevertheless, the two presented strategies illustrated via an L_2 quasi-vertical orbit and an L_2 quasi-P2HO₂ orbit allows for the identification of candidate segments to design end-to-end transfers. The alternate geometries uncovered through the use of an intermediate QPO expand the known local solution basins of end-to-end transfers. In general, the inbound and outbound segments, as well as the presented end-to-end transfers derived from an L_2 quasi-vertical and an L_2 quasi-P2HO₂ orbit yield lower maneuver cost solutions compared to the ones constructed from their underlying periodic orbits.

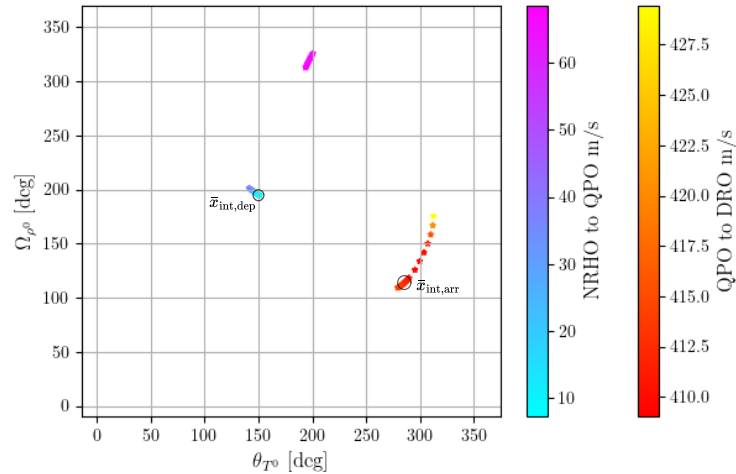


Figure 6.28. Angular variable representation of stable and unstable manifold step-off locations corresponding to families of differentially corrected outbound and inbound segments constructed through an L_2 quasi-P2HO₂ orbits. A candidate $\bar{x}_{\text{int},\text{arr}}$ state is identified that lies in the immediate upstream of a $\bar{x}_{\text{int},\text{dep}}$ state.

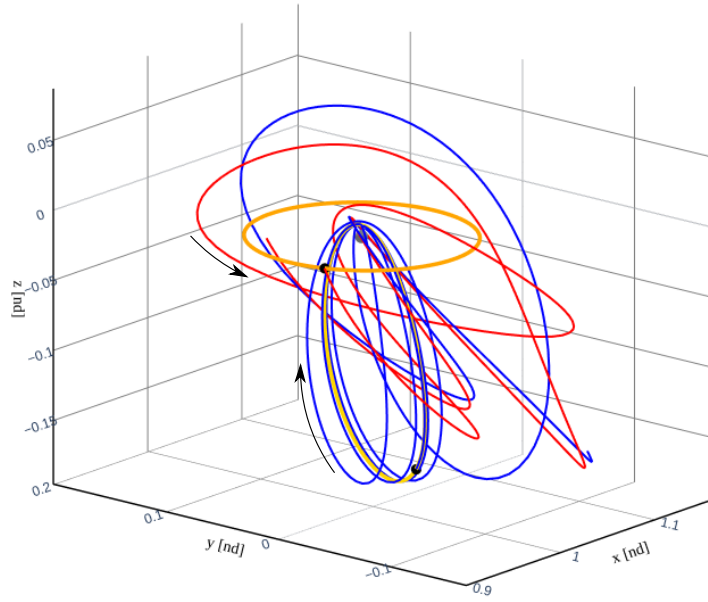


Figure 6.29. Plot of an outbound and inbound segment corresponding to the selected $\bar{x}_{\text{int,dep}}$ and $\bar{x}_{\text{int,dep}}$ states in Figure 6.28.

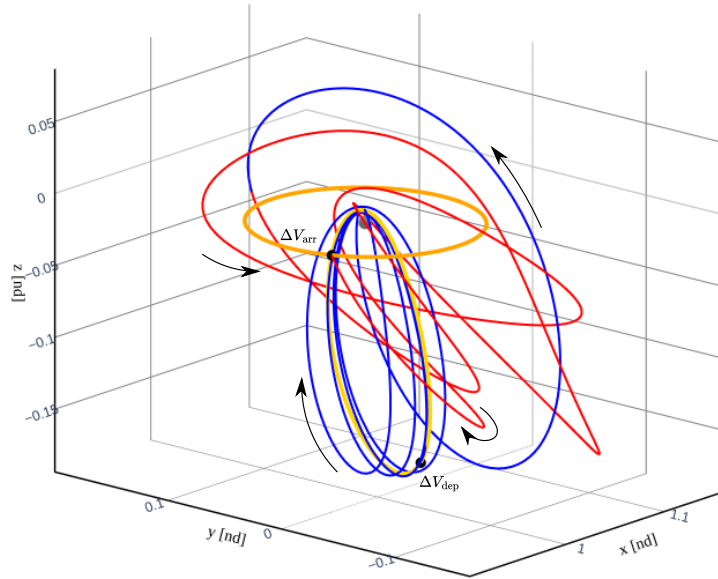


Figure 6.30. Interior-type end-to-end transfer informed by an L_2 quasi-P2HO₂ orbit. The blue and red colored portions of the full-state continuous trajectory are post differential correction remanants of the initial guess of the two segments, $\Delta V_{\text{tot}} = \Delta V_{\text{dep}} + \Delta V_{\text{arr}} = 7.815 + 473.403 = 481.217$ m/s, TOF = 73.944 days.

6.5.3 Optimized Transfers

The differentially corrected interior-type end-to-end geometries characterized by the selected intermediate orbits assist in the recognition of multiple local solution basins of the design problem and seed as the initial guess to identify locally mass-optimal solutions. The feasible end-to-end geometries presented in Figures 6.25, 6.27 and 6.30 comprise of reasonable maneuver costs and TOFs, and assist in generating lower maneuver cost transfers. A constrained direct optimization scheme, specifically IPOPT, is employed with an objective function that minimizes $|\Delta V_{\text{dep}}|^2 + |\Delta V_{\text{arr}}|^2$ to compute locally mass-optimal solutions [71]. The TOF of a pathway, and departure and arrival locations on the departure and arrival orbits, respectively, are allowed to vary during the optimization process. Additionally, multiple patch points along the continuous transfer trajectory are leveraged to reduce the propagation time. The patch points assist in ameliorating the detrimental effects of dynamical and numerical sensitivities encountered during the optimization process. Full-state continuity is enforced between the patch points, while only position continuity is incorporated between a departure orbit state and the initial state of the transfer, as well as between the final state of the transfer and an arrival orbit state. Hence, the resultant geometries only comprise a departure and an arrival maneuver.

The devised optimization scheme is demonstrated for an initial guess of an end-to-end transfer constructed through an intermediate periodic and an intermediate quasi-periodic orbit. An end-to-end transfer characterized by an L_2 P2HO₂ orbit as depicted in Figure 6.25(d) is optimized by employing the described procedure and it uncovers a lower cost solution presented in Figure 6.31. Similarly, a solution informed by an L_2 quasi-vertical orbit, Figure 6.27, is optimized to construct a locally mass-optimal geometry visualized in Figure 6.32. The presented systematic framework allows for the identification of various local solution basins characterized by the selection of an intermediate orbit, and the described shooting method and the optimization scheme assist in constructing locally mass-optimal interior-type end-to-end transfers.

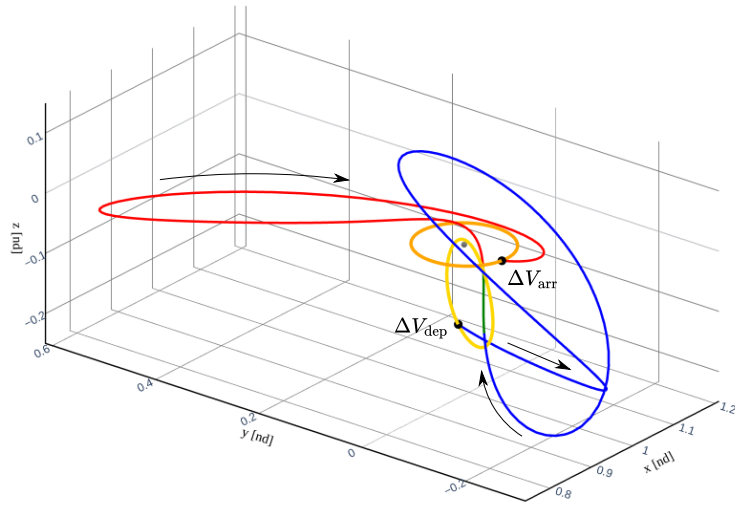


Figure 6.31. Interior-type end-to-end locally mass-optimal transfer initialized by a feasible solution, Figure 6.25(d), that is characterized by an L_2 $P2HO_2$ orbit. The blue, green and red colored portions of the full-state continuous trajectory are post-optimization remanants of the three colored arcs along the initial guess, $\Delta V_{\text{tot}} = \Delta V_{\text{dep}} + \Delta V_{\text{arr}} = 232.164 + 231.569 = 463.733$ m/s, TOF = 45.314 days.

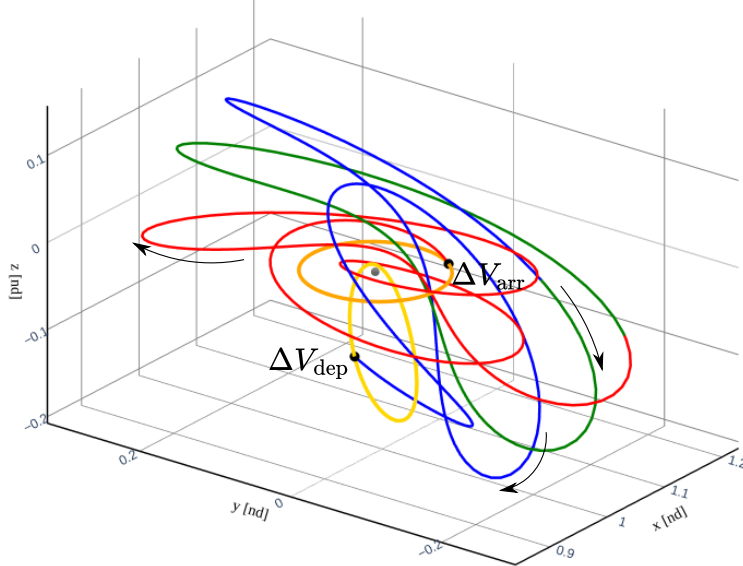


Figure 6.32. Interior-type end-to-end locally mass-optimal transfer initialized by a feasible solution, Figure 6.27, that is characterized by an L_2 quasi-vertical orbit. The blue, green and red colored portions of the full-state continuous trajectory are post-optimization remanants of the three colored arcs along the initial guess, $\Delta V_{\text{tot}} = \Delta V_{\text{dep}} + \Delta V_{\text{arr}} = 220.288 + 141.960 = 362.245$ m/s, TOF = 82.448 days.

6.6 Exterior-type Transfers

Exterior-type end-to-end transfers link the departure and arrival orbit via pathways that traverse the far-side of the Earth, and their design is informed by the dynamical structures characterized by two intermediate orbits as depicted in Figure 6.2. The design of a transfer highway is initiated through the identification of six segments: an outbound segment from the departure orbit to the first intermediate orbit, a bridging arc along the first intermediate orbit, a segment from the first intermediate orbit to the far-side of the Earth (IO1Earth), a segment from the far-side of the Earth to a second intermediate orbit (EarthIO2), a bridging arc along the second intermediate orbit, and an inbound segment to the arrival orbit from the second intermediate orbit. The potential candidates for the six segments suffice as the initial guess for the design of three maneuver end-to-end transfers.

The strategy to design each segment is elucidated and illustrated for an L_2 vertical, an L_2 quasi-vertical, an L_2 P2HO₂, and an L_2 quasi-P2HO₂ orbit as the first intermediate orbit, and a planar 3:4 RPO and a DPO as the second intermediate orbit. Important parameters associated with the selected intermediate orbits are listed in Section 6.2. The procedure to construct an outbound segment from the departure orbit and an inbound segment to the arrival orbit is the same as outlined in Sections 6.3 and 6.4. The outbound segments from an NRHO to an L_2 vertical, an L_2 quasi-vertical, an L_2 P2HO₂, and an L_2 quasi-P2HO₂ are depicted in Figures 6.18, 6.20, 6.24(a) and 6.28, respectively. The inbound segments to a DRO from an RPO and a DPO are constructed through the strategy presented in Section 6.3 and targeted segments are plotted in Figures 6.33 and 6.34, respectively. The associated transfer costs and TOFs are provided in Table 6.11 and Figure 6.34. The selection of outbound and inbound segments for end-to-end transfer design is delinked, unlike a scenario where an intermediate QPO is employed for interior-type transfer design, Section 6.5.2.

An initial guess for IO1Earth and EarthIO2 segments are identified from the unstable and stable manifold arcs associated with the first and second intermediate orbits, respectively, that reach the far-side of the Earth. If an intermediate orbit is a QPO then a subset of the unstable/stable global manifolds associated with the orbit are employed. The solution space offered by the *3-dimensional* manifolds associated with a QPO is reduced to

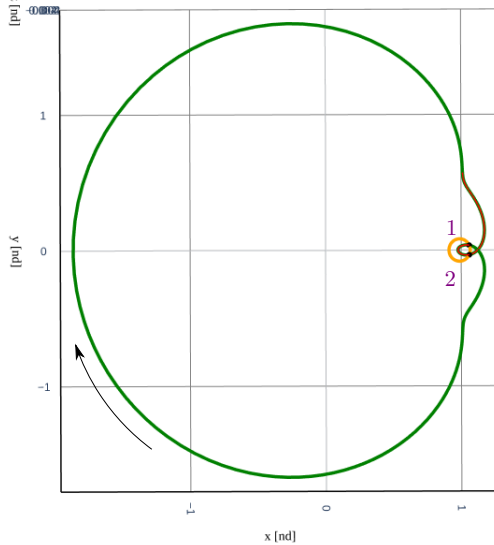


Figure 6.33. Two converged inbound segments (red) to the DRO (orange) informed by the initial guess generated through a planar 3:4 RPO (green). The transfer arcs require a single impulsive maneuver (black) to overcome the velocity discontinuity with the arrival orbit. The maneuver costs and flight times are tabulated in Table 6.11.

Table 6.11. Maneuver costs and times of flight of the two transfer options, depicted in Figure 6.33, constructed with a planar 3:4 RPO as the intermediate orbit.

Transfer arc	ΔV_{arr} (m/s)	TOF (days)
1	442.657	13.097
2	442.734	12.417

Table 6.12. Maneuver costs and times of flight of the two transfer options, depicted in Figure 6.34, constructed with a DPO as the intermediate orbit.

Transfer arc	ΔV_{arr} (m/s)	TOF (days)
1	366.728	20.057
2	653.222	29.452

assist in devising a straightforward strategy to design a bridging arc along the intermediate QPO. Hence, the manifolds associated with the QPO states that lie n_{rev} downstream/upstream from $\bar{x}_{\text{int,dep}}/\bar{x}_{\text{int,arr}}$ corresponding to an outbound/inbound segment designed with a QPO as the first/second intermediate orbit are considered for the initial guess genera-

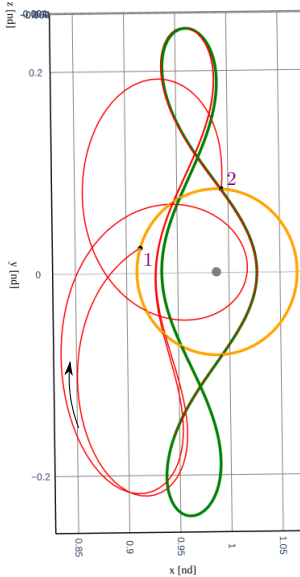


Figure 6.34. Two converged inbound segments (red) to the DRO (orange) informed by the initial guess generated through a DPO (green). The transfer arcs require a single impulsive maneuver (black) to overcome the velocity discontinuity with the arrival orbit. The maneuver costs and flight times are tabulated in Table 6.12.

tion of IO1Earth/EarthIO2 segment. Recall, n_{rev} is defined as a small positive integer that represents the number of revolutions of a quasi-periodic trajectory along a QPO. No such reduction in solution space is needed for manifolds associated with an intermediate periodic orbit. A Poincaré map with hyperplane at $y = 0$ is employed to capture the first crossing of stable and unstable manifold arcs on the far-side side of the Earth as exemplified in Figure 6.35 for an L_2 vertical orbit as the first intermediate orbit. After the determination of the hyperplane crossings, a K-Nearest Neighbors (KNN) algorithm is leveraged to recognize an unstable and a stable manifold arc that suffice as a good initial guess for IO1Earth and EarthIO2 segments, similar to the approach detailed by Pritchett [13] and LaFarge [72]. Six parameters associated with the position and velocity components of the unstable and stable states on the hyperplane populate the search space for the algorithm and the position components are scaled by a factor of 10. The L2 norm of the difference between the six components of the scaled unstable and stable states is utilized as the search criteria for the KNN algorithm to deliver potential candidates for IO1Earth and EarthIO2 segments.

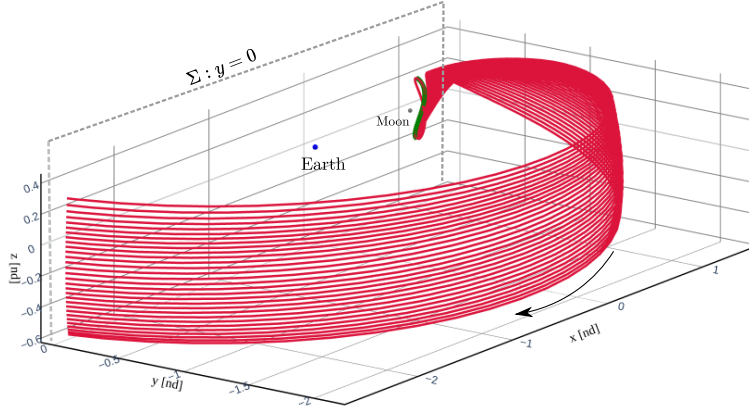


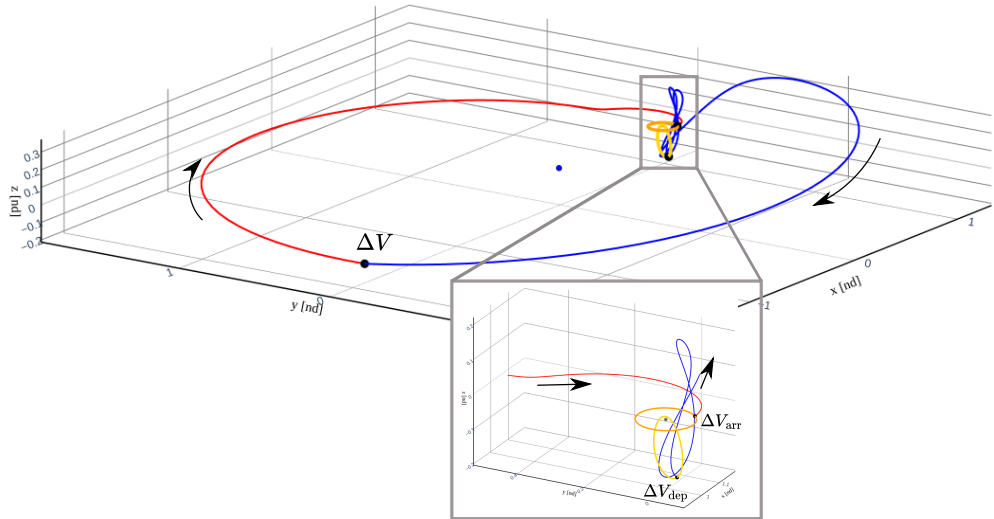
Figure 6.35. Unstable manifolds (red) associated with an L_2 vertical orbit (green) propagated till the first crossing of a Poincaré map at $y=0$ on the far-side of the Earth.

The construction of the bridging arcs to link an outbound segment with an IO1Earth segment, and an EarthIO2 segment with an inbound segment leverages the natural flow along the intermediate orbit. The selection of an approaching segment to an intermediate orbit does not influence the choice of a departing segment from the intermediate orbit, and vice versa. Hence, the framework offers greater control over the selection of intermediate segments for the design of an end-to-end transfer. An initial guess for the bridging arc is generated by flowing the stable manifold state associated with a segment approaching an intermediate orbit forward in time till the arc reaches the vicinity of the unstable manifold state corresponding to a departing segment. A reasonable TOF of the bridging arc is determined by the time it takes for the stable step-off state on the orbit associated with an approaching segment to reach the unstable step-off state corresponding to a departing segment. Since the solution space to design IO1Earth/EarthIO2 by using the unstable/stable manifold arcs associated with an intermediate QPO was reduced to step-off states that are n_{rev} downstream/upstream from the outbound/inbound segment, the TOF of the bridging arc along the QPO is known to be less than $T^0 n_{rev}$. Hence, a small value of n_{rev} is desired for a short TOF bridging arc. The six segments generated through the aforementioned strategy are differentially corrected and optimized for the construction of exterior-type end-to-end trajectories.

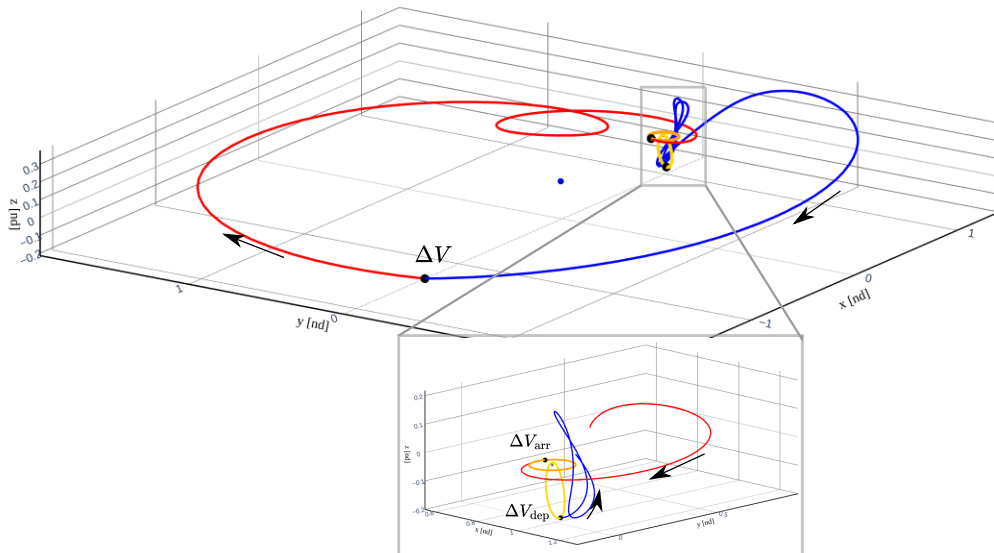
A shooting method is employed to construct position continuous exterior-type solutions that comprise three velocity discontinuities by linking the identified six segments. The de-

parture and arrival locations on the departure and arrival periodic orbits, respectively, along with the TOF of the segments are allowed to vary during the corrections process. Full-state continuity is enforced between the six segments, except between IO1Earth and EarthIO2 segments where only position continuity is imposed. The resultant geometry is full-state continuous, except for the departure location, far-side of the Earth, and arrival location, where the velocity discontinuities are overcome through impulsive maneuvers. The motivation behind employing an additional maneuver on the far-side of the Earth compared to the interior-type geometry is to identify solutions with potentially lower maneuver costs. The described scheme is leveraged to computed end-to-end transfers informed by the following pairs of intermediate orbits: L_2 vertical orbit - 3:4 RPO, L_2 quasi-vertical orbit - 3:4 RPO, L_2 P2HO₂ orbit - DPO, and L_2 quasi-P2HO₂ orbit - DPO. Exterior-type end-to-end transfers influenced by the four selected pairs of intermediate orbits are plotted in Figures 6.36(a), 6.37(a), 6.38(a) and 6.39(a). It is apparent from the presented results that the the solutions informed by intermediate QPOs result in lower maneuver cost options than the ones leveraging their underlying periodic orbits. The corrected end-to-end transfers derived by two intermediate orbits are optimized to uncover locally mass-optimal geometries.

The differentially corrected end-to-end transfers are optimized for the recognition of locally mass-optimal solutions. A methodology similar to the one employed in Section 6.5.3 is leveraged for the optimization of exterior-type transfers. An interior point method, IPOPT, with a cost function given as $|\Delta V_{\text{dep}}|^2 + |\Delta V|^2 + |\Delta V_{\text{arr}}|^2$ is utilized to minimize the transfer maneuver cost. The constraints and design variables defined for the shooting method are employed for the optimization scheme, such that the resultant geometry is a three maneuver locally mass-optimal exterior-type transfer. The end-to-end transfers presented in Figures 6.36(a), 6.37(a), 6.38(a) and 6.39(a) are optimized to realize the solutions depicted in Figures 6.36(b), 6.37(b), 6.38(b) and 6.39(b), respectively. The presented transfer design framework enables the recognition of local solutions basin characterized by selected two intermediate orbits and allows for the construction of feasible maneuver cost and TOF pathways that link an NRHO and a DRO.

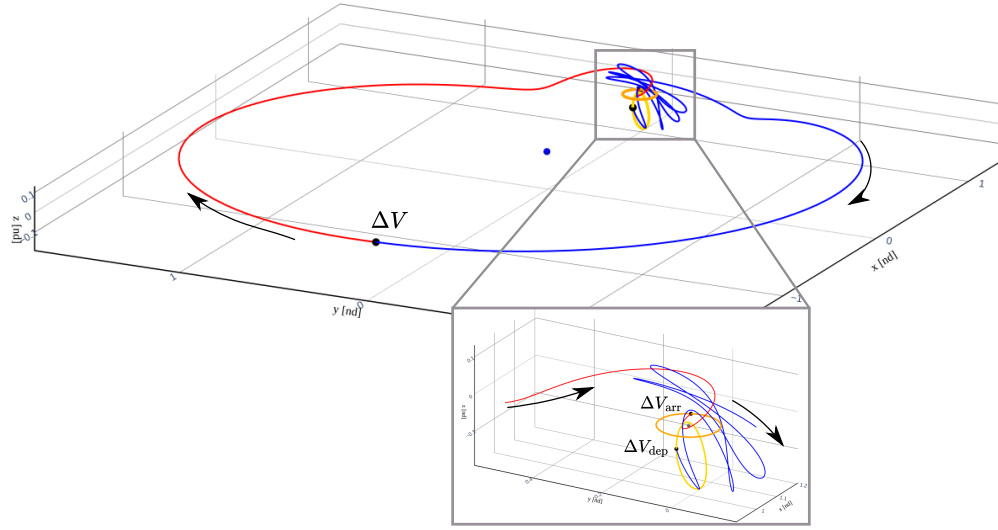


(a) Differentially corrected transfer, $\Delta V_{tot} = \Delta V_{dep} + \Delta V + \Delta V_{arr} = 273.622 + 203.583 + 425.671 = 902.876$ m/s, TOF = 99.844 days.

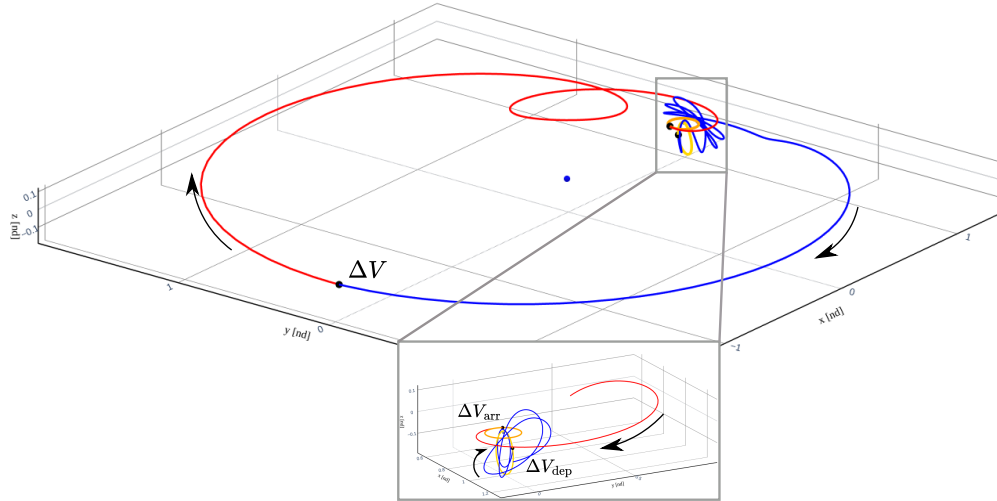


(b) Optimized transfer, $\Delta V_{tot} = \Delta V_{dep} + \Delta V + \Delta V_{arr} = 261.105 + 108.795 + 153.828 = 523.729$ m/s, TOF = 115.161 days

Figure 6.36. Exterior-type end-to-end differentially corrected and optimized transfers informed by an L_2 vertical orbit and a 3:4 RPO. The outbound segment from an NRHO to the far-side of the Earth (blue) requires a maneuver to overcome the velocity discontinuity with the inbound segment from the far-side of the Earth to a DRO (red).

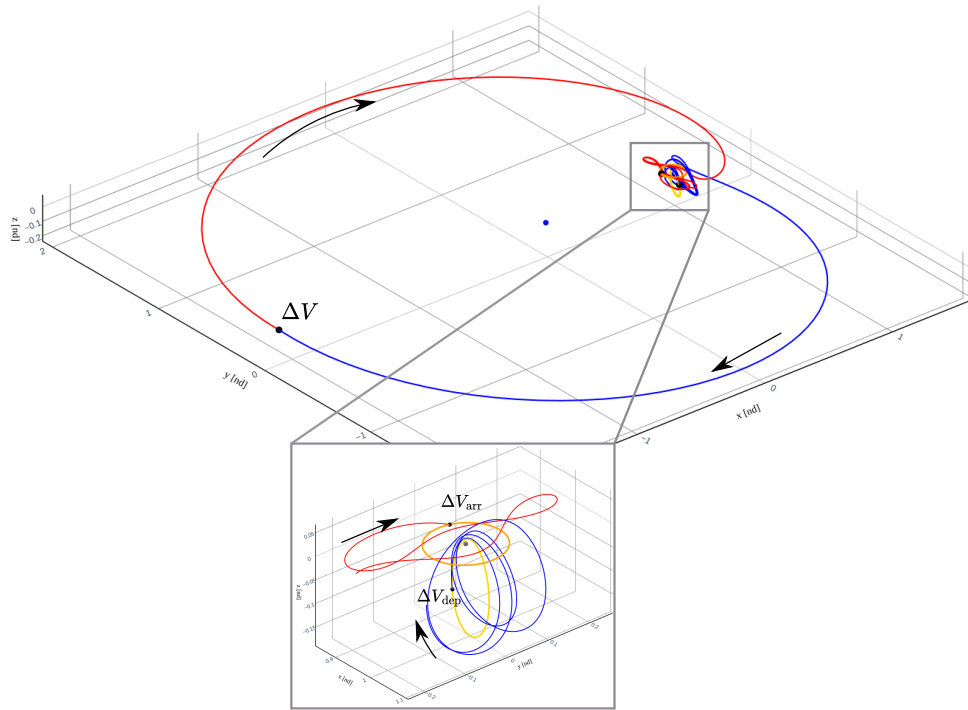


(a) Differentially corrected transfer, $\Delta V_{tot} = \Delta V_{dep} + \Delta V + \Delta V_{arr} = 130.789 + 16.231 + 472.628 = 619.649$ m/s, TOF = 127.534 days.

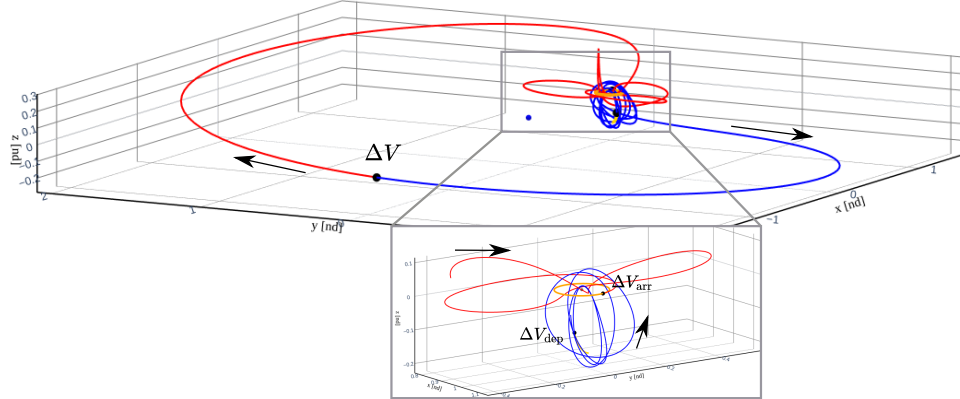


(b) Optimized transfer, $\Delta V_{tot} = \Delta V_{dep} + \Delta V + \Delta V_{arr} = 86.254 + 105.437 + 58.414 = 250.106$ m/s, TOF = 135.018 days.

Figure 6.37. Exterior-type end-to-end differentially corrected and optimized transfers informed by an L_2 quasi-vertical orbit and a 3:4 RPO. The outbound segment from an NRHO to the far-side of the Earth (blue) requires a maneuver to overcome the velocity discontinuity with the inbound segment from the far-side of the Earth to a DRO (red).

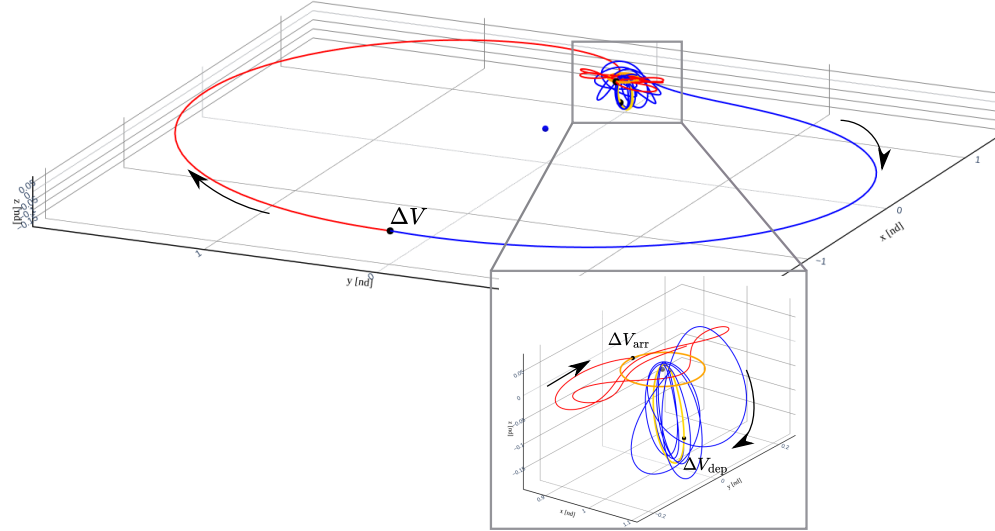


(a) Differentially corrected transfer, $\Delta V_{\text{tot}} = \Delta V_{\text{dep}} + \Delta V + \Delta V_{\text{arr}} = 103.549 + 88.261 + 366.775 = 558.585$ m/s, TOF = 150.697 days.

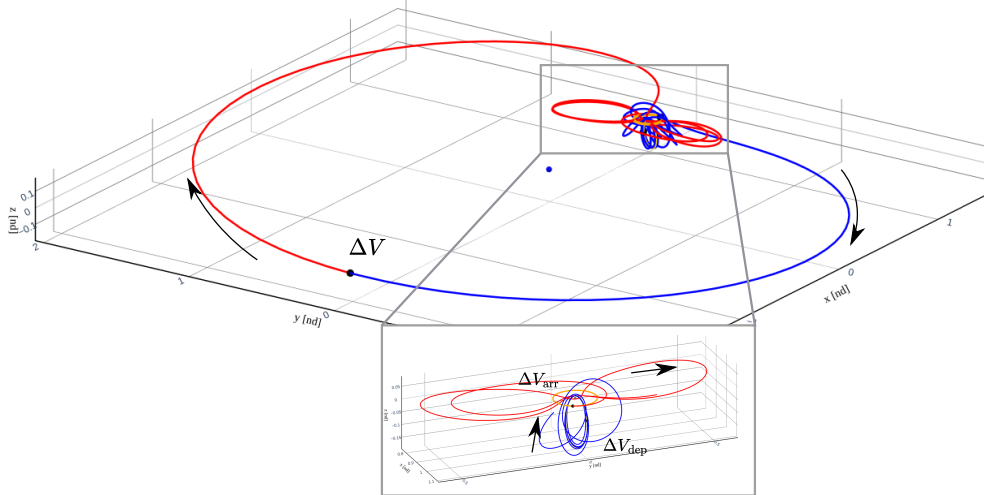


(b) Optimized transfer, $\Delta V_{\text{tot}} = \Delta V_{\text{dep}} + \Delta V + \Delta V_{\text{arr}} = 62.064 + 17.768 + 113.701 = 193.534$ m/s, TOF = 174.708 days.

Figure 6.38. Exterior-type end-to-end differentially corrected and optimized transfers informed by an L_2 P2HO₂ orbit and a DPO. The outbound segment from an NRHO to the far-side of the Earth (blue) requires a maneuver to overcome the velocity discontinuity with the inbound segment from the far-side of the Earth to a DRO (red).



(a) Differentially corrected transfer, $\Delta V_{tot} = \Delta V_{dep} + \Delta V + \Delta V_{arr} = 20.759 + 73.338 + 400.426 = 494.524$ m/s, TOF = 179.871 days.



(b) Optimized transfer, $\Delta V_{tot} = \Delta V_{dep} + \Delta V + \Delta V_{arr} = 6.033 + 82.995 + 29.289 = 118.318$ m/s, TOF = 220.296 days.

Figure 6.39. Exterior-type end-to-end differentially corrected and optimized transfers informed by an L_2 quasi-P2HO₂ orbit and a DPO. The outbound segment from an NRHO to the far-side of the Earth (blue) requires a maneuver to overcome the velocity discontinuity with the inbound segment from the far-side of the Earth to a DRO (red).

7. CONCLUDING REMARKS

The identification of low maneuver cost transfers with reasonable flight times is crucial for the development of a sustainable space economy in the cislunar region. Multiple strategies have been proposed by a number of authors to assist in uncovering feasible solutions. In this investigation, a methodology is presented that incorporates a quasi-periodic orbit as an option for design of transfer scenarios. The described framework is leveraged to construct transfers between periodic orbits. Two different classes of pathways for a sample case of transfers from an L_2 NRHO to a DRO are generated: interior-type and exterior-type transfers. The construction of the two types of connections is decomposed into multiple segments that are derived from the phase space characterized by selected intermediate orbits.

The task of constructing QPOs and incorporating their associated manifolds for transfer design is challenging due to the high dimensionality of the solution space. Nonetheless, a step-by-step strategy is defined that reduces the complexity of employing the manifolds associated with a QPO to design transfer geometries with reasonable cost. The departure and arrival orbits are selected to possess the same JC value. Hence, the *5-dimensional* manifold corresponding to a QPO family is narrowed down to the *4-dimensional* stable/unstable manifolds corresponding to a QPO constant energy family at the same JC value as the departure/arrival orbit. Thereafter, a visualization technique is presented that aids in comparing the quality of the initial guess offered by the *3-dimensional* stable/unstable manifolds associated with different QPOs along a constant energy family. A QPO member of the constant energy family is selected that delivers significantly different geometries compared to the ones derived from the underlying periodic orbit for the construction of end-to-end transfers. Additionally, the visualization method assists in constructing bridging arcs to link segments that approach and depart an intermediate QPO. The multiple segments are stitched together using a shooting method to obtain end-to-end transfers and locally mass-optimal solutions are uncovered by employing a constraint direct optimization scheme.

A number of interior-type and exterior-type geometries are computed by employing the framework with the following as intermediate orbits: L_2 vertical, L_2 southern halo, L_2 P2HO₁, L_2 P2HO₂, planar 3:4 RPO, DPO, L_2 quasi-vertical and L_2 quasi-P2HO₂ orbit.

For intermediate periodic orbits, various locally unique outbound segments from the departure orbit and inbound segments to the arrival orbit are constructed. Thereafter, the lowest maneuver cost inbound and outbound segments corresponding to a common intermediate periodic orbit are linked to design end-to-end transfers. It is notable that a mission designer has the flexibility to pair any identified outbound and inbound segments characterized by a common periodic orbit to design end-to-end transfers. Similarly, multiple local families of outbound and inbound segments are designed through intermediate QPOs. The QPO derived segments are linked with bridging arcs to obtain end-to-end geometries. Due to the non-repeatable nature of the flow along a QPO, only a subset of the inbound and outbound segments can be paired to yield maneuver-free short TOF end-to-end pathways. Nonetheless, the solutions offered by intermediate QPOs extend beyond geometries obtained through their underlying periodic orbits. Additionally, it is observed that the QPO derived transfers are more fuel efficient than the ones constructed through their underlying periodic orbits.

7.1 Recommendations for Future Work

The presented methodology allows for the design of preliminary transfer trajectories. There is a need to validate the presented end-to-end pathways in a higher-fidelity model that at least accounts for direct and indirect perturbations due to the gravity of the Sun and the Jupiter. Additionally, periodic and quasi-periodic orbits around the L_1 point can be leveraged to identify additional local solution basins of the sample case. The described methodology may even be employed to construct transfers between departure and arrival periodic/quasi-periodic orbits at different energy levels, and select potential candidate QPOs at an intermediate energy level. It is even worth incorporating low-thrust propulsion capabilities in lieu of impulsive maneuvers to reveal unrealized solution basins. A complication of employing QPOs in the design process is the computational and time complexity of computing QPOs using the GMOS algorithm. The computational complexity in constructing QPOs may be reduced by leveraging the CR3BP symmetry properties. Alternatively, it may be of interest to investigate the placement of the initial invariant curve around a QPO that

minimizes the number of states required to approximate the curve and allows for the efficient numerical continuation of QPOs along their biparameteric families.

A. PLOTS OF PERIODIC ORBITS AND THEIR STABILITY INDICES

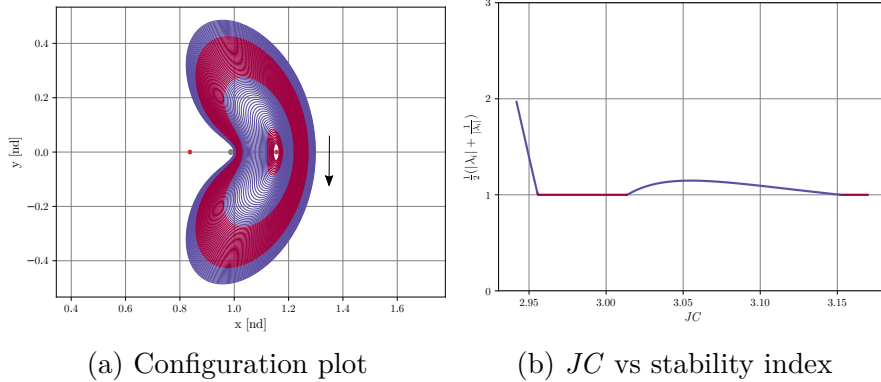


Figure A.1. The L_2 Lyapunov orbit family members in the Earth-Moon system and stability index, where crimson: family members with atleast one non-trivial *2-dimensional* center subspace

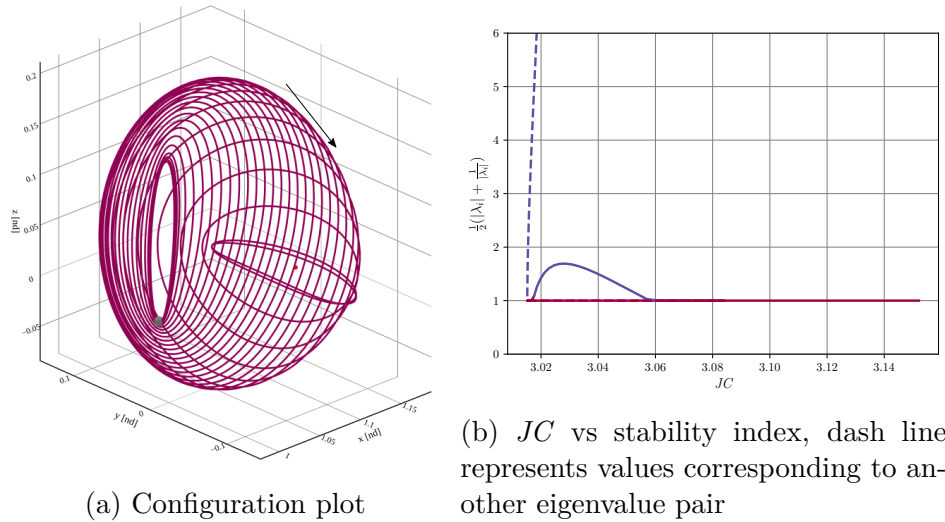


Figure A.2. The southern L_2 halo orbit family members in the Earth-Moon system and stability index, where crimson: family members with atleast one non-trivial *2-dimensional* center subspace

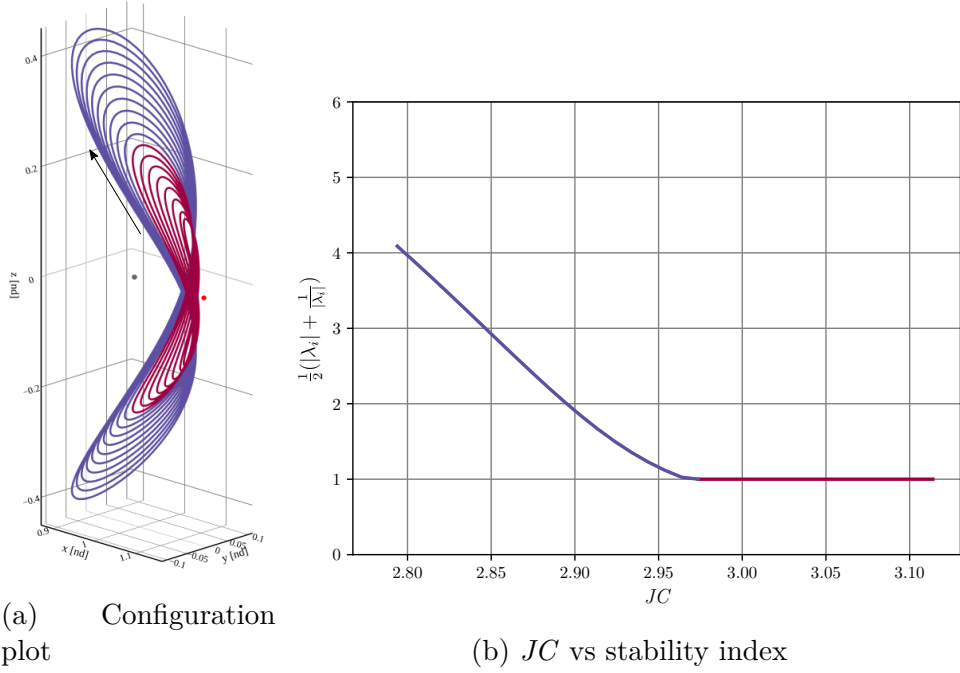


Figure A.3. The L_2 vertical orbit family members in the Earth-Moon system and stability index, where crimson: family members with atleast one non-trivial 2-dimensional center subspace

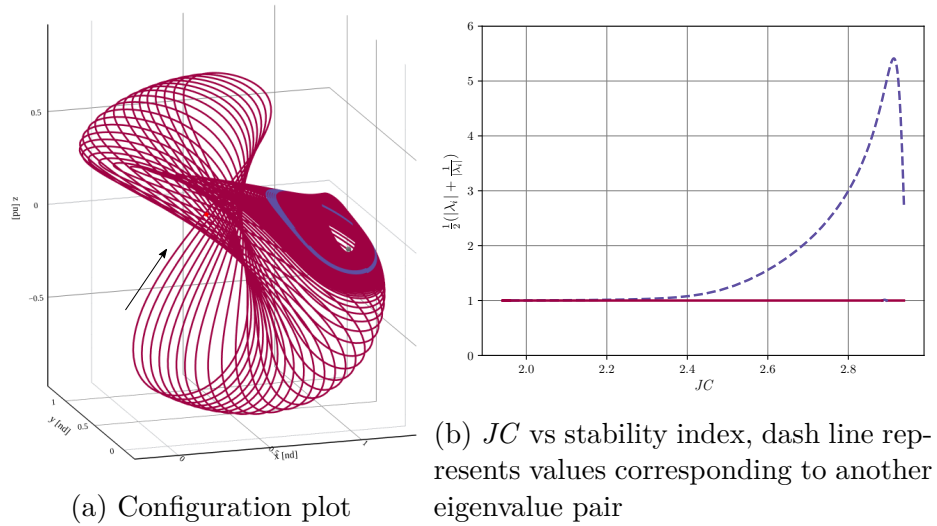


Figure A.4. The northern L_4 axial orbit family members in the Earth-Moon system and stability index, where crimson: family members with atleast one non-trivial 2-dimensional center subspace

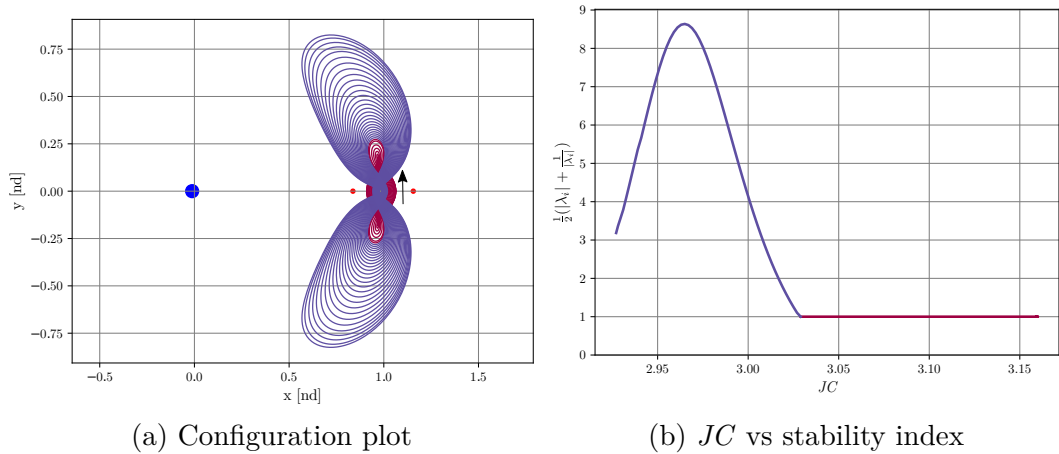


Figure A.5. The Moon-centered distant prograde orbit family members in the Earth-Moon system and stability index, where crimson: family members with atleast one non-trivial *2-dimensional* center subspace

B. INITIAL CONDITIONS FOR QPT

Table B.1. Initial conditions for an invariant curve on the L_2 quasi-halo ($T^0 = 6.56235$ days, $\rho^0 = 0.80705$ rad, $JC_{\text{avg}} = 3.04606$) in the Earth-Moon system ($\mu = 0.0121506$, $l^* = 384400$ km), depicted in Figure 5.5(c). The torus is obtained through continuation along the constant mappinng time family originating from the center subspace associated with an L_2 halo orbit ($JC = 3.04649$, $\mathbb{P} = 6.56235$ days). It is suggested to retarget the torus with $N=45$ initial states of the Fourier series described by the following 25 states.

	x	y	z	\dot{x}	\dot{y}	\dot{z}
\bar{x}_{PO}^*	1.0220282	0.0000000	-0.1821014	0.0000000	-0.1032710	0.0000000
\bar{u}_1^1	-0.0142355	0.0000018	-0.0045168	0.0000019	0.0362060	-0.0000135
\bar{u}_2^1	-0.0138507	0.0022946	-0.0043755	0.0040043	0.0352041	0.0059143
\bar{u}_3^1	-0.0127146	0.0044405	-0.0039579	0.0077594	0.0322482	0.0115448
\bar{u}_4^1	-0.0108816	0.0063016	-0.0032834	0.0110331	0.0274895	0.0165847
\bar{u}_5^1	-0.0084422	0.0077571	-0.0023850	0.0136186	0.0211768	0.0207501
\bar{u}_6^1	-0.0055217	0.0087124	-0.0013087	0.0153491	0.0136517	0.0237756
\bar{u}_7^1	-0.0022794	0.0091061	-0.0001136	0.0161105	0.0053388	0.0254291
\bar{u}_8^1	0.0010948	0.0089168	0.0011305	0.0158512	-0.0032676	0.0255319
\bar{u}_9^1	0.0043873	0.0081643	0.0023452	0.0145879	-0.0116269	0.0239844
\bar{u}_{10}^1	0.0073743	0.0069080	0.0034487	0.0124053	-0.0191837	0.0207936
\bar{u}_{11}^1	0.0098402	0.0052384	0.0043615	0.0094489	-0.0254084	0.0160998
\bar{u}_{12}^1	0.0115990	0.0032663	0.0050142	0.0059109	-0.0298439	0.0101881
\bar{u}_{13}^1	0.0125145	0.0011115	0.0053546	0.0020141	-0.0321519	0.0034796
\bar{u}_{14}^1	0.0125146	-0.0011043	0.0053548	-0.0020038	-0.0321522	-0.0035066
\bar{u}_{15}^1	0.0115993	-0.0032592	0.0050147	-0.0059009	-0.0298447	-0.0102151
\bar{u}_{16}^1	0.0098406	-0.0052316	0.0043624	-0.0094393	-0.0254097	-0.0161267
\bar{u}_{17}^1	0.0073749	-0.0069015	0.0034498	-0.0123964	-0.0191854	-0.0208207
\bar{u}_{18}^1	0.0043880	-0.0081582	0.0023465	-0.0145797	-0.0116290	-0.0240114
\bar{u}_{19}^1	0.0010956	-0.0089111	0.0011318	-0.0158438	-0.0032699	-0.0255590
\bar{u}_{20}^1	-0.0022786	-0.0091009	-0.0001122	-0.0161039	0.0053365	-0.0254561
\bar{u}_{21}^1	-0.0055210	-0.0087075	-0.0013075	-0.0153432	0.0136495	-0.0238026
\bar{u}_{22}^1	-0.0084416	-0.0077527	-0.0023839	-0.0136134	0.0211749	-0.0207772
\bar{u}_{23}^1	-0.0108811	-0.0062975	-0.0032826	-0.0110286	0.0274879	-0.0166118
\bar{u}_{24}^1	-0.0127143	-0.0044367	-0.0039573	-0.0077553	0.0322471	-0.0115719
\bar{u}_{25}^1	-0.0138506	-0.0022909	-0.0043752	-0.0040005	0.0352035	-0.0059414

Table B.2. Initial conditions for an invariant curve on the L_1 quasi-Lyapunov orbit ($T^0 = 11.87639$ days, $\rho^0 = 0.08386$ rad, $JC_{\text{avg}} = 3.17556$) in the Earth-Moon system ($\mu = 0.0121506$, $l^* = 384400$ km), plotted in Figure 5.6(b). The torus is generated through continuation along the constant frequency ratio family originating from the center subspace associated with an L_1 Lyapunov orbit ($JC = 3.17744$, $\mathbb{P} = 11.86023$ days). It is recommended to retarget the torus with $N=51$ initial states of the Fourier series described by the following 25 states.

	x	y	z	\dot{x}	\dot{y}	\dot{z}
\bar{x}_{PO}^*	0.8524151	0.0000000	0.0000000	0.0000000	-0.1174198	0.0000000
\bar{u}_1^1	0.0013393	0.0009291	0.0000624	0.0003074	-0.0088478	0.0162079
\bar{u}_2^1	0.0013229	0.0021585	-0.0033303	0.0005541	-0.0085219	0.0156199
\bar{u}_3^1	0.0012773	0.0031221	-0.0065947	0.0007574	-0.0076660	0.0141169
\bar{u}_4^1	0.0012118	0.0035865	-0.0095722	0.0008687	-0.0064750	0.0117331
\bar{u}_5^1	0.0011413	0.0034134	-0.0120569	0.0008524	-0.0052334	0.0085531
\bar{u}_6^1	0.0010839	0.0026144	-0.0138121	0.0007013	-0.0042546	0.0047426
\bar{u}_7^1	0.0010558	0.0013775	-0.0146262	0.0004494	-0.0037978	0.0005578
\bar{u}_8^1	0.0010655	0.0000316	-0.0143855	0.0001670	-0.0039878	-0.0036786
\bar{u}_9^1	0.0011101	-0.0010567	-0.0131220	-0.0000638	-0.0047730	-0.0076315
\bar{u}_{10}^1	0.0011765	-0.0016071	-0.0110002	-0.0001822	-0.0059425	-0.0110131
\bar{u}_{11}^1	0.0012467	-0.0015049	-0.0082534	-0.0001666	-0.0071941	-0.0136224
\bar{u}_{12}^1	0.0013037	-0.0008070	-0.0051127	-0.0000320	-0.0082208	-0.0153501
\bar{u}_{13}^1	0.0013353	0.0003008	-0.0017665	0.0001838	-0.0087842	-0.0161546
\bar{u}_{14}^1	0.0013351	0.0015601	0.0016416	0.0004330	-0.0087587	-0.0160294
\bar{u}_{15}^1	0.0013033	0.0026897	0.0049874	0.0006644	-0.0081506	-0.0149815
\bar{u}_{16}^1	0.0012462	0.0034283	0.0081311	0.0008273	-0.0070961	-0.0130314
\bar{u}_{17}^1	0.0011760	0.0035830	0.0108907	0.0008778	-0.0058407	-0.0102344
\bar{u}_{18}^1	0.0011098	0.0030845	0.0130404	0.0007926	-0.0046926	-0.0067127
\bar{u}_{19}^1	0.0010654	0.0020325	0.0143470	0.0005842	-0.0039492	-0.0026779
\bar{u}_{20}^1	0.0010558	0.0006946	0.0146393	0.0003067	-0.0038109	0.0015753
\bar{u}_{21}^1	0.0010841	-0.0005655	0.0138738	0.0000405	-0.0043161	0.0057102
\bar{u}_{22}^1	0.0011416	-0.0014106	0.0121545	-0.0001394	-0.0053275	0.0094085
\bar{u}_{23}^1	0.0012122	-0.0016377	0.0096897	-0.0001909	-0.0065781	0.0124231
\bar{u}_{24}^1	0.0012777	-0.0012211	0.0067193	-0.0001121	-0.0077528	0.0146003
\bar{u}_{25}^1	0.0013232	-0.0002893	0.0034555	0.0000686	-0.0085712	0.0158687

REFERENCES

- [1] I. Mitrofanov, L. Zelenyi, V. Tretyakov, and D. Kalashnikov, “Luna-25: The first polar mission to the moon,” *Solar System Research*, vol. 55, pp. 485–495, 2021.
- [2] *Chandrayaan-3*. [Online]. Available: https://www.isro.gov.in/Chandrayaan3_New.html.
- [3] X. Zeng, X. Li, and J. Liu, “Exotic clasts in change-5 regolith indicative of unexplored terrane on the moon,” *Nature Astronomy*, vol. 7, no. 2, pp. 152–159, 2023.
- [4] *Ispace hakuto-r*. [Online]. Available: <https://ispace-inc.com/hakuto-r/eng/>.
- [5] *Intuitive machines im-1*. [Online]. Available: <https://www.intuitivemachines.com/im-1>.
- [6] D. E. Lee, “Gateway destination orbit model: A continuous 15 year nrho reference trajectory,” *NASA Johnson Space Center White Paper*, 2019.
- [7] G. Chavers, L. Watson-Morgan, M. Smith, N. Suzuki, and T. Polsgrove, “Nasa’s human landing system: The strategy for the 2024 mission and future sustainability,” in *2020 IEEE Aerospace Conference*, 2020, pp. 1–9.
- [8] L Xu, Y. Zou, and L Qin, “Overview of china’s lunar exploration program and scientific vision for future missions,” in *50th Annual Lunar and Planetary Science Conference*, 2019, p. 2440.
- [9] P. Lonergan, *Air force research laboratory oracle*, 2023. [Online]. Available: <https://afresearchlab.com/news/new-afrl-mission-area-leads-integrate-execute-space-st-needs/>.
- [10] *National cislunar science technology strategy - the white house*. [Online]. Available: <https://www.whitehouse.gov/wp-content/uploads/2022/11/11-2022-NSTC-National-Cislunar-ST-Strategy.pdf>.
- [11] A. L. Batcha, J. Williams, T. F. Dawn, *et al.*, “Artemis i trajectory design and optimization,” in *2020 AAS/AIAA Astrodynamics Specialist Conference*, 2020.

- [12] E. M. Zimovan-Spreen, K. C. Howell, and D. C. Davis, “Dynamical structures nearby nrhos with applications to transfer design in cislunar space,” *The Journal of the Astronautical Sciences*, vol. 69, no. 3, pp. 718–744, 2022.
- [13] R. E. Pritchett, “Strategies for low-thrust transfer design based on direct collocation techniques,” Ph.D. dissertation, Purdue University, 2020.
- [14] B. J. P. Pino, “Energy-informed strategies for low-thrust trajectory design in cislunar space,” Ph.D. dissertation, Purdue University, 2020.
- [15] V. Muralidharan and K. C. Howell, “Stretching directions in cislunar space: Applications for departures and transfer design,” *Astrodynamicics*, vol. 7, no. 2, pp. 153–178, 2023.
- [16] S. Vutukuri, “Spacecraft trajectory design techniques using resonant orbits,” Ph.D. dissertation, Purdue University, 2018.
- [17] A. Das, “Artificial intelligence aided rapid trajectory design in complex dynamical environments,” Ph.D. dissertation, Purdue University, 2019.
- [18] S. L. McCarty, L. M. Burke, and M. McGuire, “Parallel monotonic basin hopping for low thrust trajectory optimization,” in *2018 Space Flight Mechanics Meeting*, 2018, p. 1452.
- [19] G. Lantoine, “Efficient nrho to dro transfers in cislunar space,” 2017.
- [20] R. W. Farquhar and A. A. Kamel, “Quasi-periodic orbits about the translunar libration point,” *Celestial mechanics*, vol. 7, no. 4, pp. 458–473, 1973.
- [21] D. L. Richardson and N. D. Cary, “A uniformly valid solution for motion about the interior libration point of the perturbed elliptic-restricted problem,” in *AIAA Conference on the Exploration of the Outer Planets*, 1975.
- [22] K. C. Howell and H. J. Pernicka, “Numerical determination of lissajous trajectories in the restricted three-body problem,” *Celestial mechanics*, vol. 41, no. 1-4, pp. 107–124, 1987.
- [23] G. Gómez, J. Masdemont, and C. Simó, “Quasihalo orbits associated with libration points,” *The Journal of the Astronautical Sciences*, vol. 46, pp. 135–176, 1998.

- [24] A. Jorba and J. Masdemont, “Dynamics in the center manifold of the collinear points of the restricted three body problem,” *Physica D: Nonlinear Phenomena*, vol. 132, no. 1-2, pp. 189–213, 1999.
- [25] G. Gómez and J. M. Mondelo, “The dynamics around the collinear equilibrium points of the rtbp,” *Physica D: Nonlinear Phenomena*, vol. 157, no. 4, pp. 283–321, 2001.
- [26] Z. P. Olikara and D. J. Scheeres, “Numerical method for computing quasi-periodic orbits and their stability in the restricted three-body problem,” *Advances in the Astronautical Sciences*, vol. 145, no. 911-930, pp. 911–930, 2012.
- [27] B. McCarthy, “Cislunar trajectory design methodologies incorporating quasi-periodic structures with applications,” Ph.D. dissertation, Purdue University, 2022.
- [28] J. A. O. Romero, “Trajectory design strategies from geosynchronous transfer orbits to lagrange point orbits in the sun-earth system,” Ph.D. dissertation, Purdue University, 2021.
- [29] D. B. Henry and D. J. Scheeres, “A survey of heteroclinic connections in the earth-moon system,” *system*, vol. 2, no. y2, p. 2, 2022.
- [30] S. Bonasera, “Incorporating machine learning into trajectory design strategies in multi-body systems,” Ph.D. dissertation, University of Colorado at Boulder, 2022.
- [31] N. Baresi, Z. P. Olikara, and D. J. Scheeres, “Fully numerical methods for continuing families of quasi-periodic invariant tori in astrodynamics,” *The Journal of the astronautical sciences*, vol. 65, pp. 157–182, 2018.
- [32] A. Haro, M. Canadell, J.-L. Figueras, A. Luque, and J.-M. Mondelo, “The parameterization method for invariant manifolds,” *Applied mathematical sciences*, vol. 195, 2016.
- [33] B. Kumar, R. L. Anderson, R. de la Llave, and B. Gunter, “Computation and analysis of jupiter-europa and jupiter-ganymede resonant orbits in the planar concentric circular restricted 4-body problem,” *arXiv preprint arXiv:2109.14815*, 2021.
- [34] G Gómez and J Masdemont, “Some zero cost transfers between libration point orbits,” *Advances in the Astronautical Sciences*, vol. 105, no. 2, pp. 1199–1216, 2000.

- [35] R. C. Calleja, E. J. Doedel, A. R. Humphries, A. Lemus-Rodríguez, and E. B. Oldeman, “Boundary-value problem formulations for computing invariant manifolds and connecting orbits in the circular restricted three body problem,” *Celestial Mechanics and Dynamical Astronomy*, vol. 114, no. 1-2, pp. 77106, 2012. DOI: [10.1007/s10569-012-9434-y](https://doi.org/10.1007/s10569-012-9434-y).
- [36] B. McCarthy and K. Howell, “Construction of heteroclinic connections between quasi-periodic orbits in the three-body problem,” *The Journal of the Astronautical Sciences*, vol. 70, no. 4, pp. 1–16, 2023.
- [37] R. L. Restrepo, R. P. Russell, M. W. Lo, and T. P. McElarth, “Europa lander trajectory design using lissajous staging orbits,” in *AAS/AIAA Astrodynamics Specialist Conference, Snowbird, Utah*, 2018.
- [38] D. C. Folta, M. Woodard, K. Howell, C. Patterson, and W. Schlei, “Applications of multi-body dynamical environments: The artemis transfer trajectory design,” *Acta Astronautica*, vol. 73, pp. 237–249, 2012.
- [39] I. Newton, I. B. Cohen, and K. Alexandre, *Philosophiae Naturalis Principia Mathematica*. Univesity Press, 1972.
- [40] K. R. Meyer and D. C. Offin, *Introduction to hamiltonian dynamical systems and the N-body problem*. Springer International Publishing, 2018.
- [41] V. G. Szebehely, *Theory of orbits: The restricted problem of three bodies*. Academic Press, 1967.
- [42] K. A. C. Howell, “Three-dimensional, periodic halo orbits in the restricted three-body problem,” English, Copyright - Database copyright ProQuest LLC; ProQuest does not claim copyright in the individual underlying works; Last updated - 2022-10-22, Ph.D. dissertation, 1983, p. 141, ISBN: 9798661588975. [Online]. Available: <https://www.proquest.com/dissertations-theses/three-dimensional-periodic-halo-orbits-restricted/docview/303183159/se-2>.
- [43] D. C. Folta, M. Woodard, K. Howell, C. Patterson, and W. Schlei, “Applications of multi-body dynamical environments: The artemis transfer trajectory design,” *Acta Astronautica*, vol. 73, pp. 237249, 2012. DOI: [10.1016/j.actaastro.2011.11.007](https://doi.org/10.1016/j.actaastro.2011.11.007).
- [44] J. S. Parker and R. L. Anderson, *Low-energy lunar trajectory design*. Wiley, 2014.

- [45] S. Wiggins, *Introduction to applied nonlinear dynamical systems and Chaos*. World Publishing Corporation, 2013.
- [46] J. R. Martins, P. Sturdza, and J. J. Alonso, “The complex-step derivative approximation,” *ACM Transactions on Mathematical Software*, vol. 29, no. 3, pp. 245262, 2003. DOI: [10.1145/838250.838251](https://doi.org/10.1145/838250.838251).
- [47] G. Strang, *Linear algebra and its applications. Second edition*. Academic Press, 1979.
- [48] J.-P. Almanza-Soto, “Zero-momentum point analysis and ephemeris transition for interior earth to libration point orbit transfers,” M.S. thesis, Purdue University, 2023.
- [49] H. B. Keller, “Constructive methods for bifurcation and nonlinear eigenvalue problems,” in *Computing Methods in Applied Sciences and Engineering, 1977, I*, R. Glowinski, J. L. Lions, and I. Laboria, Eds., Berlin, Heidelberg: Springer Berlin Heidelberg, 1979, pp. 241–251, ISBN: 978-3-540-35411-6.
- [50] V. Domingo, B. Fleck, and A. I. Poland, “The soho mission: An overview,” *Solar Physics*, vol. 162, no. 1-2, pp. 137, 1995. DOI: [10.1007/bf00733425](https://doi.org/10.1007/bf00733425).
- [51] M. W. Lo, B. G. Williams, W. E. Bollman, *et al.*, “Genesis mission design,” *The Journal of the astronautical sciences*, vol. 49, no. 1, pp. 169–184, 2001.
- [52] N. I. Sadaka, “There and back again: Generating repeating transfers using resonant structures,” M.S. thesis, Purdue University, 2023.
- [53] E. M. Zimovan, “Characteristics and design strategies for near rectilinear halo orbits within the earth-moon system,” M.S. thesis, Purdue University, 2017.
- [54] D. Grebow, “Generating periodic orbits in the circular restricted three-body problem with applications to lunar south pole coverage,” M.S. thesis, Purdue University, 2006.
- [55] A. E. Roy and M. W. Ovenden, “On the Occurrence of Commensurable Mean Motions in the Solar System: The Mirror Theorem,” *Monthly Notices of the Royal Astronomical Society*, vol. 115, no. 3, pp. 296–309, Jun. 1955, ISSN: 0035-8711. DOI: [10.1093/mnras/115.3.296](https://doi.org/10.1093/mnras/115.3.296). eprint: <https://academic.oup.com/mnras/article-pdf/115/3/296/9404588/mnras115-0296.pdf>. [Online]. Available: <https://doi.org/10.1093/mnras/115.3.296>.

- [56] I. A. Robin and V. V. Markellos, “Numerical determination of three-dimensional periodic orbits generated from vertical self-resonant satellite orbits,” *Celestial Mechanics*, vol. 21, no. 4, pp. 395–434, 1980. DOI: [10.1007/bf01231276](https://doi.org/10.1007/bf01231276).
- [57] E. Doedel, A. Champneys, T. Fairgrieve, Y. Kuznetsov, B. Sandstede, and X. Wang, “Auto 97: Continuation and bifurcation software for ordinary differential equations (with homcont),” Jun. 1999.
- [58] B. A. Steves, A. J. Maciejewski, and M. Hendry, *Chaotic Worlds: From Order to Disorder in Gravitational N-Body Dynamical Systems*. Springer Science & Business Media, 2006, vol. 227.
- [59] R. J. Power, “Characterization of lunar access relative to cislunar orbits,” M.S. thesis, Purdue University, 2019.
- [60] L. Perko, *Differential equations and dynamical systems*. Springer Science & Business Media, 2013, vol. 7.
- [61] T. Swenson, M. Lo, B. D. Anderson, and T. Gorordo, “The topology of transport through planar lyapunov orbits,” *2018 Space Flight Mechanics Meeting*, 2018. DOI: [10.2514/6.2018-1692](https://doi.org/10.2514/6.2018-1692).
- [62] G. Gómez, A. Jorba, J. Masdemont, and C. Simo, *Study refinement of semi-analytical Halo Orbit Theory: Executive summary*. Fundació Bosch i Gimpera, 1991.
- [63] M. J. Bolliger, “Cislunar mission design: Transfers linking near rectilinear halo orbits and the butterfly family,” M.S. thesis, Purdue University, 2019.
- [64] K. Howell, J. Guzmán, and J. Anderson, “Trajectory arcs with lunar encounters for transfers to small amplitude lissajous orbits,” vol. 108, Jan. 2001.
- [65] K. Howell, D. Mains, and B. Barden, “Transfer trajectories from earth parking orbits to sun-earth halo orbits,” *Spaceflight mechanics 1994*, pp. 399–422, 1994.
- [66] F. Schilder, H. M. Osinga, and W. Vogt, “Continuation of quasi-periodic invariant tori,” *SIAM Journal on Applied Dynamical Systems*, vol. 4, no. 3, pp. 459–488, 2005.
- [67] N. Bosanac, “Bounded motions near resonant orbits in the earth-moon and sun-earth systems,” in *AAS/AIAA Astrodynamics Specialist Conference, Snowbird, Utah*, 2018.

- [68] À. Jorba, “Numerical computation of the normal behaviour of invariant curves of n-dimensional maps,” *Nonlinearity*, vol. 14, no. 5, p. 943, 2001.
- [69] R. Gomez, “Exploring the trade space for two-maneuver transfers from earth to cis-lunar libration point orbits,” M.S. thesis, Purdue University, 2021.
- [70] P. A. Whittington, “Multi-body trajectory design in the earth-moon region utilizing poincare maps,” M.S. thesis, Purdue University, 2022.
- [71] A. Wächter and L. T. Biegler, “On the implementation of an interior-point filter line-search algorithm for large-scale nonlinear programming,” *Mathematical programming*, vol. 106, pp. 25–57, 2006.
- [72] N. B. LaFarge, “Reinforcement learning approaches for autonomous guidance and control in a low-thrust, multi-body dynamical environment,” Ph.D. dissertation, Purdue University Graduate School, 2023.